Aspects of self-gravitating solitons and hairy black holes

Supakchai Ponglertsakul

School of Mathematics and Statistics

Submitted in partial fulfillment for the degree of PhD

June 2016

Supervisor: Prof. Elizabeth Winstanley

The University of Sheffield

Acknowledgments

Firstly I would like to thank my supervisor, Elizabeth, for her guidance, encouragement, support and patience during my time in Sheffield. She always had time for me whenever I needed. I especially thank her for being so understanding and very patient answering my questions. I could not have asked for a more attentive and supportive supervisor than her.

I must also thank Sam for introducing me into the world of black hole superradiance and for his collaboration on work in this thesis. I thank all past and current CRAG members for their help and friendship. I feel very lucky to be part of this group.

I thank my small but heartwarming group of Thai friends (+1 Korean, +1 Spanish) who made me feel not very far from home. I must show my gratitude toward the first generation of "Thai-village" at the Bathfield apartment as they helped me a lot particularly during the first few months of my time in the UK. I must say thank you to Aun, who has been my flat/house mate for three years, especially for her cookery and bakery skills.

Lastly, I thank to my family for their love and support, without whom I would not have been able to complete my PhD. I'll be home soon.

62 Summer Street, Sheffield

27th May 2016

Abstract

This thesis considers two particular systems of gravity coupled to matter: Einstein-non-Abelian-Proca (ENAP) theory with gauge group $SU(2)$ in asymptotically anti-de Sitter (AdS) spacetime and Einstein-charged-scalar theory in a cavity.

The first part of this thesis is devoted to the ENAP-AdS model. For a purely magnetic gauge field we obtain spherically symmetric solitons and black holes with non-Abelian Proca hair. This is achieved by solving the corresponding field equations numerically. We prove that the equilibrium gauge field must have at least one node. Then we turn to dyons and dyonic black holes which carry both electric and magnetic charge. We show that no non-trivial dyons or dyonic black holes exist in this model. We perturb the equilibrium solutions under linear, spherically symmetric perturbations of the metric and gauge field. We find numerical evidence which reveals that the solitons and hairy black holes are linearly unstable. These hairy black holes violate the generalized no-hair conjecture in the sense that they look identical to the Schwarzschild-AdS metric when observed from infinity.

In the second part of this thesis, we investigate a plausible end-point of the charged superradiant instability. We study the Einstein-Maxwell-Klein-Gordon (EMKG) equations with a mirror-like boundary condition. We construct numerical solitons and black holes with charged scalar hair. Then we study the stability of the equilibrium solutions under linear, spherically symmetric perturbations of the metric, electromagnetic and scalar fields. When the mirror is located at the first zero of the static scalar field, we find stable solitons if the mirror radius is sufficiently large. However when the mirror radius is sufficiently small, some solitons are found to be unstable. In the black hole case, we find no evidence of instability when the mirror is located at the first zero of the static scalar field. In contrast, numerical evidence shows that the hairy black holes are unstable if the mirror is located at the second zero of the static scalar field. We conclude that these stable hairy black holes could represent an end-point of the charged superradiant instability.

Preface

The majority of the work contained in this thesis was done by the author under the supervision of Prof. Elizabeth Winstanley.

- Chapter 1 is an introductory chapter where we state the two core questions that have been investigated in this thesis.

- Chapter 2 reviews the general concepts of black hole solutions, the no-hair conjecture, hairy black holes and superradiance.

- Chapter 3 is based on work done in collaboration with E. Winstanley [139]. Some of the known results for Einstein-non-Abelian-Proca (ENAP) theory in asymptotically flat spacetime [79] are reproduced and extended. All the analytic and numerical calculations related to ENAP in asymptotically anti-de Sitter (AdS) are original contributions by the author.

- Chapter 4 is based on work done in collaboration with S. R. Dolan and E. Winstanley, and published in [61, 140]. The analytic work, numerical results and production of figures for solitons and black holes were done by the author.

- Chapter 5 is a summary of the three projects considered in this thesis. This is followed by a review of future work that can be extended from the research done in this thesis.

The metric signature $(-,+,+,+)$ and units such that $(8\pi G = c = \hbar = k_B = 1)$ are assumed throughout this thesis, unless otherwise stated. All numerical results presented in this thesis were obtained using Mathematica 9 and 10.

Contents

List of Figures

Chapter 1

Introduction

The uniqueness theorem states that stationary black hole solutions of Einstein-Maxwell equations belong to the three-parameter Kerr-Newman family (see section 2.1). Inspired by the uniqueness theorem, the no-hair theorem postulates that all four dimensional, stationary black hole solutions of the Einstein-Maxwell equations in asymptotically flat spacetime can be uniquely described by three classical parameters; mass, electric charge and angular momentum.

In other words, Wheeler suggested that "black holes have no hair" [154] where hair is a metaphor for any form of non-gravitational and non-electromagnetic field that can be accessed by an external observer. Nevertheless, Wheeler's no-hair conjecture was violated very quickly. It turns out that there exist black hole solutions that can carry non-trivial matter fields outside an event horizon. These solutions are called *hairy black holes*. In this thesis, two particular models containing hairy solutions are studied. These are Einstein-non-Abelian-Proca (ENAP) theory in asymptotically anti-de Sitter (AdS) spacetime and Einstein-charged-scalar theory in a cavity. We consider the presence of solitons and hairy black holes in both models. The stability of these solutions is also investigated.

We start chapter 2 by giving a brief review of exact asymptotically flat, black hole solutions

of the Einstein and Einstein-Maxwell equations. We discuss the physical interpretation of these known solutions. The global structure of these solutions is explored by studying their Penrose diagrams. We state the no-hair conjecture and discuss its consequences. Then some important works on hairy black holes are reviewed. We focus our investigation on the $SU(2)$ non-Abelian sector since it is relevant to the ENAP model. To better understand the behaviour of black holes with non-Abelian hair, we reproduce and discuss particle-like solutions [7] and coloured black holes [24, 81, 188]. After that, black hole superradiance is investigated and the essential conditions for a superradiance process are derived. Some connections between superradiance and black hole mechanics are also discussed. We review and investigate in detail how black hole superradiance can lead to an instability. Finally, we provide analytical and numerical calculations that demonstrate that a massless charged scalar field on a Reissner-Nordström black hole in a cavity experiences a superradiant instability.

In chapter 3, we investigate ENAP theory in asymptotically AdS. We derive a set of field equations describing a self-gravitating non-Abelian Proca field with gauge group $SU(2)$. We provide boundary conditions corresponding to solitons and hairy black holes in this theory. Then we numerically integrate the associated field equations with these boundary conditions and obtain static solitons and black holes with non-Abelian Proca hair. As a good consistency check, we reproduce some numerical solitons and hairy black holes of ENAP in asymptotically flat spacetime, discovered in [79]. We also provide an analytic calculation that shows there are no nodeless solutions in this model. By following the work of Ershov and Galt'sov [71], our analysis reveals that no non-trivial dyon solutions or dyonic black holes are allowed in both the ENAP-flat and ENAP-AdS theories. Then we consider spherically symmetric perturbations around these equilibrium solutions. The perturbation equations can be decoupled into two categories: the gravitational and sphaleronic sectors. We present numerical analysis confirming the stability status of solitons and hairy black holes both in the ENAP-flat and ENAP-AdS theories.

In chapter 4, a possible end-point of the charged superradiant instability is studied. Einstein-charged-scalar theory in a cavity is considered. We provide an analytic proof showing that no non-trivial asymptotically flat soliton and hairy black hole solutions of the Einstein-Maxwell-Klein-Gordon equations exist. However, with a mirror-like boundary, it is possible to obtain static solitons and black holes with charged scalar hair. We investigate the stability of these equilibrium solutions under linear, spherically symmetric perturbations of the metric, electromagnetic and scalar fields. We provide numerical evidence suggesting the stability of solitons and hairy black holes in a cavity. We remark that the location of the mirror is at the first node of the scalar field for most of the solutions considered in this chapter. The total electric charge of the solitons is also discussed to better understand the stability properties of equilibrium soliton solutions.

Lastly, chapter 5 concludes the thesis and comments on further extensions of this work.

Chapter 2

Black holes, hair and superradiance

In this chapter, general ideas about black holes, the no-hair conjecture, black hole solutions with hair and superradiance will be discussed. We start by outlining some of the pioneering works on black hole uniqueness theorems which play a central role behind the original no-hair conjecture. We then outline the discovery of hairy black holes with various models of hair, especially focusing on non-Abelian gauge theory. Later we briefly describe two important pieces of work on the self-gravitating non-Abelian gauge system, i.e., particle-like solutions [7] and coloured black holes [24]. After that, we review some significant works on the stability of hairy black holes. Then we discuss the basic concepts of wave amplification via superradiant scattering. We derive an essential condition for superradiant scattering by considering reflection and transmission amplitudes. Next we explain how the laws of black hole mechanics and Hawking's area theorem [83] imply superradiance for bosonic fields. Finally we consider a particular scenario where superradiance gives rise to an instability. We shall describe how a superradiant instability can be triggered on rotating and charged black holes. At the end of this chapter, we provide an analytical and numerical analysis of a massless complex scalar field on a Reissner-Nordström (RN) black

hole enclosed by a mirror. We show numerical results which confirm that the RN black hole in a cavity is unstable via a charged superradiant instability.

§2.1 Black hole zoo

In this section, we discuss some of the well-known bald, asymptotically flat, exact black hole solutions of the Einstein and Einstein-Maxwell equations. We show explicitly the analytic form of these solutions and highlight some of the main features for each spacetime.

The first non-trivial exact black hole solution was found by Karl Schwarzschild in 1916 [158]. The Schwarzschild black hole in spherical coordinates takes the form

$$ds^2 = -\left(1-\frac{2M}{r}\right)dt^2 + \left(1-\frac{2M}{r}\right)^{-1} dr^2 + r^2\left(d\theta^2 + \sin^2\theta\, d\varphi^2\right), \tag{2.1}$$

where M represents the total mass. The Schwarzschild solution is obtained by solving the vacuum Einstein equations (so that the energy-momentum tensor vanishes identically). It describes the spacetime exterior to a static spherically symmetric object. The metric (2.1) possesses two singularities within finite radius r. The first one is at $r = 0$ which is an essential singularity or curvature singularity. This singularity cannot be removed by any coordinate transformations. It is where non-zero curvature scalar invariant quantities e.g., Kretschmann scalar $R_{abcd}R^{abcd}$, where R_{abcd} is the Riemann tensor, diverge. The second singularity occurs when $r = r_h$ and

$$r_h = 2M. \tag{2.2}$$

This is the event horizon of a Schwarzschild black hole. As will be seen below, no physical signal in the region $r \leq 2M$ can reach infinity. One remarkable feature of the Schwarzschild metric is that it can be uniquely described by just one parameter M. By knowing the mass, we can determine the entire spacetime geometry.

In Fig 2.1, we show the Penrose diagram of a Schwarzschild black hole. In the diagram

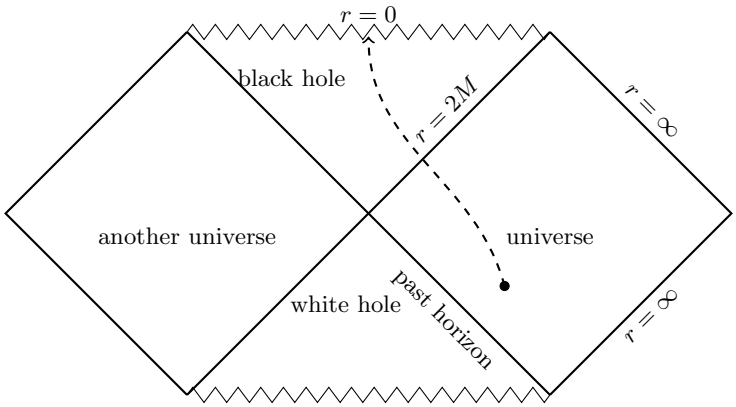

Figure 2.1: Penrose diagram of a Schwarzschild black hole. The event horizon is located at $r = 2M$ and the black hole singularity is denoted by the horizontal zigzag lines. The dashed curve linking the universe and black hole represents the timelike path of a particle. Diagram adapted from [48].

any light trajectories move at 45° from the upward vertical. Moreover, timelike paths followed by massive particles or observers have tangents at less than 45° to the vertical. Let us follow the particle trajectory depicted by the dashed line in Fig 2.1. Once the particle enters the black hole by crossing the null surface $r = 2M$ or event horizon, it is clear from the diagram that particle cannot reach $r = \infty$. To escape from the black hole, the particle would have to travel faster than the speed of light which is not allowed in general relativity (GR). Inside the Schwarzschild black hole, all particle paths are led to the same destination and that is the black hole singularity. Surprisingly, by extending the Schwarzschild solution as much as it can be, there exist other possible regions called "white hole" and "another" universe. One can think of a white hole as a time-reversed black hole. However there is no causally connected curve that leads you from our universe to a white hole. On the other hand, everything that lives inside a white hole will inevitably come out to either our universe or another universe. Another patch of the Schwarzschild spacetime is a new asymptotically flat universe labeled as "another universe" in Fig 2.1 which can not be reached from our universe.

Another exact solution describing an electrically charged black hole was discovered by

Reissner [146] and Nordström [135]. In this case, there is an electrostatic field which acts as the source of the energy-momentum tensor. The RN metric is given by

$$ds^2 = -f_{RN}dt^2 + f_{RN}^{-1}dr^2 + r^2\left(d\theta^2 + \sin^2\theta\ d\varphi^2\right), \tag{2.3}$$

where

$$f_{RN} = 1 - \frac{2M}{r} + \frac{Q^2}{r^2} = \frac{(r - r_+)(r - r_-)}{r^2}, \tag{2.4}$$

where M and Q are the black hole mass and electric charge respectively. Similarly to the Schwarzschild black hole, the curvature singularity of the RN black hole is located at $r = 0$. In contrast, f_{RN} has two roots namely, r_+ and r_-. These correspond to the outer and inner event horizons which are determined by

$$r_\pm = M \pm \sqrt{M^2 - Q^2}. \tag{2.5}$$

In the absence of an electric charge Q, the RN solution (2.3) reduces to the Schwarzschild solution (2.1). It is clear from (2.3) that the RN solution is characterized by two parameters, M and Q. From (2.5), there are three possible scenarios depending on the values of M and Q. Firstly, for $M^2 < Q^2$, the roots of f_{RN} become complex or in other words f_{RN} is always positive and can never be zero. Therefore in this case the spacetime metric (2.3) is regular everywhere for $r > 0$. However the curvature singularity still exists at $r = 0$ and we can observe it directly as there is no event horizon to cover the black hole singularity. This situation is known as a "naked singularity".

Secondly, the case $M^2 > Q^2$ is expected to happen in a realistic situation. When the energy in the electromagnetic field is less than the total energy, the metric function f_{RN} has two real roots, r_+ and r_-, as shown above (2.5). The Penrose diagram of the RN black hole corresponding to this case is shown in Fig 2.2. The timelike trajectory of a particle, once again, is depicted by a dashed curve in this figure. Suppose that we start our journey

in the asymptotically flat region $\mathscr{A}$. The particle enters the RN black hole by crossing the outer horizon $r = r_+$ which is a null surface. Once inside region $\mathscr{B}$, the particle cannot physically communicate with the outer region. In the region $\mathscr{B}$, the particle is forced to move in the $r-$decreasing direction. Eventually the particle will go across another null horizon at $r = r_-$. The curvature singularity of the RN black hole is illustrated in Fig 2.2 by the vertical zigzag line. This is crucially different from the Schwarzschild case. By considering geodesic motion of particle, it turns out that inside the inner horizon of RN black hole, gravitational force becomes repulsive. An observer falling into the RN black hole will be repelled by the singularity. Therefore, the particle will never reach $r = 0$. Even more surprisingly, the particle can manage to penetrate into another "white hole" region denoted by $\mathscr{C}'$. Then the particle is restricted to move into a new asymptotically flat region, either $\mathscr{A}'$ or $\mathscr{D}'$. Now the particle can choose to go back into a new black hole $\mathscr{B}'$ and repeat the whole journey again.

The final case is when $M^2 = Q^2$. In this case the metric function f_{RN} has only one real root, and the RN black hole has just one horizon located at $r = M$ (2.5). This particular case is known as the extremal Reissner-Nordström solution. The singularity of extremal RN is, once again, cannot be reached. The particle would be able to travel through the black hole and come out at another asymptotically flat region. However this configuration is somewhat fragile since a small change in the values of M or Q would bring this case back to one of the previous two cases.

In reality, the RN black hole might not be relevant to an astrophysical process since a black hole can be neutralised by interacting with surrounding matter. For a more realistic situation, one must include rotation into the picture. However finding an exact solution for a rotating black hole is somewhat difficult. This is because one must consider axial symmetry around the axis of rotation rather than spherical symmetry. In 1963, Kerr was able to find an exact solution that describes a rotating black hole [107]. The solution is given by (in Boyer-Lindquist coordinates)

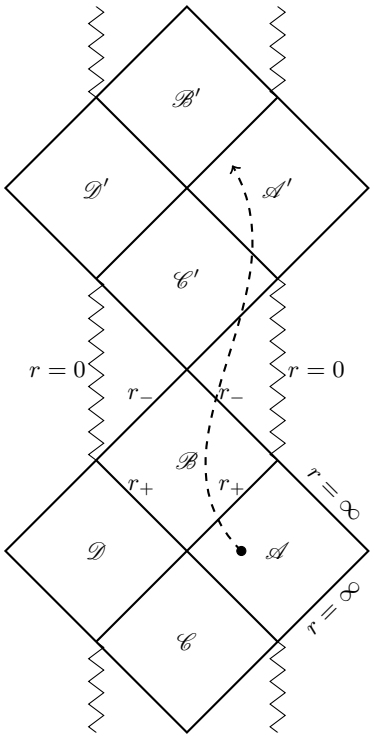

Figure 2.2: Penrose diagram of a non-extremal Reissner-Nordström black hole. The outer and inner event horizons are denoted by r_+ and r_-. The black hole singularity is denoted by the vertical zigzag line. The dashed curve represents the timelike trajectory of a particle. Diagram adapted from [48].

$$ds^2 = -\left(1 - \frac{2Mr}{\rho^2}\right) dt^2 - \frac{4Mar\sin^2\theta}{\rho^2} dt\ d\phi + \frac{\Sigma}{\rho^2}\sin^2\theta\ d\phi^2 + \frac{\rho^2}{\Delta} dr^2 + \rho^2 d\theta^2, \tag{2.6}$$

with

$$\Sigma = \left(r^2 + a^2\right)^2 - a^2\Delta\sin^2\theta, \qquad \Delta = r^2 - 2Mr + a^2, \qquad \rho^2 = r^2 + a^2\cos^2\theta, \tag{2.7}$$

where M and a are total mass and spin parameters. This metric describes the exterior spacetime of a stationary, axially symmetric object. The Kerr metric (2.6) has a curvature singularity located at $\rho^2 = 0$ and the event horizon is determined by $\Delta = 0$. This gives

$$r_\pm = M \pm \sqrt{M^2 - a^2}. \tag{2.8}$$

Similarly to the RN case, there are three possibilities: $M^2 < a^2$, $M^2 > a^2$ and $M^2 = a^2$. The first and third case correspond to a naked singularity and an extreme case which are out of our scope of interest here. Therefore we will limit ourselves to the second case only.

A static observer[1] cannot exist everywhere in the Kerr spacetime. This comes from the fact that the time-translation Killing vector $\xi = \partial_t$ is not everywhere timelike. To see this, let us consider the norm of the Killing vector ξ

$$\xi^b \xi_b = -\left(1 - \frac{2Mr}{\rho^2}\right). \tag{2.9}$$

At the horizon, this becomes

$$\xi^b \xi_b = \frac{a^2 \sin^2\theta}{\rho^2} \geq 0, \tag{2.10}$$

The Killing vector is already spacelike at the horizon. Except at $\theta = 0, \pi$ (north and south pole), it becomes null outside the horizon. The surface where the Killing vector ξ changes from timelike to spacelike is called the stationary limit surface. This occurs when $\xi^b \xi_b$ vanishes or

$$r_s = M + \sqrt{M^2 - a^2 \cos^2\theta}. \tag{2.11}$$

The stationary limit surface meets the outer horizon at $\theta = 0, \pi$. The region lying between the stationary limit surface and the outer event horizon is called the ergoregion. No static observers are allowed inside the ergoregion. In fact, in this region every particle will be dragged to co-rotate (but not necessarily with the same angular speed) with the Kerr black hole. It is possible to enter the ergoregion and escape to the outside. However once one reaches the null surface where $r = r_+$, escape is not possible. For clarification, we display the overall structure of a Kerr black hole in Fig 2.3.

[1] We define a static observer as an observer whose tangent vector is proportional to the timelike Killing vector ξ.

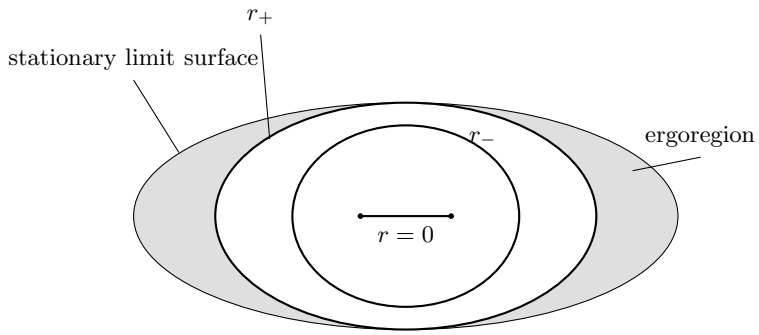

Figure 2.3: Diagram of the Kerr spacetime structure (side-view). The outer and inner event horizons are denoted by r_+ and r_-. The shaded region represents the ergoregion where an observer cannot remain at rest relative to infinity. The ring singularity is also displayed at the centre of the figure. Diagram adapted from [48].

The curvature singularity of the Kerr metric (2.6) is also worthmentioning. This singularity is located at

$$\rho^2 = r^2 + a^2 \cos^2 \theta = 0. \tag{2.12}$$

Thus the singularity occurs only when

$$r = 0, \qquad \theta = \frac{\pi}{2}. \tag{2.13}$$

The curvature singularity of a Kerr black hole is located at the edge of a ring. One can even penetrate through the ring and exit to another asymptotically flat spacetime described by the Kerr metric with $r < 0$.

The Penrose diagram of a Kerr black hole shares many features with the RN black hole. There are many copies of the asymptotic region outside the black hole. This is illustrated in Fig 2.4. A particle cannot reach the curvature singularity as in the RN case since Kerr's singularity is also repulsive, except that in the Kerr case, a particle can choose to pass through the singularity and exit into a new asymptotically flat region. The new region has no analogue in the RN case.

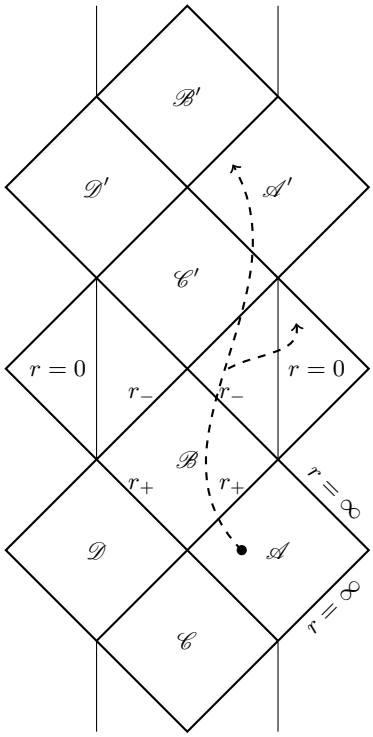

Figure 2.4: The Penrose diagram of a non-extremal Kerr black hole. Similarly to the charged case, the outer and inner event horizons are denoted by r_+ and r_-, respectively. An example of a timelike path in this spacetime is shown by the dashed curve. The curvature singularity is depicted by the vertical solid line. Diagram adapted from [48].

A generalization of the Kerr solution is to include an electric charge. An exact solution of the Einstein-Maxwell equations describing a charged rotating black hole was discovered by Newman et.al., [131, 132]. The metric representing such a spacetime is given by (in Boyer-Lindquist coordinates)

$$ds^2 = -\left(1 - \frac{2Mr - Q^2}{\rho^2}\right) dt^2 - \frac{2\left(2Mr - Q^2\right) a \sin^2\theta}{\rho^2} dt\ d\varphi + \frac{\rho^2}{\Delta} dr^2 + \rho^2 d\theta^2 + \left(r^2 + a^2 + \frac{\left(2Mr - Q^2\right) a^2 \sin^2\theta}{\rho^2}\right) \sin^2\theta\ d\varphi^2, \tag{2.14}$$

with

$$\Delta = r^2 - 2Mr + a^2 + Q^2, \qquad \rho^2 = r^2 + a^2 \cos^2\theta. \tag{2.15}$$

The outer and inner horizon of the Kerr-Newman solution (2.14) are determined by

$$r_\pm = M \pm \sqrt{M^2 - Q^2 - a^2}. \tag{2.16}$$

The stationary limit surface is defined as

$$r_s = M + \sqrt{M^2 - Q^2 - a^2 \cos^2\theta}. \tag{2.17}$$

Like the uncharged case, the stationary limit surface intersects with the outer horizon at each pole ($\theta = 0, \pi$). The interval $r_+ < r < r_s$ defines the ergoregion where it is impossible for a static observer to exist. The curvature singularity of a Kerr-Newman black hole is also located at $\rho^2 = 0$ which implies that $r = 0$ and $\theta = \pi/2$. Hence, the curvature singularity of the Kerr-Newman metric (2.14) also forms a ring-structure as happens in the Kerr case. Since the internal geometry of the Kerr-Newman solution is very much like that of the Kerr solution, the Penrose diagram of a Kerr-Newman black hole will be the same as that for a Kerr black hole (Fig 2.4). One final remark is that the Kerr-Newman solution (2.14) is uniquely determined by only three parameters; mass M, charge Q and

spin a.

As will be discussed in the next section, the Kerr-Newman metric (2.14) is the most general solution of the four-dimensional Einstein-Maxwell equations representing an asymptotically flat black hole.

§2.2 No-hair theorem

In brief, the black hole no-hair theorem simply states that "four dimensional, asymptotically flat, stationary single black hole solutions of the Einstein-Maxwell equations can be uniquely determined by three observable parameters i.e., mass, angular momentum and charge" [154]. The implication of this theorem is profoundly surprising because this means that a black hole is an extremely simple object, only a handful of parameters are needed to fully describe a black hole. To aid a better understanding of the no-hair theorem, it is useful to see how the key ideas behind the theorem developed. We remark that all the discussions below are valid only for four dimensional black holes. For a comprehensive review on higher dimensional black holes see [66].

The black hole no-hair theorem is inspired by a series of works attempting to classify black hole solutions. For obvious reasons, most of the work done in the early days focused on isolated black holes, i.e., black hole solutions of the vacuum or electrovac Einstein field equations. The story can be traced back to 1923 when Birkhoff was able to prove that any spherically symmetric solution of the vacuum (no surrounding matter) Einstein field equations in asymptotically flat spacetime must be static [23]. In 1967, Israel proved that the Schwarzschild metric is the unique solution of the vacuum field equations describing a non-rotating black hole [100]. In other words, this means that if a black hole is static, it must be spherically symmetric and the exterior spacetime must be the Schwarzschild solution. This work was followed by Müller zum Hagen et.al., in 1973 [129] and Robinson in 1977 [149], who improved and simplified the techniques used in Israel's proof. In addition, Bunting and Masood-ul-Alam in 1987 [45] used the positive energy theorem to prove the

uniqueness of the Schwarzschild metric.

As a generalization of Birkhoff and Israel's theorems, one can consider an electrically charged static black hole solution of the electrovac system, i.e., the Einstein-Maxwell equations. The uniqueness of this type of black hole solution was completed by a series of studies. The first attempt was made by Israel in 1968 [101], where he generalized his previous result for the vacuum system to the electrovac system. Later, Israel's argument was improved and simplified by Müller zum Hagen et.al., [130] and Simon [162]. After that, Ruback [152] and Masood-ul-Alam [122] also applied the positive energy theorem to prove the uniqueness theorem for the electrically charged Reissner-Nordström metric. By extending these results, Heusler was able to take magnetic charge into consideration and proved the uniqueness theorem for the Reissner-Nordström solution with both electric and magnetic charge [89].

All the studies discussed in the previous paragraph were done for the static case, now we shall provide a selection of important works on axially symmetric black holes. In vacuum, if the metric of an asymptotically flat, stationary and axisymmetric spacetime is regular on and outside the event horizon, then this metric is member of the two-parameter Kerr family [49, 148]. This is known as the *Carter-Robinson theorem*. Afterward, Bunting [44] and Mazur [125] provided the uniqueness proof for the Einstein-Maxwell system. Thus if the electromagnetic field is taken into account, the stationary, asymptotically flat black hole solution must be described by the Kerr-Newman metric [131, 132] where the solution is characterized by mass, angular momentum and charge. For historical and technical reviews of the uniqueness of black hole solutions see for example [52, 90, 91, 126, 147].

Inspired by these black hole uniqueness theorems, Wheeler suggested that all asymptotically flat, four-dimensional, stationary black holes can be completely described by three observable parameters: mass, angular momentum and charge. These quantities can be measured from infinity and are subjected to a Gauss law. He encapsulated his idea into

a famous phrase "black holes have no hair" [154]. In this context, hair is a metaphor for other information about the matter associated with black holes. Once these hairs pass through the black hole's event horizon, they are prevented from being accessed by an external observer. In other words, if a black hole absorbs a highly complex object, once the black hole returns to its final equilibrium state, there will be only changes in the total mass, total angular momentum and total charges. Thus according to the no-hair theorem, a black hole in the final equilibrium state will be completely characterized by a very small number of parameters: mass, angular momentum and charges.

Research into the no-hair theorem has a long story. Once again, we will focus our discussion on four-dimensional, asymptotically flat spacetimes. In 1971, Hartle showed that a Kerr black hole cannot possess lepton charge [82]. The same results were obtained for lepton, baryon and other quantum numbers on a Schwarzschild black hole in a series of works by Teitelboim [170, 171, 172]. Moreover, he also showed that a charged black hole can only exist if the mass of the photon is zero [172]. Another important work comes from Bekenstein in 1972 [14], where he found that a static (non-rotating) black hole cannot be equipped with massless/massive scalar or massive vector meson fields. A similar result for the scalar field was also proven by Chase in 1970 [51]. Later Bekenstein generalized his previous study, showing that it is impossible to endow a static black hole with a massive spin-2 meson field and also proving that the same held for a stationary (rotating) black hole [15, 16]. These conclusions remain valid for the charged case and in Brans-Dicke theory too [15]. Moreover, in 1995 Bekenstein proved a new no-scalar-hair theorem which rules out many scalar hair configurations [20]. This proof is formulated such that asymptotically flat, static, spherically symmetric black holes cannot be dressed by multicomponent scalar fields [20]. The primary assumptions are made on the scalar field, namely: the scalar field is minimally coupled to gravity and there is no negative energy-density in any frame of reference. The beauty of Bekenstein's argument is based on the very general principle of conservation of the energy-momentum tensor and the Einstein field equations. If a

complex scalar field is taken into account, Bekenstein's result is still intact and the black hole must be described by the Reissner-Nordström metric [20]. See [21, 25, 52, 90, 91] for more technical reviews on this subject.

A number of studies have been proposed to test the no-hair theorem. We can learn about the mass and spin of a black hole from its quasinormal modes – damping modes that are encoded in the gravitational radiation emitted from a perturbed black hole (see [112] for a review). One practical framework has been proposed by Kamaretsos et.al., [106] using black hole quasinormal modes to test GR in the strong gravitational regime and the no-hair theorem. One of the most well-known supermassive black hole candidates is Sgr A* which is located at the centre of our Milky Way galaxy. In principle, if we could measure the mass, spin and quadrupole moment of Sgr A*, then we would know how much Sgr A* may deviate from the standard Kerr black hole and therefore test the no-hair theorem. Many works have suggested ways to measure Sgr A* properties to test the no-hair theorem by using various techniques and instruments e.g., pulsar timing [143], the event horizon telescope [42] which uses the global network of radio telescope and combines the data from very-long baseline interferometry (VLBI) [104]. For a recent review on testing GR and the no-hair theorem with Sgr A* see [105]. The recent discovery of gravitational waves from merging binary black holes by the Laser Interferometer Gravitational-Wave Observatory (LIGO) finds no evidence for disagreement from GR [1]. The final mass and spin, determined by the gravitational wave signal, also agree consistently with the black hole solution predicted by GR [2]. However, more evidences are needed to confirm that there is no deviation from GR. Since the gravitational waveform used by LIGO is constructed subjected to GR template. Thus this might introduce some bias towards GR in the gravitational wave detection.

§2.3 Hairy black holes

The no-hair theorems mentioned in section 2.2 rely on a number of assumptions, such as asymptotic flatness, stationarity, four dimensional spacetime and the electrovac Einstein equations. Therefore one should not be surprised if the no-hair theorem does not hold when some of these conditions are relaxed. Let us suppose that we dismiss the electrovac condition. We then have a generalized version of the no-hair conjecture which states that [52]

"All stationary black hole solutions of general relativity coupled to any type of self-gravitating matter are determined by mass, angular momentum and a set of global charges".

Global charges are given by a surface integral of flux density over a sphere at infinity. In other words, global charges are quantities which can be measured at infinity. These global charges are the hairs (information) that are not falling into a black hole, hence we can observe them from a very distant place. This new version of the no-hair conjecture has led to a series of studies which considered the interaction between black holes and many types of self-gravitating matter or *hairy black holes*. In this context, we could define "hair" as any non-gravitational and non-electromagnetic field associated with black holes. In addition, we remark that hair could be referred as quantities that are not subjected to Gauss law.

Notwithstanding the no-hair theorems discussed in the previous section, many black hole solutions with hair have been found even in the simplest matter model: a scalar field, if the scalar field is non-minimally coupled to the scalar curvature. The first example of this type of solution was found by Bocharova, Bronnikov and Melnikov (BBM) in 1970 [30]. The BBM solution has a form resembling the extremal (electrically) charged Reissner-Nordström black hole, conformally coupled to a massless scalar field. Afterwards Bekenstein rediscovered independently the BBM-type of solution [18, 19]. However, the

scalar field in the Bekenstein and BBM solution diverges at the event horizon [18, 169] and later it was shown to be unstable [43]. These undesirable results have put Bekenstein's solution as a hairy black hole in doubt [169]. The BBM solution was generalized later to carry magnetic charge by Virbhadra et.al. [185], where the conformal scalar field again diverges at the event horizon. It should be remarked that, the contradict result about the stability of BBM solution was later found in [127], where the authors found that the solutions are stable.

The first truly hairy black hole solution with scalar hair is Gibbons solution [76]. He discovered a black hole solution with a non-trivial dilaton field in the low energy limit of $N = 4$ supergravity. The Gibbons solution possesses electric and magnetic charges but no independent dilatonic charge. Bekenstein's no-hair theorem is evaded by the Gibbons solution as there is non-trivial coupling between the dilaton and Maxwell field. Later, more dilaton black holes were found by Gibbons et.al., [77] and Garfinkle et.al., [74]. Furthermore, number of black hole solutions in string effective field theories have been found. See for example [203] for a review on black holes in string theory.

Since the no-scalar-hair theorem discussed above [20] rules out various possibilities of having black holes with scalar hair in asymptotically flat spacetime, therefore it is natural to ask whether these results extend when a cosmological constant is included. For instance, asymptotically de Sitter (dS) and anti-de Sitter (AdS) black holes with minimally coupled scalar field hair for some specific types of scalar potential were found in [173, 174]. For a minimally coupled scalar field with nonconvex scalar potential, stable solitons and black holes in asymptotically AdS have been found [174, 176]. On the other hand, when the cosmological constant is positive, black hole solutions with scalar hair are found for some specific types of scalar potential, however these solutions are unstable [173]. For investigations of non-minimally coupled scalar field hair in non-asymptotically flat spacetimes see, for example [144, 195, 196].

Recently, Herdeiro and Radu remarkably discovered asymptotically flat rotating black holes with scalar hair [87]. They carry conserved Noether charges associated with mass M, angular momentum J and scalar field hair Q, however only M and J are global charges since Q is not subject to a Gauss's law, therefore it cannot be measured by an observer at infinity [84]. Similarly to the Kerr metric, the solutions in [87] are stationary and axially symmetric, however with the matter field included the full solutions are only invariant under a single Killing vector field [87]. Therefore Bekenstein's no hair theorem [20] is not applicable here. We shall come back to Herdeiro's hairy black holes again in section 2.6 when we discuss the end-point of a superradiant instability. We refer the reader to [88, 163] for recent reviews on black holes with scalar fields.

In contrast, few black holes with Abelian vector hair have been discovered so far. This is because of the three following reasons. Firstly, uniqueness theorems for Reissner-Nordström and Kerr-Newman black holes discussed in section 2.2 limit the the possibility of having static and stationary black holes with massless vector hair. Secondly, asymptotically flat non-rotating and rotating black holes with massive vector hair are forbidden by Bekenstein's results [14, 15]. Lastly, even when the cosmological constant is positive, static spherically symmetric black holes with Proca hair (massive vector field) are excluded by Bhattacharya et.al., [22]. These results narrow down the window of existence of black holes with Abelian vector hair. However, one could cleverly evade these difficulties and obtain a black hole solution with Abelian vector hair. For instance, massive vector hair on superconducting AdS black holes has been constructed numerically [8] and the solutions are interpreted in the context of the AdS/CFT correspondence, where CFT stands for conformal field theory. In addition, static spherically symmetric soliton and black hole solutions of the Einstein-Proca equations have been studied in asymptotically AdS spacetime [119]. Moreover, it has been found recently that a harmonic time dependence complex Proca field can be endowed on a Kerr black hole [84]. Once again, these newly discovered hairy black holes do not violate Bekenstein's no-hair theorem [14, 15], since the

matter field does not share all the spacetime symmetries [84].

§2.4 Non-Abelian black holes

Another interesting type of self-gravitating matter is the non-Abelian gauge field (Yang-Mills field). Yang-Mills (YM) theory is a gauge theory with a non-Abelian gauge group. It can describe electroweak theory with gauge group $U(1) \times SU(2)$ (unification of the electromagnetic force and weak interaction) and the strong interaction with gauge group $SU(3)$. Hence, inspired by the standard model of elementary particle physics, the gravity-particle physics community have extensively studied one particular model: Einstein-Yang-Mills (EYM) theory. The pioneering work on the self-gravitating Yang-Mills system began with the discovery of particle-like solutions of the $SU(2)$ EYM equations in asymptotically flat spacetime by Bartnik and McKinnon (BM) [7] (see the following subsection for more details). Later black hole counterparts in the same system, namely coloured black holes, were discovered in [24, 81, 188]. In addition, slowly rotating coloured black holes in $SU(2)$ EYM theory were found by Volkov and Straumann [191] whereas no slowly rotating analogue for a globally regular solution exists [191]. The authors in [184] also reported the absence of rotating regular solutions of pure EYM theory. Later, static axially symmetric and asymptotically flat regular and black hole solutions in $SU(2)$ EYM theory were constructed numerically [98, 99, 108, 109]. One can also consider the EYM system with gauge group larger than $SU(2)$. For example, black hole solutions of the EYM equations with gauge group $SU(3)$ were discovered in [73, 150, 151]. Furthermore, static spherically symmetric solutions of the EYM equations for arbitrary gauge group $SU(N)$ have been explored and black hole solutions were obtained within this model [110]. Despite the numerous solitons and black holes in EYM theory that have been discovered and studied, all the solutions found in the asymptotically flat EYM system are unstable [40, 41].

For non-asymptotically flat systems, soliton [192] and black hole solutions [175] of $SU(2)$ EYM were constructed in asymptotically de Sitter (dS) spacetime [34]. These solutions

with positive cosmological constant were (not surprisingly) found to be unstable [39, 68, 175]. On the other hand, by investigating the $SU(2)$ EYM equations in asymptotically AdS, magnetically charged black hole solutions were constructed [194]. In addition, some solutions where the gauge field function has no zeroes were shown to be linearly stable [194]. Likewise, monopole, dyon[2] and black hole solutions were found in $SU(2)$ EYM-AdS and for a class of monopole solutions which have no zeroes were shown to be linearly stable [28, 29]. Recent studies reveal that dyons and dyonic black holes in the $SU(2)$ [134] EYM-AdS system are linearly stable. Moreover, new purely magnetic, hairy black hole solutions of $SU(N)$ EYM-AdS theory were presented and some of them were shown to be linearly stable [10, 11, 12, 13]. These black holes can be equipped with an arbitrary number of stable YM hairs. These solutions are described by $N+1$ parameters and possess $N-1$ independent gauge fields [10]. In addition, the global charges for these $SU(N)$ black holes in asymptotically AdS were discussed in [159]. Finally numerical dyons and black holes of $SU(N)$ EYM-AdS are constructed in [160] and later their existence is confirmed analytically in [9].

Besides pure EYM theory discussed above, there are many variant models containing Einstein gravity coupled to a non-Abelian gauge field plus an additional matter field. For instance, asymptotically flat, static, spherically symmetric solitons and hairy black holes in EYM-dilaton theory have been constructed and possess a dilaton charge [62]. Furthermore, regular and black hole solutions of the Einstein-Skyrme[3] model have been found numerically [63] and their stability was discussed in [92, 93] for Skyrme stars and Skyrme black holes respectively. In this model, a topological winding number renders the solutions stable. Additionally, for asymptotically dS [36] and AdS [161], regular and black hole solutions of the Einstein-Skyrme equations have been obtained. Moreover, asymptotically flat, static, spherically symmetric regular and black hole solutions of EYM with a Higgs

[2] A dyon is a hypothetical particle with both electric and magnetic charges.
[3] The skyrmion is a classical field solution of a non-linear sigma model.

(EYMH) field were considered in [4, 69, 79]. It was shown by van der Bij and Radu that regular and black hole solutions of EYMH-AdS with a doublet Higgs field are linearly unstable [183]. Lastly, Einstein-non-Abelian-Proca (ENAP) theory in asymptotically flat spacetime was studied in [79]. Solitons and black holes with (non-Abelian) Proca hair were obtained numerically. The ENAP-AdS system remains unexplored territory and one of the main chapters in this thesis will be devoted to this particular model (see chapter 3). Since a vast number of studies have paid attention to self-gravitating non-Abelian gauge fields, it is impossible for us to cover all of them, therefore we refer the reader to [25, 186, 189, 197] and references therein for more details of this subject.

In the next subsection, we will outline two pioneering works in the area of self-gravitating non-Abelian gauge fields namely, BM's particle-like solutions [7] and Bizon's coloured black holes [24]. We will explain briefly the numerical solutions founded in both scenarios.

2.4.1 Particle-like solutions and coloured black holes

Before 1988, it was widely believed amongst physicists that the EYM system in four dimensional spacetime admits no non-trivial black hole solutions. This folklore arose from the fact that there are no solitons in the following scenarios (see [52, 197] and references therein):

- Firstly, in the pure gravity system, there is no globally regular solution. The only static, asymptotically flat, globally regular solution of Einstein's vacuum equations is the Minkowski metric.

- Secondly, the Einstein-Maxwell equations admit the Reissner-Nordström metric as the only static single black hole solution. No non-trivial solitons are found in the same system apart from Minkowski spacetime.

- Thirdly, in the absence of gravity, there is no non-trivial globally regular solution of the Yang-Mills equations [56] except Minkowski spacetime.

- Lastly, there is no non-trivial soliton solution in three dimensional EYM theory [57] apart from Minkowski spacetime.

For all these reasons, one might expect that there should be no regular or black hole solutions of the $3+1$ dimensional EYM system other than the Minkowski and Reissner-Nordström spacetimes. However, the situation was turned upside down, when Bartnik and McKinnon [7] discovered non-trivial particle-like solutions of $SU(2)$ EYM theory in asymptotically flat spacetime. They found self-gravitating soliton solutions of the EYM equations numerically. These solutions exist due to the balancing of the gravitational attraction and the repulsion of the non-Abelian gauge field.

The Einstein-Yang-Mills action is given by

$$S = \frac{1}{2}\int d^4x\sqrt{-g}\left(\mathcal{R} - \mathrm{Tr}F_{ab}F^{ab}\right), \tag{2.18}$$

with

$$F_{ab} = \partial_a A_b - \partial_b A_a + e\left[A_a, A_b\right], \tag{2.19}$$

where $\mathcal{R}$ and e are the Ricci scalar and coupling constant respectively. We use "Tr" to denote a Lie algebra trace. Varying this action (2.18), we obtain two equations of motion

$$G_{ab} = \mathrm{Tr}F_{ac}F_b{}^c - \frac{1}{4}g_{ab}\mathrm{Tr}F_{cd}F^{cd}, \tag{2.20}$$

$$0 = \nabla_a F_b{}^a + [A_a, F_b{}^a]. \tag{2.21}$$

A static, spherically symmetric, asymptotically flat spacetime is defined by

$$ds^2 = -\left(1 - \frac{2m(r)}{r}\right)S^2dt^2 + \left(1 - \frac{2m(r)}{r}\right)^{-1}dr^2 + r^2d\theta^2 + r^2\sin^2\theta\, d\varphi^2, \tag{2.22}$$

where $m(r)$ is the Misner-Sharp mass function [128]. This mass function, in spherically symmetric spacetime, can be interpreted as a measurement of total mass within a sphere radius r. The purely magnetic gauge field ansatz is given by

$$A = \frac{1}{e}\left(1+\omega(r)\right)\left[-\hat{\tau}_{\varphi}d\theta + \hat{\tau}_{\theta}\sin\theta d\varphi\right], \tag{2.23}$$

where $\tau_\theta, \tau_\varphi$ are the elements of the $SU(2)$ basis in spherical coordinates. The Yang-Mills field is denoted by one function $\omega(r)$. From these ansatze (2.22, 2.23), we obtain the following field equations [7]

$$\begin{aligned} m' &= \left(1-\frac{2m}{r}\right)w'^2 + \frac{1}{2}\frac{\left(1-\omega^2\right)^2}{r^2}, \\ 0 &= r^2\left(1-\frac{2m}{r}\right)w'' + \left(2m - \frac{\left(1-\omega^2\right)^2}{r}\right)\omega' + \left(1-\omega^2\right)\omega. \end{aligned} \tag{2.24}$$

We denote derivative with respect to r by $'$. The first equation is one component of the Einstein field equations (2.20) and the second equation is the Yang-Mills equation (2.21). Asymptotic flatness requires that $\omega \to \pm 1$ as $r \to \infty$. As will be seen later, this is one of the features of the solutions of the EYM equations and the ENAP equations. The field equations (2.24) are numerically integrated with appropriate boundary conditions, to give ω and m as functions of radius r. The solutions are classified by the number of zeros or nodes of the gauge function ω. The number of zeros of ω will be denoted by n. We note that for each fixed n, there is a single regular solution. Also there is no nodeless BM solution [33].

In Fig 2.5(a)−2.5(c), the first three regular solutions are illustrated. The gauge connection ω and the mass function m approach constants as $r \to \infty$. Additionally in Fig 2.5(d), the local energy density (00-component of the energy-momentum tensor) of the node=3 solution is shown. It displays the high density interior region of the self-gravitating solitons.

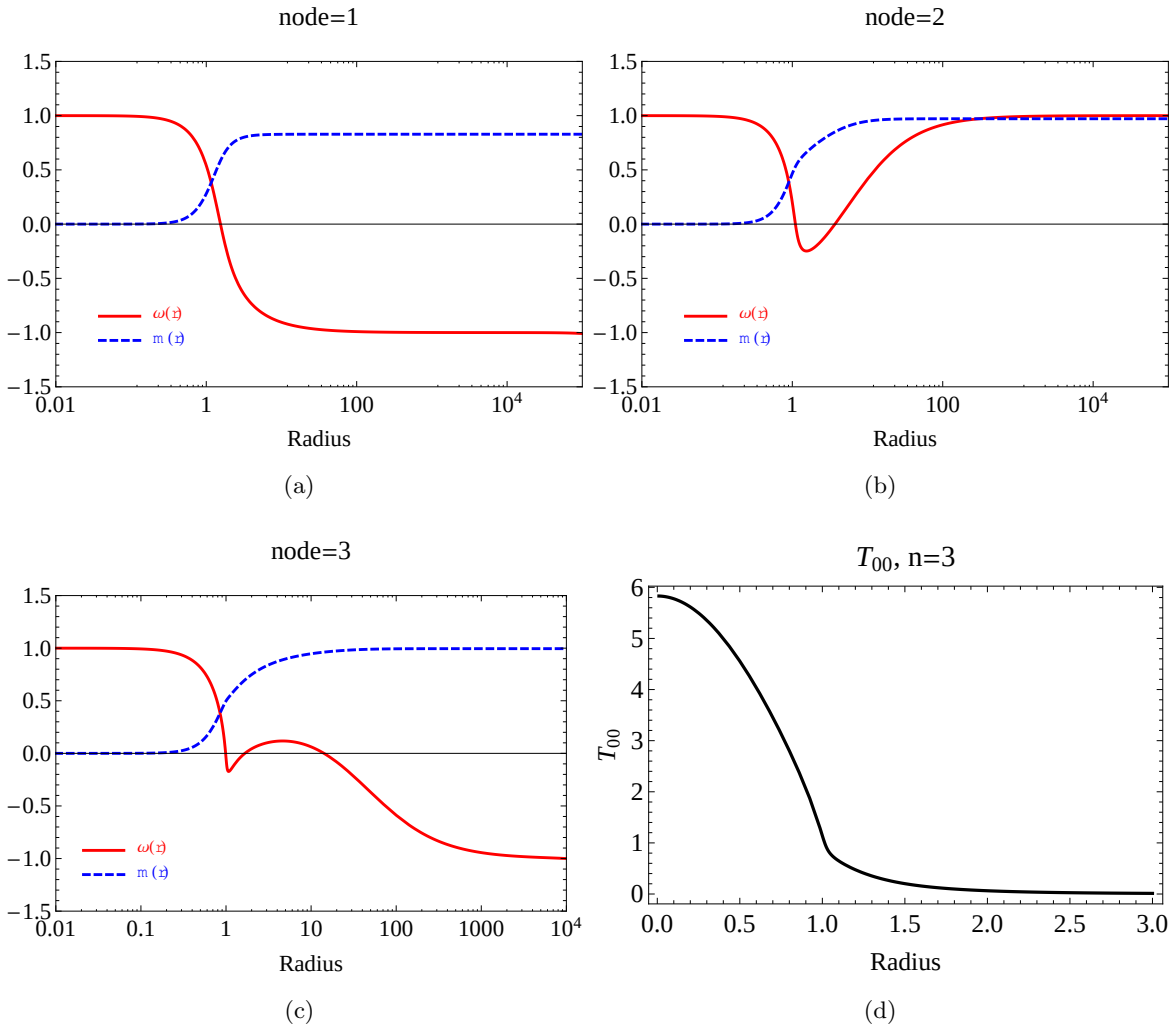

Figure 2.5: Regular solutions of the $SU(2)$ EYM equations in asymptotically flat spacetime. (a)−(c) First three regular solutions, (d) the local energy density of node=3 solutions [7].

In 1990, Bizon discovered "coloured black holes" in $SU(2)$ EYM theory [24]. He investigated static, spherically symmetric, asymptotically flat metrics with an $SU(2)$ YM field. By using different boundary conditions to the soliton case, he numerically constructed the black hole solutions of EYM theory. Bizon's solutions are, as in the Bartnik and McKinnon case, characterized by the number of zeros or nodes of the YM field ω. Fig 2.6(a)−2.6(d)

show the first four black hole solutions. For each fixed event horizon radius r_h, it is found that there is a single black hole solution for each n, and also it is found that $n > 0$ [33]. We remark that all the solutions plotted in Fig 2.5 and 2.6 are re-constructed by our numerical codes. Our plots are in excellent agreement with the results in [7] and [24].

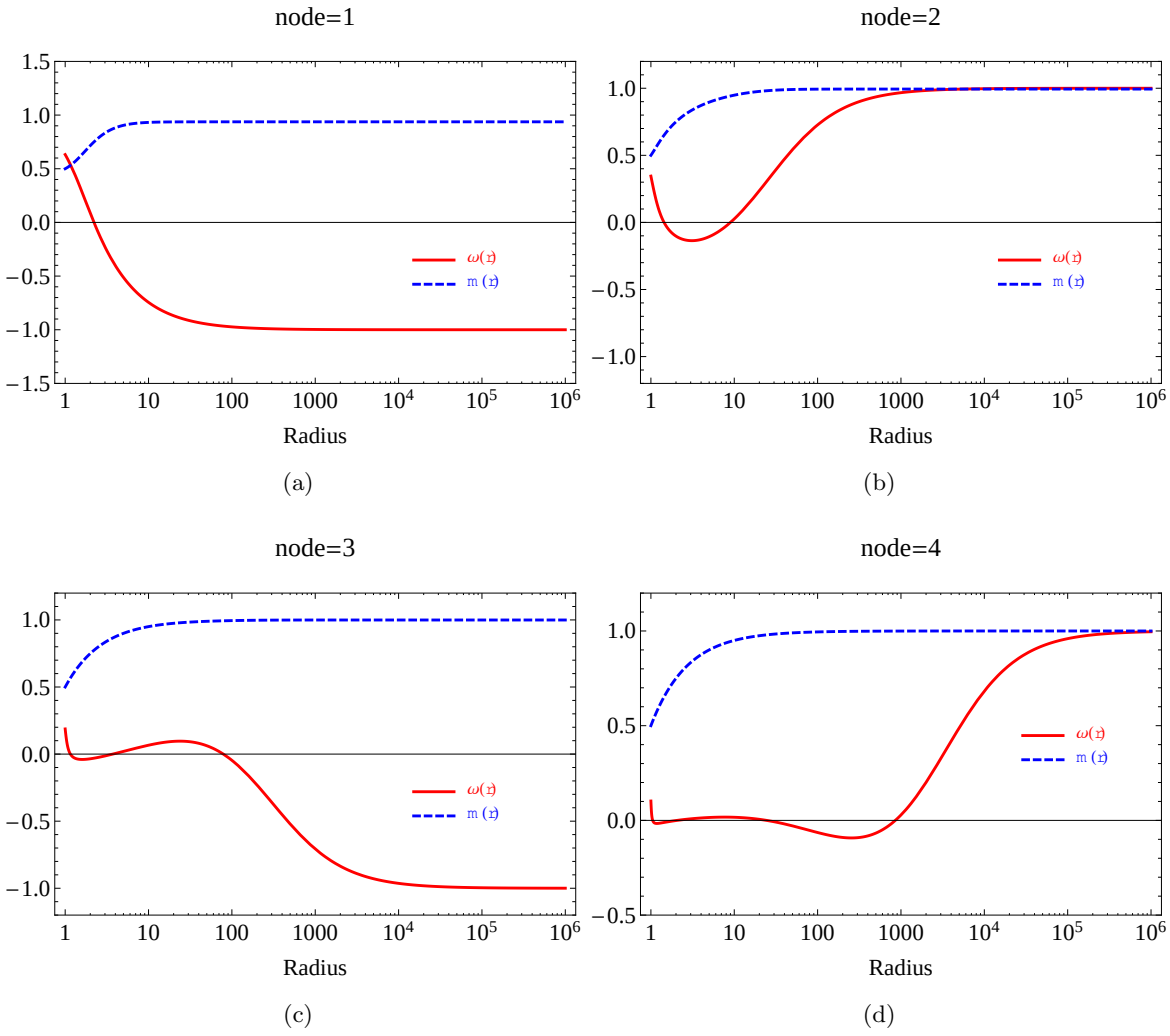

Figure 2.6: The black hole solutions of $SU(2)$ EYM equations in asymptotically flat spacetime. The first four Bizon solutions [24].

The regular and black hole solutions of EYM theory have a common character, namely the total mass function $m(r)$ of both type of solutions approaches some positive constant M as $r \to \infty$. Near the horizon, Bizon's solutions are very similar to the Reissner-Nordström solution [24]. This is because, there is non-zero gauge field near the horizon of Bizon's solutions. However as we move away from the horizon the local magnetic charge decreases and becomes zero as the gauge connection reaches ± 1 at infinity. The coloured black holes are then indistinguishable at infinity from the Schwarzschild black hole with mass M. For this reason, the coloured black holes are the first black hole solutions in the non-Abelian sector with $SU(2)$ YM hair that violate the generalized no-hair conjecture as stated in section 2.3.

However one might argue that despite Bizon's solutions violating the generalized no-hair conjecture, the true meaning of this conjecture still holds. That is, the coloured black holes are very simple objects since they need only a few parameters to completely describe them. Nevertheless, it has been found that both the Bartnik and McKinnon solutions and the Bizon solutions are unstable [27, 167, 168]. In addition, studies of the non-linear evolution [206, 207] of these hairy solutions reveal that, once perturbed, these solutions will lose their gauge hair by either radiating it away or it disappearing behind the event horizon. Finally, what remains is the hairless Schwarzschild solution or pure Minkowski spacetime. Therefore, to make the generalized no-hair conjecture more physically robust, Bizon proposed a new version of the no-hair conjecture [25] which states that

"Within a given model a stable stationary black hole is uniquely determined by global charges."

This version of no-hair conjecture is of course much more restrictive than the generalized no-hair conjecture stated at the beginning of section 2.3. However there are some cases where even this *weak* no-hair conjecture does not hold. For example, asymptotically flat, static, spherically symmetric, black holes with Skyrme hair were proven to be stable [26]. Nevertheless, since they do not carry a global Skyrme charge, therefore they cannot be

distinguished from the Schwarzschild metric at infinity.

The stability of self-gravitating solitons and hairy black holes is one of the central interests of this thesis. Therefore, the following subsection will be devoted to this topic. We will outline some of the important works on the stability of black holes in self-gravitating non-Abelian models.

2.4.2 Stability of non-Abelian black holes

Questions relevant to the stability of perturbed black holes were first investigated by Regge and Wheeler in 1957 [145]. They carried out a stability analysis of the Schwarzschild black hole by considering perturbations of the metric tensor itself. The key idea behind their analysis is that a small perturbation evolving in the background metric, if found to be exponentially growing in time, would mean that such a system is unstable and could not represent a physical object. Therefore the question of the (in)stability of equilibrium solutions is very important in terms of the physical interpretation of the solutions. In addition, when the stability of a stationary black hole is taken into account, Bizon has formulated a *weak* no-hair conjecture [25] (discussed in the previous subsection) as a modification of the generalized no-hair conjecture. Therefore according to Bizon's no-hair conjecture, the stability of hairy black holes becomes a crucial part of investigating new black hole solutions.

In general, when we consider purely magnetic charged, spherically symmetric solutions of the EYM system, the background solutions are often parity-invariant, that is, invariant under a spatial coordinate reflection. Although the static field equations are invariant under a parity transformation, however at the linearised level, the perturbation equations transform differently under a parity transformation. Some preserve sign under a parity transformation (known as even-parity) while others change sign under a parity transformation (called odd-parity). This decoupling is caused by the spherical symmetry and parity-invariance of the equilibrium field equations for the purely magnetic gauge

field [190]. These two types of perturbation equations are sometimes referred to as gravitational (polar) and sphaleronic (axial) sectors [50, 70, 115], respectively. In particle physics, "sphaleron" refers to the static solution of the Weinberg-Salam electroweak theory [111] which can be considered to be a flat space analogue of the EYMH theory.

As one might expect, there are many studies devoted to the problem of stability of solitons and black holes in non-Abelian EYM theory, considering both the gravitational and sphaleronic sectors. Here are few examples which are useful for our discussion. Unstable modes of the BM solitons and coloured black holes were first found in the gravitational sector by using numerical methods [167, 168]. For the sphaleronic sector, soliton solutions of $SU(2)$ EYM in asymptotically flat space were shown analytically to admit unstable modes [72] and later this result was extended to hold for solitons and black holes with arbitrary gauge group [40, 41]. Also by using an analytical approach called the variational method, it can be proven that all known black hole solutions in $SU(2)$ EYM theory must at least contain one unstable mode in the sphaleronic sector [190]. It was also proven that there are n unstable modes for the n^{th} solitons and the n^{th} non-Abelian black holes in $SU(2)$ EYM theory [115, 187] in the sphaleronic sector and the same result is expected to hold for the gravitational sector as well [123].

For gravitating regular sphaleron and sphaleron black hole solutions of EYM with a doublet (fundamental representation) Higgs field in asymptotically Minkowski spacetime, instabilities were discovered by the variational technique in [32, 199] respectively. Finally the relationship between the number of unstable modes and the number of nodes of the equilibrium function $\omega(r)$ was also found for the EYMH black hole in both perturbation sectors [123]. It has been conjectured that the regular and black hole solutions of asymptotically flat ENAP theory are also unstable [79], however this has been demonstrated only for those solutions where $n = 1$.

When the cosmological constant is non-zero, a number of studies have been devoted to the

stability of soliton and hairy black hole solutions of the EYM equations both in asymptotically de Sitter (dS) and anti-de Sitter (AdS) (see [197] and references therein for a review on this subject). Here a selection of results are described. Solitons and black holes in the $SU(2)$ EYM-dS theory are all unstable [39, 68, 175]. For $\Lambda < 0$, some purely magnetic nodeless soliton and black hole solutions were found to be stable [28, 29, 194]. The stability of dyonic solutions in the $SU(2)$ EYM-AdS theory has recently been proven [134]. A detailed study of the stability of nodeless purely magnetic solitonic solutions of the same model showed that all such solitons are stable in sphaleronic sector, however there exist unstable modes in the gravitational sector for some solutions while others are stable [35]. In addition, the stability of solitons and black holes in $SU(N)$ EYM-AdS theory was discussed in [12]. They found no unstable modes for some soliton and black hole solutions in both the gravitational and sphaleronic sectors.

Lastly, soliton solutions of $SU(2)$ EYMH with a doublet Higgs field theory in asymptotically AdS are found to be unstable in the sphaleronic sector by the variational method [183]. The black hole solutions of the same model have recently been proven to be unstable [198]. We refer the reader to [189, 197] and references therein for comprehensive reviews of this subject.

In the next section, we turn our attention to another interesting aspect of black hole physics. We briefly outline some aspects of the physics of fundamental fields on a black hole background. In particular, *superradiant* scattering will be mainly discussed since this plays a central role in the work in chapter 4.

§2.5 Superradiant scattering in black hole physics

Imagine that an incoming wave propagates toward a black hole. The incident wave will partially be scattered to infinity by the black hole gravitational potential while the rest will pass through the event horizon and be captured by the black hole. We would normally expect that the amplitude of the scattered wave must be smaller than that of the incident

wave (or equal in the total reflection scenario). On the contrary, analysis of the scalar wave equation on Kerr spacetime reveals that the amplitude of the scattered wave can be amplified as the wave scatters off the black hole. The excess of energy comes directly from the rotational energy of the Kerr black hole. This was first investigated by Zeldovich [204] and later by Press and Teukolsky [141], and has become known as *superradiance*. Amplification of scalar, electromagnetic and gravitational waves by a rotating black hole was investigated by Starobinskii [164, 165]. It is possible to deduce superradiant phenomena from Hawking's area theorem without analysing the wave equation, this was shown by Bekenstein [17]. Moreover he found that charged superradiance can occur if a charged scalar field is reflected by a charged black hole. As a result, the black hole loses its charge and Coulomb energy.

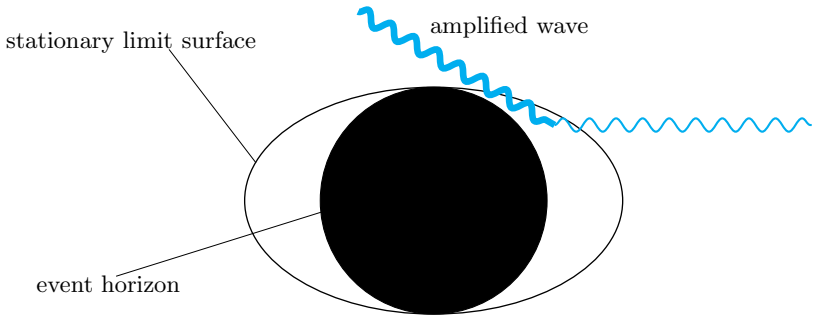

Figure 2.7: Diagram showing a superradiant scattering process.

Fig 2.7 displays the superradiance mechanism on a Kerr black hole. In this figure, the incoming wave travels toward the black hole from the right hand side of the diagram. If some condition is satisfied (this condition will be given in the following subsection), the amplitude of the outgoing wave can increase.

2.5.1 Wave amplification

In this section, we will outline a proof of superradiant scattering on particular black hole spacetimes. The conditions necessary for superradiant phenomena for the rotating and the charged cases will be derived and discussed. The treatment that we consider here is

mainly adapted from the arguments and calculations discussed in [38, 70].

For simplicity, we will consider only the dynamics of a massless charged scalar field on the Kerr-Newman black hole described by the metric (2.14). The equation of motion for the scalar field on a curved background is given by

$$D_a D^a \Phi = 0, \tag{2.25}$$

where $D_a \equiv \nabla_a - iqA_a$. Here q denotes the scalar field charge. By taking the ansatz [113]

$$\Phi(t, r, \theta, \varphi) = \frac{\phi(r)}{\sqrt{r^2 + a^2}} S(\theta) e^{-i\sigma t + im\varphi}, \tag{2.26}$$

$$A_a(r) = \left[-\frac{rQ}{\rho^2}, 0, 0, \frac{arQ \sin^2 \theta}{\rho^2} \right], \tag{2.27}$$

where σ and m are the frequency and azimuthal quantum number respectively, the Klein-Gordon equation (2.25) can be separated into two parts, a radial and an angular part defined by $\phi(r)$ and $S(\theta)$ respectively. The radial part of this equation can be written in the Regge-Wheeler form [113]

$$-\frac{d^2\phi}{dr_*^2} + V_{\text{eff}}\phi = 0, \tag{2.28}$$

with

$$V_{\text{eff}} = \frac{\Delta}{(r^2 + a^2)^2} \left(\lambda + \frac{(r\Delta)'}{r^2 + a^2} - \frac{3\Delta r^2}{(r^2 + a^2)^2} \right) - \left(\sigma - \frac{ma + qQr}{r^2 + a^2} \right)^2, \tag{2.29}$$

where λ is the separation constant and Δ is given explicitly in (2.15). The tortoise coordinate r_* is defined by [113]

$$\frac{dr_*}{dr} = \frac{r^2 + a^2}{\Delta}. \tag{2.30}$$

This new radial coordinate maps the interval of r exterior to the horizon to the real line

i.e., $r_* \in (-\infty, \infty)$. The black hole event horizon is located at $r_* \to -\infty$. The effective potential (2.29) takes the following form at the horizon and at infinity

$$V_{\text{eff}}(r_* \to -\infty) = \tilde{\sigma}^2 \equiv \left(\sigma - \frac{ma + qQr_+}{r_+^2 + a^2}\right)^2,$$
$$V_{\text{eff}}(r_* \to \infty) = \sigma^2, \tag{2.31}$$

where r_+ is the outer horizon of the Kerr-Newman black hole (2.16). The solutions to (2.28) near the horizon and at infinity are given by

$$\phi_{in} \sim \begin{cases} e^{-i\tilde{\sigma}r_*}, & \text{as } r_* \to -\infty \\ C_1 e^{-i\sigma r_*} + C_2 e^{i\sigma r_*}, & \text{as } r_* \to \infty. \end{cases} \tag{2.32}$$

In (2.32), at the horizon no outgoing flux emerges from the black hole (at a classical level), whereas near infinity, there are both ingoing and outgoing modes. One can construct another linearly independent solution to (2.28) by taking the complex conjugate of (2.32). We thus define $\phi_{out} = \phi_{in}^*$. We shall now compute the Wronskian of these two linearly independent solutions. The Wronskian is defined by

$$W(\phi_{in}, \phi_{out}) = \phi_{in}\frac{d\phi_{out}}{dr_*} - \phi_{out}\frac{d\phi_{in}}{dr_*}. \tag{2.33}$$

Next, we obtain the following by evaluating the Wronskian at the horizon and infinity,

$$W\Big|_{r_*=-\infty} = 2i\tilde{\sigma}, \tag{2.34}$$
$$W\Big|_{r_*=\infty} = 2i\sigma\left(|C_1|^2 - |C_2|^2\right). \tag{2.35}$$

Since the solutions ϕ_{in} and ϕ_{out} are linearly independent, their Wronskian must be a

constant. This implies that

$$\frac{\tilde{\sigma}}{\sigma} = |C_1|^2 - |C_2|^2. \tag{2.36}$$

We now define the coefficients $|C_1|$ and $|C_2|$

$$C_1 = \frac{1}{T}, \qquad \frac{C_2}{C_1} = R, \tag{2.37}$$

where $|T|^2$ is the transmission coefficient and $|R|^2$ is the reflection coefficient. Therefore (2.36) has now become

$$\frac{\tilde{\sigma}}{\sigma}|T|^2 = 1 - |R|^2. \tag{2.38}$$

It is clear that if $\frac{\tilde{\sigma}}{\sigma} < 0$ then $|R| > 1$. Thus we have superradiance. In general, we often write $\tilde{\sigma} = \sigma - \sigma_c$. Thus superradiance occurs if $0 < \sigma < \sigma_c$. The critical frequency σ_c for a Kerr-Newman black hole is given by (2.31)

$$\sigma_c = \frac{ma + qQr_+}{r_+^2 + a^2}. \tag{2.39}$$

This critical frequency σ_c is quite general. We can obtain the corresponding critical frequencies for RN or Kerr black holes by simply setting $a = 0$ or $Q = 0$ in (2.39) respectively. We obtain the following [17]

$$\frac{\sigma - \sigma_c}{\sigma} = \begin{cases} \left(1 - \frac{qQ}{\sigma r_h}\right), & \text{for RN case} \\ \left(1 - \frac{ma}{2M\sigma r_h}\right), & \text{for Kerr case} \end{cases} \tag{2.40}$$

where q, Q, m, M and a are the charge of the scalar field, the total charge of the RN black hole, the azimuthal quantum number, the mass and spin parameters of Kerr black hole, respectively. In both expressions r_h refers to the location of the outer event horizon of either the RN (2.5) or Kerr black hole (2.8). Finally the superradiant condition $\frac{\tilde{\sigma}}{\sigma} < 0$

implies that

$$\begin{aligned} 0 < \sigma < q\Phi_H \equiv \frac{qQ}{r_h}, \qquad & \text{for RN case} \\ 0 < \sigma < m\Omega_H \equiv \frac{ma}{2Mr_h}, \qquad & \text{for Kerr case} \end{aligned} \tag{2.41}$$

where Φ_H and Ω_H are electric potential and angular velocity of the event horizon respectively. If the frequency of the scalar field obeys either of the inequalities (2.41), then the reflection amplitude $|R|$ will be greater than unity, and we will have superradiance. If the black hole is non-rotating ($a = 0$) and either the BH or the scalar field has vanishing charge ($q = 0$ or $Q = 0$), the inequalities (2.41) are trivial, $\sigma_c = 0$ and $\tilde{\sigma} = \sigma$ in (2.38). Therefore the relationship between T and R turns out to be, in this case

$$|T|^2 + |R|^2 = 1. \tag{2.42}$$

This is the standard scattering relation. The part of incident wave that is not absorbed by the black hole will be reflected back to infinity [70]. We remark that other forms of bosonic field such as an electromagnetic field also experience superradiance. For example the massive photon (Proca field) around a slowly rotating Kerr black hole has been shown to exhibit a superradiant instability (see section 2.6 for more details) [137, 138].

Before leaving this section, we emphasize that fermionic fields cannot induce superradiant phenomena. This fact has been observed in many studies. For example, superradiance of massless and massive spin-1/2 fields cannot exist on the Kerr background [102, 121, 182]. Also, by analysing the transmission and reflection coefficients of a massive Dirac field on the Kerr background, it was shown explicitly that superradiance does not exist, since its reflection amplitude $|R|$ is always less than unity [38]. The non-existence of superradiant scattering for fermions can also be understood from a physical point of view. Unlike the bosonic fields, fermions are governed by Pauli exclusion principle which does not allow fermions to condensate and hence no superradiance can occur.

2.5.2 Superradiance and black hole mechanics

In 1973, Bekenstein [17] realized that superradiance can be deduced directly from Hawking's area theorem [83]. The area theorem states that a black hole's surface area never decreases. In this section, we will discuss Bekenstein's argument and derive the superradiance condition. As will be seen, this approach requires no knowledge of the wave equation on a curved background. Thoughout this section, we will mainly follow the calculations in [17, 38, 70].

We consider the first law of black hole mechanics. When a stationary black hole is perturbed, the change in mass M is related to the change of horizon area A, angular momentum J and charge Q by [6]

$$\delta M = \frac{\kappa}{8\pi}\delta A + \Omega_H \delta J + \Phi_H \delta Q, \tag{2.43}$$

where κ denotes the black hole surface gravity. The behaviour of a scalar field mode with frequency σ and azimuthal number m may be described by (2.26) [17]. We assume that this wave carries charge q and has energy σ and angular momentum m (since we have set $\hbar = 1$). Hence, the ratios between the angular momentum and charge to the energy carried by the wave are equal to m/σ and q/σ, respectively [70]. The change in black hole mass, angular momentum and charge caused by the interaction of the scalar field Φ are therefore related by [70]

$$\delta J = \frac{m}{\sigma}\delta M, \quad \delta Q = \frac{q}{\sigma}\delta M. \tag{2.44}$$

Substituting these results into the first law above (2.43), we obtain

$$\delta M = \frac{\kappa\sigma}{8\pi}\frac{\delta A}{(\sigma - m\Omega_H - q\Phi_H)}. \tag{2.45}$$

Since Hawking's theorem implies that $\delta A \geq 0$, thus an interesting phenomena occurs if

$$\sigma < m\Omega_H + q\Phi_H. \tag{2.46}$$

This yields $\delta M < 0$, hence the energy of the black hole is reduced. This is the superradiance effect. Note that condition (2.46) is equivalent to those superradiant conditions obtained in the previous subsection (2.41). Thus, we have shown how superradiance can be directly deduced from Hawking's area theorem. It is worth mentioning that this treatment does not cover the fermionic case since the energy momentum tensor of a fermion violates the weak energy condition, which is a necessary energy condition in Hawking's proof of the area theorem.

§2.6 Superradiant instability

Superradiant scattering allows bosonic fields to gain energy from a black hole. Consequently, the wave amplitude of a test field is enhanced if its mode frequency satisfies a certain condition (2.46). Furthermore, if the system is confined, the matter field is forced to repeatedly interact with the black hole. Subsequently, the wave amplitude increases exponentially and causes an instability. Additionally, this amplified wave will ultimately create a non-negligible back-reaction on the spacetime background and the weak-field approximation breaks down. This type of instability was investigated by Press and Teukolsky [141], they named this phenomenon the *black hole bomb*. Fig 2.8 illustrates this behaviour. In this diagram, a superradiant wave is bounced back and forth between the region near the horizon and a reflective mirror. At each scattering, the amplitude of the wave becomes bigger. Note that, without the reflective boundary or mirror, the scattered wave would escape to infinity as shown in Fig 2.7.

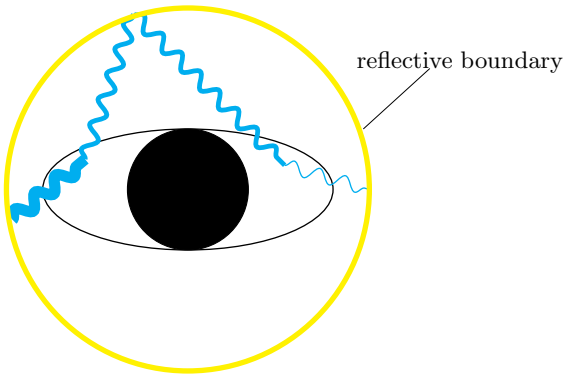

Figure 2.8: Diagram showing a superradiant instability induced by a reflective boundary.

For a rotating black hole, there are many ways to create such a trapping mechanism. One possibility is by enclosing the black hole and test field inside an artificial reflecting mirror. This was first suggested by Zel'dovich [205]. He considered a cylindrical rotating object with a mirror and found that this could lead to an instability [205]. Moreover, a scalar field around a spinning black hole surrounded by a mirror was found to experience a superradiant instability [47, 141]. On the other hand, a number of studies have shown that the mass term of a massive scalar field can play the same role as a mirror. A massive scalar field on a Kerr background was proven to be unstable via the superradiant mechanism [53, 58, 208]. Most of the works that we have mentioned so far, considered the frequency-domain. However, a time-domain analysis of superradiant instabilities of a spinning black hole for both the mirror case and a massive scalar field was investigated in [60] and the maximum instability growth rates were calculated. The time scale for the superradiant instability is inversely proportional to the imaginary part of the frequency, i.e., $\mathrm{Im}(\sigma) = 1/\tau$. For massive fields the instability time scale is shown to be $\tau \approx 0.57 \times 10^7 M$ [60] and for the mirror-like boundary condition $\tau \approx 1.66 \times 10^5 M$ [47], where M is black hole mass. Note that these timescales are extremely long. Besides a fundamental scalar field, other types of bosonic field can also induce a superradiant instability. For instance, a massive vector field (Proca field) can be used to generate a rotating black hole bomb

[137]. Lastly, a natural confining box is provided automatically when the asymptotic structure of spacetime is AdS rather than asymptotically flat. Analytical and numerical studies reveal that a small (horizon radius small compared to the AdS radius of curvature) Kerr-AdS black hole is unstable under scalar perturbations via superradiance [46, 181].

While a number of studies have indicated that the Kerr black hole is superradiantly unstable at the linearised level, however, the end-point of this instability remains mysterious. It has been proposed that the end-point could be reached after an explosive event called a *bosenova* [202]. The non-linear study of a self-interacting axion field around a Kerr black hole reveals that the axion field would eventually collapse and followed by explosive phenomena (bosenova) [202]. A full non-linear analysis of the time-evolution is required to completely understand the end-point of Kerr's instability induced by superradiant processes. This could be a very challenging task, since the development of the rotating superradiant instability has very long timescales. Recently, Kerr black holes with scalar hair and Proca hair have been found numerically [84, 87]. These hairy solutions describe asymptotically flat, stationary, axisymmetric black holes with scalar/Proca hair and regular event horizons. In the absence of a horizon, these hairy solutions reduce to rotating boson/Proca stars. These new types of hairy black hole solutions are constructed by considering the evolution of complex massive scalar and complex Proca fields at the threshold of the superradiant regime ($\sigma = \sigma_c$) [84, 87]. At this critical value the imaginary part of the frequency vanishes, i.e., $\mathrm{Im}(\sigma) = 0$. Thus, there is no decaying or growing mode, therefore there exits a bound state mode. This bound state mode is sometimes referred to as a scalar/Proca stationary cloud.

In contrast, it turns out that a massive complex scalar field on a Reissner-Nordström black hole does not lead to a superradiant instability [54, 95, 96, 155]. This is because, even though the field is massive, modes in the superradiant regime (that is satisfying (2.46)) are not trapped near the horizon and escape to infinity. The same results were found for a charged Proca field on the Reissner-Nordström geometry [155]. These studies provide

strong evidence that a charged massive bosonic field does not experience a superradiant instability on a Reissner-Nordström black hole. On the other hand, a charged superradiant instability has been observed when a massive charged scalar field on a Reissner-Nordström black hole is enclosed by an artificial mirror [85]. Frequency [85] and time-domain [55] analyses of such a system reveal that the unstable modes grow a lot faster than in the rotating case. The spherically symmetric mode $l = 0$ has faster growth rate than the $l = 1$ mode [55, 85], where l is the total angular momentum quantum number. The time scale of the charged superradiant instability is $\tau \approx 0.14 \times 10^2 M$ [85]. We should remark that this timescale is obtained via numerical study. In addition, the instability timescale is derived analytically in [94]. It turns out that one can make this timescale as short as one desires since the imaginary part of the frequencies is proportional to qQ. By investigating the quasinormal modes of a massless charged scalar field on a small RN-AdS black hole, it was shown that small RN-AdS black holes are also unstable if their quasinormal frequency lives in the superradiant regime [180].

Finding the end-point of the charged superradiant instability is less complicated than the rotating case because of the spherical symmetry of the problem. As a result, several authors have investigated this problem. For instance, by considering a fully coupled system of gravity, an electromagnetic field and a massless complex scalar field, stable hairy black hole solutions were found [61] (more details of this work can be found in chapter 4). Recently, an unstable mode of a massive charged scalar field on a RN black hole enclosed by a mirror was tracked into the non-linear regime using numerical relativity [156, 157]. The end-point of the superradiant instability was shown to be a new black hole with scalar hair. The evolution towards the end-point can be divided into two scenarios depending on the value of the scalar field charge q. For small scalar field charge, the unstable mode develops smoothly into a new black hole with scalar hair. On the other hand, an explosive "bosenova" event releases some energy back into the black hole when scalar field charge is large [157]. Moreover, the charge extraction process stops before all the charge is

extracted from the black hole [157]. In addition, the end-point of the charged superradiant instability of a massive charged scalar field with self-interaction term on a RN black hole in a cavity has been recently reported [156]. The end-point of the superradiant instability of a massless scalar field on RN-AdS background was also studied recently using a fully non-linear development of unstable modes [31]. In the early stages, superradiant modes extract mass and charge from the black hole and grow exponentially as expected from linearised studies. As the system evolves, the field enters into the non-superradiant regime. This non-superradiant mode falls back into the black hole and returns energy and charge to the black hole via a "bosenova". The final state is a black hole with stable scalar hair [31].

Since chapter 4 of this thesis will be devoted to the study of potential end-points of the charged superradiant instability, as a preliminary work, in following subsection, the analysis of a charged test scalar field on a Reissner-Nordström black hole in a cavity will be discussed. We shall obtain exponentially growing modes which can be associated with the superradiant instability in the charged case.

2.6.1 Charged superradiant instability

To demonstrate that a massless charged scalar field experiences a superradiant instability, in this subsection, we shall consider a linear perturbation of Reissner-Nordström (RN) spacetime in a cavity.

We start by considering a linear scalar perturbation on the RN background for which the back-reaction on the gravitational and electromagnetic fields can be neglected. We use the RN metric (2.3) as the background spacetime. In the test field limit, the evolution of a complex scalar field is described by the Klein-Gordon equation

$$D_a D^a \Phi = 0, \tag{2.47}$$

where D_a is gauge covariant derivative defined by $D_a \equiv \nabla_a - iqA_a$ and A_a is the elec-

tromagnetic potential for the RN black hole given by $A_a = [-Q/r, 0, 0, 0]$. We assume a small spherically symmetric perturbation taking the following form

$$\Phi = \frac{\phi(r)}{r} e^{-i\sigma t}, \tag{2.48}$$

where σ is the frequency of the scalar field. Substituting (2.48) into (2.47), the Klein-Gordon equation becomes

$$f_{RN}\frac{d^2\phi}{dr^2} + f'_{RN}\frac{d\phi}{dr} + \left[\frac{1}{f_{RN}}\left(\sigma - \frac{qQ}{r}\right)^2 - \frac{f'_{RN}}{r}\right]\phi = 0, \tag{2.49}$$

where $f'_{RN} = df_{RN}/dr$ and f_{RN} is shown explicitly in (2.4). This equation can be put into Regge-Wheeler form by introducing the tortoise coordinate r_*. Thus (2.49) takes the form

$$\frac{d^2\phi}{dr_*^2} + \left[\left(\sigma - \frac{qQ}{r}\right)^2 - \frac{f_{RN}}{r}f'_{RN}\right]\phi = 0, \tag{2.50}$$

where

$$\frac{dr_*}{dr} = \frac{1}{f_{RN}}. \tag{2.51}$$

Note that in this coordinate, the outer event horizon r_+ is located at $r_* \to -\infty$. This equation takes the same form as that found by Herdeiro et.al. [85] when assuming that the total angular momentum quantum number $l = 0$ and considering a massless scalar field. By imposing the following boundary conditions, equation (2.50) can be solved numerically,

$$\begin{aligned} &\phi \sim e^{-i(\sigma-\sigma_c)r_*} \qquad \text{as} \qquad r_* \to -\infty, \\ &\phi = 0 \qquad\qquad\quad \text{at} \qquad r_* = r_m, \end{aligned} \tag{2.52}$$

where r_m is the location of mirror and $\sigma_c \equiv qQ/r_+$. If $\sigma < \sigma_c$, then the ingoing wave as seen by a local observer, will behave as the wave coming out of the black hole as seen by

observer at infinity. This implies that the energy can be extracted from the black hole when $\sigma < \sigma_c$. The scalar perturbation behaves as an ingoing wave near the horizon, and it is required to vanish at the location of mirror. These boundary conditions lead to a set of discrete complex eigenfrequencies σ. It can be clearly seen from (2.48) that an exponential growth (decay) of the scalar perturbation corresponds to a positive (negative) imaginary component of the frequency σ.

Ultimately, our aim is to fully solve the Klein-Gordon equation (2.49). This means, we will numerically obtain the frequency σ which makes the scalar field mode satisfy the boundary conditions (2.52). It is possible to construct an analytic approximation for σ which can be used as an approximation for the real numerical value. For a massless scalar field on a Kerr background, an analytic frequency for the scalar field was derived by Cardoso et.al. [47]. Later, an analogous formula was found by Li, et.al. [117], who considered a massless charged scalar field on a d-dimensional Reissner-Nordström spacetime. The works [47, 117] both use a solution matching technique where the radial scalar equation is divided into two regions: the near and the far region (see below for more details). Then the wave equation is solved separately in both regions and the solutions are matched in the overlap area. Finally, an approximation is obtained for the real and imaginary parts of the frequency of the scalar field.

Here, we will outline how to obtain this formula for σ analytically. This formula will become useful later when we set-up a shooting method scheme for solving the Klein-Gordon equation (2.49) numerically. By adopting the matching method used in [47, 117], we will construct an analytic formula for the frequency of the massless charged scalar field on the four dimensional Reissner-Nordström background.

We consider the following ansatz for the scalar field

$$\Phi = e^{-i\sigma t} Y_l^m(\theta, \varphi) R(r), \tag{2.53}$$

where Y_l^m is a spherical harmonic, l is the total angular momentum quantum number and m is the azimuthal harmonic index. Inserting (2.53) in the Klein-Gordon equation (2.47), we find that the radial function $R(r)$ obeys

$$\Delta\partial_r\left(\Delta\partial_r R\right) + \left[\left(\sigma r^2 - qQr\right)^2 - \Delta l(l+1)\right] R = 0, \tag{2.54}$$

where $\Delta \equiv (r - r_+)(r - r_-)$.

We keep l for completeness at this stage; later we will consider only the spherically symmetric mode ($l = 0$). The master equation (2.54) governs the stationary evolution of the massless charged scalar field on the Reissner-Nordström spacetime. Now we will implement the matching method to obtain an approximation formula for σ. Following [47, 117], we assume that the Compton wavelength of the scalar field is much larger than the size of the black hole, i.e., $\sigma \ll 1/M$. With this assumption, it is possible to divide the spacetime outside the black hole horizon into two distinct regions, the "near" region for which $(r - r_+) \ll 1/\sigma$ and the "far" region where $(r - r_+) \gg M$. Then the wave equation (2.54) will be solved in each region. After that, the solutions from both ends will be matched in the intermediate region, i.e., $M \ll (r - r_+) \ll 1/\sigma$.

For the near region, $(r - r_+) \ll 1/\sigma$, the master equation (2.54) can be approximated as

$$\Delta\partial_r\left(\Delta\partial_r R\right) + \left[r_+^4\left(\sigma - q\Phi_H\right)^2 - \Delta l(l+1)\right] R = 0, \tag{2.55}$$

where $\Phi_H = Q/r_+$ is the electric potential at the black hole horizon. To solve this equation analytically, we introduce a new radial coordinate x

$$x = \frac{r - r_+}{r - r_-}, \tag{2.56}$$

where the black hole horizon is now located at $x = 0$ and infinity is $x = 1$. Thus we have

$\Delta\partial_r = (r_+ - r_-)x\partial_x$. Hence the near region wave equation (2.55) transforms to

$$x(1-x)\partial_x^2 R + (1-x)\partial_x R + \left[\bar{\sigma}^2 \frac{1-x}{x} - \frac{l(l+1)}{1-x}\right] R = 0, \tag{2.57}$$

where the frequency parameter $\bar{\sigma}^2$ is defined by

$$\bar{\sigma}^2 = (\sigma - q\Phi_H)^2 \frac{r_+^4}{(r_+ - r_-)^2}. \tag{2.58}$$

We define a new radial function

$$R = x^{i\bar{\sigma}}(1-x)^{l+1}F(x). \tag{2.59}$$

Substituting this into the near region radial equation (2.57), we obtain the canonical hypergeometric differential equation

$$x(1-x)\partial_x^2 F + [c - (a+b+1)\,x]\,\partial_x F - abF = 0, \tag{2.60}$$

with

$$a = 1 + l + 2i\bar{\sigma}, \qquad b = 1 + l, \qquad c = 1 + 2i\bar{\sigma}. \tag{2.61}$$

Near the horizon $x = 0$, the most general solution of the radial equation (2.57) can be therefore written down in terms of hypergeometric functions [3]

$$\begin{aligned} R = {} & Ax^{-i\bar{\sigma}}(1-x)^{l+1}F(a-c+1, b-c+1, 2-c, x) \\ & + Bx^{i\bar{\sigma}}(1-x)^{l+1}F(a, b, c, x), \end{aligned} \tag{2.62}$$

where A and B are arbitrary constants. The first term represents the ingoing wave at the horizon while the second term is an outgoing wave at the horizon. Since at the classical level, there is no outgoing flux at the horizon, we set $B = 0$. Furthermore, the near region solution (2.62) will be matched later with the far region solution, hence we will

consider the behaviour of the near region solution in the large r limit, i.e., $x \to 1$. This can be achieved by using the following property of hypergeometric functions under the transformation $x \to 1-x$ [3]

$$F(a-c+1,b-c+1,2-c,x) = \mathcal{X}F(a-c+1,b-c+1,a+b-c+1,1-x) + \mathcal{Y}F(1-a,1-b,c-a-b+1,1-x). \tag{2.63}$$

with

$$\mathcal{X} = \frac{\Gamma(2-c)\Gamma(c-a-b)}{\Gamma(1-a)\Gamma(1-b)}, \qquad \mathcal{Y} = (1-x)^{c-a-b}\frac{\Gamma(2-c)\Gamma(a+b-c)}{\Gamma(a-c+1)\Gamma(b-c+1)}. \tag{2.64}$$

We remark that the gamma function in $\mathcal{X}$ has a pole when $l=0$. However, the alternative formulas which cover this case have been provided in [3] (page 559). For large r ($x \to 1$), now (2.63) becomes

$$F(a-c+1,b-c+1,2-c,x) = \mathcal{X}+\mathcal{Y}, \tag{2.65}$$

where we apply $F(a,b,c,0) = 1$ above. Now the large r behaviour of the near region solution (2.62) is described as follows

$$R \sim A\Gamma(1-2i\bar{\sigma})\left[\frac{(r_+-r_-)^{-l}\Gamma(2l+1)}{\Gamma(l+1)\Gamma(l+1-2i\bar{\sigma})}r^l + \frac{(r_+-r_-)^{l+1}\Gamma(-2l-1)}{\Gamma(-l-2i\bar{\sigma})\Gamma(-l)}r^{-l-1}\right]. \tag{2.66}$$

At large distances $(r-r_+) \gg M$ or $r \to \infty$, the spacetime is assumed to be flat and all the effects of the black hole are negligible [117]. With these approximations, the master equation (2.54) simplifies to the massless scalar wave equation on a flat background. It reads

$$\partial_r^2(rR) + \left[\sigma^2 - \frac{l(l+1)}{r^2}\right](rR) = 0. \tag{2.67}$$

This can be solved by a combination of Bessel functions. The solution is given by

$$R = \frac{C_1}{\sqrt{r}} J_{l+1/2}(\sigma r) + \frac{C_2}{\sqrt{r}} J_{-l-1/2}(\sigma r), \tag{2.68}$$

where C_1 and C_2 are arbitrary constants. To compare (2.68) with the near region solution (2.62), we need to consider (2.68) in small r limit. For small r, the Bessel function of the first kind can be approximated as

$$J_\nu(r) \sim \frac{1}{\Gamma(\nu+1)} \left(\frac{r}{2}\right)^\nu. \tag{2.69}$$

Therefore (2.68) can be re-written in the small r limit as

$$R \sim \frac{C_1 \left(\sigma/2\right)^{l+1/2}}{\Gamma(l+3/2)} r^l + \frac{C_2 \left(\sigma/2\right)^{-l-1/2}}{\Gamma(-l+1/2)} r^{-l-1}. \tag{2.70}$$

We are now ready to match the large r near horizon region solution (2.66) with the small r far region solution (2.70) in the overlapping region defined by $M \ll (r - r_+) \ll 1/\sigma$. This can be done by comparing the coefficients of r^l and r^{-l-1} in each equation. From the coefficient of r^l, we obtain

$$A = \frac{(r_+ - r_-)^l \Gamma(l+1)\Gamma(l+1-2i\bar{\sigma})}{\Gamma(l+3/2)\Gamma(2l+1)\Gamma(1-2i\bar{\sigma})} \left(\frac{\sigma}{2}\right)^{l+1/2} C_1. \tag{2.71}$$

From the coefficient of r^{-l-1}, the matching yields a relationship between A and C_2. However, we can use (2.71) and obtain the following ratio

$$\frac{C_2}{C_1} = \frac{\Gamma(l+1)\Gamma(-l+1/2)\Gamma(-2l-1)\Gamma(l+1-2i\bar{\sigma})(r_+ - r_-)^{2l+1}}{\Gamma(2l+1)\Gamma(l+3/2)\Gamma(-l)\Gamma(-l-2i\bar{\sigma})} \left(\frac{\sigma}{2}\right)^{2l+1}. \tag{2.72}$$

To simplify this further, we use the properties of the gamma function $\Gamma(1+x) = x\Gamma(x)$,

in particular [3, 47]

$$\begin{aligned}
\frac{\Gamma(l+1)}{\Gamma(2l+1)} &= \frac{l!}{(2l)!}, \\
\frac{\Gamma(-l+1/2)}{\Gamma(l+3/2)} &= \frac{(-1)^l 2^{2l+1}}{\left((2l-1)!!\right)^2}, \\
\frac{\Gamma(-2l-1)}{\Gamma(-l)} &= \frac{(-1)^{l+1} l!}{(2l+1)!}, \\
\frac{\Gamma(l+1-2i\bar{\sigma})}{\Gamma(-l-2i\bar{\sigma})} &= (-1)^{l+1} 2i\bar{\sigma} \prod_{k=1}^{l} \left(k^2 + 4\bar{\sigma}^2\right),
\end{aligned} \tag{2.73}$$

where !! denotes the double factorial $n!! = \prod_{\alpha=0}^{\beta}(n-2\alpha)$. The ratio (2.72) becomes

$$\frac{C_2}{C_1} = \frac{2i\bar{\sigma}(-1)^l}{2l+1}\left[\frac{l!}{(2l-1)!!}\right]^2 \frac{(\sigma(r_+ - r_-))^{2l+1}}{(2l)!(2l+1)!} \prod_{k=1}^{l}\left(k^2 + 4\bar{\sigma}^2\right). \tag{2.74}$$

To proceed further, we place the mirror near infinity at the radius $r = r_m \gg M$. We also demand that at the mirror surface the scalar wave must vanish. Thus (2.68) implies the following (when $R = 0$)

$$\frac{C_2}{C_1} = -\frac{J_{l+1/2}(\sigma r_m)}{J_{-l-1/2}(\sigma r_m)}. \tag{2.75}$$

Thus we can substitute this into the LHS of (2.74). This yields

$$\frac{J_{l+1/2}(\sigma r_m)}{J_{-l-1/2}(\sigma r_m)} = \frac{2i\bar{\sigma}(-1)^{l+1}}{2l+1}\left[\frac{l!}{(2l-1)!!}\right]^2 \frac{(\sigma(r_+ - r_-))^{2l+1}}{(2l)!(2l+1)!} \prod_{k=1}^{l}\left(k^2 + 4\bar{\sigma}^2\right). \tag{2.76}$$

This equation is very useful, since it gives a condition relating the location of the mirror r_m and the frequency of the scalar field σ. For a very small frequency $|\sigma| \ll 1$ and $\mathrm{Re}(\sigma) \gg \mathrm{Im}(\sigma)$, the condition (2.76) gives the analytic formula for the frequency σ of the scalar field wave in a cavity. For very small frequency, the RHS of (2.76) can be approximated

to be zero. We now have

$$J_{l+1/2}(\sigma r_m) = 0. \tag{2.77}$$

We define the n^{th} root of the Bessel function to be $\sigma r_m = j_{l+1/2,n}$, where n is a non-negative integer. We assume that the complete solution of (2.76) can be written in the form

$$\sigma_n \sim \frac{j_{l+1/2,n}}{r_m} + \frac{i\delta}{r_m}, \tag{2.78}$$

for $|\delta| \ll 1$. The extra imaginary part δ can be thought of as a small correction term added to σ. By using a Taylor expansion for small δ, (2.76) now becomes

$$\frac{J'_{l+1/2}(j_{l+1/2,n})}{J_{-l-1/2}(j_{l+1/2,n})}\delta = \frac{2\bar{\sigma}(-1)^{l+1}}{2l+1}\left[\frac{l!}{(2l-1)!!}\right]^2 \frac{(\sigma(r_+ - r_-))^{2l+1}}{(2l)!(2l+1)!}\prod_{k=1}^{l}\left(k^2 + 4\bar{\sigma}^2\right), \tag{2.79}$$

therefore

$$\begin{aligned}
\delta &= -\frac{(-1)^l}{r_m^{2l+1}}\frac{J_{-l-1/2}(j_{l+1/2,n})}{J'_{l+1/2}(j_{l+1/2,n})}\left(\frac{j_{l+1/2,n}}{r_m} - q\Phi_H\right)\beta, \\
\beta &= \left(j_{l+1/2,n}\right)^{2l+1}\frac{2r_+^2(r_+ - r_-)^{2l}}{(2l+1)(2l)!(2l+1)!}\left[\frac{l!}{(2l-1)!!}\right]^2\prod_{k=1}^{l}\left(k^2 + 4\bar{\sigma}^2\right),
\end{aligned} \tag{2.80}$$

where we have used

$$\begin{aligned}
\sigma^{2l+1} &= \left(\frac{j_{l+1/2,n}}{r_m}\right)^{2l+1}, \\
\bar{\sigma} &= \left(\frac{j_{l+1/2,n}}{r_m} - q\Phi_H\right)\frac{r_+^2}{r_+ - r_-}.
\end{aligned} \tag{2.81}$$

We can use the formula (2.78) to obtain an approximate numerical value for the frequency σ_n of the scalar field. One can read out the real part of σ_n via $\mathrm{Re}(\sigma_n) = \frac{j_{l+1/2,n}}{r_m}$ and the imaginary part comes from $\mathrm{Im}(\sigma_n) = \delta/r_m$. This result has a similar structure to that

found in [47] where they obtain the "boxed quasinormal" frequencies of a massless scalar field on Kerr spacetime. Moreover, the result (2.78) agrees well with those of [85] and [117] (when the number of spacetime dimensions is equal to four).

Now we are ready to numerically solve the radial equation (2.49). This equation can be solved by using the shooting method (see details in Appendix A). We seek the frequency σ for which the radial mode ϕ satisfies the boundary conditions (2.52). Thus, the frequency will play the role of the shooting parameter. We use the formula above (2.78) as an initial input for σ. Note that we only consider the fundamental and spherically symmetric mode, hence $n = 0$ and $l = 0$. We remark that the derivation of (2.78) is valid only if $l > 0$ due to the pole of the gamma function. Nonetheless, as will be seen later, (2.78) provides a useful approximation to σ for our numerical analysis even in the $l = 0$ case. The black hole mass M is fixed to be unity throughout this subsection.

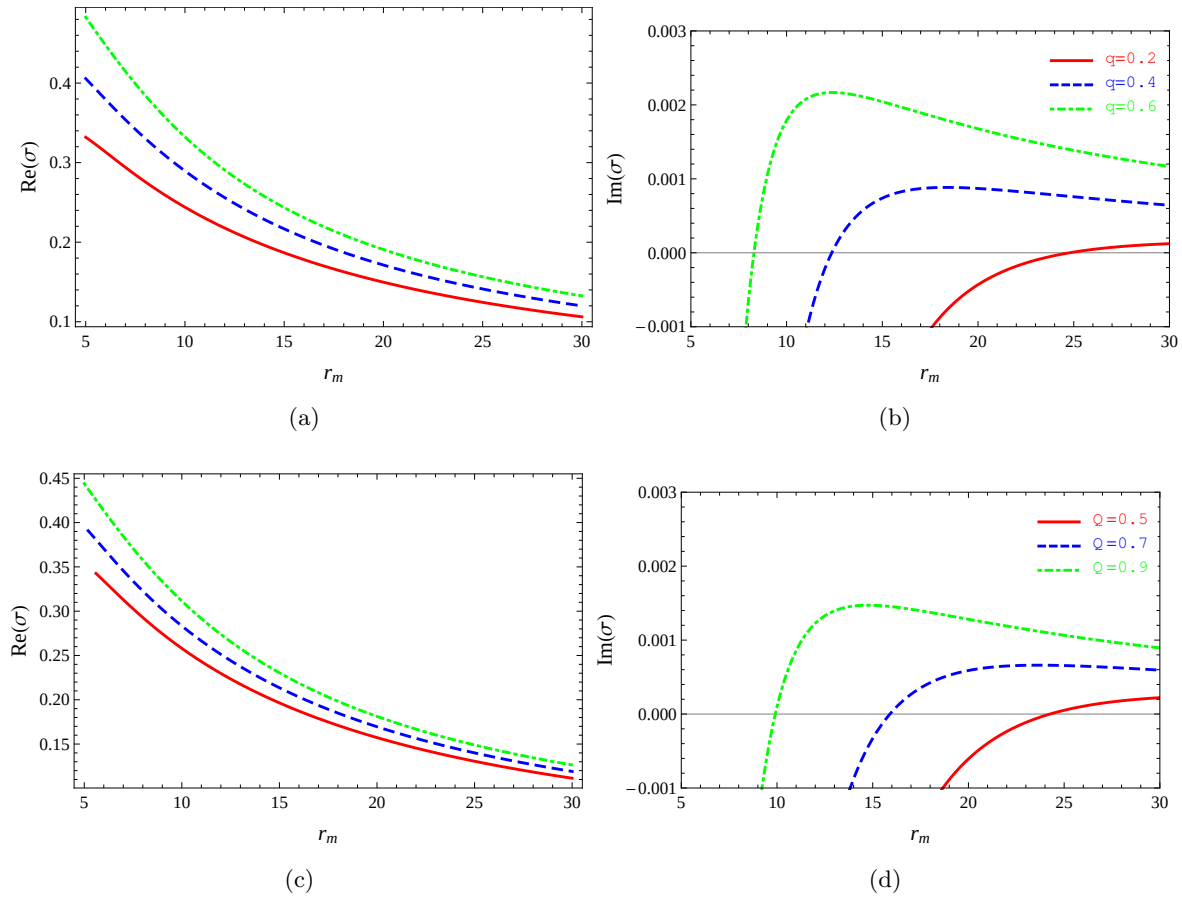

Figure 2.9: The real (left) and imaginary (right) part of the fundamental frequency σ_0 plotted as a function of mirror radius r_m with (a),(b) fixed black hole charge $Q = 0.9$ and (c),(d) fixed scalar field charge $q = 0.5$. The right-hand plots display the region where $\mathrm{Im}(\sigma_0)$ changes sign from negative to positive [61].

In Fig 2.9, the fundamental frequency σ_0 of the massless charged scalar perturbation on RN spacetime in a cavity is plotted against the location of mirror r_m. On the right-hand plots, the region where $\mathrm{Im}(\sigma_0) > 0$ implies the exponential growth of the scalar perturbation, on the other hand, the region $\mathrm{Im}(\sigma_0) < 0$ refers to exponential decay of the perturbation field. One can learn from these plots that, with sufficiently small r_m (mirror located near the black hole), the perturbation modes decay exponentially; with sufficiently large r_m (mirror located far from the black hole) the scalar fields experience

a charged superradiant instability. Moreover at the exact point where $\mathrm{Im}(\sigma_0) = 0$, the scalar field is in equilibrium with black hole, i.e., $\mathrm{Re}(\sigma_0) = \sigma_c = q\Phi_H$. From these plots, the largest imaginary part of frequency is $\mathrm{Im}(\sigma) \approx 0.0021$ when $q = 0.6, Q = 0.9$ and $r_m \approx 12$. Therefore the maximum growth rate for the values of q and Q shown in Fig 2.9 is $\tau \approx 4.76 \times 10^2 M$. Our instability time scale is slower than the massive charged case [85] but still significantly faster than the superradiant instabilities for a Kerr black hole [47, 60].

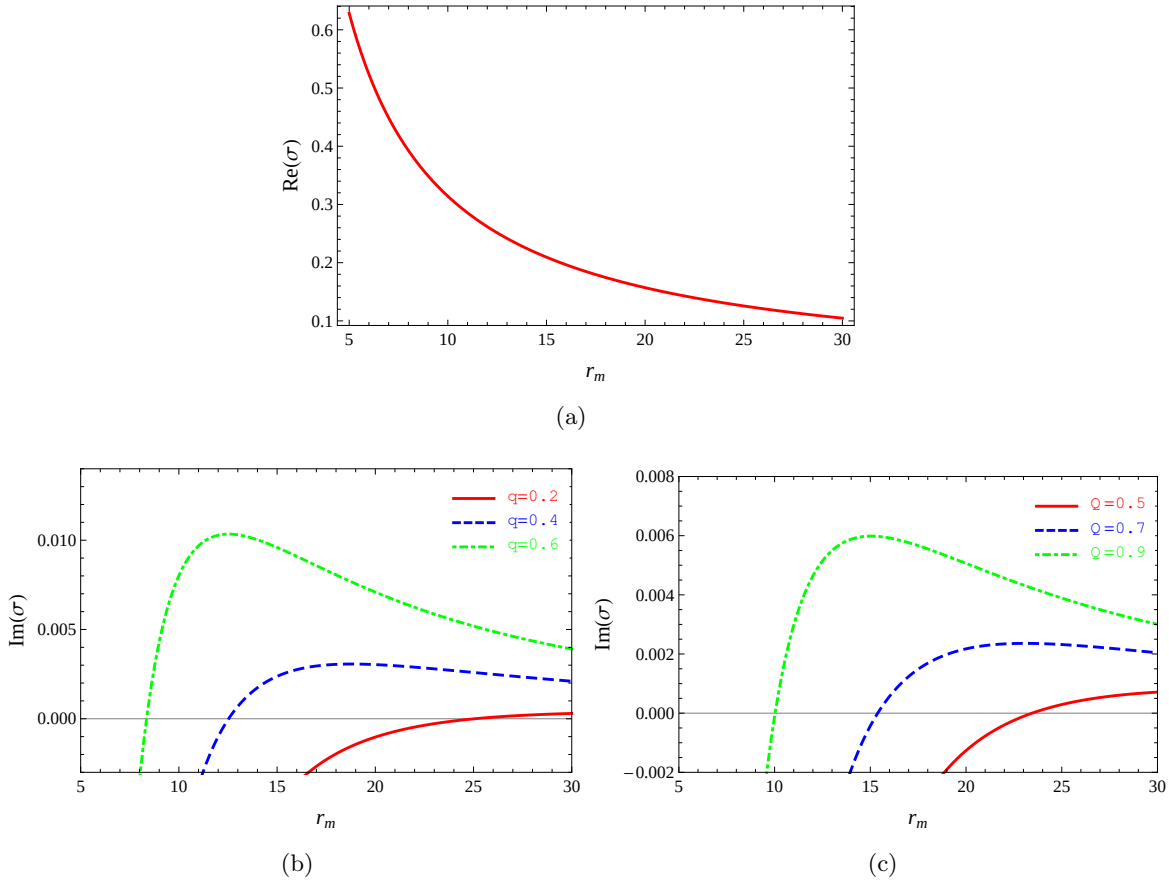

Figure 2.10: The plot of real and imaginary part of analytic frequency σ_0 (2.78) as a function of mirror radius r_m for various values of q and Q (a) $\mathrm{Re}(\sigma)$ is independent of q and Q. (b) Fixed black hole charge $Q = 0.9$. (c) Fixed scalar field charge $q = 0.5$.

As a comparison to Fig 2.9, we display the analytic frequency (both real and imaginary parts) obtained from (2.78) as a function of mirror radius r_m in Fig 2.10. From (2.78), $\mathrm{Re}(\sigma)$ depends only on r_m, therefore we display only one curve for fixed $q = 0.2$ and $Q = 0.9$ in Fig 2.10(a). The values of $\mathrm{Re}(\sigma)$ and $\mathrm{Im}(\sigma)$ obtained from (2.78) are slightly larger than the numerics shown in Fig 2.9, however both analytic and numeric σ share the same trends for each corresponding case. Therefore, (2.78) can be used as a good approximation even when $l = 0$.

The charged superradiant instability for a massive scalar field has been explored in both the frequency-domain [85] and time-domain [55]. The charged superradiant instability of a massive charged scalar field with a mirror-like boundary has been observed in [85] where they consider only massive scalar modes with $l = m = 1$, when l is the total angular momentum mode number and m the azimuthal mode number. In the frequency-domain, they find the transition from stable to unstable when the mirror r_m becomes sufficiently large. In addition, the time evolution of this system is carried out in [55], where the previous results for the $l = 1$ mode are confirmed. Additionally, they discover that for the spherically symmetric mode ($l = 0$), the unstable mode grows much quicker than the $l = m = 1$ mode.

§2.7 Summary

In this chapter, we gave a brief overview of some well-known exact black hole solutions. Then we discussed the definition of the no-hair theorem and its consequences. Next, studies of hairy black holes in general were explored. After that, we focused our investigation on black holes in EYM theory and their stability. On the superradiance side, we described a basic picture of superradiant scattering in black hole physics. Finally, we explored in detail how superradiant scattering can lead to an instability. In particular, we showed that a massless charged scalar field on the RN background with a reflecting boundary is superradiantly unstable.

Chapter 3

Einstein-non-Abelian-Proca theory in AdS spacetime

§3.1 Introduction

As discussed in the previous chapter, the Bartnik and McKinnon (BM) [7] and Bizon [24] solutions opened up a new era of studying self-gravitating matter in the form of non-Abelian gauge fields. A number of non-Abelian black hole solutions were found violating the no-hair conjecture. In this chapter we discuss one particular system, called the Einstein-non-Abelian-Proca (ENAP) model, in the presence of a negative cosmological constant. We consider static, spherically symmetric, four dimensional, asymptotically anti-de Sitter (AdS) spacetimes with an $SU(2)$ non-Abelian Proca field. As will be seen later, this system admits regular and black hole solutions. In addition the black holes in this sector violate the generalized no-hair conjecture in the sense that they are indistinguishable from the Schwarzschild-AdS black hole at infinity. We also prove that no dyon solutions are allowed in this model. Linear perturbations are also considered. The soliton and black hole solutions are shown to be unstable.

We start with a short review of Proca and ENAP theory in the next section, together with

a few examples of regular and black hole solutions of the ENAP-flat theory [79]. Then the ENAP-AdS action, equations of motion, metric and gauge field ansatz are defined in section 3.3. We derive the spherically symmetric Einstein field equations and non-Abelian Proca field equations in section 3.4. Since all the field equations are ordinary differential equations, to solve them, we need to determine appropriate boundary conditions. We present these boundary conditions in section 3.4. Next we use the shooting technique (discussed in Appendix A.2) to solve the field equations and in section 3.5 we present regular and black hole solutions of the ENAP theory in asymptotically flat and AdS spacetimes. As will be seen below, all of the solutions discussed so far are purely magnetic. Then the next step will be to include the electric component of the gauge field i.e., dyon solutions. However by following the argument made by Ershov and Galt'sov [71], in section 3.6, we provide an analytic proof that there are no dyon solutions in the ENAP-flat and the ENAP-AdS sector. We then proceed to the stability analysis in section 3.7. By assuming first order perturbations, we derive all the perturbation equations. These equations can be categorized into two sectors i.e., gravitational sector and sphaleronic sector. After that we present numerical evidence which confirms that the equilibrium soliton and black hole solutions in asymptotically flat and AdS are all unstable against small perturbations.

§3.2 Proca and ENAP theory

In field theory, the Proca field describes a massive spin-1 particle. This type of vector boson field is used to represent spin-1 vector mesons (quark-antiquark pairs) or the force carriers of the weak interaction i.e. $W^{\pm}, Z$. The Proca Lagrangian is basically a $U(1)$ electromagnetic Lagrangian with an extra mass term. The Proca Lagrangian [80] is a special case of the Stueckelberg theory which describes a $U(1)$ massive photon coupled to a scalar field [153]. In the limit where there is no scalar field, the Stueckelberg action yields the Proca action.

Including a coupling between the $U(1)$ Proca field and gravity yields Einstein-Proca theory.

It was proposed by Tucker and Wang that Einstein-Proca theory can be used as a dark matter model [179]. An exact static spherically symmetric solution was derived in [193]. Since Einstein-Proca theory reduces to Einstein-Maxwell theory when the Proca mass vanishes, this solution resembles the Reissner-Nordström metric when the Proca mass is set to zero and also possesses a naked singularity. In addition the existence of naked singularities in the Einstein-Proca model was shown numerically by independent studies of Obukhov and Vlachynsky [136] and Toussaint [177]. In a self-gravitating system of a massive vector, solutions are either black holes without vector hair or naked singularities with non-zero vector hair [114]. Note that this should not be a surprise since Bekenstein's results showed that a static black hole cannot support massive vector hair [14] and later this was generalized to the stationary case [15]. These results, which rule out the existence of Proca hair in many scenarios, rely on many restrict assumptions. Therefore one should not be surprised to find a black hole solution with Proca hair in a model for which these assumptions are not met. For example, it was found that the $U(1)$ Einstein-Proca system admits soliton and black hole solutions in the presence of a negative cosmological constant. We refer the reader to [119] where numerical solutions and their thermodynamic properties i.e., the first law, were constructed. Moreover the Hawking radiation of a $U(1)$ Proca black hole was discussed in [201] for both asymptotically dS and AdS cases. By considering a complex Proca field minimally coupled to gravity, Proca stars [37] and black hole solutions with Proca hair [84] were recently discovered. These solutions are made possible because the Proca field does not inherit spacetime symmetries and therefore evades Bekenstein's results [14, 15].

However the standard model of particle physics is governed mathematically by a non-Abelian theory. In fact the weak and strong interaction in the standard model theory can be written in terms of the $SU(2)$ and $SU(3)$ non-Abelian gauge groups which are special cases of Yang-Mills theory. As an extension of Yang-Mills theory, one could study the non-Abelian version of the Proca field. While Yang-Mills theory (without symmetry breaking)

describes massless bosons, non-Abelian Proca (NAP) theory, on the other hand, attempts to characterize massive gauge fields. The NAP theory is not gauge invariant, however it should be able to provide an approximate picture of a massive gauge field. Even though black hole solutions of Einstein-(Abelian) Proca theory cannot have non-trivial structure outside the event horizon, Einstein-non-Abelian-Proca (ENAP) theory with gauge group $SU(2)$ in asymptotically flat spacetime admits numerical regular and black hole solutions. These solutions were studied by Greene et.al's. [79] as a prelude to the study of black holes in Einstein-Yang-Mills-Higgs (EYMH) theory. A few examples of Greene et.al., results are shown in section 3.5, which are reproduced by our numerical codes. As can be seen later, the black holes are very similar to Schwarzschild when observed from infinity, hence they violate the generalized no hair conjecture [25, 52, 197].

A natural question that one might ask is: do regular and black hole solutions exist in the ENAP system when a negative cosmological constant is included? If they do, are they stable? The motivation behind these questions is the following: (1) although black hole solutions found in EYM-flat theory possesses zero non-Abelian global charge [24] and are also unstable [27, 168], the asymptotically AdS counterpart theory admits stable hairy black hole solutions [194]; (2) AdS spacetime has become more interesting especially in high-energy physics because of the duality between conformal field theory and gravity known as the AdS/CFT correspondence [120]. From these two viewpoints, we believe that asymptotically AdS spacetimes can be worth studying. Therefore this chapter will be devoted to answering the above questions.

§3.3 Equations of motion, metric ansatz and gauge connection

We consider four dimensional ENAP theory in asymptotically AdS spacetime with gauge group $SU(2)$. This theory is described by the following action

$$S_{ENAP} = \int d^4x\sqrt{-g}\left(\frac{\mathcal{R}}{2} - 2\Lambda + \mathcal{L}_{NAP}\right), \tag{3.1}$$

with

$$\mathcal{L}_{NAP} = -\frac{1}{2}\left(\mathrm{Tr}F_{ab}F^{ab} + 2\mu^2\mathrm{Tr}A_cA^c\right), \tag{3.2}$$

$$F_{ab} = \partial_a A_b - \partial_b A_a + e\left[A_a, A_b\right]. \tag{3.3}$$

Here $\mathcal{R} = g^{ab}R_{ab}$ is the Ricci scalar, Λ is the cosmological constant, e is the gauge coupling constant, μ is the Proca field mass and the Lie algebra trace is denoted by Tr.

By varying the action (3.1) with respect to the inverse metric g^{ab}, we find the Einstein equations

$$R_{ab} - \frac{1}{2}g_{ab}\mathcal{R} + \Lambda g_{ab} = T_{ab}, \tag{3.4}$$

where the energy-momentum tensor of the non-Abelian Proca field is given by

$$T_{ab} = 2\mathrm{Tr}F_{ac}F_b{}^c - \frac{1}{2}g_{ab}\mathrm{Tr}F_{cd}F^{cd} + \mu^2\left(2\mathrm{Tr}A_aA_b - g_{ab}\mathrm{Tr}A_cA^c\right). \tag{3.5}$$

The Proca equations are obtained by varying (3.1) with respect to A_a

$$\nabla_a F_b{}^a + e\left[A_a, F_b{}^a\right] + \mu^2 A_b = 0. \tag{3.6}$$

By taking ∇_b of the Proca equation, we can show that the gauge potential must satisfy the following constraint

$$\nabla_a A^a = 0. \tag{3.7}$$

Thus there is limited gauge freedom in the Proca theory.

§3.4 Field equations and boundary conditions

3.4.1 Field equations

We consider static, spherically symmetric spacetimes which can be written in Schwarzschild-like coordinates as follows,

$$ds^2 = -RS^2dt^2 + R^{-1}dr^2 + r^2d\theta^2 + r^2\sin^2\theta\ d\varphi^2. \tag{3.8}$$

The metric functions R and S are functions of the radial coordinate r. We can express the metric function $R(r)$, including the cosmological constant, as

$$R(r) = 1 - \frac{2m(r)}{r} - \frac{\Lambda r^2}{3}, \tag{3.9}$$

where $m(r)$ is the Misner-Sharp mass function [128]. The mass function is constant on each sphere with radius r.

The most general $SU(2)$ gauge potential with spherical symmetry is [200]

$$A = \frac{1}{e}\left\{a\hat{\tau}_r dt + b\hat{\tau}_r dr + [d\hat{\tau}_\theta - (1+c)\hat{\tau}_\varphi]d\theta + [(1+c)\hat{\tau}_\theta + d\hat{\tau}_\varphi]\sin\theta\ d\varphi\right\}. \tag{3.10}$$

Since we consider only the static case for the moment (for the time dependent case, see section 3.7), a, b, c and d are then functions of the radial coordinate r alone. The $SU(2)$ matrices satisfy

$$[\hat{\tau}_a, \hat{\tau}_b] = \epsilon_{abc}\hat{\tau}_c, \tag{3.11}$$

the indices ranging over (r, θ, φ). These matrices in spherical polar coordinates are explic-

itly given by

$$\hat{\tau}_r = -\frac{i}{2}\left[\sigma_1 \sin\theta\cos\varphi + \sigma_2 \sin\theta\sin\varphi + \sigma_3\cos\theta\right], \tag{3.12}$$

$$\hat{\tau}_\theta = -\frac{i}{2}\left[\sigma_1 \cos\theta\cos\varphi + \sigma_2 \cos\theta\sin\varphi - \sigma_3\sin\theta\right], \tag{3.13}$$

$$\hat{\tau}_\varphi = -\frac{i}{2}\left[-\sigma_1 \sin\varphi + \sigma_2 \cos\varphi\right], \tag{3.14}$$

where the σ_j's (with $j \in (1,2,3)$) are the Pauli matrices

$$\sigma_1 = \begin{pmatrix} 0 & 1 \\ 1 & 0 \end{pmatrix}, \qquad \sigma_2 = \begin{pmatrix} 0 & -i \\ i & 0 \end{pmatrix}, \qquad \sigma_3 = \begin{pmatrix} 1 & 0 \\ 0 & -1 \end{pmatrix}. \tag{3.15}$$

The gauge connection (3.10) has a residual $U(1)$ gauge freedom

$$A \to hAh^{-1} + \frac{1}{e}h\, dh^{-1}, \tag{3.16}$$

under the transformation matrix $h = \exp[\beta(t,r)\hat{\tau}_r]$. The gauge connection transforms as [79]

$$\begin{pmatrix} a \\ b \\ c \\ d \end{pmatrix} \to \begin{pmatrix} \hat{a} \\ \hat{b} \\ \hat{c} \\ \hat{d} \end{pmatrix} = \begin{pmatrix} a - \dot{\beta} \\ b - \beta' \\ c\cos\beta - d\sin\beta \\ d\cos\beta + c\sin\beta \end{pmatrix}. \tag{3.17}$$

In the static limit $\dot{\beta} = 0$. Since the metric (3.8) and gauge ansatz (3.10) depend solely on the radial coordinate r, the gauge condition (3.7) gives

$$Rb' + \left[\frac{2R}{r} + \frac{(RS)'}{S}\right] b - \frac{2}{r^2} d = 0. \tag{3.18}$$

By an appropriate choice of β', we can impose radial gauge such that $\hat{b} \equiv 0$. Therefore the

constraint (3.18) implies that $\hat{d} = 0$. The electric part of the gauge potential is excluded by setting $a \equiv 0$ (no dyons, see section 3.6). Hence the gauge connection takes the form

$$A = \frac{1}{e}\left[1 + \omega(r)\right]\left[-\hat{\tau}_{\varphi} d\theta + \hat{\tau}_{\theta} \sin\theta \; d\varphi\right], \tag{3.19}$$

where we have set $c \equiv \omega(r)$. This form of the gauge connection satisfies the gauge condition (3.7).

By substituting the metric ansatz (3.8) and the reduced gauge connection (3.19), into (3.6) the non-Abelian Proca (NAP) equations reduce to one equation (θ component)

$$r^2 \frac{d}{dr}\left[\omega' R\right] + \frac{r^2 R S'}{S}\omega' + (1-\omega^2)\omega - r^2\mu^2(1+\omega) = 0, \tag{3.20}$$

where a prime $'$ denotes d/dr. By defining

$$S(r) = e^{-\delta(r)}, \tag{3.21}$$

we obtain the following first order differential equations from the Einstein equations (3.4)

$$m' = R\left(\frac{\omega'}{e}\right)^2 + \frac{(1-\omega^2)^2}{2e^2 r^2} + \frac{\mu^2}{e^2}(1+\omega)^2, \tag{3.22}$$

$$\frac{S'}{S} = -\delta'(r) = \frac{2\omega'^2}{e^2 r}. \tag{3.23}$$

Equations (3.22) and (3.23) are derived from the (00), (11) components of the Einstein equations respectively. It is noteworthy to mention that the (22) component is redundant because of the Bianchi identity and the (33) component is proportional to the (22) component due to the spherical symmetry. We can use the two Einstein equations to eliminate

the metric function S from the NAP equation (3.20) to give

$$r^2 R\omega'' + \left[2m - \frac{2r^3\Lambda}{3} - \frac{(1-\omega^2)^2}{e^2 r} - \frac{2\mu^2}{e^2}(1+\omega)^2 r\right]\omega' + \left(1-\omega^2\right)\omega - (1+\omega)\mu^2 r^2 = 0. \tag{3.24}$$

Note that the field equations (3.22–3.24) reduce to the field equations of $SU(2)$ EYM-AdS theory [197] when $\mu \to 0$. However, unlike the ENAP system, the field equations of the EYM system have the discrete symmetry $\omega \to -\omega$. This property does not hold in the ENAP theory since the μ^2 term of the ENAP equations breaks the symmetry. If $\Lambda = 0$, the field equations (3.22–3.24) reduce to the set of field equations in the ENAP-flat system [79].

Although the field equations (3.22–3.24) are complicated, there are some trivial solutions that are worth mentioning. For instance, if we set $\omega(r) \equiv -1, m(r) \equiv M$ and $\delta(r) \equiv 0$ for all r, where M is a constant, we have the Schwarzschild-AdS black hole as a solution of (3.22–3.24). In contrast, setting $\omega(r) \equiv 0, m(r) \equiv M$ and $\delta(r) \equiv 0$ for all r, does not yield the Reissner-Nordström-AdS black hole because equation (3.24) is not satisfied by this ansatz.

3.4.2 Boundary conditions

The field equations (3.22–3.24) have three interesting asymptotic regions of relevance for regular and black hole solutions. These are: the origin $r = 0$, black hole event horizon $r = r_h$ where $R(r_h) = 0$ and infinity $r \to \infty$. Moreover these points are also the places where the field equations (3.22–3.24) become singular. We then need to analyze the behaviour of ω, m and δ near these singular points.

Origin: We use a regular Taylor series expansion about $r = 0$,

$$\begin{aligned} m(r) &= m_0 + m_1 r + m_2 r^2 + m_3 r^3 + m_4 r^4 + m_5 r^5 + O(r^6), \\ \delta(r) &= \delta_0 + \delta_1 r + \delta_2 r^2 + \delta_3 r^3 + \delta_4 r^4 + O(r^5), \\ \omega(r) &= \omega_0 + \omega_1 r + \omega_2 r^2 + \omega_3 r^3 + \omega_4 r^4 + O(r^5). \end{aligned} \tag{3.25}$$

Since R needs to be regular everywhere including at the origin (for regular solutions), we have $m_0 = 0$. The regularity of the Ricci scalar at $r = 0$ also implies that $m_1 = m_2 = \omega_1 = 0$. Thus, equation (3.22) implies that we must choose $\omega_0 = -1$ (from the fact that $m_1 = 0$). This is a significant difference from the EYM theory. In the EYM system, we can choose ω_0 to be ± 1 from the m' equation at the origin. This difference in boundary conditions has an effect on the numerical results which will be discussed later in section 3.5.

The field equation (3.23) implies that δ_0 is arbitrary and $\delta_1 = 0$. The fact that the field equations depend only on δ' means that δ is determined only up to an arbitrary constant. This constant is fixed by the requirement that at infinity $\delta \to 0$. Moreover in practice, δ_0 is chosen to be zero for convenience.

By analyzing the field equations, the remaining constants $m_3, m_5, \delta_2, \delta_4$ and ω_4 can be expressed in terms of ω_2. Therefore the series above (3.25) take the following forms

$$\begin{aligned} m(r) &= \frac{2\omega_2^2}{e^2} r^3 + \frac{1}{5e^2}\left[-8\omega_2^3 + 3\mu^2\omega_2^2 + \frac{8\Lambda\omega_2^2}{3}\right] r^5 + O(r^6), \\ \delta(r) &= -\frac{4\omega_2^2}{e^2} r^2 - \frac{4}{5e^2}\left[2\Lambda\omega_2^2 + \mu^2\omega_2^2 - 3\omega_2^3 + \frac{8\omega_2^4}{e^2}\right] r^4 + O(r^5), \\ \omega(r) &= -1 + \omega_2 r^2 + \frac{1}{10e^2}\left[2e^2\Lambda\omega_2 + e^2\mu^2\omega_2 - 3e^2\omega_2^2 + 8\omega_2^3\right] r^4 + O(r^5). \end{aligned} \tag{3.26}$$

From these series, we have a three parameter family of solutions near the origin, given by ω_2, μ and Λ. Note that our results reduce to those of Greene et.al., [79] in the limit $\Lambda \to 0$.

Event horizon: For a black hole solution, there is a regular event horizon located at $r = r_h$. Taylor series expansions of the field variables near the horizon assume the form

$$\begin{aligned} m(r) &= m(r_h) + m'_h(r - r_h) + O(r - r_h)^2, \\ \delta(r) &= \delta(r_h) + \delta'_h(r - r_h) + O(r - r_h)^2, \\ \omega(r) &= \omega(r_h) + \omega'_h(r - r_h) + O(r - r_h)^2. \end{aligned} \tag{3.27}$$

The existence of a regular event horizon at $r = r_h$ implies the two following conditions on the metric functions

$$\begin{aligned} \delta(r_h) &< \infty, \\ m(r_h) &= \frac{r_h}{2} - \frac{\Lambda r_h^3}{6}, \end{aligned} \tag{3.28}$$

where the last expression comes from the fact that $R(r_h) = 0$ at the horizon. As with the expansions near the origin, the value of $\delta(r_h)$ is fixed by the requirement that $\delta \to 0$ as $r \to \infty$. The constants $m'_h,\ \delta'_h$ and ω'_h are determined by the field equations to be

$$\begin{aligned} m'_h &= \frac{(1-\omega_h^2)^2}{2e^2 r_h^2} + \frac{\mu^2(1+\omega_h)^2}{e^2}, \\ \delta'_h &= -\frac{2\omega_h'^2}{r_h e^2}, \\ \omega'_h &= \frac{\mu^2(1+\omega_h)r_h^2 - (1-\omega_h^2)\omega_h}{(r_h - \Lambda r_h^3) - \frac{(1-\omega_h^2)^2}{e^2 r_h} - \frac{2\mu^2(1+\omega_h)^2 r_h}{e^2}}. \end{aligned} \tag{3.29}$$

Infinity with $\Lambda < 0$: Our metric (3.8) must reduce to the AdS metric as $r \to \infty$. This means that as $r \to \infty$, we have $m(r) \to M =$ constant and $\delta(r) \to 0$, where M can be interpreted as the total mass of the soliton or black hole. For the ENAP and the EYMH equations in asymptotically flat spacetime [79], the field variables decay exponentially at infinity. However in the EYMH-AdS system [183], the field variables decay as a power-law. By comparison with the EYMH-AdS theory, we expect our field variables $m(r),\ \delta(r)$ and $\omega(r)$

to decay by power-laws at infinity. By analysing the behaviour of the field equations at infinity up to the leading order, we find that ω decays more slowly than m and δ. Thus we make an educated guess as follows,

$$m(r) = M + \frac{\tilde{A}}{r^{2\Delta-1}} + ..., \qquad \delta(r) = \delta_\infty + \frac{\tilde{B}}{r^{2\Delta+2}} + ..., \qquad \omega(r) = -1 + \frac{\tilde{C}}{r^{\Delta}} + ..., \quad (3.30)$$

where $\tilde{A}, \tilde{B}, \tilde{C}, \Delta$ are undetermined parameters. Substituting these into the field equations (3.22–3.24), we obtain

$$\begin{aligned} m(r) &= M + \frac{\left(\Delta^2\Lambda - 3\mu^2\right)}{3e^2\Delta}\frac{\tilde{C}^2}{r^{-1+2\Delta}} + ..., \\ \delta(r) &= \delta_\infty + \frac{2\Delta}{e^2}\frac{\tilde{C}^2}{r^{2+2\Delta}} + ..., \\ \omega(r) &= -1 + \frac{\tilde{C}}{r^{\Delta}} + ..., \end{aligned} \quad (3.31)$$

where $\tilde{C}$ is a constant and

$$\Delta \equiv \Delta_\pm = \frac{1}{2} \pm \frac{1}{2}\sqrt{1 - \frac{12\mu^2}{\Lambda}}. \quad (3.32)$$

We choose the upper root Δ_+, since $\Delta_- < 0$. Note that, if $\mu = 0$ then $\Delta_+ = 1$, therefore power law decay of the field variables is recovered as the ENAP-AdS system reduces to EYM-AdS, except that $\omega(\infty)$ is not fixed in EYM-AdS [197]. Strictly speaking δ_∞ should be zero, but as can be seen later, this is not true in the numerical solutions. However one can add a constant to δ to make it vanish as $r \to \infty$. The leading order of ω is fixed to be -1 due to the fact that the mass function $m(r)$ needs to be constant at infinity. In contrast, the zeroth order of ω is ± 1 in asymptotically flat EYM theory [7, 24] and an arbitrary constant in the EYM-AdS theory [197]. This difference will play an important role when discussing regular solutions and the space of solutions. The behaviour of the field variables at infinity (3.31) is very similar to that in EYMH-AdS [183]. Moreover, the boundary condition (3.31) for the Proca field ω implies that at infinity the NAP field is vacuum, therefore the solutions look like Schwarzschild-AdS.

Infinity without Λ: If $\Lambda = 0$, the ENAP-AdS system becomes ENAP-flat. Hence the spacetime metric (3.8) must reduce to the Minkowski metric at infinity. By following the work done in [79], we expect that the field variables will decay exponentially. We therefore assume

$$m(r) = M + \bar{A}e^{-2\bar{\Delta}r}, \qquad \delta(r) = \delta_\infty + \frac{\bar{B}e^{-2\bar{\Delta}r}}{r}, \qquad \omega(r) = -1 + \bar{C}e^{-\bar{\Delta}r}, \tag{3.33}$$

where $\bar{A}, \bar{B}, \bar{C}$ and $\bar{\Delta}$ are undetermined constants. Substituting (3.33) into (3.22–3.24), we obtain

$$\begin{aligned} m(r) &= M - \frac{2\mu\bar{C}^2}{e^2}e^{-2\mu r}, \\ \delta(r) &= \delta_\infty + \frac{2\mu\bar{C}^2}{e^2}\frac{e^{-2\mu r}}{r}, \\ \omega(r) &= -1 + \bar{C}e^{-\mu r}, \end{aligned} \tag{3.34}$$

where $\bar{C}$ is an arbitrary constant. Therefore the field variables of the ENAP-flat theory decay much more quickly as $r \to \infty$ than those in ENAP-AdS (3.31) and EYMH-AdS [183]. Note that the boundary conditions (3.34) agree with those [79].

3.4.3 No nodeless solutions

As will be seen later, the regular and black hole solutions of ENAP equations both in asympototically flat and AdS are also classified by the number of zeros of the gauge field ω. We shall denote the number of zeros or node of ω by n. Before exploring the space of regular and black hole solutions, in this subsection we will provide a simple argument showing that there are no nodeless ($n = 0$) solutions for both solitons and black holes. In other words, these solutions must at least have one node ($n > 0$). This fact will be demonstrated numerically later in section 3.5.

We shall start by considering the NAP field equation (3.24) at a turning point r_0 where

$\omega'(r_0) = 0$. Then, at $r = r_0$ we have

$$r_0^2 R\omega'' = \left(\omega^2 - 1\right)\omega + (1+\omega)\,\mu^2 r_0^2. \tag{3.35}$$

Near the origin $r = 0$, the leading order of the gauge field is -1 and from the boundary condition (3.26), we find, for $r \ll 1$

$$\omega' \sim 2\omega_2 r. \tag{3.36}$$

Therefore the sign of ω' near $r = 0$ depends on the sign of ω_2.

Suppose that $\omega_2 < 0$, therefore $\omega < -1$ near the origin. This means ω must have a minimum at some value of the radius since $\omega \to -1$ as $r \to \infty$ (3.31). We thus define r_0 as the location of the minimum and $\omega(r_0) \equiv \omega_0 < -1$. Since ω has minimum at $r = r_0$ hence $\omega''(r_0) > 0$, then (3.35) implies that (at $r = r_0$)

$$\omega_0\left(\omega_0^2 - 1\right) + \mu^2 r_0^2\,(1+\omega_0) > 0. \tag{3.37}$$

Both terms in the above condition are negative when $\omega_0 < -1$. Hence we have a contradiction with our assumption and so ω_2 must be positive. Therefore, we must have $\omega' > 0$ near the origin. So ω must have maximum at some radius r_0 where $\omega(r_0) \equiv \omega_0 > -1$. This time (3.35) implies (at $r = r_0$)

$$\omega_0\left(\omega_0^2 - 1\right) + \mu^2 r_0^2\,(1+\omega_0) < 0. \tag{3.38}$$

Now consider the situation where ω_0 lies in the interval $-1 < \omega_0 < 0$. In this case, both term on the LHS of the above equation are positive. So we must have $\omega_0 > 0$. This means, the maximum value of the gauge field is positive. Hence to satisfy the boundary conditions near the origin (3.26) and infinity (3.31), ω must have at least two nodes. Additionally, regular solutions of ENAP-AdS must be such that ω has an even number of nodes.

At the black hole horizon $r = r_h$, the NAP equation (3.24) can be written as

$$\omega_h' = \frac{\omega_h\left(\omega_h^2 - 1\right) + \mu^2 r_h^2\left(1 + \omega_h\right)}{r_h^2 R_h'}. \tag{3.39}$$

We begin by assuming that $\omega_h < -1$, therefore (3.39) tells us that $\omega_h' < 0$ since $R_h' > 0$. According to this, ω must have a minimum at some point $r = r_0$ where $\omega(r_0) \equiv \omega_0 < -1$ and $\omega'' > 0$. However, equation (3.35) is not satisfied if $\omega_0 < -1$ and $\omega''(r_0) > 0$. Therefore ω_0 must be larger than -1. In this case, we can deduce that $\omega_h' > 0$ from (3.39). So the gauge field must have a maximum at some $r = r_0$, where (3.35) once again implies

$$\omega_0\left(\omega_0^2 - 1\right) + \mu^2 r_0^2\left(1 + \omega_0\right) < 0, \tag{3.40}$$

with $\omega(r_0) \equiv \omega_0 > -1$ the maximum value of the gauge field. Now if ω_0 lies in the interval $-1 < \omega_0 < 0$, this condition does not hold since both terms in (3.40) are positive. Therefore it must be the case that $\omega_0 > 0$. Thus for the black hole case, as for the solitons, the maximum value ω_0 is positive. This means, for $-1 < \omega_h < 0$, the gauge function ω must have at least two nodes to satisfy the boundary condition at infinity (3.31). Further more when $\omega_h > 0$, the gauge field must have at least one node, so that $\omega \to -1$ as $r \to \infty$.

Hence in this subsection, we have shown that all the static solitons and black holes of ENAP-AdS must have at least one node. Similar behaviour is observed in the ENAP-flat model as well for both regular and black hole solutions [79]. This should not be a surprise since, the proof in this section does not rely on the asymptotic structure of the spacetime. So this proof is also valid for the solutions in ENAP-flat theory.

§3.5 Numerical solutions

In this section, numerical regular and black hole solutions are discussed. We consider static, spherically symmetric solutions of the ENAP equations both in asymptotically flat and AdS spacetimes. These solutions are constructed by a numerical shooting scheme

(see Appendix A). Firstly, we state the numerical method used in this problem. As a preliminary setup for our numerical codes, we re-construct the soliton and black hole solutions of the ENAP-flat equations discovered by Greene et.al., [79]. After that, we provide new numerical regular and black hole solutions of the ENAP-AdS system.

3.5.1 Numerical methods

To construct regular solutions of the ENAP-AdS equations (3.22−3.24), we use a one parameter shooting method. The boundary conditions at the origin $r = 0$ (3.26) are defined as follows

$$\begin{aligned} m(r) &= \frac{2b^2}{e^2}r^3 + \frac{1}{5e^2}\left[-8b^3 + 3\mu^2 b^2 + \frac{8\Lambda b^2}{3}\right] r^5 + O(r^6), \\ \delta(r) &= -\frac{4b^2}{e^2}r^2 - \frac{4}{5e^2}\left[2\Lambda b^2 + \mu^2 b^2 - 3b^3 + \frac{8b^4}{e^2}\right] r^4 + O(r^5), \\ \omega(r) &= -1 + br^2 + \frac{1}{10e^2}\left[2e^2\Lambda b + e^2\mu^2 b - 3e^2 b^2 + 8b^3\right] r^4 + O(r^5), \end{aligned} \tag{3.41}$$

where $b \equiv \omega_2$. In this case, the free parameter in the numerical integration is b. Note that, we cannot start our integration from the origin $r = 0$, because the field equations become singular at this point. Therefore we use these equations as initial conditions, integrating outward from (near) the origin, $r = 10^{-3}$, to infinity. We set the gauge coupling constant $e = 1$. With fixed μ and Λ, we scan for a possible value of b that allows us to satisfy the boundary conditions at infinity (3.31) or (3.34) if $\Lambda = 0$. When $\Lambda = 0$, our numerical method should yield the solutions of the ENAP-flat theory [79]. We then use these solutions as starting points and slowly turn on the value of the cosmological constant Λ.

A similar shooting procedure can be used to obtain numerical black hole solutions of ENAP-flat/AdS. We cannot numerically integrate the field equations (3.22−3.24) from the horizon because of singularities in the equations. Thus, we start our numerical integration from near the horizon, $(r - r_h) = 10^{-13}$, using the field expansions (3.29) as initial data.

The initial value of Proca field i.e., $\omega(r_h)$, will now become our shooting parameter. We follow [24] by setting the horizon radius, $r_h = 1$. We can obtain black hole solutions of ENAP-flat by setting $\Lambda = 0$ in the field equations (3.22−3.24) and the expansion (3.29). Then, we integrate the field equations in the same manner. It should be remarked that the starting point of integration for solitons and black holes i.e., 10^{-3} and 10^{-13} respectively, were chosen such that they were the smallest values that we could find a converge solution.

As will be seen later, both soliton and black hole solutions are classified by the node number. The node number is the number of zeros of the function $\omega(r)$ and will be denoted as n. For instance, $n = 2$ black hole solutions refers to the black hole solution for which $\omega(r)$ has two zeroes. Here we shall consider only the two possible lowest node solutions. As shown in subsection 3.4.2, there are no odd-node soliton solutions in both asymptotically flat and AdS, due to the boundary conditions at the origin (3.26) and infinity (3.31, 3.34). In contrast, for the black hole case, there is no restriction on the possible number of nodes of the solutions, except that $n > 0$ as proven in subsection 3.4.3.

3.5.2 Asymptotically flat solutions

As a good consistency check, in this subsection we reproduce the solutions of ENAP equations in asymptotically flat spacetime [79]. In the limit where $\Lambda \to 0$, our system becomes ENAP-flat theory. It can be seen later in this subsection that our results are in good agreement with the results in [79]. We plot $1 + \omega$ in our figures, so that we can clearly see in the plots that the asymptotic value of the NAP field as $r \to \infty$ is -1.

Fig 3.1 shows examples of regular solutions of the ENAP theory for which ω has two zeros. There are two classes of solutions called the $n = 2$ and quasi$-n = 1$ branches. More precisely, the quasi$-n = 1$ solutions are solutions that resemble the node=1 regular solutions of Bartnik and McKinnon [7] as $\mu \to 0$, while the $n = 2$ solutions tend to the node=2 BM solution as $\mu \to 0$. Fig 3.1(a) displays the $n = 2$ solutions. These solutions can be found in the interval $0.5790 < b < 0.6441$, and have masses in the interval

$0.9755 < M < 0.9949$. The quasi$-n = 1$ solutions are shown in Fig 3.1(b). These solutions are described by $0.4580 < b < 0.5800$ and have $0.8780 < M < 0.9950$. We note that at each value of μ, there are two solutions where ω has n nodes, for fixed n. These give two branches of solutions as μ varies.

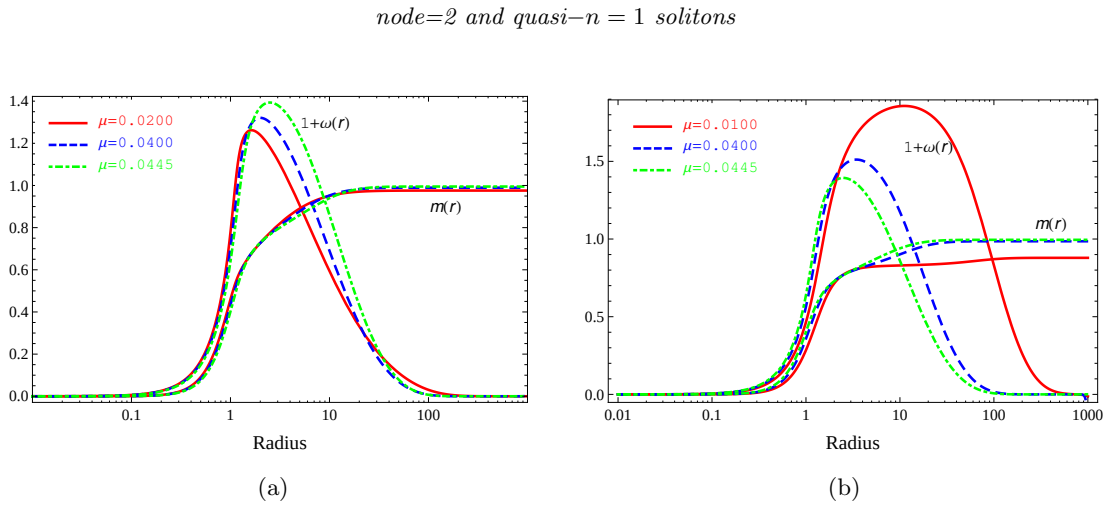

Figure 3.1: Regular solutions of ENAP theory in asymptotically flat spacetime with varying boson mass μ. (a) node=2 solutions (b) quasi$-n = 1$ solutions. The gauge connection $1 + \omega(r)$ and total mass function $m(r)$ are plotted as functions of the radius r.

Black hole solutions are illustrated in Fig 3.2. As in the soliton case, at each value of μ, there are two solutions where ω has n nodes, for fixed n. These give two branches of solutions as μ varies. The $n = 2$ solutions are shown in Fig 3.2(a). The shooting parameter varies in the interval $-0.5020 < \omega(r_h) < -0.3450$ and the total masses are given by $0.9935 < M < 1.0052$. Fig 3.2(b) displays the quasi$-n = 1$ black hole solutions. These solutions can be found in the intervals $-0.6320 < \omega(r_h) < -0.5035$, $0.9420 < M < 1.0052$. In addition, $n = 1$ and quasi$-n = 0$ black hole solutions are displayed in Fig 3.2(c) and 3.2(d), respectively. Fig 3.2(c) shows $n = 1$ solutions described by $0.6300 < \omega(r_h) < 0.8480$, with masses $0.9370 < M < 1.0053$. The quasi$-n = 0$ solutions plotted in Fig 3.2(d) are given by $0.8520 < \omega(r_h) < 1.0000$ and have masses in the interval $0.5070 < M < 1.0051$.

node=2, quasi$-n=1$, node=1 and quasi$-n=0$ black holes

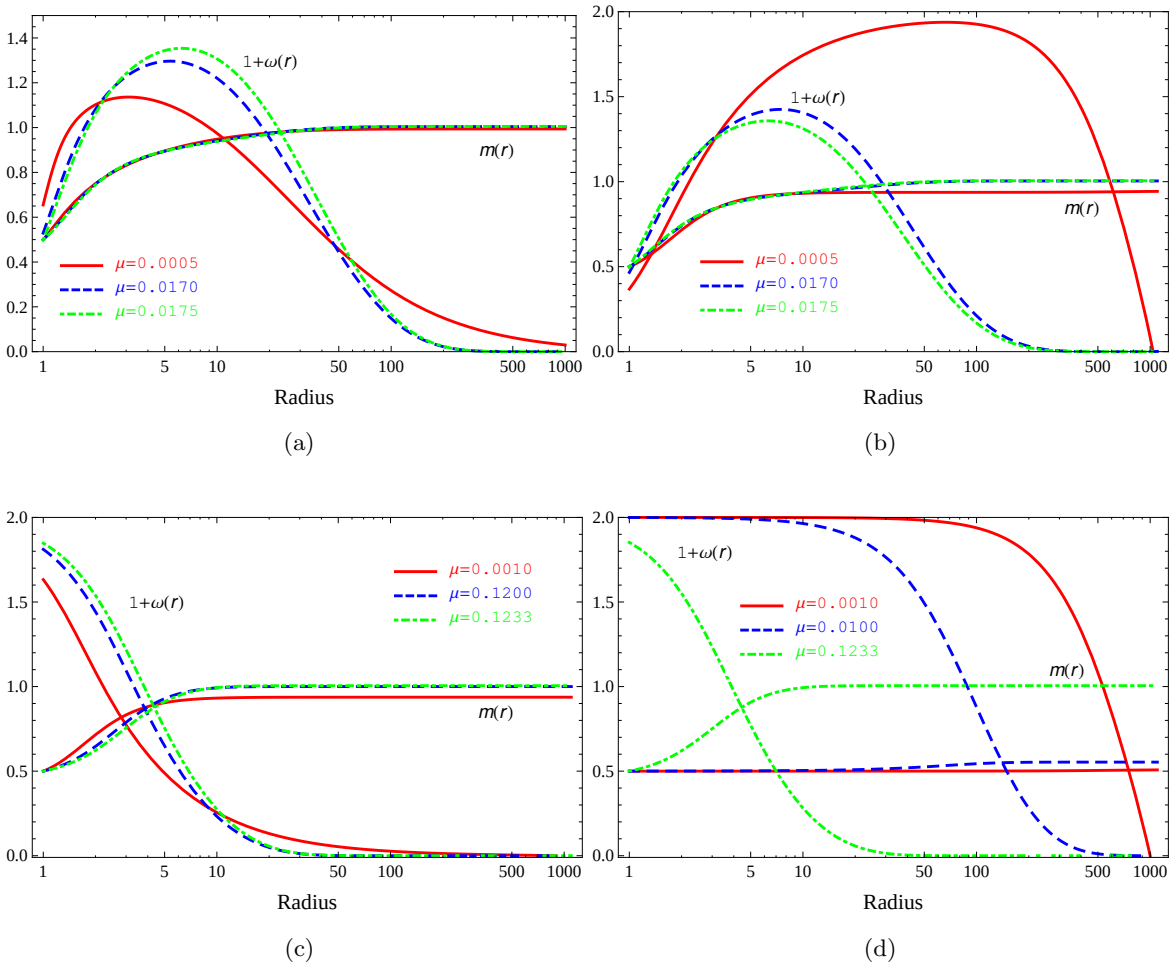

Figure 3.2: Black hole solutions of ENAP theory in asymptotically flat spacetime with varying boson mass μ. (a) node=2 solutions, (b) quasi$-n=1$ solutions, (c) node=1 solutions, (d) quasi$-n=0$ solutions. We set $r_h=1$ in these plots.

An important characteristic of the quasi-solutions is that when $\mu \to 0$, the maximum value of the NAP field increases. Moreover as μ decreases, the outermost node of ω moves further away to infinity. Note that, for each branch of solutions, there is a maximum value of μ for which we find non-trivial solutions. At the maximum value of the Proca mass, given by $\mu_{max}=0.04454$ for $n=2$ and quasi$-n=1$ regular solutions, $\mu_{max}=0.0175$ for $n=2$ and quasi$-n=1$ black hole solutions and $\mu_{max}=0.1233$ for $n=1$ and quasi$-n=0$

black hole solutions, the ordinary branch and quasi branch bifurcate from each other.

More importantly, the black hole solutions are indistinguishable from a Schwarzschild black hole when observed at infinity. This is because the NAP field is in a vacuum near infinity. Therefore, the black hole solutions in the ENAP theory violate the generalized no-hair conjecture as stated in section 2.3. Greene et.al., expected that these solitons and black holes are unstable [79], however no detailed analysis on the stability has been performed so far. We will come back to this point later in section 3.7. In the following subsections, we present new regular and black hole solutions of the ENAP equations in asymptotically AdS spacetime.

3.5.3 Regular solutions

The asymptotic behaviour of the ENAP-AdS equations is different from that of the EYM-AdS equations as $r \to \infty$. The leading behaviour of the gauge connection near infinity is $\omega = -1$. Unlike the EYM-AdS system, ENAP-AdS possesses no odd-node regular solutions due to these boundary conditions (see subsection 3.4.3). Another remarkable difference from the EYM theory is that there exist two branches of soliton solutions: ordinary even-node solutions and quasi-solutions which will now be discussed case by case.

We consider the first branch of solutions, $n = 2$ regular solutions. Fig 3.3 shows $n = 2$ nontrivial solutions of the ENAP equations in AdS spacetime with fixed vector boson mass and cosmological constant. These plots illustrate the values of $1 + \omega(r)$, $m(r)$ and $\delta(r)$ at given radius r. The shooting parameters associated to these solutions are given by $b = 0.6416$ and $b = 0.6048$ in Fig 3.3(a) and Fig 3.3(b), respectively. Fig 3.3(a) displays an $n = 2$ solution with $\mu = 0.02$ and $\Lambda = -0.001$. The total mass M and δ_∞ (the value of δ as $r \to \infty$) are $0.9777, -3.6825$ respectively. Fig 3.3(b) shows an $n = 2$ solution for which μ and Λ are fixed to be $0.035, -0.003$ respectively. The total mass M and δ_∞ are $0.9923, -3.1797$ in this case. Note that, in these plots δ is zero at $r = 0$ and the boundary

node=2 solitons for fixed $\mu = 0.02, \Lambda = -0.001$ *(left panel) and* $\mu = 0.035, \Lambda = -0.003$ *(right panel)*

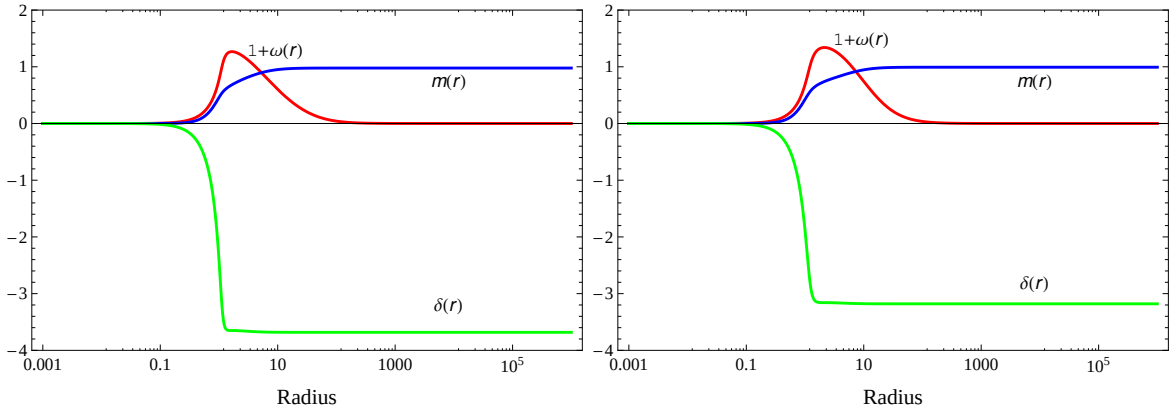

Figure 3.3: Two node regular solutions of ENAP theory in AdS spacetime for fixed vector field mass and cosmological constant. (a) $n = 2$ regular solution, $\mu = 0.02$ and $\Lambda = -0.001$. (b) $n = 2$ regular solution, $\mu = 0.035$ and $\Lambda = -0.003$. The gauge connection $1 + \omega(r)$, total mass function $m(r)$ and metric function $\delta(r)$ are plotted as functions of the radius r.

condition at infinity on δ (namely $\delta \to 0$) is not satisfied. Thus we need to add a constant to δ so that $\delta \to 0$ as $r \to \infty$. As discussed in subsection 3.4.2, we can do this since the ENAP-AdS equations depend only on δ' and not on δ.

Examples of two-node regular solutions for fixed vector field mass and varying cosmological constant (and vice versa) are presented in Fig 3.4. We suppress $\delta(r)$ since it is not relevant to our discussion. The shooting parameter lies in the interval $0.6000 < b < 0.6500$. Fig 3.4(a) shows non-trivial solutions when μ is fixed. Increasing $|\Lambda|$ corresponds to increasing the maximum value of ω. Also, with increasing $|\Lambda|$ the peak of ω slightly moves to the right (greater radius). The total mass M and δ_∞ vary in the range $0.9760 < M < 0.9940, -3.7100 < \delta_\infty < -3.1700$. The $n = 2$ solution for fixed Λ is shown in Fig 3.4(b). It shares the same trend as the previous case. An increasing maximum value of ω is caused by the growth of μ. Its peak also slightly shifts to the right. The total mass M and δ_∞ vary in the range $0.9770 < M < 0.9930, -3.6800 < \delta_\infty < -3.1900$. We remark that varying Λ and μ does not affect much the mass function $m(r)$ and $\omega(r)$ only changes slightly.

node=2 solitons for fixed $\mu = 0.02$ *(left panel) and* $\Lambda = -0.001$ *(right panel)*

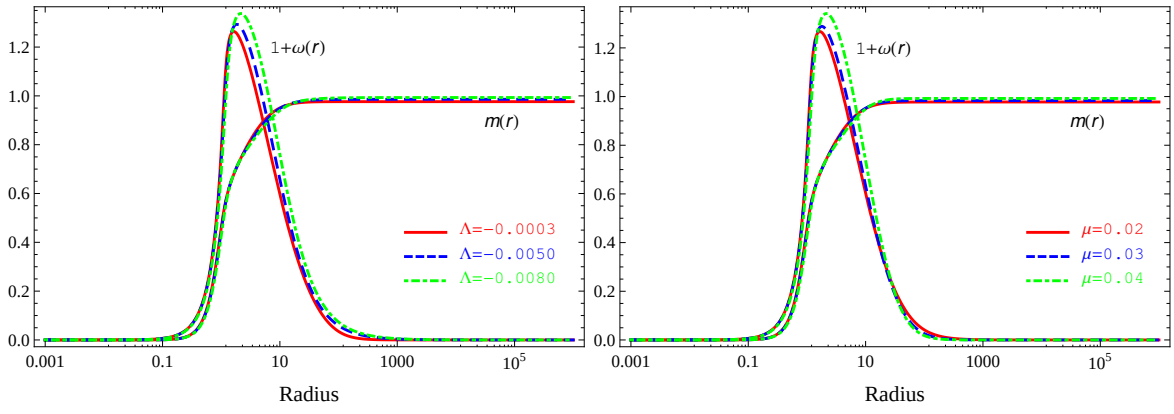

Figure 3.4: Two node regular solutions of ENAP theory in AdS spacetime. (a) $n = 2$ regular solution, $\mu = 0.02$ and $\Lambda = -0.008, -0.005, -0.0003$. (b) $n = 2$ regular solutions, $\Lambda = -0.001$ and $\mu = 0.04,\ 0.03,\ 0.02$.

quasi$-n = 1$ *solitons for fixed* $\mu = 0.02$ *(left panel) and* $\Lambda = -0.0005$ *(right panel)*

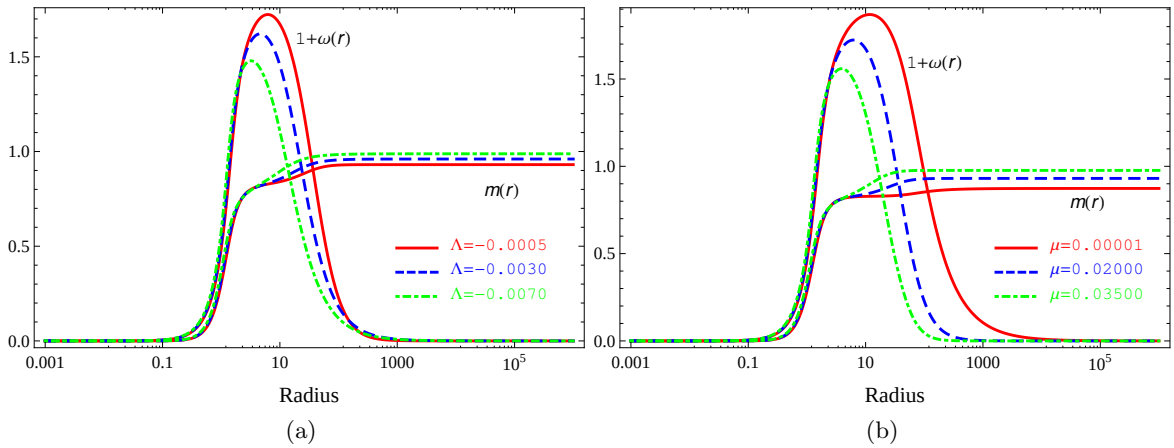

Figure 3.5: Quasi$-n = 1$ regular solutions of the ENAP theory in AdS spacetime. (a) $\mu = 0.02$, $\Lambda = -0.007, -0.003, -0.0005$, (b) $\Lambda = -0.0005$, $\mu = 0.035,\ 0.020,\ 0.00001$.

We now discuss another branch of solutions, called quasi-solutions. These solutions, even though they have the same value of μ and Λ as one even-node class, can be numerically found in a different interval of the shooting parameter b. For ENAP in asymptotically

Minkowski space [79], the quasi-branch is a class of solutions that behave in the same way as odd-node solutions of [7] when $\mu \to 0$. With $\omega(0) = -1$, the asymptotic value of odd-node BM solutions as $r \to \infty$ is $+1$, which is not allowed by the boundary condition in the ENAP system (3.31). Hence another node in ω will occur in order to match up with the boundary condition as $r \to \infty$ namely, $\omega \to -1$. Therefore, it is not obvious how to define the quasi-solutions of the ENAP equations in asymptotically AdS spacetime. The difficulty comes from the two parameters μ and Λ in the theory. We could expect that our quasi-solutions should behave in the same manner as the quasi-solutions defined in [79] (second node located at a large distance from the origin). However this turns out not to be the case. As will be seen below, our quasi-solutions behave more like the quasi-solutions of EYMH equations in AdS spacetime [183]. For this reason, in our case, the quasi-solutions are defined to be the solutions that resemble the EYMH-AdS quasi-solutions [183].

Fig 3.5 shows the quasi$-n = 1$ solutions with fixed μ and Λ. These plots show the character of this branch of solutions. The turning points of ω increase as a result of decreasing $|\Lambda|$ and μ. In Fig 3.5(a), we plot the quasi$-n = 1$ solutions for fixed $\mu = 0.02$ and varying cosmological constant. The shooting parameters vary as $0.4760 < b < 0.5500$. The total mass and δ_∞ are in the intervals $0.9300 < M < 0.9885, -2.6140 < \delta_\infty < -2.1920$, respectively. Fig 3.5(b), the quasi$-n = 1$ solutions are plotted for $\Lambda = -0.0005$ and varying vector field mass μ. The solutions are found in the intervals $0.4568 < b < 0.5180$ with $0.8730 < M < 0.9770$ and $-2.4506 < \delta_\infty < -2.0100$. Increasing μ in Fig 3.5(b) leads to the decreasing of the radius at which the gauge connection $1 + \omega(r)$ reaches zero. This character is also shared by the quasi-solutions of Greene et.al., [79]. When compared with the $n = 2$ solutions shown in Fig 3.4, the quasi solutions vary more significantly with varying cosmological constant Λ and Proca mass μ.

We now compare the $n = 2$ and quasi$-n = 1$ solutions in more detail (see Fig 3.6). In Fig 3.6(a), the total mass M and δ_∞ are 0.9817 and -3.5784 (for $n = 2$), 0.9603 and -2.3168 (for quasi$-n = 1$). Fig 3.6(b), the total mass M and δ_∞ are 0.9879 and -3.3729

Fixed $\Lambda = -0.003$, $\mu = 0.02$ *(left panel) and* $\mu = 0.03$ *(right panel)*

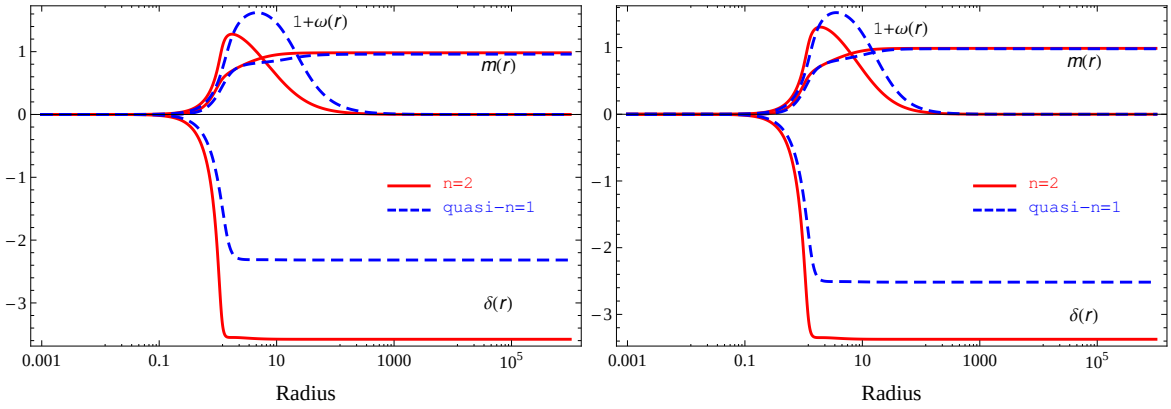

(a) (b)

Fixed $\Lambda = -0.001$, $\mu_{max} = 0.0420$

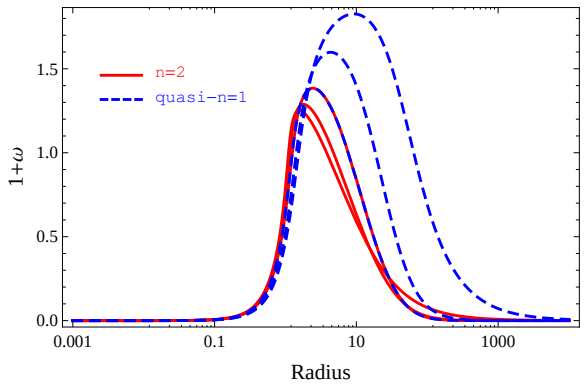

(c)

Figure 3.6: Comparison of the $n = 2$ branch and quasi$-n = 1$ branches of regular solutions with fixed μ and Λ, (a) $\mu = 0.02$, $\Lambda = -0.003$, (b) $\mu = 0.03$, $\Lambda = -0.003$, (c) $n = 2$ and quasi$-n = 1$ solutions bifurcate at $\mu_{max} = 0.0420$ for fixed $\Lambda = -0.001$, the other curves represent $n = 2$ and quasi$-n = 1$ solutions with fixed $\mu = 0.030$ and $\mu = 0.00005$.

(for $n = 2$), 0.9820 and -2.5166 (for quasi$-n = 1$). The difference between these two branches has become less significant as the vector field mass increases. This trend is expected to continue as μ increases. In general, a quasi$-n = 1$ solution has lower mass M than the corresponding $n = 2$ solution. The shape of $1 + \omega$ is also different, the peak width of an $n = 2$ solution is smaller than for an quasi$-n = 1$ solution. In addition, in Fig 3.6(c) we find that for fixed $\Lambda = -0.001$, the maximum value of Proca mass for which non-trivial solutions exist is $\mu_{max} = 0.0420$. We note that this value of μ_{max} is less than the value when $\Lambda = 0$ (see Fig 3.1). We anticipate that μ_{max} decreases as $|\Lambda|$ increases, leading to a maximum $|\Lambda|$ for which solutions exist. In general for fixed Λ, as $\mu \to \mu_{max}$, the second node of both the $n = 2$ and quasi$-n = 1$ solutions moves closer to the origin. Moreover, the peak of the gauge field increases in the case of $n = 2$ and decreases for quasi$-n = 1$ as μ increases. When $\mu = \mu_{max}$, the two branches of solutions merge into each other as illustrated in Fig 3.6(c).

In general, the space of soliton solutions of ENAP-AdS theory (both ordinary and quasi solutions) is discrete rather than continuous. This can be seen from the fact that all the solitons given in this subsection are found at two particular values of the shooting parameter b when Λ and μ are fixed. This happens because the leading order behaviour of the gauge field ω at infinity is fixed to be -1 (3.31) rather than being arbitrary as in the EYM-AdS sector [197]. The solutions of ENAP-flat theory [79] discussed in subsection 3.5.2 also share this property.

Another general property that we can observe from our new ENAP-AdS solutions is that for fixed μ, there exists a maximum value of $|\Lambda|$ for which solutions have been found. There also exists a maximum value of μ for fixed $|\Lambda|$ for which we find solutions as in [183]. At the maximum value of the vector boson mass, the two branches of solutions (ordinary and quasi) merge into the same solution. This behaviour could be easily seen by plotting the domain of existence in the μ and Λ space. However, since the solution space of ENAP-AdS system is discrete, therefore finding regular and black hole solutions is a not

straightforward task. This makes plotting the $\mu - \Lambda$ phase space in our case impractical.

We also consider the local energy density, defined as the time-time component of the stress energy momentum tensor (3.5), given by

$$T_{00} = \frac{Re^{2\delta}}{e^2 r^2}\left[\frac{\left(\omega^2-1\right)^2}{r^2} + 2R\omega'^2 + 2\mu^2\left(1+\omega\right)^2\right]. \tag{3.42}$$

We have included the gauge coupling constant e for the sake of completeness. Equation (3.42) is plotted in Fig 3.7 for fixed Proca mass μ and cosmological constant Λ for an $n = 2$ Fig 3.7(a) and a quasi$-n = 1$ solution Fig 3.7(b). These plots show that these solutions have a compact, high density region. They have a large energy density close to the origin. However in the outer region, the energy density decreases very quickly. Furthermore the energy density at the core of the $n = 2$ regular solution is much higher and its decay rate is faster compared with the corresponding quasi$-n = 1$ solution. Therefore the $n = 2$ horizonless solution represents a compact object that is denser and more compact than the quasi$-n = 1$ solution.

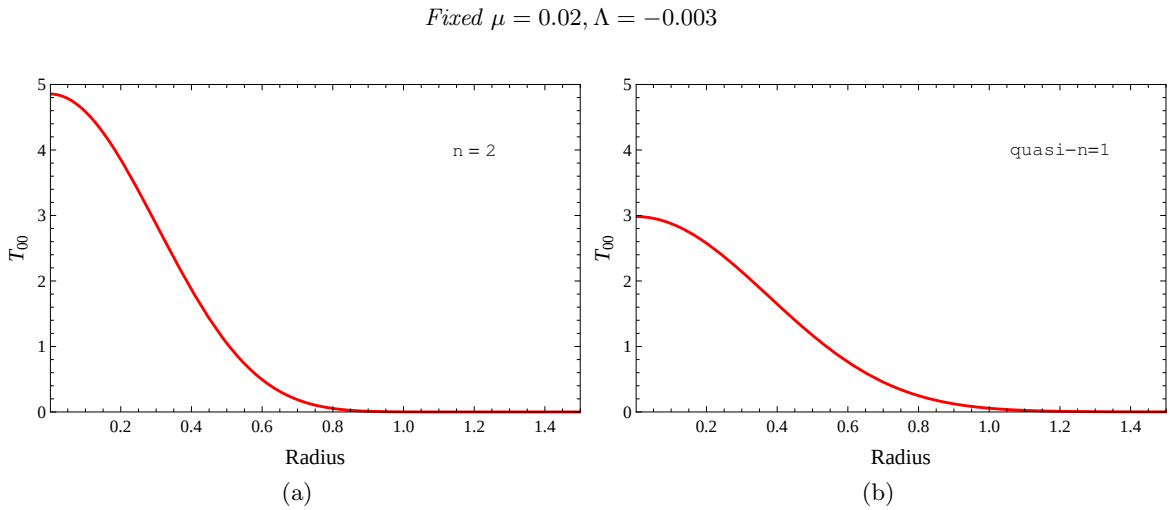

Figure 3.7: Energy density of two regular solutions (a) $n = 2$ (b) quasi$-n = 1$.

3.5.4 Black hole solutions

Similarly to the soliton case just discussed, numerical black hole solutions are found with two branches of solution i.e., ordinary and quasi branches. However the initial conditions (3.27, 3.29) in this case are different from the solitons. As a consequence, now there can be both odd and even numbers of nodes of $\omega(r)$.

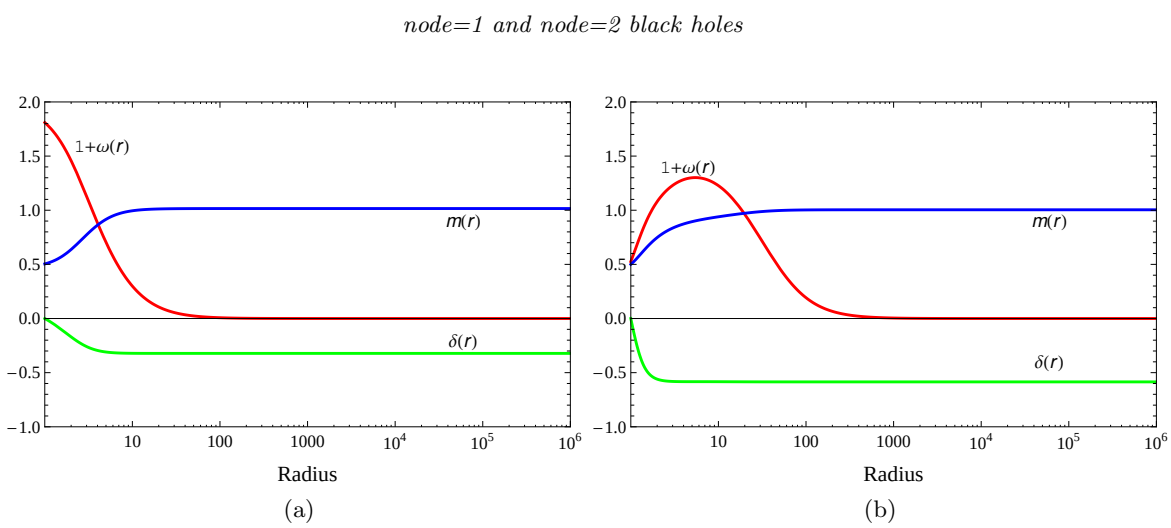

Figure 3.8: Two examples of black hole solutions of ENAP theory in AdS spacetime for fixed vector field mass and cosmological constant. (a) $n = 1$ black hole solution with $\mu = 0.1$ and $\Lambda = -0.025$. (b) $n = 2$ black hole solution with $\mu = 0.014$ and $\Lambda = -0.0005$.

In Fig 3.8, example $n = 1$ and $n = 2$ non-trivial black hole solutions are shown. As in the previous case, these solutions are given in term of the gauge connection $1 + \omega(r)$, mass function $m(r)$ and metric function $\delta(r)$. For the $n = 1$ example, the shooting parameter $\omega(r_h)$, total mass M and δ_∞ are given by $0.8097, 1.0155$ and -0.3220, respectively. For the $n = 2$ example, the shooting parameter $\omega(r_h)$, total mass M and δ_∞ are given by $-0.4741, 1.0041$ and -0.5852.

In addition, black hole solutions are plotted in Fig 3.9 for $n = 1, 2$ branch solutions with fixed values of the vector field mass and cosmological constant. We fix μ and then vary Λ in Fig 3.9(a)$-$3.9(b). The shooting parameters $\omega(r_h)$ are adjusted within the intervals

$0.6430 < \omega(r_h) < 0.7500$ and $-0.4740 < \omega(r_h) < -0.4075$ for $n = 1$ and $n = 2$ solutions respectively. The solutions are described by $0.9415 < M < 1.0335, -0.5380 < \delta_\infty < -0.3365$ $(n = 1)$ and $0.9995 < M < 1.0050, -0.5920 < \delta_\infty < -0.5830$ $(n = 2)$. In Fig 3.9(c)−3.9(d) $n = 1$ and $n = 2$ solutions are shown with fixed Λ and varying μ. These solutions are given by $0.6395 < \omega(r_h) < 0.7610,\ 0.9480 < M < 0.9925, -0.5220 < \delta_\infty < -0.4120$ $(n = 1)$ and $-0.4600 < \omega(r_h) < -0.3740,\ 0.9960 < M < 1.0035, -0.5915 < \delta_\infty < -0.5870$ $(n = 2)$. The plots in Fig 3.9(c)−3.9(d) have a common behaviour. That is, as the vector field mass increases, the radius where $1 + \omega$ vanishes becomes smaller. Additionally, as μ and Λ vary, the mass function $m(r)$ varies more in the $n = 1$ case than $n = 2$.

As happened for the regular solutions, there is another class of black hole solutions, namely quasi-solutions. In Fig 3.10, we show some plots of the quasi-solution branches with fixed values of the gauge boson mass and cosmological constant. Fig 3.10(a)−3.10(b) show quasi$-n = 0$ and quasi$-n = 1$ black hole solutions. The shooting parameter is given by $0.8870 < \omega(r_h) < 0.9885$ (quasi$-n = 0$) and $-0.6000 < \omega(r_h) < -0.5360$ (quasi$-n = 1$). The solutions are described by $0.7470 < M < 1.030,\ -0.0210 < \delta_\infty < -0.1680$ and $0.9880 < M < 1.0030,\ -0.6200 < \delta_\infty < -0.5400$ for quasi$-n = 0$ and quasi$-n = 1$ solutions respectively. In Fig 3.10(c)−3.10(d), these solutions are found in the intervals $0.9180 < \omega(r_h) < 0.9935$ and $-0.6200 < \omega(r_h) < -0.5400$ for quasi$-n = 0$ and quasi$-n = 1$ solutions respectively. The total mass M and δ_∞ vary over $0.7020 < M < 0.9770, -0.0130 < \delta_\infty < -0.1400$ (quasi$-n = 0$) and $0.9740 < M < 1.0030, -0.5530 < \delta_\infty < -0.5730$ (quasi$-n = 1$). In the quasi-branches of black hole solutions, when μ or $|\Lambda|$ decrease the maximum value of the Proca field, ω, increases. Moreover, the solutions in Fig 3.10(c)−3.10(d) behave in the same manner as those solutions in Fig 3.5(b). That is, increasing μ leads to the decreasing of the radius at which the gauge connection $1 + \omega(r)$ reduces to its vacuum value. These quasi-solutions follow the same trends as those of the EYMH-AdS theory [183]. That is, the outermost node of our quasi-solutions does not

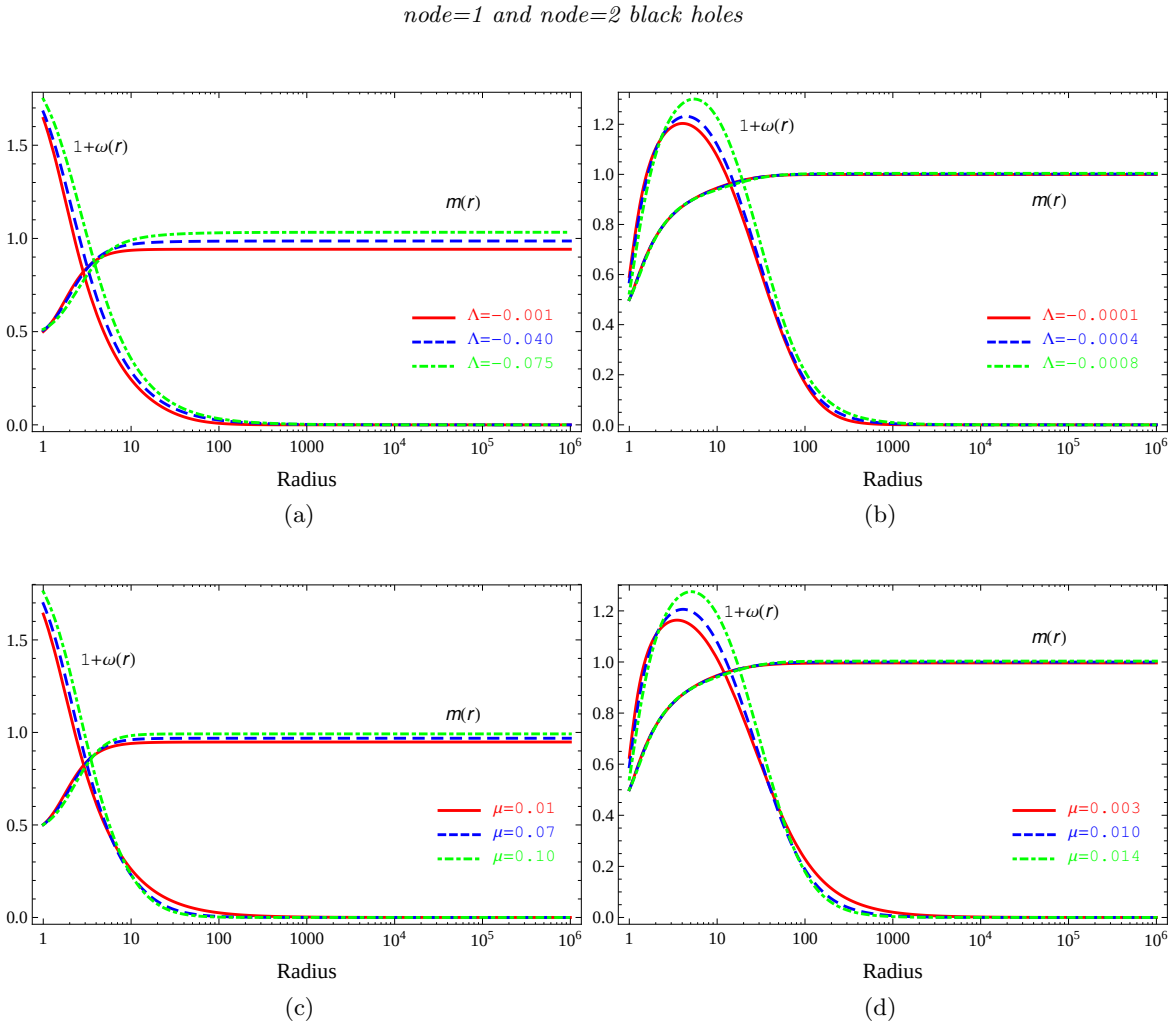

Figure 3.9: $n = 1$ and $n = 2$ black hole solutions of ENAP theory in AdS spacetime. (a) $n = 1$ solutions with fixed $\mu = 0.03$, $\Lambda = -0.075, -0.04, -0.001$, (b) $n = 2$ solutions with fixed $\mu = 0.012$, $\Lambda = -0.0008, -0.0004, -0.0001$, (c) $n = 1$ solutions with fixed $\Lambda = -0.01$, $\mu = 0.1,\ 0.07,\ 0.01$ (d) $n = 2$ solutions with fixed $\Lambda = -0.0004$, $\mu = 0.014,\ 0.01,\ 0.003$.

move to a much larger radius as $\mu \to 0$.

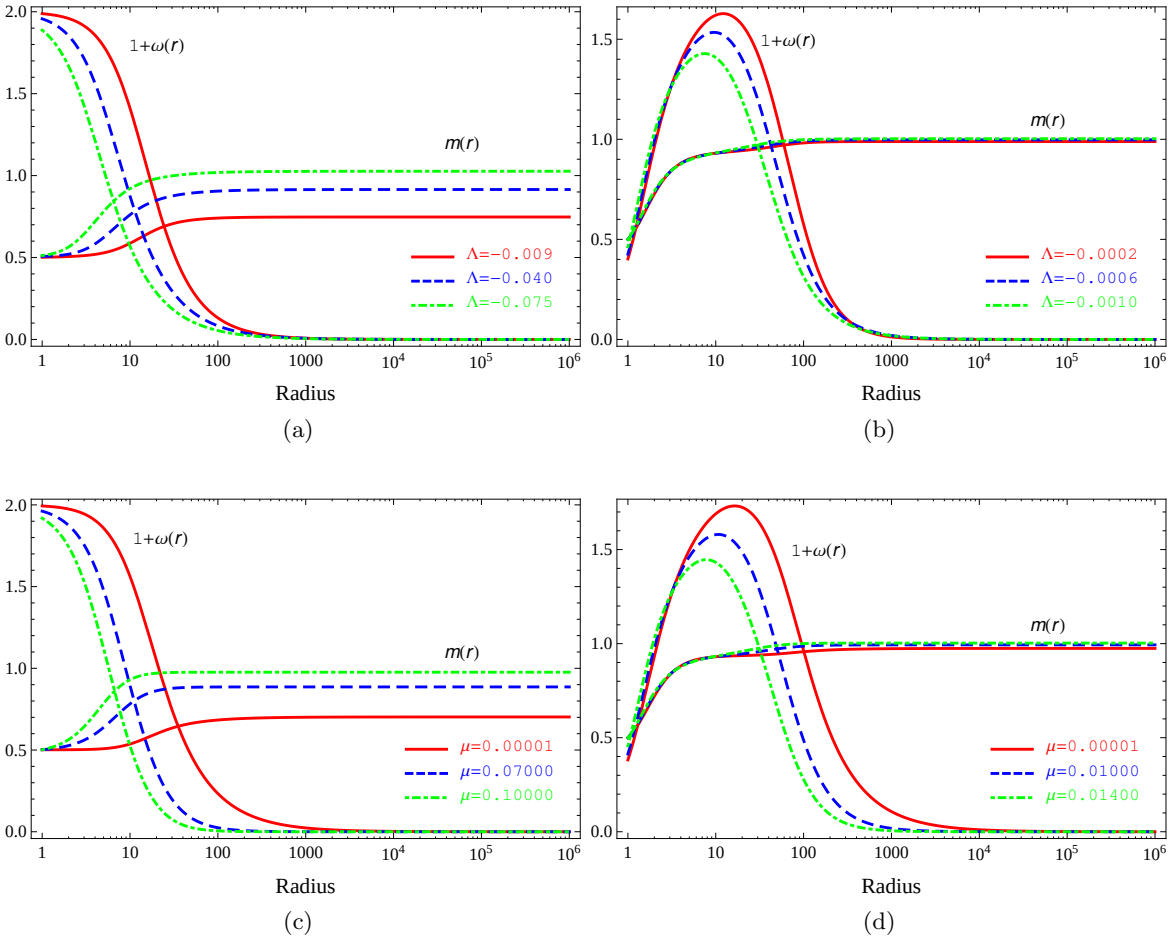

Figure 3.10: Quasi$-n=0$ and quasi$-n=1$ black hole solutions of ENAP theory in AdS spacetime. (a) quasi$-n=0$ solutions with fixed $\mu=0.03,\ \Lambda=-0.075,-0.04,-0.009$, (b) quasi$-n=1$ solutions with fixed $\mu=0.01,\ \Lambda=-0.001,-0.0006,-0.0002$, (c) quasi$-n=0$ solutions with fixed $\Lambda=-0.01,\ \mu=0.1,\ 0.07,\ 0.00001$, (d) quasi$-n=1$ solutions with fixed $\Lambda=-0.0004,\ \mu=0.014,\ 0.01,\ 0.00001$.

A comparison between two $n=1$ and $n=2$ solutions and their corresponding quasi-solutions is illustrated in Fig 3.11. In Fig 3.11(a), the total mass M and δ_∞ are 1.0037 and -0.3614 (for $n=1$), 1.0033 and -0.1933 (for quasi$-n=0$). In Fig 3.11(b), the total mass and δ_∞ are 1.0041 and -0.5852 (for $n=2$), 1.0040 and -0.5770 (for quasi$-n=1$). Note that the total mass M of the quasi solution is slightly less than that of the ordinary

node solution.

There exists merging behaviour in the black hole case as well as the soliton case. This is demonstrated in Fig 3.11(c) and Fig 3.11(d). For fixed $\Lambda = -0.025$, when $\mu = \mu_{max} = 0.1018$, the $n = 1$ and quasi$-n = 0$ branches black hole solutions bifurcate from each other. In addition, the $n = 2$ and quasi$-n = 1$ branches separate at $\mu = \mu_{max} = 0.01442$ when the cosmological constant is fixed to be -0.0005.

In the same fashion as the regular solutions, the solution space of ENAP-AdS black holes is discrete. This means that the black hole solutions discussed in this subsection are found at discrete values of $\omega(r_h)$. This should not be a surprise since the gauge field ω at infinity is still fixed to be -1. We find that for fixed μ, there exists a certain value of $|\Lambda|$ beyond which black hole solutions cannot be found. This is also true the other way round, there exists a maximum value of μ for fixed Λ for which non-trivial solutions can be found. Also, similarly to the regular solution case, at some certain value of the Proca mass μ, the two categories of solution, i.e., ordinary and quasi node, are merged together. This property can be observed in the ENAP-flat sector as well [79] (see Fig 3.2 and subsequent discussion).

3.5.5 Summary

In this section, we presented new numerical regular and black hole solutions of the ENAP equations in AdS spacetime. Some of the regular and black hole solutions of ENAP-flat theory [79] are also reproduced to test our numerical codes. For asymptotically AdS solutions, both regular and black hole solutions share some significant properties:

- They possess two branches of solutions: ordinary node solution, quasi-node solution.
- Unlike the solution space of EYM with negative cosmological constant [28, 194], for ENAP-AdS the solution space for fixed Λ and μ is found at discrete values of the free parameter b (for regular solutions) and $\omega(r_h)$ (for black hole solutions) rather than

Fixed $\Lambda = -0.02,\ \mu = 0.1$ *(left panel) and* $\Lambda = -0.0005,\ \mu = 0.0140$ *(right panel)*

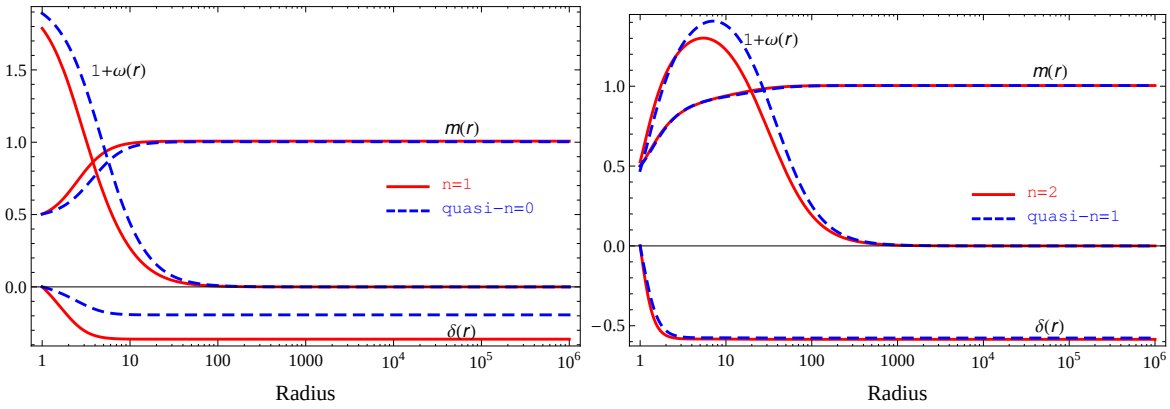

Fixed $\Lambda = -0.025, \mu_{max} = 0.10180$ *(left panel) and* $\Lambda = -0.0005, \mu_{max} = 0.01442$ *(right panel)*

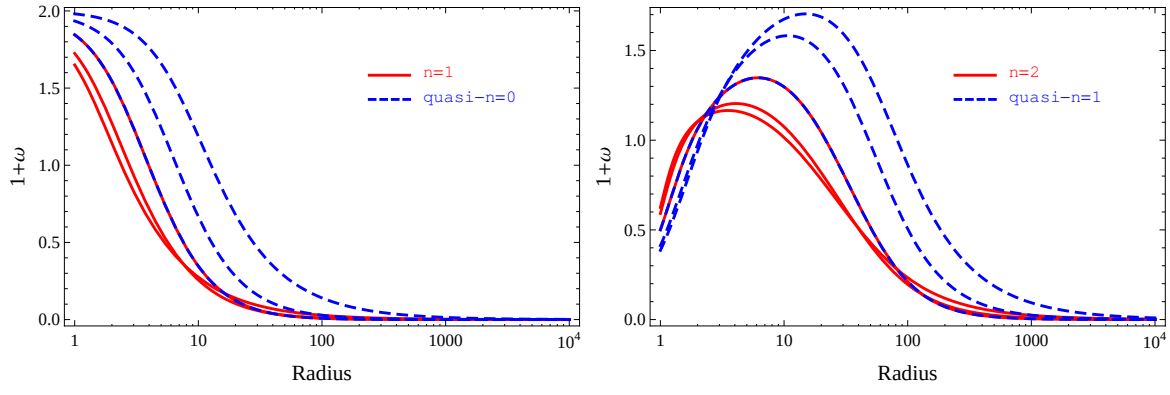

Figure 3.11: Comparison of $n = 1, 2$ branches and quasi$-n = 0, 1$ branches of black hole solutions with fixed μ and Λ, (a) $\mu = 0.1,\ \Lambda = -0.02$, (b) $\mu = 0.014,\ \Lambda = -0.0005$. (c) $n = 1$ and quasi$-n = 0$ solutions bifurcate at $\mu_{max} = 0.10180$ for fixed $\Lambda = -0.025$, the other curves show $n = 1$ and quasi$-n = 0$ black hole solutions with fixed $\mu = 0.075$ and $\mu = 0.00001$. (d) $n = 2$ and quasi$-n = 1$ solutions bifurcate at $\mu_{max} = 0.01442$ for fixed $\Lambda = -0.0005$, the other curves show $n = 2$ and quasi$-n = 1$ black hole solutions with fixed $\mu = 0.009$ and $\mu = 0.00001$.

continuous values. This is because the boundary condition on the gauge function ω as $r \to \infty$ in EYM-AdS is less restrictive than that for ENAP-AdS theory. As a result, our solution spaces for ENAP-AdS are significantly smaller than those of [28, 194] for EYM-AdS.

- For fixed μ, there exists a maximum value of $|\Lambda|$ for which solutions have been found. There also exists a maximum value of μ for fixed $|\Lambda|$ for which we find solutions. In addition at these maximum values of the Proca mass, we observed the bifurcation of ordinary node branches and their corresponding quasi node branches. However these maximum values of μ are smaller for $n = 2/\text{quasi}{-}n = 1$ branches than for $n = 1/\text{quasi}{-}n = 0$ branches in the black hole case. Note that the solutions in ENAP-flat and EYMH-AdS also possess these behaviours [79, 183].

- Ordinary node solutions for both regular and black hole cases do not vary much with changing μ and Λ. However, this is not the case for the quasi-solutions, varying μ significantly affects the gauge connection ω much more than varying Λ.

- One cannot tell the difference between the ENAP-AdS black hole solutions and the Schwarzschild-AdS metric when observed at infinity. For this reason, the generalized no-hair conjecture [25, 52] is violated by the black hole solutions in the ENAP-AdS theory.

We have presented solutions where the number of nodes of $\omega(r)$ is either one or two. We expect that solutions with more nodes could exist, but they will be harder to find numerically. We expect these $n > 2$ solutions to have smaller maximum $|\Lambda|$ and μ.

§3.6 Non-existence of dyonic solutions

In the last section, we considered purely magnetic solutions, since the electric part of the gauge field was set to be zero. Therefore we will now consider the existence of dyons and dyonic black holes in ENAP theory in asymptotically AdS spacetime. A dyon is a

hypothetical particle with both electric and magnetic charges. Dyonic solutions in various theories have been investigated by many authors. The no-go theorem proved by Ershov and Gal'tsov [67, 71] eliminated the possibility of having a non-trivial electric part of the gauge field for static solutions of the $SU(2)$ EYM equations in asymptotically Minkowski space, apart from an embedded Abelian Reissner-Nordström black hole with an electric field. Dyonic solutions of EYM theory in asymptotically de Sitter spacetime are forbidden as well [29]. This is because a non-zero electric component of the gauge field, at the cosmological horizon, creates a divergence in the determinant of the metric tensor. On the other hand, when the cosmological constant is negative, the no-go theorem does not hold anymore, thus allowing the existence of dyonic solutions. For instance, for EYM theory in AdS spacetime with gauge group $SU(2)$, dyonic solutions have been found numerically [28, 29]. Later the existence of dyon and dyonic black hole solutions of EYM-AdS theory was proven analytically [133]. Thus one might expect that the asymptotic structure of AdS space allows the existence of dyonic solutions. However this is not always the case since it was shown that dyon solutions are not allowed in $SU(2)$ EYM with a Higgs doublet and a negative cosmological constant [183]. In addition their asymptotically flat analogues were also proven to possess no dyonic solution [79].

These facts raise the next question: do dyons or dyonic black holes exist in ENAP theory? Greene et.al., [79] only discuss purely magnetic regular and black hole solutions in the ENAP-flat theory. So the existence of dyons and dyonic black holes in this sector is still left open. Therefore the main focus of this section is proving the non-existence of dyons and dyonic black hole solutions of the ENAP equations in asymptotically flat and AdS spacetimes.

3.6.1 Field equations and boundary conditions

To study the existence of dyons in the ENAP-AdS system, it is necessary to derive all the field equations and analyse the behaviour of the field variables in the three asymptotic

regions. We start by introducing the gauge connection with non-zero electric part and set $b = 0$ as before by choice of gauge, giving

$$A = \frac{1}{e}\left\{a\hat{\tau}_r dt + (1+\omega)\left[-\hat{\tau}_\varphi d\theta + \hat{\tau}_\theta \sin\theta \; d\varphi\right]\right\}. \tag{3.43}$$

With this ansatz, the NAP equations (3.6) and Einstein field equations (3.4) are derived to be

$$a'' = -\frac{2a'}{r} + \frac{a'S'}{S} + \frac{2a\omega^2}{r^2 R} + \frac{a\mu^2}{R}, \tag{3.44}$$

$$\omega'' = -\frac{a^2\omega}{R^2S^2} - \frac{\omega'S'}{S} - \frac{\omega'R'}{R} + \frac{\omega\left(\omega^2-1\right)}{r^2R} + \frac{(1+\omega)\,\mu^2}{R}, \tag{3.45}$$

$$m' = \frac{r^2a'^2}{2e^2S^2} + \frac{a^2\omega^2}{Re^2S^2} + \frac{a^2\mu^2r^2}{2Re^2S^2} + \frac{R\omega'^2}{e^2} + \frac{\left(\omega^2-1\right)^2}{2e^2r^2} + \frac{(1+\omega)^2\,\mu^2}{e^2}, \tag{3.46}$$

$$\frac{S'}{S} = \frac{2a^2\omega^2}{re^2R^2S^2} + \frac{ra^2\mu^2}{e^2R^2S^2} + \frac{2\omega'^2}{re^2}. \tag{3.47}$$

The first two equations are obtained from the NAP equations, the t component and θ component respectively. The rest come from the Einstein field equations, (tt) component and (rr) component. In the limit $a = 0$, we recover the previous field equations (3.22–3.24). Moreover equations (3.44–3.47) are in agreement with EYM-AdS system [133] when $\mu = 0$. We then follow the same procedure as in subsection 3.4.2 by analyzing the field variables in three asymptotic regions.

Origin: We assume a regular Taylor series expansion about $r = 0$ as in (3.25) but with an additional field variable

$$\begin{aligned} a(r) &= a_0 + a_1 r + a_2 r^2 + a_3 r^3 + O(r^4), \\ m(r) &= m_0 + m_1 r + m_2 r^2 + m_3 r^3 + O(r^4), \\ S(r) &= S_0 + S_1 r + S r^2 + O(r^3), \\ \omega(r) &= \omega_0 + \omega_1 r + \omega_2 r^2 + O(r^3). \end{aligned} \tag{3.48}$$

As in the previous case, m_0 is eliminated since R needs to be regular everywhere. From the Ricci scalar, regularity tells us that $m_1 = m_2 = S_1 = 0$. We set $\omega = -1$ to satisfy the condition that $m' = 0$ at the origin. Equation (3.44) implies that $a_0 = a_2 = 0$. In addition, $\omega_1 = 0$ is derived from (3.45). Then the field variables near the origin become

$$\begin{aligned}
a(r) &= a_1 r + \frac{a_1}{5}\left(-2\omega_2 + \frac{2a_1^2}{e^2 S_0^2} + \frac{8\omega_2^2}{e^2} + \frac{\Lambda}{3} + \frac{\mu^2}{2}\right) r^3 + O(r^4), \\
m(r) &= \left(\frac{a_1^2}{2e^2 S_0^2} + \frac{2\omega_2^2}{e^2}\right) r^3 + O(r^4), \\
S(r) &= S_0 + \left(\frac{a_1^2}{e^2 S_0} + \frac{4S_0\omega_2^2}{e^2}\right) r^2 + O(r^3), \\
\omega(r) &= -1 + \omega_2 r^2 + O(r^3).
\end{aligned} \tag{3.49}$$

Thus we have a four-parameter family depending on parameters $a_1, \omega_2, \mu, \Lambda$. In practice the value of S_0 is fixed by the requirement that $S \to 1$ as $r \to \infty$. As $\mu \to 0$, these expansions of the field variables reduce to those in [133] as expected. In addition if $\Lambda \to 0$, we obtain the expansion for dyons in the ENAP-flat theory.

Event horizon: We perform Taylor series expansions of the field variables near the horizon. They nearly have the same expressions as in (3.27) except for the additional expansion of the electric part of the gauge potential. The Taylor series expansions are

$$\begin{aligned}
a(r) &= a'_h(r - r_h) + O(r - r_h)^2, \\
m(r) &= \left(\frac{r_h}{2} - \frac{\Lambda r_h^3}{6}\right) + m'_h(r - r_h) + O(r - r_h)^2, \\
S(r) &= S(r_h) + S'_h(r - r_h) + O(r - r_h)^2, \\
\omega(r) &= \omega(r_h) + \omega'_h(r - r_h) + O(r - r_h)^2.
\end{aligned} \tag{3.50}$$

Equation (3.44) forces us to choose $a(r_h) = 0$, otherwise a singularity will occur. The first

derivatives are given in terms of $a'(r_h) = a'_h$ and $\omega(r_h) = \omega_h$

$$\begin{aligned} m'_h &= \frac{r_h^2 a_h'^2}{2S_h^2 e^2} + \frac{\left(\omega_h^2 - 1\right)^2}{2r_h^2 e^2} + \frac{\left(1+\omega_h\right)^2 \mu^2}{e^2}, \\ S'_h &= \frac{2\omega_h^2 a'_h}{r_h S_h e^2 R_h'^2} + \frac{2\omega_h'^2 S_h}{r_h e^2} + \frac{\mu^2 r_h a_h'^2}{S_h e^2 R_h'^2}, \\ \omega'_h &= \frac{\omega_h\left(\omega_h^2 - 1\right)}{r_h^2 R_h'^2} + \frac{\left(1+\omega_h\right)\mu^2}{R'_h}. \end{aligned} \tag{3.51}$$

Therefore we obtain a five-parameter family of solutions, with parameters $r_h, \mu, \Lambda, \omega_h, a'_h$. As in the previous case, the value of S_h is again fixed by the requirement that $S \to 1$ as $r \to \infty$.

Infinity with $\Lambda < 0$: The spacetime metric (3.8) approaches the pure AdS metric as $r \to \infty$. The field variables have similar forms as for the purely magnetic solutions with the addition of the extra variable a. They are given by

$$\begin{aligned} a(r) &= \alpha_0 + \frac{\alpha_\infty}{r^\Delta} + ..., \\ m(r) &= M + \frac{m_\infty}{r^{2\Delta-1}} + ..., \\ S(r) &= 1 + \frac{S_\infty}{r^{2\Delta+2}} + ..., \\ \omega(r) &= -1 + \frac{\omega_\infty}{r^\Delta} + ... \end{aligned} \tag{3.52}$$

We remark that a and ω decay at the same rate as $r \to \infty$. This is implied by the field equations (3.44, 3.45). The quantities $\alpha_0,\ \alpha_\infty,\ m_\infty,\ S_\infty$ and ω_∞ are all undetermined parameters. The leading order of (3.44) forces us to set $\alpha_0 = 0$. Thus the analysis of the

field equations at infinity gives

$$a(r) = \frac{\alpha_\infty}{r^\Delta} + ..., \tag{3.53}$$

$$m(r) = M + \frac{\left(\Delta^2\Lambda - 3\mu^2\right)\left(2\Lambda\omega_\infty^2 - 3\alpha_\infty^2\right)}{6e^2\Delta\Lambda}\frac{1}{r^{2\Delta-1}} + ..., \tag{3.54}$$

$$S(r) = 1 - \frac{\left(9\alpha_\infty^2\mu^2 + 2\Delta^2\Lambda^2\omega_\infty^2\right)}{\Delta e^2\Lambda^2}\frac{1}{r^{2\Delta+2}} + ..., \tag{3.55}$$

$$\omega(r) = -1 + \frac{\omega_\infty}{r^\Delta} + ..., \tag{3.56}$$

where

$$\Delta \equiv \Delta_\pm = \frac{1}{2} \pm \frac{1}{2}\sqrt{1 - \frac{12\mu^2}{\Lambda}}. \tag{3.57}$$

Since $\Delta_- < 0$, the only possible root is Δ_+. The above expansions of the field variables near the origin and near the horizon reduce to those in [133] when $\mu = 0$. However this is not the case as $r \to \infty$. If $\mu \neq 0$ the leading orders of a (3.53) and ω (3.56) are different from those in the EYM-AdS theory. In particular, the leading order of a in the EYM-AdS system goes to $\alpha_0 =$ constant as $r \to \infty$. Moreover, when setting $a = 0$, equations (3.53–3.56) yield the same results as shown in (3.31).

In addition, to prove that there are no dyons in asymptotically flat case, we need to investigate the asymptotic behaviour of the field variables when $\Lambda = 0$. At the origin and the event horizon, the expressions shown in (3.49) and (3.50) are all valid when the cosmological constant is set to zero. In contrast, in the asymptotic region, i.e., $r \to \infty$, the behaviour of the field variables when $\Lambda = 0$ cannot be deduced directly from the asymptotically AdS case. This is because the asymptotic structure of the AdS spacetime is different from asymptotically flat spacetime.

Infinity without Λ: We assume that the asymptotic expansions of the field variables take

the following form [79]

$$
\begin{aligned}
a(r) &= \hat{\alpha}_0 + \hat{\alpha}_\infty e^{-\hat{\Delta} r}, \\
m(r) &= \hat{M} + \hat{m}_\infty e^{-2\hat{\Delta} r}, \\
S(r) &= 1 + \frac{\hat{S}_\infty e^{-2\hat{\Delta} r}}{r}, \\
\omega(r) &= -1 + \hat{\omega}_\infty e^{-\hat{\Delta} r},
\end{aligned} \tag{3.58}
$$

where $\hat{\Delta}, \hat{\alpha}_\infty, \hat{m}_\infty, \hat{S}_\infty$ and $\hat{\omega}_\infty$ are all undetermined parameters. By inserting the expansions (3.58) into the field equations (3.44–3.47), these parameters can be determined. We thus obtain the behaviour of the field variables at infinity as follows

$$a(r) = \hat{\alpha}_\infty e^{-\mu r}, \tag{3.59}$$

$$m(r) = \hat{M} - \left(\frac{\hat{\alpha}_\infty^2 (1 + r^2 \mu^2) + 2\mu^2 \hat{\omega}_\infty^2}{\mu e^2} \right) e^{-2\mu r}, \tag{3.60}$$

$$S(r) = 1 - \left(\frac{\hat{\alpha}_\infty^2 (2 + r^2 \mu^2) + 2\mu^2 \hat{\omega}_\infty^2}{\mu e^2} \right) \frac{e^{-2\mu r}}{r}, \tag{3.61}$$

$$\omega(r) = -1 + \hat{\omega}_\infty e^{-\mu r}. \tag{3.62}$$

These results agree with those of [79] when $a(r)$ is set to zero (see (3.34)).

We now have all the essential ingredients for constructing the proof of the non-existence of dyonic solutions. This will be investigated in the following subsection.

3.6.2 Proof of the non-existence of dyonic solutions

We now provide the proof of the non-existence of dyonic solutions in ENAP theory with zero or negative cosmological constant. We follow a beautiful argument for EYM which is given by Ershov and Galt'sov [71]. The proof starts by re-writing the field equation

(3.44),

$$\left[\frac{r^2a'a}{S}\right]' = \frac{2a^2\omega^2}{RS} + \frac{a^2\mu^2r^2}{RS} + \frac{r^2a'^2}{S}. \tag{3.63}$$

Then we integrate this equation throughout space,

$$\begin{aligned}\int_{r_h/0}^{\infty}\left[\frac{r^2a'a}{S}\right]' dr &= \int_{r_h/0}^{\infty}\left(\frac{2a^2\omega^2}{RS} + \frac{a^2\mu^2r^2}{RS} + \frac{r^2a'^2}{S}\right) dr,\\ \left.\frac{r^2a'a}{S}\right|_{r_h/0}^{\infty} &= \int_{r_h/0}^{\infty}\frac{r^2}{S}\left(\frac{2a^2\omega^2}{r^2R} + \frac{a^2\mu^2}{R} + a'^2\right) dr,\end{aligned} \tag{3.64}$$

where the lower limit of these integrals, denoted by $(r_h/0)$, refers to the black hole and regular solutions respectively. At the lower limit, since both S and a' are regular at the origin and the horizon, therefore the LHS of (3.64) is always zero, since $r = 0$ for dyons and $a(r_h) = 0$ for dyonic black holes. For the upper limit, in the asymptotically AdS case, we consider (since $S \to 1$ as $r \to \infty$)

$$r^2a'a \approx -\Delta_+\alpha_\infty^2 r^{1-2\Delta_+} + ..., \tag{3.65}$$

where (3.53) is applied and Δ_+ is given in (3.57). Since

$$1 - 2\Delta_+ = -\sqrt{1 - \frac{12\mu^2}{\Lambda}} < 0, \tag{3.66}$$

therefore the LHS of (3.64) tends to zero as $r \to \infty$. The RHS of (3.64) is the sum of positive terms, thus each term must vanish identically (to satisfy the equation), i.e., $a' = 0$. This implies that a is a constant. As a consequence of this, a must be zero everywhere if $\omega \neq 0$ and $\mu \neq 0$. Therefore we have shown that the electric part of the gauge field (3.43) cannot be non-zero. Hence ENAP-AdS theory does not allow the existence of dyon solutions.

In the asymptotically flat scenario, equation (3.64) is still valid. The lower limit of the LHS of this equation can be seen to be zero by following the same argument discussed above. For the upper limit, since the asymptotic structure of the spacetime changes dramatically from the AdS case, the metric functions R and $S \to 1$ as $r \to \infty$. Hence equation (3.44) implies that the leading order of the electric part of the gauge field $a(r)$ decays exponentially rather than polynomially as shown in (3.62). It is straightforward to show that in this case

$$r^2 a' a \approx -\mu \hat{\alpha}_\infty^2 r^2 e^{-2\mu r} + \dots \,. \tag{3.67}$$

Thus the upper limit of the LHS of (3.64) is also zero as $r \to \infty$. To satisfy the whole equation (3.64), we now reach the same conclusion as in the AdS scenario, which is that the electric part a must be zero everywhere.

Therefore, we have shown that the ENAP theory in both asymptotically flat and asymptotically AdS spacetimes possesses no dyons or dyonic black hole solutions. The proof provided here breaks down for the EYM-AdS system, since the boundary conditions are different. Indeed, regular and black hole solutions with non-vanishing electric part are found in EYM-AdS sector [28, 29, 97].

§3.7 Stability analysis

In section 3.5, we presented numerical regular and black hole solutions of ENAP-AdS theory. These solutions violate the generalized no-hair conjecture (see section 2.3) in the sense that they look very similar to the Schwarzschild-AdS metric at infinity. However, one needs to take the stability of these equilibrium solutions into account, if one were to consider Bizon's version of no-hair conjecture [25] (see details in subsection 2.3). Therefore, in this section, a detailed analysis of the perturbed static regular and black hole solutions of the ENAP equations in asymptotically flat and AdS spacetimes is discussed. We expect

that the ENAP-AdS solutions, like the ENAP-flat and EYMH-AdS solutions, will be unstable.

3.7.1 Perturbation equations

We consider spherically symmetric perturbations of the static equilibrium solutions of the ENAP-AdS equations by using the following notation

$$\omega = \omega_0(r) + \epsilon\omega_1(t,r), \tag{3.68}$$

and similarly for all the quantities in the theory, $m,\ \omega,\ R,\ S,\ a,\ b,\ d$. Here ϵ is a small parameter. We are now considering the full gauge potential ansatz (3.10). Recall that a, b and d vanish for purely magnetic equilibrium solutions. The zeroth order in (3.68) e.g., $\omega_0(r)$, denotes the equilibrium solution. In this section, any variables with subscript "1" denote the perturbed part of the variables. By substituting (3.68) and similar expressions for the other field variables into the field equations (3.4, 3.6), the zeroth order gives the static field equations (3.22–3.24). The linearised NAP field equations up to order ϵ are

$$\begin{aligned}
0 &= -r^2 R_0 S_0 a_1'' + r R_0 \left(r S_0' - 2S_0\right) a_1' + S_0 \left(r^2\mu^2 + 2\omega_0^2\right) a_1 \\
&\quad + r^2 R_0 S_0 \dot{b}_1' - r R_0 \left(r S_0' - 2S_0\right) \dot{b}_1 + 2 S_0 \omega_0 \dot{d}_1, && (3.69)\\
0 &= \frac{1}{R_0 S_0^2}\dot{a}_1' - \frac{1}{R_0 S_0^2}\ddot{b}_1 - \left(\mu^2 + \frac{2\omega_0^2}{r^2}\right) b_1 - \frac{2\omega_0}{r^2} d_1' + \frac{2\omega_0'}{r^2} d_1, && (3.70)\\
0 &= \frac{1}{R_0 S_0^2}\ddot{d}_1 - R_0 d_1'' - \frac{(R_0 S_0)'}{S_0} d_1' + \left(\mu^2 + \frac{\omega_0^2 - 1}{r^2}\right) d_1 + \frac{\omega_0}{R_0 S_0^2}\dot{a}_1 - R_0\omega_0 b_1' \\
&\quad - \left(\omega_0 \frac{(R_0 S_0)'}{S_0} + 2 R_0 \omega_0'\right) b_1, && (3.71)\\
0 &= -r^3 \ddot{\omega}_1 + r^3 R_0^2 S_0^2 \omega_1'' + r^3 R_0 S_0 (R_0 S_0)' \omega_1' - r R_0 S_0^2 \left(3\omega_0^2 + r^2\mu^2 - 1\right)\omega_1 \\
&\quad - 2 r^2 R_0 S_0^2 \omega_0' m_1' - 2 r R_0 S_0 \left[\omega_0' \left(r S_0' - S_0\right) + \omega_0'' S_0 r\right] m_1 \\
&\quad + r^3 R_0^2 S_0 \omega_0' S_1' - r^3 R_0^2 S_0' \omega_0' S_1, && (3.72)
\end{aligned}$$

where $\dot{}$ denotes $\partial/\partial t$ and $\prime$ denotes $\partial/\partial r$. Another constraint equation comes from the gauge condition i.e., $\nabla_a A^a = 0$ (3.7), which reads

$$0 = \frac{1}{R_0 S_0^2}\dot{a}_1 - R_0 b_1' - \left(\frac{2R_0}{r} + \frac{(R_0 S_0)'}{S_0}\right) b_1 + \frac{2}{r^2} d_1. \tag{3.73}$$

Moreover m_1' and S_1' can be found explicitly from the (tt) and (rr) components of the Einstein field equations (3.4)

$$m_1' = \frac{2R_0\omega_0'}{e^2}\omega_1' + \frac{2\left(1+\omega_0\right)\left(r^2\mu^2 + \left(\omega_0 - 1\right)\omega_0\right)}{e^2 r^2}\omega_1 - \frac{2\omega_0'^2}{e^2 r} m_1, \tag{3.74}$$

$$S_1' = \frac{4S_0\omega_0'}{e^2}\omega_1' + \frac{2\omega_0'^2}{e^2 r} S_1. \tag{3.75}$$

One additional equation comes from the tr component of the Einstein field equations and is given by

$$\dot{m}_1 = \frac{2R_0\omega_0'}{e^2}\dot{\omega}_1. \tag{3.76}$$

Integrating with respect to time, we obtain

$$m_1 = \frac{2R_0\omega_0'}{e^2}\omega_1 + \mathcal{F}(r), \tag{3.77}$$

where the arbitrary function $\mathcal{F}(r)$ can be determined by inserting (3.77) into (3.74). Hence we obtain a first order ordinary differential equation for $\mathcal{F}(r)$

$$\frac{\mathcal{F}'}{\mathcal{F}} = -\frac{2\omega_0'^2}{e^2 r}. \tag{3.78}$$

The solution to this equation is

$$\mathcal{F} = \mathcal{K}\exp\left[-\int_{r_h/0}^{r} \frac{2\omega_0'^2(\tilde{r})}{e^2\tilde{r}}\, d\tilde{r}\right]. \tag{3.79}$$

Here $\mathcal{K}$ is a constant of integration. However the boundary conditions at the horizon or origin require that every perturbation vanishes. Hence $\mathcal{F}(r_h)$ or $\mathcal{F}(0)$ is zero from (3.77),

therefore we have no choice but to set $\mathcal{K} = 0$. This means that $\mathcal{F} \equiv 0$ everywhere. Hence m_1 (3.77) can be expressed as

$$m_1 = \frac{2R_0\omega_0'}{e^2}\omega_1. \tag{3.80}$$

The equations (3.69–3.75) can be separated into two sectors. The first sector (3.72, 3.74, 3.75) is called the gravitational sector and involves the perturbations ω_1, m_1, S_1. The second part (3.69–3.71) and (3.73) is the sphaleronic sector, involving the perturbations a_1, b_1, d_1. In EYM theory with $\mu = 0$, the remaining gauge freedom allows us to set $a_1 = 0$ in the perturbation equations (3.69–3.72). However in ENAP theory, gauge invariance is broken because of the mass term. Therefore in the ENAP theory, we simply cannot set $a_1 = 0$ because there is no gauge freedom left. In addition, the gauge condition $\nabla_a A^a = 0$ gives us an extra constraint equation (3.73).

In the next two subsections, we will discuss the gravitational and sphaleronic sector perturbations of solitons and black hole solutions in more detail.

3.7.2 Gravitational sector

As its name might suggest, the gravitational sector contains contributions from the perturbations of the metric functions m_1, S_1 and the gauge field ω_1. The equations belonging to this category are equations (3.72, 3.74, 3.75). Moreover we use (3.74, 3.75, 3.80) to eliminate the metric perturbations from (3.72) and use the static field equations (3.23, 3.24) to eliminate S_0' and ω_0'' respectively. Finally, we can rewrite (3.72) as follows

$$0 = -\ddot{\omega}_1 + R_0^2 S_0^2 \omega_1'' + R_0 S_0 (R_0 S_0)' \omega_1' + V(r)\omega_1, \tag{3.81}$$

where

$$V(r) = R_0 S_0^2 \left[\frac{1}{r^2} - \mu^2 - \frac{3\omega_0^2}{r^2} - \frac{8\mu^2\omega_0'}{e^2 r} + \frac{8\omega_0\omega_0'}{e^2 r^3} - \frac{8\mu^2\omega_0\omega_0'}{e^2 r} - \frac{8\omega_0^3\omega_0'}{e^2 r^3} + \frac{4R_0\omega_0'^2}{e^2 r^2} + \frac{4R_0'\omega_0'^2}{e^2 r} + \frac{8R_0\omega_0'^4}{e^4 r^2} \right]. \tag{3.82}$$

This equation, in the limit $\mu \to 0$, agrees with the perturbation equation in the gravitational sector of the EYM-AdS theory [194, 197]. We assume periodic time-dependent perturbations with frequency σ

$$\omega_1(t, r) = e^{-i\sigma t}\omega_1(r). \tag{3.83}$$

From now on, ω_1 will denote a function of one variable $\omega_1(r)$. We also define a tortoise coordinate r_*,

$$\frac{dr_*}{dr} = \frac{1}{R_0 S_0}. \tag{3.84}$$

The tortoise coordinate r_* ranges from $0 < r_* < r_c$, where $r_c > 0$ is a positive constant, for solitons and $-\infty < r_* < 0$ for black holes, in each case choosing an appropriate constant of integration. Then the gravitational perturbation equation (3.81) takes the form

$$\sigma^2\omega_1 = -\frac{d^2\omega_1}{dr_*^2} - V(r)\omega_1. \tag{3.85}$$

The condition for instability is having an imaginary frequency mode, i.e.

$$\sigma^2 < 0. \tag{3.86}$$

This is equivalent to exponential growth in time of (3.83). The problem reduces from a linear partial differential equation (3.81) to a linear ordinary differential equation (3.85). In fact (3.85) is in the Sturm−Liouville form with eigenvalue σ^2 when ω_1 is required to satisfy

some boundary conditions. Thus to find an instability in this sector, we need to solve (3.85) for negative eigenvalue σ^2 while demanding that the corresponding eigenfunction ω_1 must vanish at each end-point, i.e. the perturbation does not change the asymptotic structure of the spacetime.

Suitable boundary conditions for (3.85) are

$$\begin{aligned}
&\omega_1 \sim r^{\alpha} && \text{for} \quad r \to 0, \\
&\omega_1 \sim (r - r_h)^{\beta} && \text{for} \quad r \to r_h, \\
&\omega_1 \sim r^{\rho} && \text{for} \quad r \to \infty, \Lambda < 0, \\
&\omega_1 \sim e^{\eta r} && \text{for} \quad r \to \infty, \Lambda = 0.
\end{aligned} \tag{3.87}$$

We require $\alpha, \beta > 0$ and $\rho, \eta < 0$ so that ω_1 vanishes at the origin (for solitons), event horizon (for black holes) and at infinity. By substituting these into the perturbation equation (3.85), α, β, ρ and η are then determined to be

$$\begin{aligned}
\alpha &= 2, \\
\beta &= \pm \frac{i e^2 r_h^3 \sigma}{\left(1 - \omega_{0_h}^2\right)^2 - e^2 r_h^2 + e^2 r_h^4 \Lambda + 2(1 + \omega_{0_h})^2 r_h^2 \mu^2}, \\
\rho &= -\frac{1}{2}\left(1 + \sqrt{1 - \frac{12\mu^2}{\Lambda}}\right), \\
\eta &= -\sqrt{\mu^2 - \sigma^2},
\end{aligned} \tag{3.88}$$

where $\omega_{0_h} = \omega_0(r_h)$. Clearly these parameters (3.88) satisfy our requirements, i.e. $\alpha > 0$, $\rho < 0$ and $\eta < 0$. For β, the sign is chosen such that $\mathrm{Re}(\beta) > 0$ i.e., the perturbations vanish on the horizon. Since $\alpha = 2$ and the expression for β is regular when $\Lambda = 0$, therefore, these boundary conditions at the origin and event horizon are applicable when $\Lambda = 0$. In ENAP-flat theory, the static field variables decay exponentially rather than polynomially [79] (see also equation (3.34) in subsection 3.4.2) at infinity. Thus we expect

that ω_1 should have different behaviour as $r \to \infty$ in the ENAP-flat and ENAP-AdS cases.

With these boundary conditions, we are ready to solve the perturbation equation (3.85). To do that we numerically integrate (3.85) from 0 (r_h) to ∞ for the regular (black hole) cases. As one may observe, the complete profile of the unperturbed solution is necessary to determine the solution of (3.85).

To solve equation (3.85), we initially construct the equilibrium solution ω_0 and substitute it back into equation (3.85). We integrate the perturbation equation outward from (near) the origin, $r = 10^{-3}$ or non-zero r_h to infinity. Then the shooting method is implemented in order to find an eigenvalue σ that satisfies the instability condition (3.86). We scan for purely imaginary σ for which ω_1 vanishes at the end-points. Hence σ will act as the shooting parameter. Our intention is to show that each branch of solutions, i.e. ordinary-node and quasi-node of solitons and black hole solutions, possesses at least one unstable mode. That will be sufficient to show an instability of the solutions of the ENAP-AdS theory. Note that the gauge coupling constant e and the black hole radius r_h will be set to 1 throughout the numerical calculation.

As mentioned earlier, the perturbation equation (3.85) is in Sturm-Liouville or self-adjoint form. Thus we expect the following trend: for each eigenvalue σ_i^2 where $i = 1, 2, 3...$ and $\sigma_1^2 < \sigma_2^2 < \sigma_3^2 < ...$, there is a corresponding eigenfunction (solution) with $i-1$ zeroes. For instance the lowest eigenvalue σ_1^2 will correspond to the "nodeless" eigenfunction $\omega_1(r)$. To prevent the confusion that might occur, we will denote the number of zeroes of the perturbation mode ω_1 as "N".

3.7.2.1 Asymptotically flat solutions

In [79], it is stated that spherically symmetric smooth and black hole solutions of ENAP in asymptotically flat are unstable. However they did not present a detailed stability analysis of those solutions. Thus in this section, integration of the perturbation equation (3.85) of the gravitational sector for the ENAP-flat theory will be performed. The perturbation

equations discussed above reduce to those for the ENAP-flat case when the cosmological constant is set to zero.

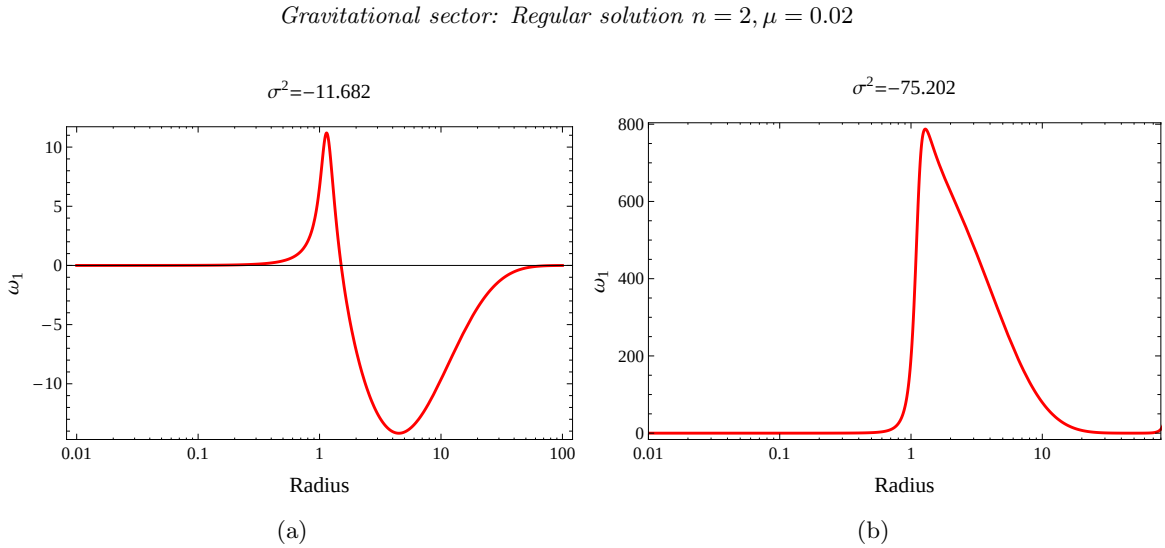

Figure 3.12: Two unstable modes of the asymptotically flat $n = 2$ regular solution for fixed $\mu = 0.02$, (a) $N = 1$ eigenfunction ω_1 with corresponding frequency $\sigma^2 = -11.682$, (a) nodeless mode $N = 0$ with frequency $\sigma^2 = -75.202$.

Here we present examples of numerical results which confirm the statement made in [79] that spherically symmetric solutions are linearly unstable. First, $N = 1$ and $N = 0$ unstable modes of the $n = 2$ regular solution with Proca mass $\mu = 0.02$ are shown in Fig 3.12. Additionally, according to the Sturm-Liouville theorem stated above, these two unstable modes are expected to correspond to the first two lowest possible eigenvalues. Moreover, the corresponding eigenvalues σ^2 satisfy the instability condition (3.86), thus the results in Fig 3.12 show that this particular equilibrium regular solution is unstable. In addition, the instability of a quasi$-n = 1$ regular solution is demonstrated in Fig 3.13. In this case, the mass of the gauge boson is fixed to be 0.04454.

For the black hole case, we consider an $n = 2$ solution when μ is set to be 0.017. The two lowest eigenfunctions $N = 1$ and $N = 0$ are plotted as functions of radius in Fig 3.14(a) and Fig 3.14(b) respectively. The $N = 0$ unstable mode of the $n = 1$ black hole with Proca

mass $\mu = 0.1233$ is illustrated in Fig 3.15. We clearly see that in the example plots $|\sigma^2|$ for the black holes is significantly smaller than $|\sigma^2|$ of the solitons. While in EYM-flat, $|\sigma^2|$ for both solitons [167] and black holes [168] seems to be of the same order of magnitude.

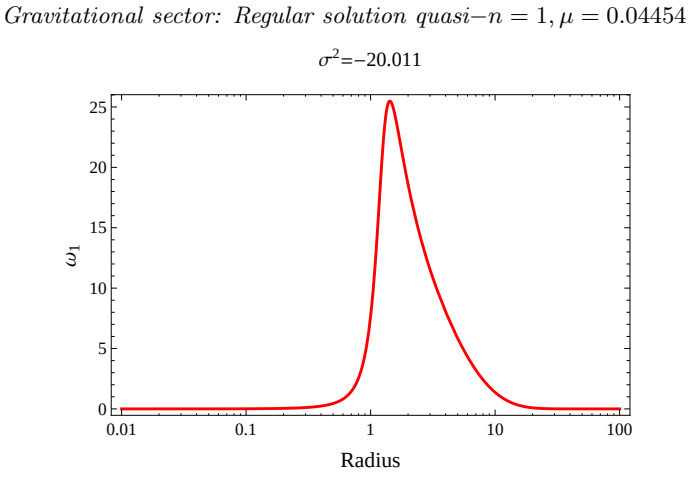

Figure 3.13: Lowest unstable mode of a quasi$-n = 1$ regular solution of the asymptotically flat ENAP equations for fixed $\mu = 0.04454$ with eigenvalue $\sigma^2 = -20.011$.

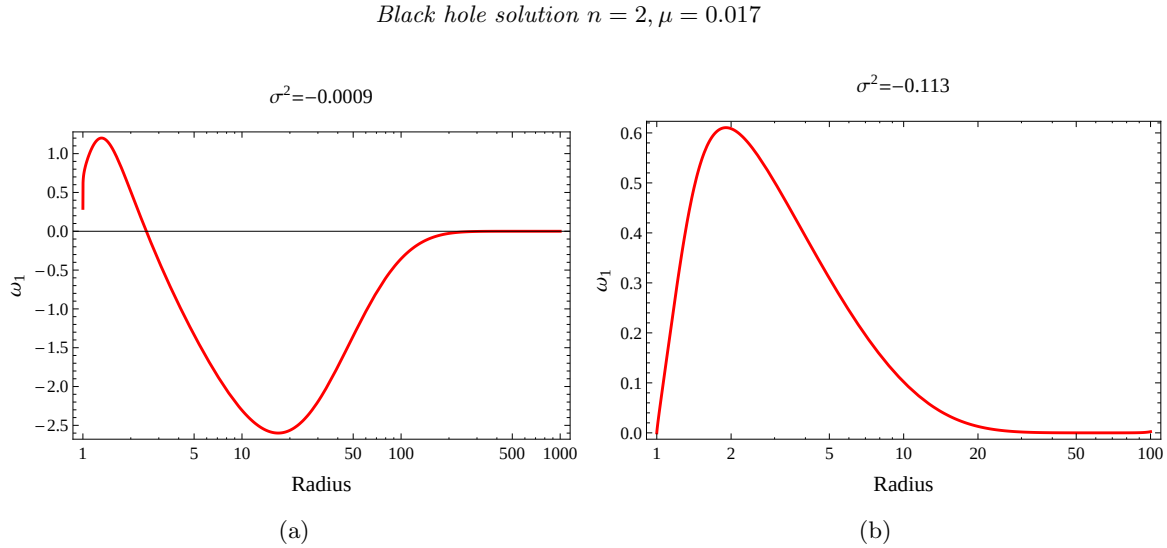

(a) (b)

Figure 3.14: Two unstable modes of an asymptotically flat $n = 2$ black hole solution for fixed $\mu = 0.017$, (a) $N = 1$ eigenfunction ω_1 with corresponding frequency $\sigma^2 = -0.0009$, (b) nodeless mode $N = 0$ with frequency $\sigma^2 = -0.113$.

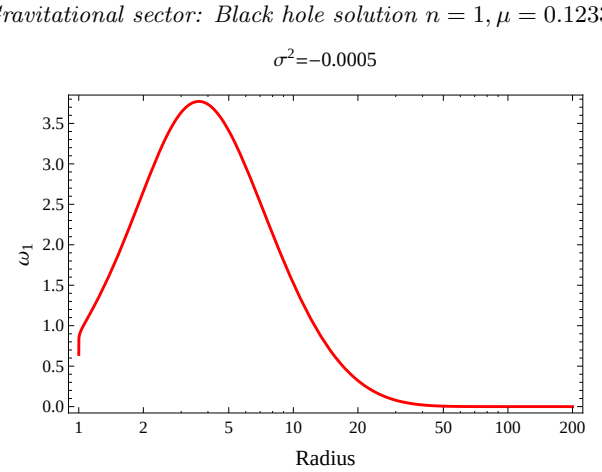

Figure 3.15: Lowest unstable mode of an $n = 1$ black hole solution of the asymptotically flat ENAP equations for fixed $\mu = 0.1233$ with eigenvalue $\sigma^2 = -0.0005$.

3.7.2.2 Regular solutions

We now investigate the stability of solitons in ENAP-AdS theory in the gravitational sector. In particular, Fig 3.16(a) and Fig 3.16(b) illustrate unstable modes of an $n = 2$ soliton solution with Proca mass $\mu = 0.02$ and cosmological constant $\Lambda = -0.005$. It is clear to see that ω_1 vanishes at the origin and as $r \to \infty$. Additionally these eigenfunctions ω_1 correspond to the two lowest possible eigenvalues σ_1^2 and σ_2^2 in accordance with the Sturm-Liouville theorem.

More examples of unstable modes for various equilibrium solutions are shown in Fig 3.17. In these plots, we investigate the first two unstable modes of $n = 2$ regular solutions for fixed Proca mass $\mu = 0.02$ and cosmological constant $\Lambda = -0.001$. For ordinary branch regular solutions of EYM-flat and EYMH-flat theories, the number of unstable modes in the gravitational sectors is equal to the number of nodes of the equilibrium solutions ω_0 [115, 123]. Therefore, $n = 2$ regular solutions are expected to have two unstable modes ($N = 1$ and $N = 0$). For $N = 1$ eigenfunctions, the corresponding eigenvalues σ^2 are less negative than those of the $N = 0$ eigenfunctions. For the $N = 1$ case, the zero of ω_1 is at roughly the same location as we vary μ or Λ. In addition, in Fig 3.17 we see that, the less

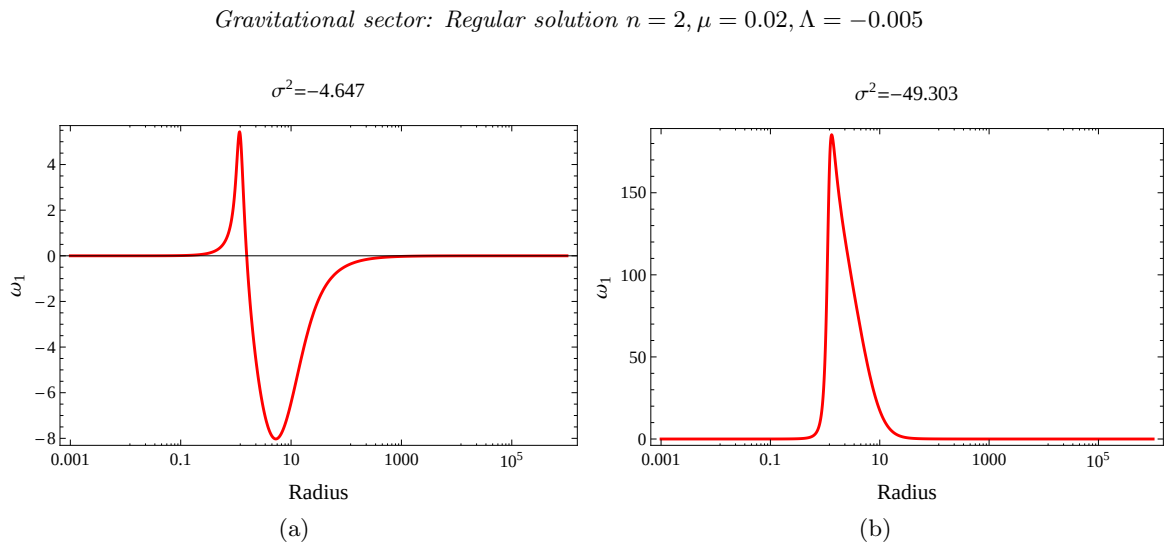

Figure 3.16: The first two unstable modes of ω_1, (a) $N = 1$ eigenfunction with $\sigma^2 = -4.647$, (b) nodeless eigenfunction with $\sigma^2 = -49.303$ for an $n = 2$ regular solution with $\mu = 0.02$ and $\Lambda = -0.005$.

negative the value of σ^2 is, the smaller the peak of ω_1 is. However, since we have a linear equation for ω_1, the overall scale is not important.

In EYMH-flat theory, for the quasi$-n$ branch, a quasi$-n = \tilde{n} - 1$ solution has $\tilde{n} - 1$ unstable modes in the gravitational sector [123]. Thus, the quasi$-n = 1$ regular solution might be expected to have only one unstable mode ($N = 0$). This result is illustrated in Fig 3.18, where a nodeless eigenfunction ω_1 is shown. The corresponding eigenvalue σ^2 is -7.892. In addition, in Fig 3.19 various equilibrium solutions are explored for fixed Proca field mass $\mu = 0.02$ and varying Λ Fig 3.19(a), and for fixed $\Lambda = -0.001$ and varying μ Fig 3.19(b). One can see from these plots for quasi$-n = 1$ solution that, the less negative the value of σ^2, the smaller the peak of ω_1.

Our results in Fig 3.16–3.19 provide strong evidence that the solitonic solutions of the ENAP-AdS equations are linearly unstable in the gravitational sector, since, we have shown that all regular solutions studied here have perturbation modes with $\sigma^2 < 0$. We also remark that all $n = 2$ solutions seem to have exactly two unstable modes. However,

we can only find one unstable mode for the quasi$-n = 1$ branch.

Gravitational sector: Regular solution $n = 2$

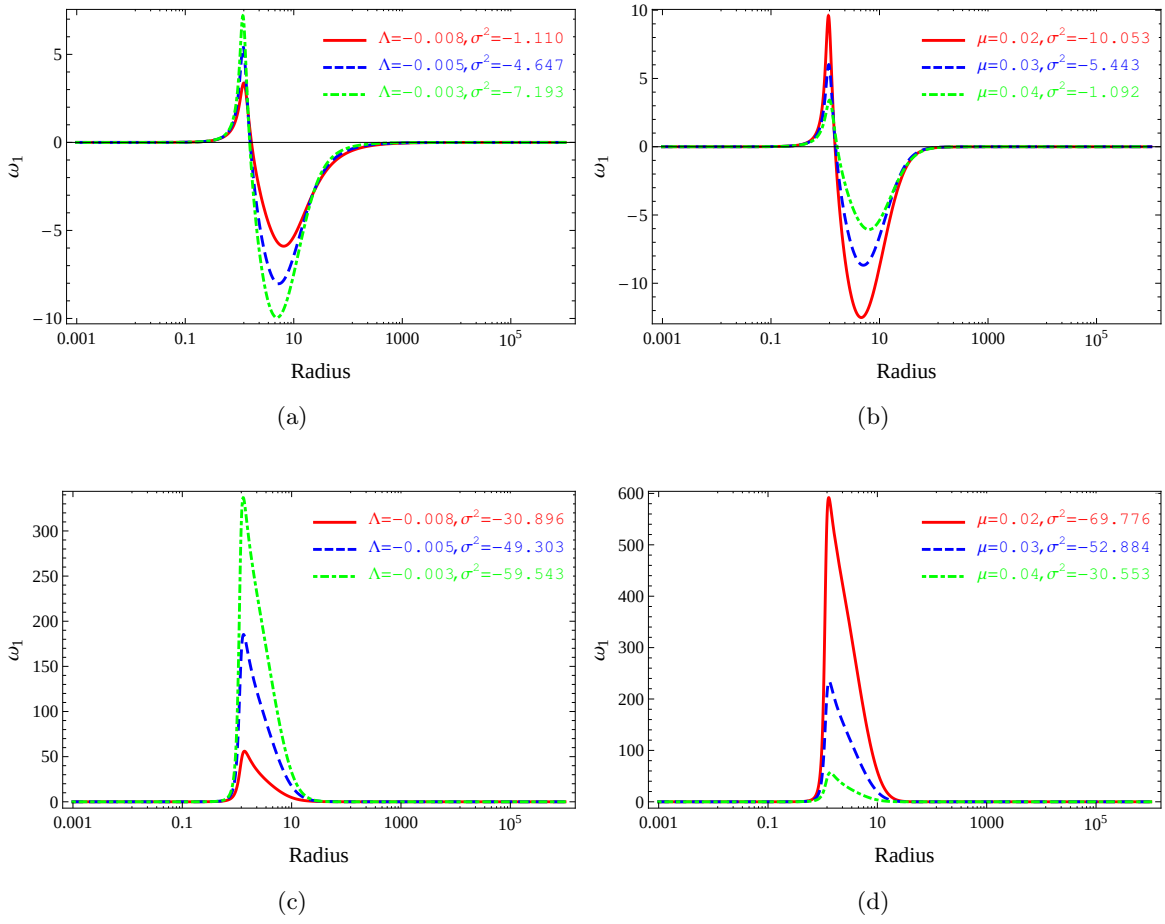

(a) (b)

(c) (d)

Figure 3.17: The first two lowest unstable modes ω_1 for $n = 2$ equilibrium regular solutions, $(a), (c)$ $N = 1$ and $N = 0$ eigenfunctions for fixed $\mu = 0.02$ and varying Λ, $(b), (d)$ $N = 1$ and $N = 0$ eigenfunctions for fixed $\Lambda = -0.001$ and varying μ.

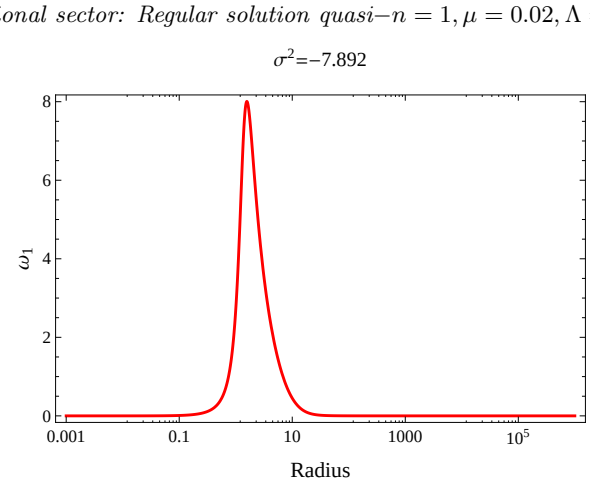

Figure 3.18: Nodeless eigenfunction with $\sigma^2 = -7.892$ for a quasi$-n = 1$ regular solution with fixed $\mu = 0.02$ and $\Lambda = -0.005$.

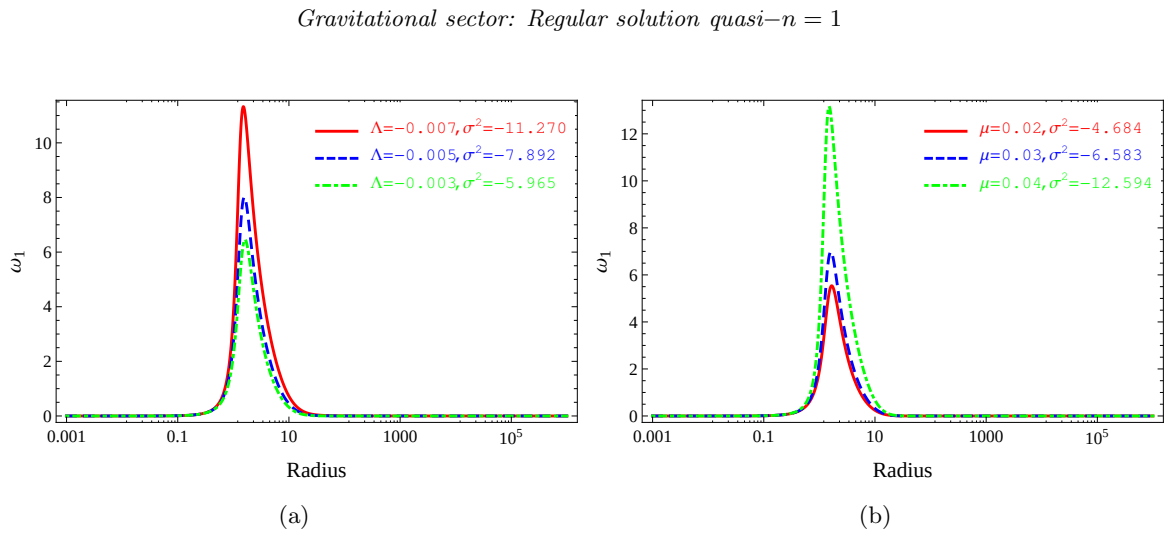

Figure 3.19: Nodeless eigenfunctions ω_1 for quasi$-n = 1$ regular solutions, (a) fixed $\mu = 0.02$ and varying Λ, (b) fixed $\Lambda = -0.001$ and varying μ.

3.7.2.3 Black hole solutions

The stability of the black hole solutions in ENAP-AdS theory is now investigated. In a similar way to the regular solutions, in this case an exponentially growing in time mode with eigenvalue that satisfies (3.86) is expected for each branch of solutions. The relevant

branches are $n = 2$, quasi$-n = 1$, $n = 1$ and quasi$-n = 0$ black hole solutions. For the black hole case, the number of unstable modes and the number of nodes of the equilibrium solutions are expected to be connected in the same way as in the regular case. For example we expect that an $n = 2$ black hole solution has two unstable modes and a quasi$-n = \tilde{n}-1$ solution has $\tilde{n} - 1$ unstable modes.

Gravitational sector: Black hole solution $n = 2, \mu = 0.01, \Lambda = -0.001$

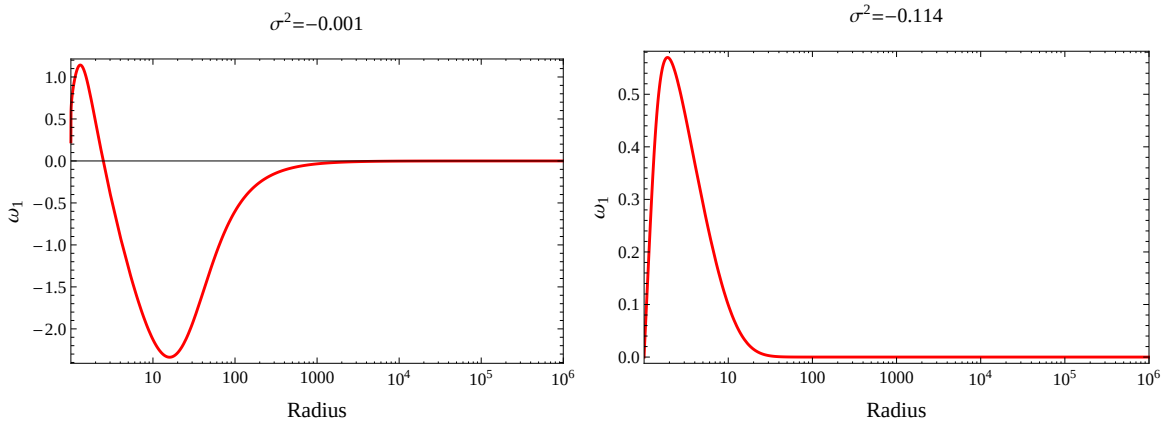

(a) (b)

Figure 3.20: The unstable modes of an $n = 2$ black hole solution, (a) $N = 1$ with $\sigma^2 = -0.001$, (b) $N = 0$ with $\sigma^2 = -0.114$.

For an $n = 2$ black hole solution, the first two unstable eigenfunctions are plotted in Fig 3.20, namely, an $N = 1$ and a nodeless perturbation (Fig 3.20(a),(b) respectively) with corresponding eigenvalues $\sigma^2 = -0.001, -0.114$. To illustrate more examples of equilibrium $n = 2$ black hole solutions, Fig 3.21 shows the first two lowest eigenvalues σ^2 for $n = 2$ black hole solutions with fixed Proca mass $\mu = 0.01$ and varying Λ (left panel), and fixed cosmological constant $\Lambda = -0.0004$ and varying mass of the vector boson μ (right panel). From these plots, we see that as σ^2 increases, the peak of ω_1 increases. This trend however, does not follow in Fig 3.21(d). We also notice that the eigenvalues in the black hole case have much smaller magnitudes than in the soliton case.

For $n = 1$ and quasi$-n = 1$ solutions, only one unstable mode is expected to be found

in each case. In Fig 3.22, nodeless ($N = 0$) eigenfunctions are plotted with eigenvalue $\sigma^2 = -0.070$ and -0.090 respectively for an $n = 1$ and a quasi$-n = 1$ black hole. Fig 3.23 and Fig 3.24 display examples of $N = 0$ eigenfunctions for various $n = 1$ and quasi$-n = 1$ black hole solutions for different values of Λ and μ. In these plots, we observe that as σ^2 becomes larger, the peak of the eigenfunction ω_1 increases. We observe that $|\sigma^2|$ for the $N = 0$ modes in the $n = 1$ and quasi$-n = 1$ cases are smaller than the $N = 0$ modes in the $n = 2$ cases.

We have shown that all the black hole solutions considered so far in this section, namely $n = 2, n = 1$ and quasi$-n = 1$ branches, are unstable. We find exactly two unstable modes ($N = 1$ and $N = 0$) for $n = 2$ black hole solutions while only one unstable mode is found for the $n = 1$ and quasi$-n = 1$ solutions. For the quasi$-n = 0$ solution, our numerical code can not find an example of an exponentially growing mode which satisfies the boundary conditions. Hence the stability of the black hole solutions in the quasi$-n = 0$ branch remains unclear at this point. This should not be too much of a surprise, since the quasi$-n = 0$ solutions should have zero unstable modes in the gravitational sector according to the work done by Mavromatos and Winstanley [123] for EYMH-flat theory. Hence, in order to determine whether the quasi$-n = 0$ branch of solutions is stable, we need to consider the sphaleronic sector of perturbations.

Gravitational sector: Black hole solution $n = 2$

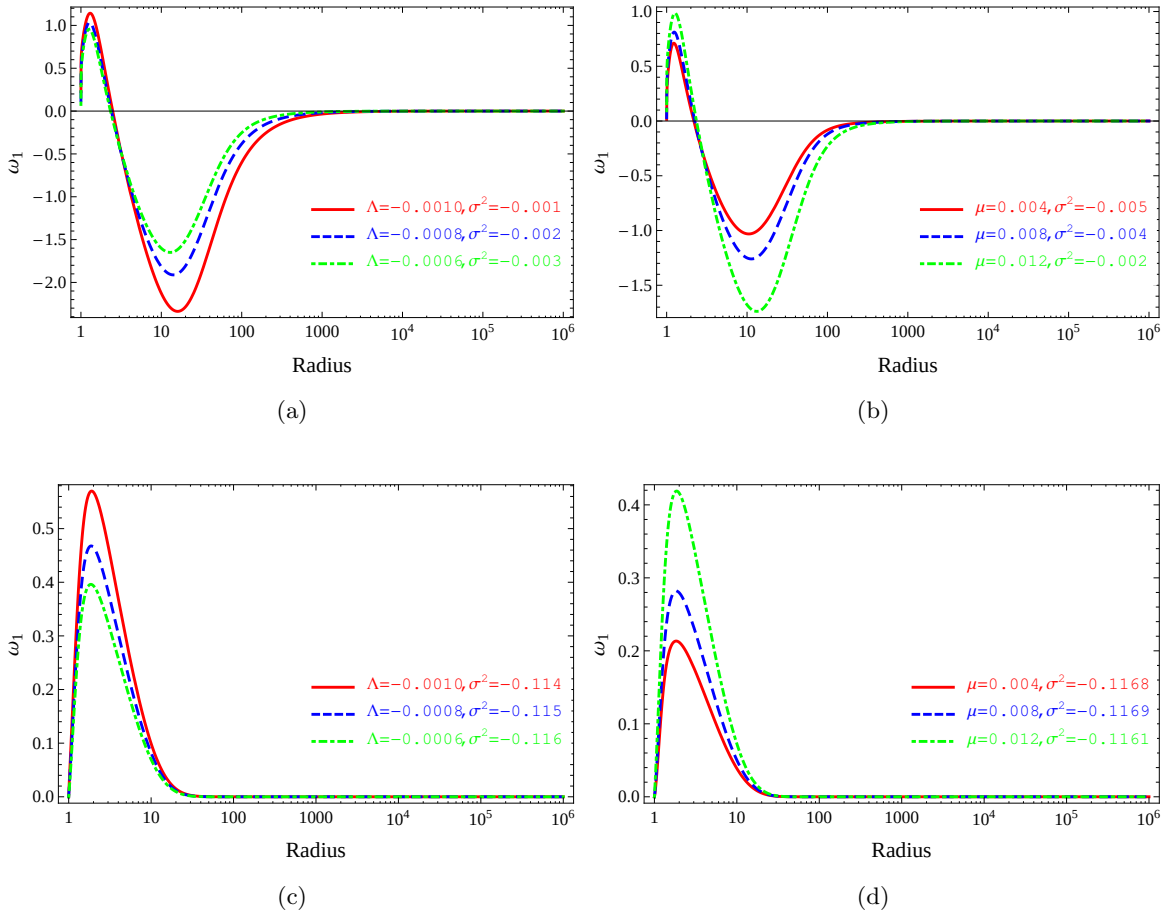

Figure 3.21: The first two lowest unstable modes of ω_1 for $n = 2$ equilibrium black hole solutions, $(a), (c)$ $N = 1$ and $N = 0$ eigenfunctions for fixed $\mu = 0.01$ and varying Λ, $(b), (d)$ $N = 1$ and $N = 0$ eigenfunctions for fixed $\Lambda = -0.0004$ and varying μ.

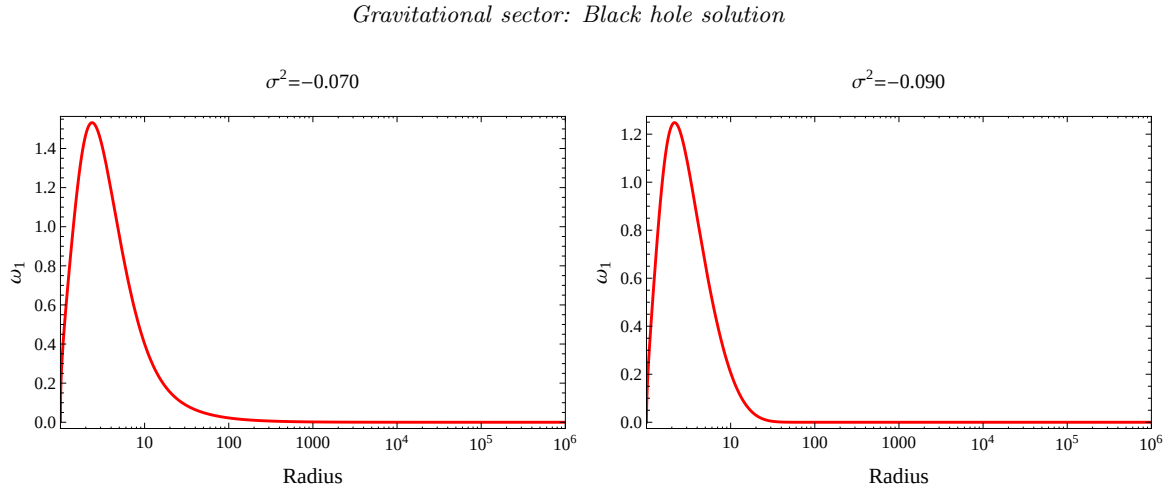

Figure 3.22: Two unstable modes of an $n = 1$ (left) and a quasi$-n = 1$ (right) black hole solution, (a) nodeless perturbation mode with $\sigma^2 = -0.070,\ \mu = 0.03,\ \Lambda = -0.02$, (b) $\sigma^2 = -0.090,\ \mu = 0.01,\ \Lambda = -0.0002$.

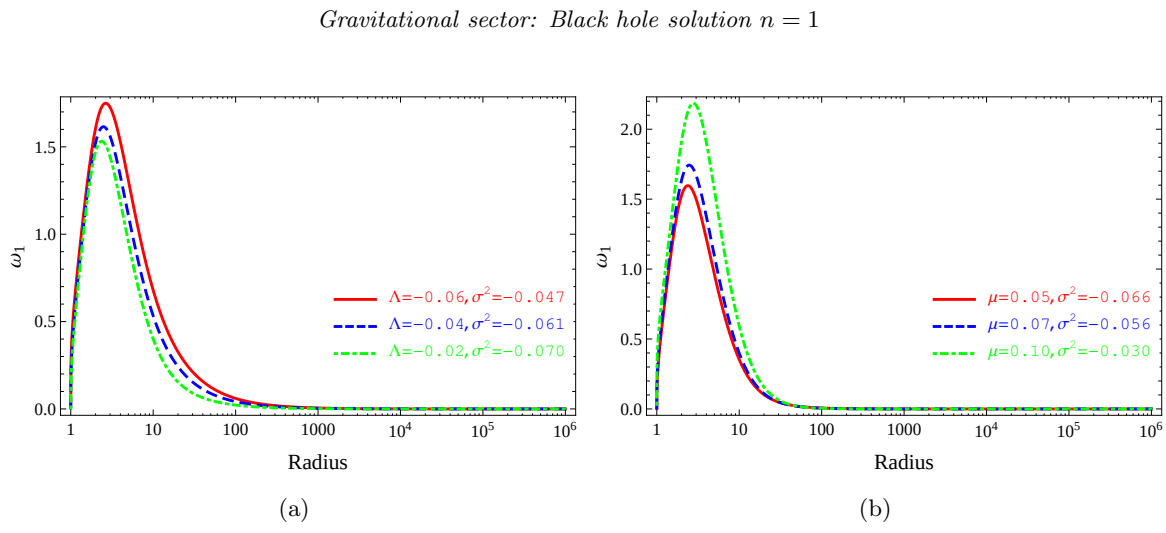

Figure 3.23: Nodeless eigenfunctions ω_1 for $n = 1$ black hole solutions, (a) fixed $\mu = 0.03$ and varying Λ, (b) fixed $\Lambda = -0.01$ and varying μ.

Gravitational sector: Black hole solution quasi$-n = 1$

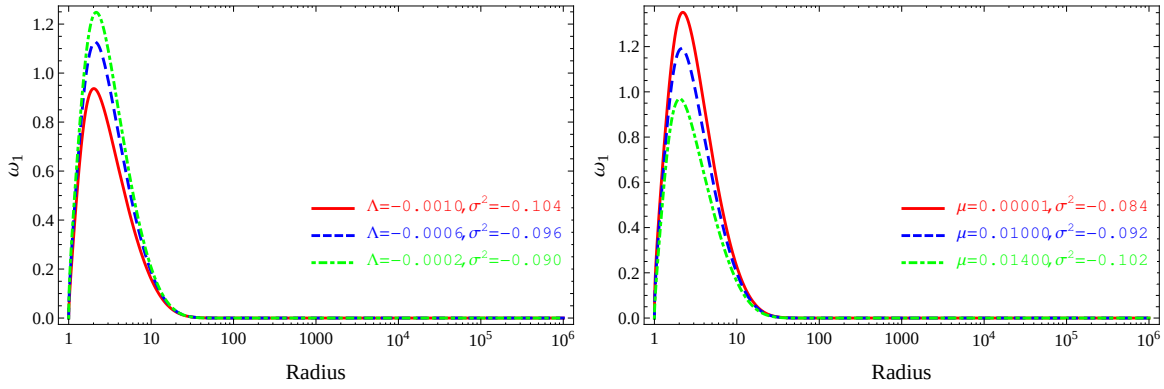

(a) (b)

Figure 3.24: Nodeless eigenfunctions ω_1 for quasi$-n = 1$ black hole solutions, (a) fixed $\mu = 0.01$ and varying Λ, (b) fixed $\Lambda = -0.0004$ and varying μ.

3.7.3 Sphaleronic sector

Instead of dealing with a single equation as in the gravitational sector, we now have four equations (3.69–3.71) and (3.73) considered to be in the sphaleronic sector. In fact equation (3.73) is a consequence of the other three. Therefore only the first three equations (3.69–3.71) need to be considered for the stability analysis.

First we need to put these equations into a more manageable form. We introduce the following quantities $(\psi, \gamma, \xi, \eta)$

$$a_1' - \dot{b}_1 \equiv \psi, \qquad a_1 + \dot{\gamma} \equiv \xi, \qquad b_1 + \gamma' \equiv \eta, \qquad d_1 \equiv \omega_0 \gamma. \tag{3.89}$$

Under the gauge transformation (3.17), d_1 transforms as

$$\begin{aligned} d_1 = \omega_0 \gamma &\to \omega_0 \gamma + \omega_0 \beta, \\ \therefore \gamma &\to \gamma + \beta. \end{aligned} \tag{3.90}$$

The other field variables ψ, ξ and η are unchanged by the gauge transformation (3.17). The perturbed field equations (3.69–3.71) can be rewritten in term of these new variables as

$$0 = -r^2 R_0 S_0 \psi' + r R_0 \left(r S_0' - 2 S_0\right) \psi - S_0 r^2 \mu^2 \dot{\gamma} + S_0 \left(r^2 \mu^2 + 2\omega_0^2\right) \xi, \tag{3.91}$$

$$0 = \frac{1}{R_0 S_0^2} \dot{\psi} - \left(\mu^2 + \frac{2\omega_0^2}{r^2}\right) \eta + \mu^2 \gamma', \tag{3.92}$$

$$0 = -\mu^2 \gamma - R_0 \omega_0 \eta' - \left(2 R_0 \omega_0' + \frac{\omega_0 (R_0 S_0)'}{S_0}\right) \eta + \frac{\omega_0}{R_0 S_0^2} \dot{\xi}. \tag{3.93}$$

By redefining $\psi \equiv \dot{\chi}$ and $\xi \equiv \dot{\Theta}$, then integrating with respect to time, we can rewrite (3.91) as

$$\mu^2 \gamma = \left(\mu^2 + \frac{2\omega_0^2}{r^2}\right) \Theta + R_0 \left(\frac{S_0'}{S_0} - \frac{2}{r}\right) \chi - R_0 \chi'. \tag{3.94}$$

Note that an arbitrary function of r has been set to zero in the above equation. We have freedom to add any arbitrary functions of r to χ and to Θ without changing the physical perturbations ψ and ξ. We then use the first freedom to eliminate an arbitrary function of r in (3.94). We remark that $\dot{\eta} = -\dot{\chi} + \dot{\Theta}'$. This implies that $\eta = -\chi + \Theta'$ where we use the second freedom to fix an arbitrary function of r in this expression. Equation (3.94) can be used to eliminate γ from the other two (3.92, 3.93), they now read

$$\begin{aligned} 0 = &-\frac{\ddot{\chi}}{R_0 S_0^2} + R_0 \chi'' + \left(R_0' + \frac{2R_0}{r} - \frac{R_0 S_0'}{S_0}\right) \chi' \\ &- \left(\mu^2 + \frac{2\omega_0^2}{r^2} + \frac{2R_0}{r^2} - \frac{2R_0'}{r} + \left(\frac{R_0 S_0'}{S_0}\right)'\right) \chi - \left(\frac{2\omega_0^2}{r^2}\right)' \Theta, \end{aligned} \tag{3.95}$$

$$\begin{aligned} 0 = &\frac{\ddot{\Theta}}{R_0 S_0^2} - R_0 \Theta'' - \left(\frac{(R_0 S_0)'}{S_0} + \frac{2R_0 \omega_0'}{\omega_0}\right) \Theta' - \left(\mu^2 + \frac{2\omega_0^2}{r^2}\right) \frac{\Theta}{\omega_0} + \frac{R_0 (1+\omega_0)}{\omega_0} \chi' \\ &+ \left(\frac{(R_0 S_0)'}{S_0} + \frac{2R_0 \omega_0'}{\omega_0} + \frac{2R_0}{r\omega_0} - \frac{R_0 S_0'}{\omega_0 S_0}\right) \chi. \end{aligned} \tag{3.96}$$

Next, periodic time dependent perturbations with frequency σ are introduced

$$\chi(t,r) = e^{-i\sigma t}\chi_1(r), \qquad \Theta(t,r) = e^{-i\sigma t}\Theta_1(r). \tag{3.97}$$

Therefore equations (3.95) and (3.96) become

$$\begin{aligned}\sigma^2\chi_1 = &-R_0^2S_0^2\chi_1'' - R_0S_0^2\left(\frac{2R_0}{r} + R_0' - \frac{R_0S_0'}{S_0}\right)\chi_1' + R_0S_0^2\left(\mu^2 + \frac{2\omega_0^2}{r^2} + \frac{2R_0}{r^2}\right.\\ &\left. - \frac{2R_0'}{r} + \left(\frac{R_0S_0'}{S_0}\right)'\right)\chi_1 + R_0S_0^2\left(\frac{2\omega_0^2}{r^2}\right)'\Theta_1, \end{aligned}\tag{3.98}$$

$$\begin{aligned}\sigma^2\Theta_1 = &-R_0^2S_0^2\Theta_1'' - R_0S_0\left(\frac{2R_0S_0\omega_0'}{\omega_0} + (R_0S_0)'\right)\Theta_1' - R_0S_0^2\left(\mu^2 + \frac{2\omega_0^2}{r^2}\right)\frac{\Theta_1}{\omega_0}\\ &+ \frac{R_0^2S_0^2(1+\omega_0)}{\omega_0}\chi_1' + R_0S_0^2\left(\frac{(R_0S_0)'}{S_0} + \frac{2R_0\omega_0'}{\omega_0} + \frac{2R_0}{r\omega_0} - \frac{R_0S_0'}{\omega_0S_0}\right)\chi_1. \end{aligned}\tag{3.99}$$

The system of perturbation equations has now been reduced to two equations (3.98, 3.99) for two unknown variables χ_1, Θ_1. We have a coupled system of linear second order differential equations. It turns out that we have not been able to put these two equations (3.98, 3.99) into self-adjoint form via a change of variables. Thus here in the sphaleronic sector, Sturm-Liouville theory cannot be applied to this case. This non-self-adjointness means that the analytical techniques used to obtain the connection between the number of unstable modes and the number of nodes of the static solutions (n) in EYM-flat theory [187] are no longer valid.

To proceed further, note that equation (3.99) will diverge when ω_0 has a zero. To avoid this difficulty, we redefine the field variable such that $\Theta_1 \equiv \frac{\tilde{\Theta}_1}{\omega_0}$. Equations (3.98) and

(3.99) are then given by

$$\sigma^2\chi_1 = -R_0^2S_0^2\chi_1'' - R_0S_0^2\left(\frac{2R_0}{r} + R_0' - \frac{R_0S_0'}{S_0}\right)\chi_1' + R_0S_0^2\left(\mu^2 + \frac{2\omega_0^2}{r^2} + \frac{2R_0}{r^2} - \frac{2R_0'}{r} + \left(\frac{R_0S_0'}{S_0}\right)'\right)\chi_1 + \omega_0 R_0S_0^2\left(\frac{2\omega_0^2}{r^2}\right)'\tilde{\Theta}_1, \tag{3.100}$$

$$\begin{aligned}\sigma^2\tilde{\Theta}_1 = &-R_0^2S_0^2\tilde{\Theta}_1'' - R_0S_0(R_0S_0)'\tilde{\Theta}_1' + R_0S_0^2\left(\mu^2 - \frac{1}{r^2} - \frac{2\omega_0}{r^2} + \frac{\omega_0^2}{r^2}\right)\tilde{\Theta}_1 \\ &+ R_0^2S_0^2(1+\omega_0)\chi_1' \\ &+ R_0S_0^2\left(\frac{(R_0S_0)'\,\omega_0}{S_0} + 2R_0\omega_0' + \frac{2R_0}{r} - \frac{R_0S_0'}{S_0}\right)\chi_1.\end{aligned} \tag{3.101}$$

These equations are now regular when ω_0 has a zero. By demanding that the field variables $\chi_1, \tilde{\Theta}_1$ must vanish at each end-point, we have the following boundary conditions for ENAP-AdS

$$\chi_1 \sim r^3, \qquad \tilde{\Theta}_1 \sim r^3, \qquad \text{for } r \to 0, \tag{3.102}$$

$$\chi_1 \sim (r-r_h)^\beta, \qquad \tilde{\Theta}_1 \sim (r-r_h)^\beta, \qquad \text{for } r \to r_h, \tag{3.103}$$

$$\chi_1 \sim r^\rho, \qquad \tilde{\Theta}_1 \sim r^\rho, \qquad \text{for } r \to \infty. \tag{3.104}$$

The constants β and ρ are defined in the same way as (3.88). Note that the behaviour at $r \to r_h$ and $r \to \infty$ of the sphaleronic sector perturbations is the same as those in the gravitational sector. However, at the origin, they behave differently. We need to numerically integrate equations (3.100, 3.101), aiming for an eigenvalue σ^2 and eigenfunctions which satisfy these boundary conditions.

Here in the sphaleronic sector, we consider only the quasi$-n = 0$ branch of black hole solutions since we have already presented numerical evidence that the other branches of solutions are unstable. Fig 3.25 shows two unstable modes, i.e., $N = 2$ and $N = 1$ eigenfunctions, for the quasi$-n = 0$ black hole solution with Proca mass $\mu = 0.03$ and cosmological constant $\Lambda = -0.075$. It can be clearly seen that both χ_1 and $\tilde{\Theta}_1$ vanish at

the horizon and infinity, as expected. In addition a small window is given in Fig 3.25(b) to show that both matter perturbations in this case have one zero ($N = 1$). These results clearly demonstrate that this particular black hole solution is unstable since $\sigma^2 < 0$.

More results on the instability of quasi$-n = 0$ black holes for various fixed values of μ and Λ are displayed in Fig 3.26 and Fig 3.27. In the former figure, two unstable eigenfunctions $N = 2$ Fig 3.26(a) and $N = 1$ Fig 3.26(b) are plotted for black hole solutions with fixed Proca mass $\mu = 0.03$ and varying Λ. Note that in Fig 3.26(b), the perturbation fields χ_1 and $\tilde{\Theta}_1$ have been re-scaled by factors of 10^{-1} and 10^{-4} when $\Lambda = -0.04$ and $\Lambda = -0.02$ respectively. This can be done, since the perturbation equations (3.100, 3.101) are linear in χ_1 and $\tilde{\Theta}_1$. In Fig 3.27, on the other hand, we show the instability of black hole solutions for fixed cosmological constant $\Lambda = -0.01$ and varying mass μ. In this case, only $N = 2$ perturbation modes are found by our numerical codes.

Some general behaviour can be observed from the perturbation plots in the sphaleronic sector. First, $\tilde{\Theta}_1$ is generally larger in magnitude than χ_1. Second, perturbations vary more with changing Λ or μ than in the gravitational sector. Furthermore, changing Λ or μ affects $\tilde{\Theta}_1$ more than χ_1. Finally, we remark that all quasi$-n = 0$ solutions investigated here are linearly unstable since all the σ^2 discovered have negative values.

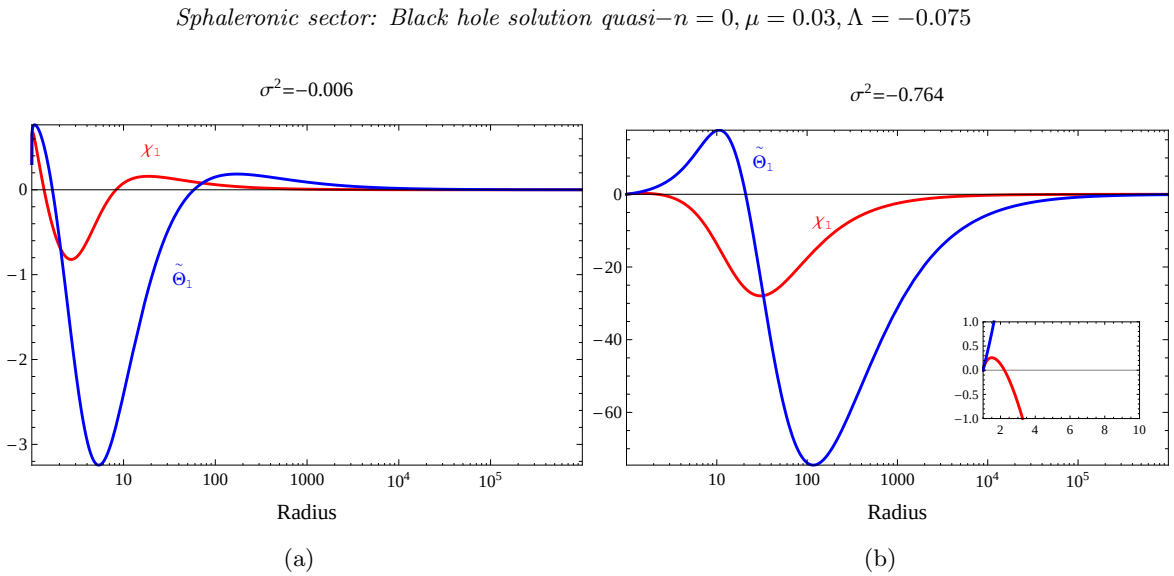

Figure 3.25: $N = 2$ and $N = 1$ perturbation modes with $\sigma^2 = -0.006, -0.746$, respectively for a quasi$-n = 0$ black hole solution with $\mu = 0.03, \Lambda = -0.075$. A subplot in the right-hand figure shows the behaviour of the perturbation variables near the black hole horizon. Note that χ_1 and $\tilde{\Theta}_1$ are denoted by red and blue colours respectively.

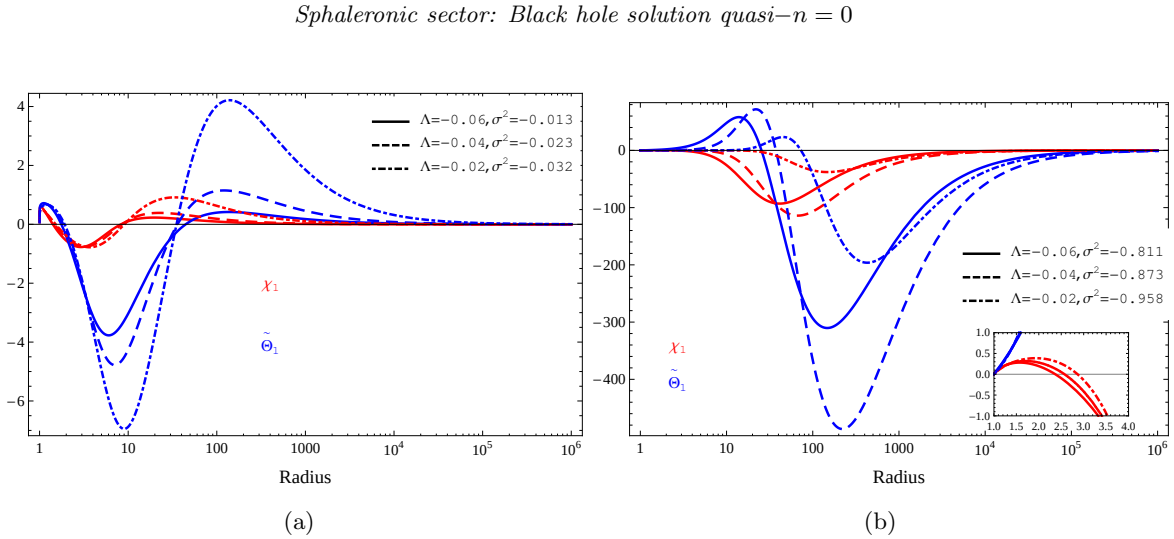

Figure 3.26: Two unstable modes (a) $N = 2$ and (b) $N = 1$ of quasi$-n = 0$ black hole solutions for fixed $\mu = 0.03$ and varying Λ. A subplot in the right-hand figure shows the behaviour of the perturbation variables near the black hole horizon. Note that χ_1 and $\tilde{\Theta}_1$ are denoted by red and blue colours respectively.

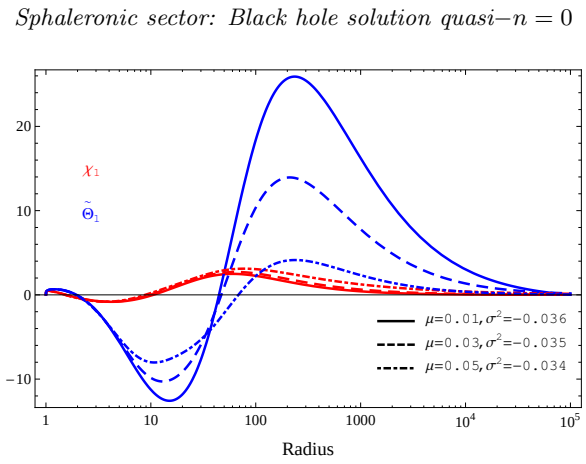

Figure 3.27: $N = 2$ eigenfunctions of quasi$-n = 0$ black hole solutions for fixed $\Lambda = -0.01$ and varying μ. Note that χ_1 and $\tilde{\Theta}_1$ are denoted by red and blue colours respectively.

Combining these instability results for quasi$-n = 0$ black hole solutions in the sphaleronic sector and the results for regular and black hole solutions in the gravitational sector in subsection 3.7.2, we conclude that spherically symmetric regular and black hole solutions of $SU(2)$ ENAP in asymptotically AdS are unstable against linear, spherically symmetric perturbations.

§3.8 Summary

In this chapter, $SU(2)$ Einstein-non-Abelian-Proca theory in asymptotically AdS spacetime was considered. This configuration reduces to EYM theory in AdS spacetime if the Proca mass $\mu = 0$ and goes to ENAP in asymptotically flat spacetime if $\Lambda = 0$. We presented new spherically symmetric regular and black hole solutions of the ENAP-AdS equations. We also presented examples of regular and black hole solutions of the ENAP-flat equations [79] as well. These solutions are found numerically by using the standard one-parameter shooting method. The solutions are classified by the number of zeroes of ω. The restriction due to the boundary conditions for regular solutions rules out the gauge field function odd-node solutions. This property has also been observed in asymptotically flat regular solutions [79]. In addition, we find that the hairy black holes with non-zero Λ

violate the generalized no-hair conjecture [197]. This is because these new hairy black hole solutions are not distinguishable from the Schwarzschild-AdS black hole when observed at infinity.

In section 3.6, we also provided an analytic proof that confirmed the non-existence of dyonic solutions of the ENAP theory. Our result holds for asymptotically flat and asymptotically AdS spacetimes. In section 3.7 we discussed the methodology for finding an instability of solitons and black hole solutions in the ENAP-AdS theory. We found that the solutions investigated numerically are linearly unstable against small perturbations in either the gravitational or sphaleronic sector. Moreover, for the asymptotically flat analogues, both regular and black hole solutions were shown to be unstable. This confirms the statement made in [79] where they expected the solutions of the ENAP-flat equations to be unstable.

Despite the fact that our solutions violate the generalized no-hair conjecture, however, one might suggest that the no-hair conjecture still holds since these solutions are unstable, so they are physically irrelevant. If one consider Bizon's no-hair conjecture [25] where the stability of solutions is taken into account, these solutions found in ENAP-AdS theory are irrelevant since they are not stable.

To conclude, a number of self-gravitating solutions involving non-Abelian gauge fields have been found in the literature. However, most of them are unstable, including solutions in EYM-flat, ENAP-flat/AdS (as illustrated in this chapter) and EYMH-flat/AdS theories. On the other hand, only EYM in asymptotically AdS seems to have stable solutions [194]. Moreover, EYM-AdS black holes also possess non-trivial global charges at infinity. In addition, these charges characterize stable solutions [159]. Thus, these stable solutions support the generalized no-hair conjecture.

Chapter 4

Einstein-charged-scalar theory in a cavity

§4.1 Introduction

It was shown in section 2.6.1 that a massless complex scalar field on a Reissner-Nordström background with a reflecting boundary experiences a superradiant instability. However, the final fate of the charged superradiant instability remains unknown. This chapter will be devoted to answering this open question. Our main goal is to explore possible end-points of the charged superradiant instability with a mirror-like boundary.

We start by considering a self-gravitating system consisting of a massless charged scalar field and an electromagnetic field in a cavity. Four coupled field equations of the Einstein-Maxwell-Klein-Gordon (EMKG) action are derived in section 4.3. We find the corresponding boundary conditions near the origin (for solitons), the event horizon (for black holes) and at the mirror. By performing a fully numerical integration of these field equations, static spherically symmetric solitons and hairy black holes are obtained. These numerical solutions are not asymptotically flat because we impose a mirror-like boundary condition at some radius. In fact, we provide an analytic proof in subsection 4.3.3 that an

asymptotically flat solution of the EMKG system is either Minkowski spacetime or a bald Reissner-Nordström black hole. In section 4.4, we present numerical results for solitons and hairy black holes. By demanding that the scalar field must vanish at the location of the mirror, we obtain soliton/black hole-in-a-cavity solutions. For the majority of this work, the mirror will be located at the first zero of the equilibrium scalar field.

To confirm that these solutions can be possible end-points of the charged superradiant instability, we investigate the stability of the equilibrium solutions in section 4.5. All the field variables including the metric functions now become time-dependent, and all the field equations are re-derived. By assuming spherically symmetric metric, scalar and electric potential perturbations, in subsection 4.5.2 we derive dynamical equations to first order in the perturbations. We find that the metric perturbations can be expressed in terms of the matter perturbations (scalar field and electric potential). We make use of this to obtain two dynamical equations and one constraint equation which govern the evolution of the linear perturbations. Time-periodic and ingoing boundary conditions are assumed for solitons and hairy black holes respectively where in both cases the scalar perturbations are required to vanish at the mirror. Three master equations together with these boundary conditions form an eigenvalue problem. This eigenvalue problem is then solved by the numerical shooting method (see details in Appendix A). The numerical analysis of the stability of the solitons and hairy black holes is discussed in subsections 4.5.4 and 4.5.7 respectively. By working in the frequency domain, our numerical results reveal the following. Firstly, when the mirror is fixed at the first node of the equilibrium scalar field, we find both stable and unstable soliton solutions. The stability depends on the free parameters in the theory. Secondly, for the black hole solutions we have considered in this work, we find no evidence which suggests that these black holes are unstable when the mirror is located at the first node of the scalar field. In contrast, when the mirror is fixed at the second node, unstable modes are found.

Most of this chapter is based on the following works [140] for solitons and [61] for black

holes.

§4.2 Basic equations

We consider a fully coupled system consisting of gravity, an electromagnetic field and a massless complex scalar field. The action is described by

$$S = \int \sqrt{-g} \left[\frac{\mathcal{R}}{2} - \frac{1}{4} F_{ab} F^{ab} - \frac{1}{2} g^{ab} D^*_{(a} \Phi^* D_{b)} \Phi \right] d^4x, \tag{4.1}$$

where $\mathcal{R}$ is the Ricci scalar. The Faraday tensor and gauge covariant derivative are given by

$$F_{ab} = \nabla_a A_b - \nabla_b A_a, \tag{4.2}$$

$$D_a = \nabla_a - iqA_a, \tag{4.3}$$

with ∇_a is standard covariant derivative, A_a is the electromagnetic vector potential and q is the charge of the scalar field Φ. Round brackets denote symmetrization, $X_{(ab)} = \frac{1}{2}(X_{ab} + X_{ba})$.

Varying the action (4.1), the Einstein equations, Maxwell equations and Klein-Gordon equations are obtained

$$G_{ab} = T^F_{ab} + T^\Phi_{ab}, \tag{4.4}$$

$$\nabla_a F^{ab} = J^b, \tag{4.5}$$

$$D_a D^a \Phi = 0, \tag{4.6}$$

where the energy momentum tensor of electromagnetic field, scalar field, and the field

current J^a are defined by, respectively

$$T^F_{ab} = F_{ac}F_b{}^c - \frac{1}{4}g_{ab}F_{cd}F^{cd}, \tag{4.7}$$

$$T^\Phi_{ab} = D^*_{(a}\Phi^* D_{b)}\Phi - \frac{1}{2}g_{ab}\left[g^{cd}D^*_{(c}\Phi^* D_{d)}\Phi\right], \tag{4.8}$$

$$J^a = \frac{iq}{2}\left[\Phi^* D^a\Phi - \Phi(D^a\Phi)^*\right]. \tag{4.9}$$

The asterisk $*$ denotes complex conjugate. We note that the energy momentum tensor defined above is covariantly conserved, i.e. $\nabla_a T^{ab}$, since the Einstein tensor is divergence-free. Moreover one can see that the current J^a is also conserved, by considering

$$\begin{aligned}
2\nabla_b\nabla_a F^{ab} = \nabla_b\nabla_a F^{ab} - \nabla_a\nabla_b F^{ab} &= g^{ac}g^{bd}\left(\nabla_b\nabla_a F_{cd} - \nabla_a\nabla_b F_{cd}\right), \\
&= g^{ac}g^{bd}\left(F_{fd}R^f{}_{cab} + F_{cf}R^f{}_{dab}\right), \\
&= g^{ac}F^{fb}R_{fcab} + g^{bd}F^{af}R_{fdab}, \\
&= -g^{ac}F^{fb}R_{abcf} + g^{bd}F^{af}R_{badf}, \\
&= -F^{fb}R_{bf} + F^{af}R_{af}, \\
&= 0,
\end{aligned} \tag{4.10}$$

where the contraction between a symmetric and an anti-symmetric tensor yields zero. The Ricci tensor is defined by $R_{ab} = R^c{}_{acb}$. This simple proof shows that $\nabla_b\nabla_a F^{ab} = 0$. Therefore the Maxwell equation (4.5) implies that $\nabla_b J^b = 0$.

The action (4.1) is invariant under a $U(1)$ gauge transformation. Both the scalar field Φ and gauge potential A_a are defined up to the gauge freedom

$$\Phi \to e^{i\chi}\Phi, \qquad A_a \to A_a + q^{-1}\chi_{,a}, \tag{4.11}$$

where χ is any (real) scalar field. This freedom will be used later when we consider static equilibrium solutions and time-dependent, spherically symmetric perturbations.

§4.3 Field equations and boundary conditions

4.3.1 Field equations

We now consider static spherically symmetric spacetimes defined by

$$ds^2 = -fh\,dt^2 + f^{-1}dr^2 + r^2(d\theta^2 + \sin^2\theta\; d\varphi^2), \tag{4.12}$$

where $f = f(r)$ and $h = h(r)$. The metric function f can be written as

$$f(r) \equiv 1 - \frac{2m(r)}{r}, \tag{4.13}$$

where $m(r)$ can be interpreted as a total mass within the given radius r (see also the discussion in subsection 4.5.5). The scalar field is assumed to be real, thus we may write $\Phi = \phi(r)$ for a static equilibrium solution. Since the spacetime is spherically symmetric, A_θ and A_φ can be set to zero. We also fix $A_r = 0$ by using the gauge freedom defined in (4.11). Therefore, the gauge potential is given by

$$A_a = [A_0(r), 0, 0, 0]. \tag{4.14}$$

Instead of using the standard Einstein field equations (4.4), we could instead consider in the trace-reversed version which is given by

$$R_{ab} = \tilde{T}^F_{ab} + \tilde{T}^\Phi_{ab}, \tag{4.15}$$

where $\tilde{T}_{ab} = T_{ab} - \frac{1}{2}g_{ab}T$ and $T = g_{ab}T^{ab} = T^a{}_a$. Here we give the relevant components of the Ricci tensor:

$$\begin{aligned}
R_{00} &= \frac{f}{2}\left(hf'' + fh'' + \frac{3}{2}f'h' - \frac{f(h')^2}{2h} + \frac{2hf'}{r} + \frac{2fh'}{r}\right), \\
R_{11} &= -\frac{1}{2fh}\left(hf'' + fh'' + \frac{3}{2}f'h' - \frac{f(h')^2}{2h} + \frac{2hf'}{r}\right), \\
R_{22} &= -\frac{r}{h}\left(f'h + \frac{1}{2}fh' + \frac{h}{r}(f-1)\right),
\end{aligned} \tag{4.16}$$

and the trace-reversed energy-momentum tensor $\tilde{T}_{ab}$:

$$\begin{aligned}
\tilde{T}^F_{00} &= \frac{1}{2}fE^2, & \tilde{T}^\Phi_{00} &= q^2A_0^2\phi^2, \\
\tilde{T}^F_{11} &= -\frac{1}{2fh}E^2, & \tilde{T}^\Phi_{11} &= (\phi')^2, \\
\tilde{T}^F_{22} &= \frac{r^2E^2}{2h}, & \tilde{T}^\Phi_{22} &= 0.
\end{aligned} \tag{4.17}$$

where a prime $'$ denotes d/dr and $E^2 = (A_0')^2$. The spherical symmetry of the metric (4.12) implies that $R_{33} = \sin^2\theta R_{22}$ and the same holds for the corresponding components of the stress tensor. We can obtain a first order equation in h by considering $f^{-2}R_{00} + hR_{11}$. Also, R_{22} gives a first order equation in f. Therefore, we obtain four static field equations

$$h' = r\left[\left(\frac{qA_0\phi}{f}\right)^2 + h(\phi')^2\right], \tag{4.18}$$

$$E^2 = -\frac{2}{r}\left[f'h + \frac{1}{2}fh' + \frac{h}{r}(f-1)\right], \tag{4.19}$$

$$0 = fA_0'' + \left(\frac{2f}{r} - \frac{fh'}{2h}\right)A_0' - q^2\phi^2A_0, \tag{4.20}$$

$$0 = f\phi'' + \left(\frac{2f}{r} + f' + \frac{fh'}{2h}\right)\phi' + \frac{(qA_0)^2}{fh}\phi, \tag{4.21}$$

We remark that the first two equations (4.18, 4.19) are the results of trace-reversed Einstein field equations (4.15). In addition, we find that the $rr-$component of (4.15), which gives a second order equation in f, is merely a consequence of the other components of the

Einstein field equations (4.15), hence it is redundant. The only non-vanishing component of the Maxwell equations (4.5) is shown in (4.20) and the Klein-Gordon equation (4.6) is given by (4.21). If the scalar field vanishes identically $\phi \equiv 0$, the only static spherically symmetric solution representing a black hole solution of these equations is the Reissner-Nordström metric. This can be seen by setting

$$f = 1 - \frac{2M}{r} + \frac{Q^2}{r^2}, \qquad h = 1, \qquad A_0 = -\frac{Q}{r}, \tag{4.22}$$

where M and Q are total mass and electric charge respectively. See subsection 4.3.3 for more a detailed analysis of this.

The equilibrium field equations (4.18–4.21) possess two scaling symmetries. First we shall consider the length scaling symmetry. We define two new variables R and $\tilde{Q}$ by

$$r = LR, \qquad q = L^{-1}\tilde{Q}, \tag{4.23}$$

where L is an arbitrary length scale. This transformation leaves f, h, A_0 and ϕ unchanged. Under this re-scaling, the static equations (4.18–4.21) become

$$\begin{aligned}
\frac{dh}{dR} &= R\left[\left(\frac{\tilde{Q}A_0\phi}{f}\right)^2 + h\left(\frac{d\phi}{dR}\right)^2\right], \\
\left(\frac{dA_0}{dR}\right)^2 &= -\frac{2}{R}\left[\frac{df}{dR}h + \frac{1}{2}f\frac{dh}{dR} + \frac{h}{R}(f-1)\right], \\
0 &= f\frac{d^2A_0}{dR^2} + \left(\frac{2f}{R} - \frac{f}{2h}\frac{dh}{dR}\right)\frac{dA_0}{dR} - \tilde{Q}^2\phi^2A_0, \\
0 &= f\frac{d^2\phi}{dR^2} + \left(\frac{2f}{R} + \frac{df}{dR} + \frac{f}{2h}\frac{dh}{dR}\right)\frac{d\phi}{dR} + \frac{(\tilde{Q}A_0)^2}{fh}\phi.
\end{aligned} \tag{4.24}$$

We see that the field equations (4.18–4.21) are invariant under the transformation (4.23). In addition, a time scaling symmetry can be seen by introducing new variables H and $\mathcal{A}_0$

by

$$h = T^{-2}H, \qquad A_0 = T^{-1}\mathcal{A}_0, \tag{4.25}$$

where T is an arbitrary time scaling for which f, ϕ and q remain the same. Inserting (4.25) into the equilibrium field equations (4.18–4.21) gives the following

$$\begin{aligned}
H' &= r\left[\left(\frac{q\mathcal{A}_0\phi}{f}\right)^2 + H(\phi')^2\right], \\
\left(\mathcal{A}_0'\right)^2 &= -\frac{2}{r}\left[f'H + \frac{1}{2}fH' + \frac{H}{r}(f-1)\right], \\
0 &= f\mathcal{A}_0'' + \left(\frac{2f}{r} - \frac{fH'}{2H}\right)\mathcal{A}_0' - q^2\phi^2\mathcal{A}_0, \\
0 &= f\phi'' + \left(\frac{2f}{r} + f' + \frac{fH'}{2H}\right)\phi' + \frac{(q\mathcal{A}_0)^2}{fH}\phi,
\end{aligned} \tag{4.26}$$

which are identical to the static equations (4.18–4.21). These scaling symmetries will become useful when the boundary conditions corresponding to solitons and black holes are discussed.

4.3.2 Boundary conditions

With a non-zero scalar field, equations (4.18–4.21) cannot be solved analytically. As will be seen later, however, these equations are solvable by a numerical method. To construct solutions representing solitons and black holes, boundary conditions on the field variables m, h, A_0, ϕ at the origin, event horizon and mirror are required.

Origin: We assume that all field variables and all physical quantities (electric field strength, curvature etc.) are regular. With these assumptions, regular Taylor series expansions of

the field variables for small r are given by

$$\begin{aligned} m(r) &= m_0 + m_1 r + m_2 r^2 + m_3 r^3 + O(r^4), \\ h(r) &= h_0 + h_1 r + h_2 r^2 + O(r^3), \\ A_0(r) &= a_0 + a_1 r + a_2 r^2 + O(r^3), \\ \phi(r) &= \phi_0 + \phi_1 r + \phi_2 r^2 + O(r^3). \end{aligned} \tag{4.27}$$

The constant m_0 must be zero otherwise the metric function f (4.13) will diverge at the origin. The regularity of the Ricci scalar $\mathcal{R}$ at $r = 0$ requires that $m_1 = m_2 = 0$. In addition, equations (4.18, 4.20, 4.21) imply that h_1, a_1 and ϕ_1 are all zero respectively. All remaining undetermined parameters are specified by inserting the series expansions (4.27) into the field equations (4.18–4.21). We thus obtain

$$\begin{aligned} m &= \left(\frac{q^2\phi_0^2 a_0^2}{12 h_0}\right) r^3 + O(r^4), \\ h &= h_0 + \left(\frac{q^2\phi_0^2 a_0^2}{2}\right) r^2 + O(r^3), \\ A_0 &= a_0 + \left(\frac{a_0 q^2 \phi_0^2}{6}\right) r^2 + O(r^3), \\ \phi &= \phi_0 - \left(\frac{\phi_0 q^2 a_0^2}{6 h_0}\right) r^2 + O(r^3), \end{aligned} \tag{4.28}$$

where h_0, a_0 and ϕ_0 are arbitrary constants. The only restriction is $h_0 > 0$, to preserve the signature of the metric (4.12). Normally $h(r) \to 1$ as $r \to \infty$ in an asymptotically flat spacetime, however our solutions are not asymptotically flat. Therefore, we make use of the time scaling symmetry (4.25) to set $h_0 = 1$ without loss of generality. This leaves a_0 and ϕ_0 as two free parameters.

Event horizon: We assume that there is a regular event horizon defined by $f(r_h) = 0$ and $f'(r_h) > 0$. This means $m(r_h) \equiv m_h = \frac{r_h}{2}$. To avoid a singularity in the field equations at $r = r_h$, we must set $A_0(r_h) = 0$. Moreover we can set $h(r_h) = 1$, without loss of generality,

since this is equivalent to re-scaling the time coordinate t (4.25). Equation (4.21) implies that $\phi'(r_h) = 0$. Therefore Taylor series expansions of the field variables around $r = r_h$ are given by

$$\begin{aligned} m &= m_h + m'_h(r - r_h) + O(r - r_h)^2, \\ h &= 1 + h'_h(r - r_h) + O(r - r_h)^2, \\ A_0 &= E_h(r - r_h) + \frac{A''_h}{2}(r - r_h)^2 + O(r - r_h)^3, \\ \phi &= \phi_h + \frac{\phi''_h}{2}(r - r_h)^2 + O(r - r_h)^3, \end{aligned} \tag{4.29}$$

where $E_h = A'_0(r_h)$ is the electric field on the horizon. By substituting these expansions back into the field equations (4.18–4.21) we obtain

$$\begin{aligned} m'_h &= \frac{r_h^2 E_h^2}{4}, \\ h'_h &= \frac{4q^2 r_h^3 \phi_h^2 E_h^2}{\left(r_h^2 E_h^2 - 2\right)^2}, \\ A''_h &= \frac{2E_h}{r_h}\left[\frac{2q^2 r_h^2 \phi_h^2}{(r_h^2 E_h^2 - 2)^2} - 1\right], \\ \phi''_h &= -\frac{2\phi_h q^2 r_h^2 E_h^2}{(r_h^2 E_h^2 - 2)^2}. \end{aligned} \tag{4.30}$$

The boundary conditions at the horizon are determined by the four parameters r_h, q, E_h and ϕ_h.

Mirror: At the mirror's location $r = r_m$, we only require that the scalar field vanishes

$$\phi(r_m) = 0. \tag{4.31}$$

There is no constraint on the rest of the field variables f, h and A_0 at the location of the mirror, except that they must be finite. With the condition (4.31), one ensures that the electromagnetic current J^a (4.9) is zero at the mirror, so this is the appropriate reflection

condition.

4.3.3 Non-existence of asymptotically flat solutions

In this subsection, we provide an analytic proof that asymptotically flat, static spherically symmetric solitons and hairy black holes do not exist in Einstein-Maxwell-Klein-Gordon theory. The results of [14] do rule out non-trivial asymptotically flat black holes in EMKG theory. We note that the generalization of Bekenstein's result [14] was done later in [124]. By focusing on a spherically symmetric configuration, here we mainly follow the method of [14] and show that it can be extended to rule out both solitons and black holes.

We begin by assuming that both the electric potential A_0 and the scalar field ϕ are not identically zero. Later in this subsection, we will consider the case where one of A_0, ϕ (but not both) vanish identically. We mention that if $A_0 \equiv 0$ and $\phi \equiv 0$, then the only static spherically symmetric solution is either Minkowski or Schwarzschild.

By multiplying the static scalar field equation (4.21) by the factor $-r^2\phi\sqrt{h}$, we can integrate from $r = 0, r_h$ to $r = \infty$, where the lower limits $r = 0, r_h$ are relevant for the soliton and black hole cases respectively. We find

$$\begin{aligned} 0 &= \int_{0,r_h}^{\infty} \left[-\phi \frac{d}{dr}\left(r^2 f \sqrt{h} \phi' \right) - \frac{(q r A_0 \phi)^2}{f\sqrt{h}} \right] dr \\ &= \left[-r^2 f \sqrt{h} \phi \phi' \right]_{0,r_h}^{\infty} + \int_{0,r_h}^{\infty} \left[r^2 f \sqrt{h} \phi'^2 - \frac{(q r A_0 \phi)^2}{f\sqrt{h}} \right] dr, \end{aligned} \tag{4.32}$$

where we have used integration by parts. By multiplying the electromagnetic field equation (4.20) by the factor $-\frac{r^2 A_0}{f\sqrt{h}}$, and integrating from $r = 0, r_h$ to $r = \infty$, we find

$$\begin{aligned} 0 &= \int_{0,r_h}^{\infty} \left[-A_0 \frac{d}{dr}\left(\frac{r^2 A_0'}{\sqrt{h}} \right) + \frac{(q r A_0 \phi)^2}{f\sqrt{h}} \right] dr \\ &= \left[-\frac{r^2}{\sqrt{h}} A_0 A_0' \right]_{0,r_h}^{\infty} + \int_{0,r_h}^{\infty} \left[\frac{r^2 A_0'^2}{\sqrt{h}} + \frac{(q r A_0 \phi)^2}{f\sqrt{h}} \right] dr. \end{aligned} \tag{4.33}$$

Once again, we have applied integration by parts. The field variables f, h, ϕ and ϕ' must

be finite at the origin and also h is non-zero at the origin. The metric function f and the electric gauge potential A_0 vanish at the horizon $r = r_h$. Therefore, there is no contribution to the boundary terms in (4.32, 4.33) when $r = 0$ and $r = r_h$.

Our spacetime must approach the Minkowski metric as $r \to \infty$ (if an asymptotically flat solution exists). Therefore, we require the metric functions f and h to behave like

$$f = 1 + O(r^{-\rho}), \qquad h = 1 + O(r^{-\rho}), \tag{4.34}$$

as $r \to \infty$, where $\rho > 0$. The notation $O(r^{-\rho})$ used above refers to the largest subleading term in *one* of f or h. We do not assume that this is the largest non-unity term in *both* f and h. Thus, it is possible that in (4.34), one (but not both) of the $O(r^{-\rho})$ terms should be $o(r^{-\rho})$. To prevent the confusion that might occur, we will use the notation $O(r^{-\tilde{\rho}})$ for some $\tilde{\rho}$ where this means "no larger than $r^{-\tilde{\rho}}$ as $r \to \infty$".

We now consider the behaviour of the components of the Ricci tensor as $r \to \infty$. By using (4.34), we find that the components of the Ricci tensor (4.16) behave like

$$R_{tt} \sim O(r^{-\rho-2}), \quad R_{rr} \sim O(r^{-\rho-2}), \quad R_{\theta\theta} \sim O(r^{-\rho}), \tag{4.35}$$

as $r \to \infty$. By the Einstein field equations (4.15), we require that each component of the trace-reversed stress tensor (4.17) must behave in the same way as the corresponding Ricci tensor component (4.35) as $r \to \infty$. Therefore the $\theta\theta-$component (4.17) immediately implies that $A_0' \sim O(r^{-1-\rho/2})$. The tt and the rr components then give $A_0\phi \sim O(r^{-1-\rho/2})$ and $\phi' \sim O(r^{-1-\rho/2})$, respectively. Using these results, the field equations (4.20, 4.21) give $A_0 \sim O(r^{-1})$ and $\phi \sim O(r^{-1})$. From the behaviour of A_0, ϕ and their derivatives, we conclude that $A_0, \phi \sim O(r^{-\tilde{\rho}})$ as $r \to \infty$, where $\tilde{\rho} = \max\{1, \rho/2\}$. The behaviour of these quantities at infinity is the same for solitons and black holes. Thus we conclude that there is no contribution to the boundary term from the $r \to \infty$ limit in (4.32, 4.33) for both solitons and black holes. This leaves only the integral terms in equations (4.32, 4.33).

Now we consider the RHS of (4.33). Since this is the sum of two positive terms, the only possibility that this sum can yield zero is if both terms vanish identically. Therefore we have $A_0' \equiv 0$ and $A_0\phi \equiv 0$ for all values of r. These identities imply that A_0 is a constant everywhere and either A_0 or ϕ is zero. Furthermore, if we apply $A_0\phi \equiv 0$, there is only one positive term left on the RHS of (4.32). This means $\phi' \equiv 0$ for all $r \in [0, \infty)$ in the soliton case and for all $r \in [r_h, \infty)$ for the black hole case. Hence from this analysis, the electric gauge potential A_0 and scalar field ϕ are constant everywhere. From the statement discussed above A_0 and ϕ approach zero as $r \to \infty$. Thus they must both vanish identically.

Ultimately, we conclude that the only possible asymptotically flat, spherically symmetric soliton solution of the field equations (4.18–4.21) is the Minkowski metric with $f \equiv h \equiv 1$ and $A_0 \equiv \phi \equiv 0$. This should not be a surprise because the Einstein-Maxwell equations do not admit soliton solutions [90]. For the black hole case, one would expect to have the Schwarzschild metric when $A_0 \equiv \phi \equiv 0$.

We began our work in this part by assuming that the electric potential A_0 and scalar field ϕ were both not identically zero. Now we shall consider the special case where either $A_0 \equiv 0$ or $\phi \equiv 0$ (but not both). If we assume that $A_0 \equiv 0$, then (4.33) becomes trivial and (4.32) becomes

$$0 = \left[-r^2 f\sqrt{h}\phi\phi'\right]_{0,r_h}^{\infty} + \int_{0,r_h}^{\infty} r^2 f\sqrt{h}\phi'^2 dr. \tag{4.36}$$

Moreover the $tt-$ and $\theta\theta-$components of $\tilde{T}_{ab}$ (4.17) vanish identically. As $r \to \infty$, the $rr-$component however implies that $\phi' \sim O(r^{-1-\rho/2})$. Then we deduce that $\phi \sim \phi_\infty + O(r^{-\rho/2})$, where ϕ_∞ is a constant. Furthermore when $A_0 \equiv 0$, the field equations (4.18–4.21) depend on ϕ' not on ϕ. Therefore, we can set $\phi_\infty = 0$ without loss of generality. Hence the boundary term in (4.36) vanishes both at infinity and origin/horizon. This leaves us with only a positive integral term which that implies $\phi' \equiv 0$ and then $\phi \equiv 0$.

Here we can see that by setting $A_0 \equiv 0$, no non-trivial scalar field is allowed in this scenario. This is in agreement with the Bekenstein no-scalar-hair theorem [20].

On the other hand, suppose the scalar field vanishes identically $\phi \equiv 0$. In this case, (4.32) is trivial and (4.33) now becomes

$$0 = \left[-\frac{r^2}{\sqrt{h}} A_0 A_0'\right]_{0,r_h}^{\infty} + \int_{0,r_h}^{\infty} \frac{r^2 A_0'^2}{\sqrt{h}} dr. \tag{4.37}$$

The $\theta\theta-$component of the trace-reversed stress tensor implies that $A_0' \sim O(r^{-1-\rho/2})$ as $r \to \infty$, then $A_0 \sim A_{0,\infty} + O(r^{-\rho/2})$, where $A_{0,\infty}$ is a constant. Once again we can set $A_{0,\infty} = 0$ without loss of generality since the field equations (4.18–4.21) depend on A_0' and not A_0. The boundary term in (4.37) vanishes at the origin and infinity. Therefore for the solitons, we must have $A_0' \equiv 0$ and then $A_0 \equiv 0$. For the soliton case, the only asymptotically flat solution of the field equations (4.18–4.21) is the Minkowski metric. At the horizon, however, $A_0(r_h)$ does not necessarily equal zero anymore when $\phi \equiv 0$. Hence for the black holes, we must have

$$0 = \frac{r_h^2}{\sqrt{h(r_h)}} A_0(r_h) A_0'(r_h) + \int_{r_h}^{\infty} \frac{r^2 A_0'^2}{\sqrt{h}} dr. \tag{4.38}$$

This can be satisfied if $A_0(r_h)A_0'(r_h) < 0$. In the absence of a scalar field, our field equations (4.18–4.21) reduce to the Einstein-Maxwell equations and the only possible known black hole solution is the Reissner-Nordström metric. Setting $h = 1$ and $A_0 = -Q/r$, we can see that (4.38) is satisfied.

§4.4 Numerical solutions

To obtain non-trivial solitons and black holes, we numerically integrate the Einstein-Maxwell-Klein-Gordon (EMKG) equations (4.18–4.21). Since these equations are singular at the origin ($r = 0$) and event horizon $r = r_h$, we use the series expansions (4.28) and (4.29) as initial conditions, evaluated at $r = \epsilon$ and $r = r_h + \epsilon$ for solitons and black

holes respectively, where $\epsilon \sim 10^{-12}$. We implement a numerical shooting method which is suitable for this particular problem (see Appendix A for more details). The numerics become more difficult when r_m is large. This corresponds to small values of ϕ_0, a_0 for solitons and ϕ_h, E_h for black holes. Therefore, we will restrict our attention to the case where $r_m < 100$.

4.4.1 Solitons in a cavity

To explore soliton solutions of the EMKG equations, we first set $h_0 = 1$ (4.28) by using the time coordinate re-scaling (4.25). In addition, the scalar field charge q will be always set to 0.1 throughout the soliton case. This can be accomplished via the length scale symmetry (4.23). Note that, unlike black holes, solitons have no intrinsic length scale. Therefore soliton solutions are determined by only two free parameters, a_0 and ϕ_0, according to the series expansions (4.28).

In Fig 4.1, we display a typical soliton solution with fixed $q = 0.1, a_0 = 1.6$ and $\phi_0 = 0.7$ where the metric functions $f(r)$ and $h(r)$, time-component of the gauge potential $A_0(r)$ and scalar field $\phi(r)$ are plotted. As $r \to \infty$, the field variables $f(r), h(r)$ and $A_0(r)$ will not necessarily approach finite values. This is because, in this model, there is no soliton solution with a non-trivial scalar field in asymptotically flat spacetime (see subsection 4.3.3 for more details).

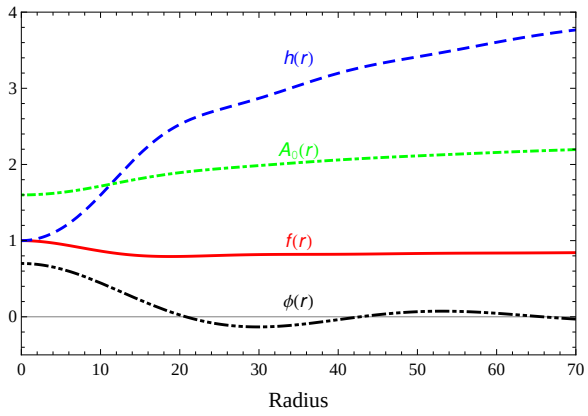

Figure 4.1: An example plot of the field variables f, h, A_0 and ϕ as functions of radius for a particular static soliton, with scalar field charge $q = 0.1, a_0 = 1.6$ and $\phi_0 = 0.7$.

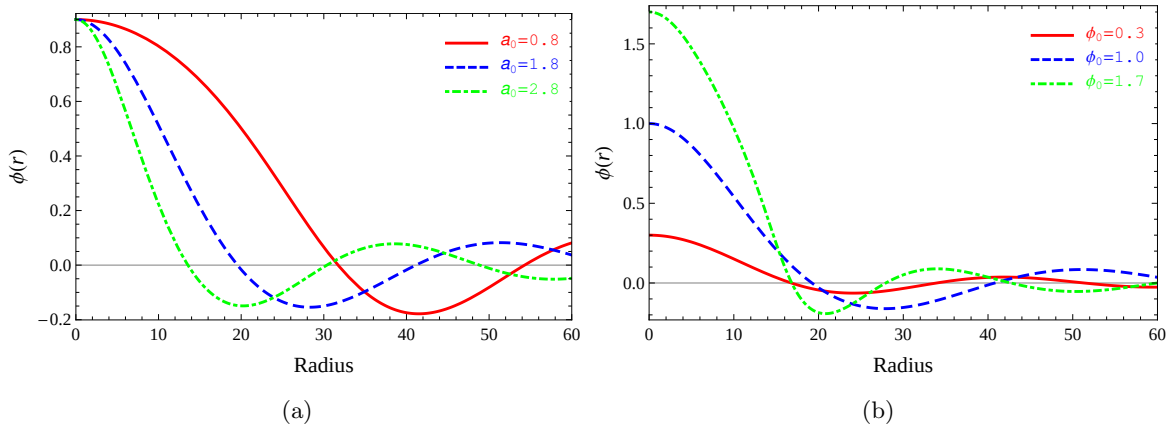

(a) (b)

Figure 4.2: Plots of solitons with a non-trivial charged scalar field. (a) Fixed $\phi_0 = 0.9$ and three different values of a_0. (b) Fixed $a_0 = 1.9$ and three different values of ϕ_0.

Fig 4.2 shows the scalar field profile for various soliton solutions. In Fig 4.2(a), three distinct scalar fields are plotted as a function of radius for fixed $\phi_0 = 0.9$. With fixed $a_0 = 1.9$, we show three distinct solitons with different values of ϕ_0 in Fig 4.2(b). We observe that for fixed ϕ_0 as a_0 increases the radius of the first node of scalar field also increases. The behaviour for fixed a_0, on the other hand, is not so obvious. It can be clearly seen from these plots that the scalar field $\phi(r)$ oscillates around zero. Therefore the mirror can be located at any of these zeros. In [61], it was found that hairy black

hole solutions of the EMKG equations are stable when the mirror is located at the first node of the static scalar field (this can be seen later in subsection 4.5.7). Therefore, for the solitons, we will focus our attention on the case that the mirror is at the first node of ϕ. From now on, r_m will refer to the radius of the first node of the scalar field where the reflecting boundary condition (4.31) is imposed.

Generally speaking, different soliton solutions will have distinct values of r_m. Nevertheless as shown in Fig 4.3, it is possible to find three (or more) separate solitons which share a common node. The left plot Fig 4.3(a) illustrates scalar field profiles for different values of a_0 and ϕ_0 representing different soliton solutions but still having a common location of their first zero, at $r_m \approx 18$. Similarly, three different scalar field profiles are displayed in Fig 4.3(b), where in this case, the first, second and third zeros are located at $r_m \approx 30$.

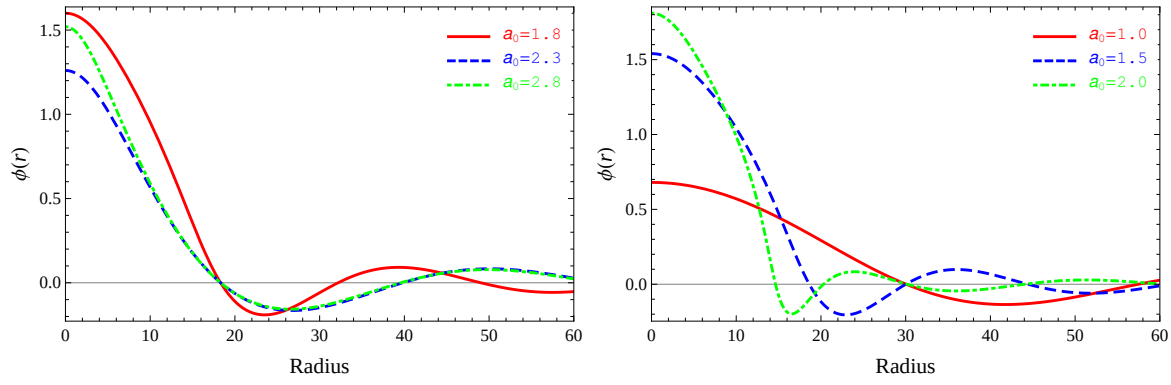

(a) (b)

Figure 4.3: Distinct scalar field profiles for static soliton solutions. (a) Three different solitons with the same location of their first node at $r_m \approx 18$. (b) Three different solitons with a common node, their first (red, solid), second (blue, dashed) and third (green, dot-dashed) nodes coincide at $r_m \approx 30$.

We display a numerical exploration of the soliton phase space with fixed $q = 0.1$ in Fig 4.4. The scaling symmetry (4.23) implies that the phase space is independent of the scalar field charge q. On the $a_0 = 0$ or $\phi_0 = 0$ axis, there are no non-trivial soliton solutions, see subsection 4.3.3. Solutions exist in the shaded region. All the solutions labeled in the

coloured area are well-defined. This means, that the first zero of the scalar field ϕ exists before f has a zero, i.e., $r_m < r_{singular}$, where $f(r_{singular}) = 0$, otherwise the system of ODEs (4.18–4.21) will become stiff. Hence, we exclude all configurations for which this condition is not met. The mirror radius of each soliton solution is displayed by the colour gradient. The darker the colour, the smaller the value of r_m. As we move toward the centre of the parameter space, the mirror radius increases.

For a fixed value of a_0, solitons are found within some interval of values of ϕ_0. Beyond this interval, we discover that there is no well-defined soliton. On the other hand, we find that for each fixed value of ϕ_0, there seems to be no upper bound on the value of a_0. In fact, the phase space plot can be extended further into the region where $|a_0| > 3$. To confirm this, for fixed $\phi_0 = 1$, we found numerically a non-trivial solution with $a_0 = 10^5$ and the first node of the scalar field at $r_m \approx 4 \times 10^{-4}$. Therefore, the phase space plot shown in Fig 4.4 is merely a small portion of the complete soliton solution space. As will be seen later in this chapter, in contrast, the phase space of the black hole solutions does not share with this feature due to the existence of event horizon. In particular, for fixed q, there will be upper limits on the values of the other free parameters ϕ_h and E_h. Hence, the size of black hole solution space cannot be arbitrarily large. This will become clear later when we discuss the hairy black holes in a cavity in the next subsection.

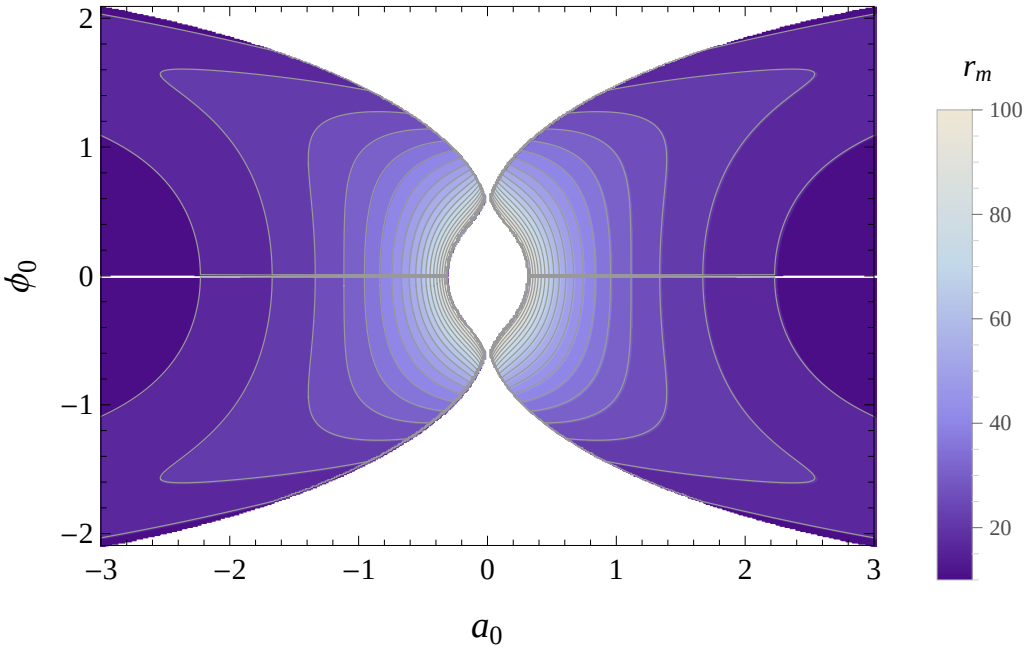

Figure 4.4: Phase space of soliton solutions with charged scalar field in a cavity for fixed scalar field charge $q = 0.1$. The solutions are parameterized by two free parameters a_0 (horizontal axis) and ϕ_0 (vertical axis). The shaded area is where solutions exist with the scalar field having at least one node. The contour lines show the lines of constant r_m where the mirror is located at the first zero of the scalar field; lighter colours refer to larger values of the mirror radius r_m and darker colours smaller values of r_m. In the central region where a_0 and ϕ_0 approach zero, solutions also exist with $r_m > 100$. There are no solutions on the $a_0 = 0$ or $\phi_0 = 0$ axes.

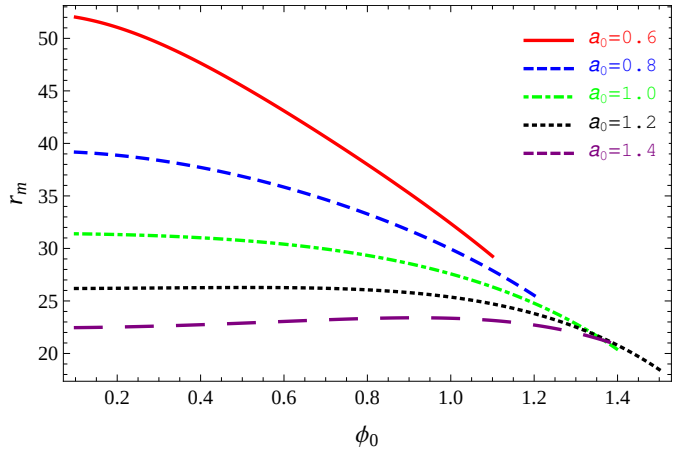

Figure 4.5: For soliton solutions, mirror radius r_m plotted as a function of ϕ_0 for various fixed values of a_0.

In Fig 4.5 and 4.6, we examine how the free parameters a_0 and ϕ_0 affect the location of the mirror (where the mirror is located at the first node of the scalar field). For fixed values of a_0, the mirror radius is plotted as a function of ϕ_0 in Fig 4.5. It can be seen from this figure that for each fixed value of a_0, there is an upper bound on the values of ϕ_0 where solutions can be found. For instance, with fixed $a_0 = 0.6$ (red, solid), the soliton solutions lie within $\phi \in [0.1, 1.1]$. For smaller values of a_0, it is clear that as ϕ_0 increases, the mirror radius decreases. However, this trend becomes less obvious when a_0 is larger. For example, with fixed $a_0 = 1.4$ (purple, dashed), the radius slightly increases and then decreases as ϕ_0 increases.

We also explore the dependence of the mirror location on the value of a_0 (for fixed ϕ_0) in Fig 4.6. For smaller values of ϕ_0, the mirror radius r_m decreases as a_0 increases (see for example in Fig 4.6(b)). In Fig 4.6(c), we see that r_m firstly increases as a_0 increases, and after reaching its maximum value, the radius starts to decrease again as a_0 increases for intermediate values of ϕ_0. Finally, for larger values of ϕ_0, the location of mirror r_m increases as a_0 increases up to $a_0 = 3$ as illustrated by Fig 4.6(d).

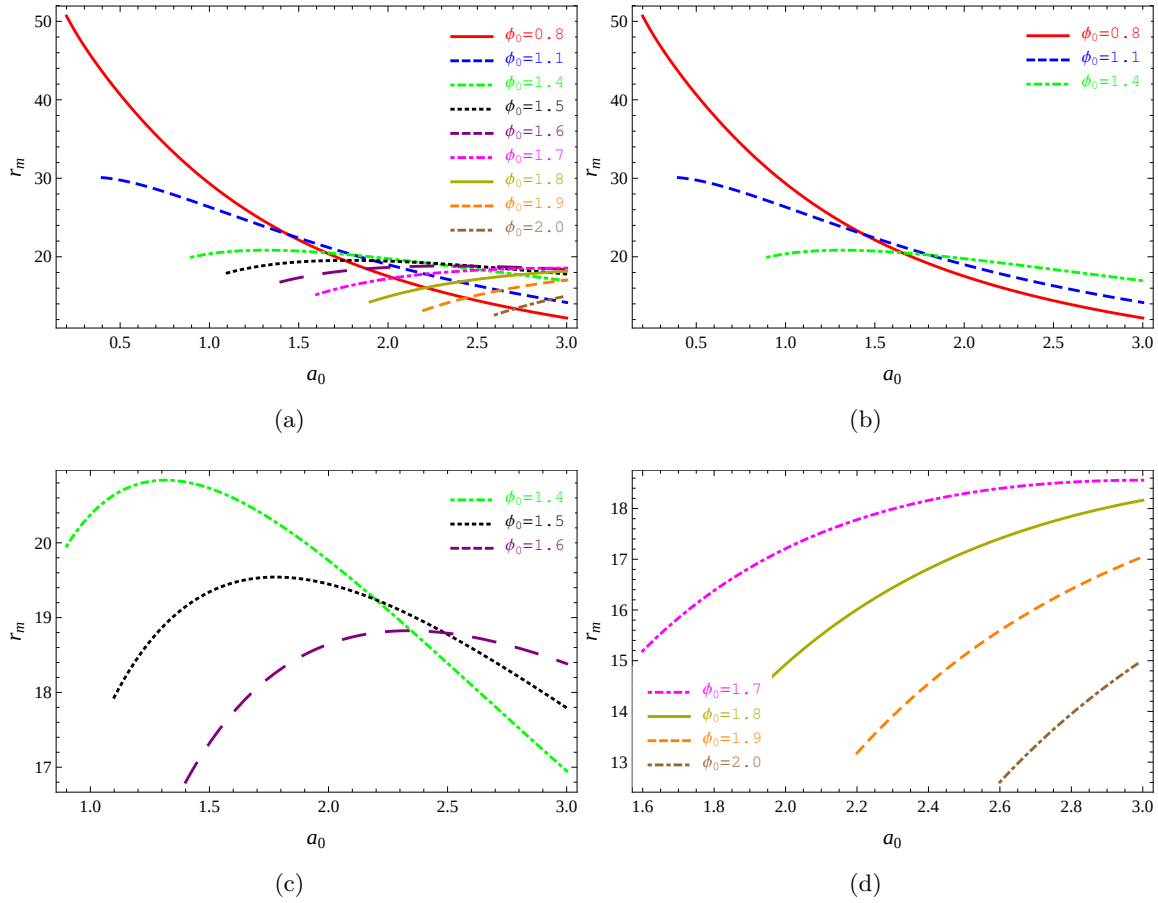

Figure 4.6: For soliton solutions, mirror radius r_m plotted as a function of a_0 for various fixed values of ϕ_0. For clarity, (b)–(d) are constructed by using the data in the top-left plot.

In Fig 4.7, the portion of the contour $r_m = 18$ for charged scalar solitons with $q = 0.1$ is shown. To plot these, we vary a_0 from $1 - 4$ then scan for the values of ϕ_0 such that the scalar field vanishes at the mirror radius $r_m = 18$. As a_0 increases, there exist two branches of solitons. For fixed a_0 there are two values of ϕ_0 with the same mirror radius, one is larger than the other. We anticipate that these two branches might merge together for a larger value of a_0.

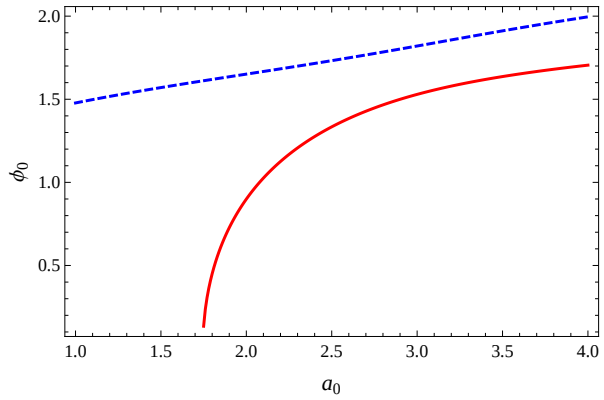

Figure 4.7: Part of the $r_m = 18$ contour in the solution space of solitons with $q = 0.1$ and the mirror at the first zero of the scalar field.

4.4.2 Black holes in a cavity

For black hole solutions, due to the scaling symmetry (4.23), we choose the length scale by setting $r_h = 1$ (hence $m_h = \frac{1}{2}$). From (4.30), this leaves only three unconstrained parameters, scalar field charge q, the value of the scalar field at the horizon ϕ_h and the electric field at the horizon E_h. Therefore unlike soliton case, we need to consider different values of q. We also use time-rescaling (4.25) to set $h = 1$ on the horizon.

In Fig 4.8, the four field variables f, h, A_0 and ϕ are plotted as functions of radius for a spherically symmetric black hole with fixed $q = 0.9, \phi_h = 0.4$ and $E_h = 0.8$. In a similar way to the soliton case, the scalar field profile for the static black hole also oscillates around zero. Likewise, we will mainly consider the case when the mirror is located at the first node of the scalar field, as we anticipate that such configurations are likely to be stable. Apart from the scalar field, the other field variables f, h and A_0 increase monotonically with r. These variables are not expected to be bounded as $r \to \infty$. This is because there is no asymptotically flat black hole solution that can support scalar hair [14, 15] (see subsection 4.3.3).

Three more different static black hole solutions are shown in Fig 4.9 for fixed $\phi_h = 0.3$ and $E_h = 0.6$ with three distinct values of scalar field charge q. We see that the mirror

radius r_m (the location of the first zero of the scalar field) decreases as q increases for these values of ϕ_h and E_h.

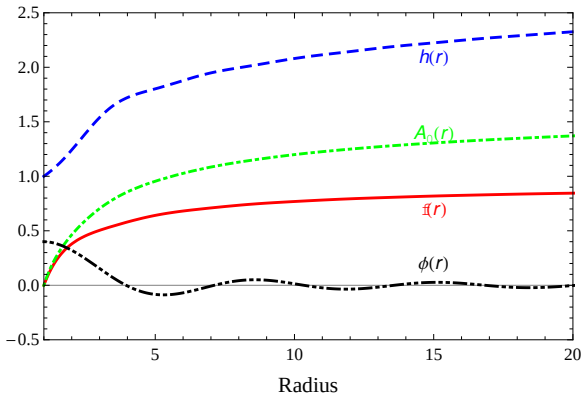

Figure 4.8: Metric functions $f(r), h(r)$, gauge field function $A_0(r)$ and scalar field function $\phi(r)$ for a static black hole with fixed $q = 0.9, \phi_h = 0.4$ and $E_h = 0.8$.

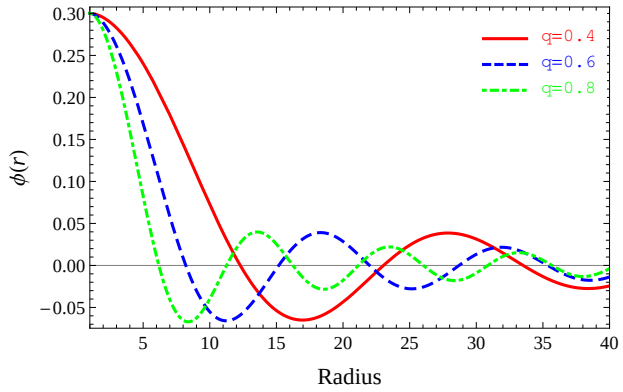

Figure 4.9: Scalar field profiles for three different black hole solutions with fixed $\phi_h = 0.3$ and $E_h = 0.6$ and three values of the scalar field charge q.

Fig 4.10 shows that different black hole solutions could share the same mirror location. With fixed scalar charge $q = 0.1$, three scalar field profiles for static black holes found to have a common mirror radius at $r_m \approx 27$ are shown in Fig 4.10(a). A further three distinct scalar field profiles are illustrated in Fig 4.10(b). With given $q = 0.1$ and $E_h = 1$, we have three different black hole solutions for which their, first, second and third zeros are located at $r_m \approx 27$.

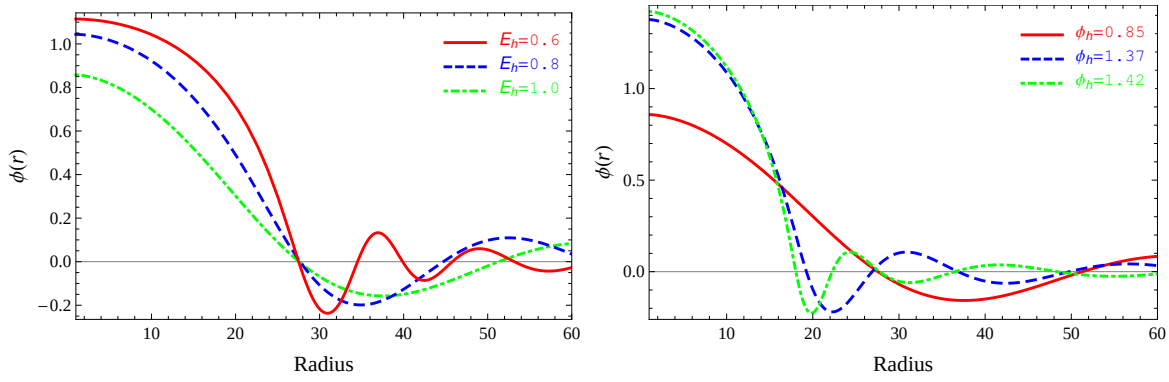

(a) (b)

Figure 4.10: Scalar field profiles for static black holes with fixed scalar charge $q = 0.1$. (a) Three distinct black hole solutions with the same mirror location $r_m \approx 27$. (b) Three distinct black hole solutions with a common node at the same location $r_m \approx 27$, first node (red, solid), second node (blue, dashed) and third node (green, dot-dashed).

With fixed r_h, the boundary conditions (4.30) imply that black hole solutions are characterized by three parameters: the scalar field charge q, the value of the scalar field at the horizon ϕ_h and the electric field at the horizon E_h. Therefore if the numerical value of q is specified, all possible black hole-in-a-cavity solutions can be displayed in a two dimensional phase space of ϕ_h and E_h, as shown in Fig 4.11.

We explore four different phase spaces of black hole solutions with fixed $q = 0.1, 0.2, 0.4$ and 0.8 in Fig 4.11. The coloured regions represent the areas where black hole solutions exist, with the scalar field having at least one node. We seek solutions where the first node of the scalar field r_m forms before the metric function f reaches the "second horizon", i.e., $f(\tilde{r}_{singular}) = 0$ for $r_h < r_m < \tilde{r}_{singular}$. The shaded areas in Fig 4.11 only include black hole solutions where the mirror radius is less than 100, with the mirror placed at the first node of the scalar field. Solutions with $r_m > 100$ also exist in the central areas where ϕ_h and E_h approach zero. On the $\phi_h = 0$ axis, the only non-trivial black hole solution is the Reissner-Nordström metric, see also subsection 4.3.3. For the non-charged case (either $E_h = 0$ or $q = 0$), the scalar field profile does not develop a node and hence it is irrelevant,

see subsection 4.3.3 for more details.

It is clear from the plots that the black hole solution space is much more restricted than the soliton phase space shown in Fig 4.4. This difference comes from the requirement to have a regular event horizon defined by $f(r_h) = 0$ and $f'(r_h) > 0$. To satisfy these conditions, we can deduce from (4.19) that $|E_h| < \sqrt{2}$, when $r_h = 1$ and $h(r_h) = 1$. In contrast with the soliton solutions, in this case the phase space of hairy black holes has a restriction on the range of values of E_h. There are no well-defined black hole solutions when $E_h \geq \sqrt{2}$ for $r_h = 1$ and $h(r_h) = 1$. This can be clearly seen in Fig 4.11. Moreover we see that as the scalar charge q increases, the solution space is smaller. This is because, as q gets larger, the coupling between the charged scalar field and the gauge field becomes stronger. As a consequence of this, the metric function f develops a "second node" (where $r = \tilde{r}_{singular}$) at smaller values of r for the higher q case. For $r \geq \tilde{r}_{singular}$, the ODE system (4.18–4.21) becomes stiff and numerical integration is impractical.

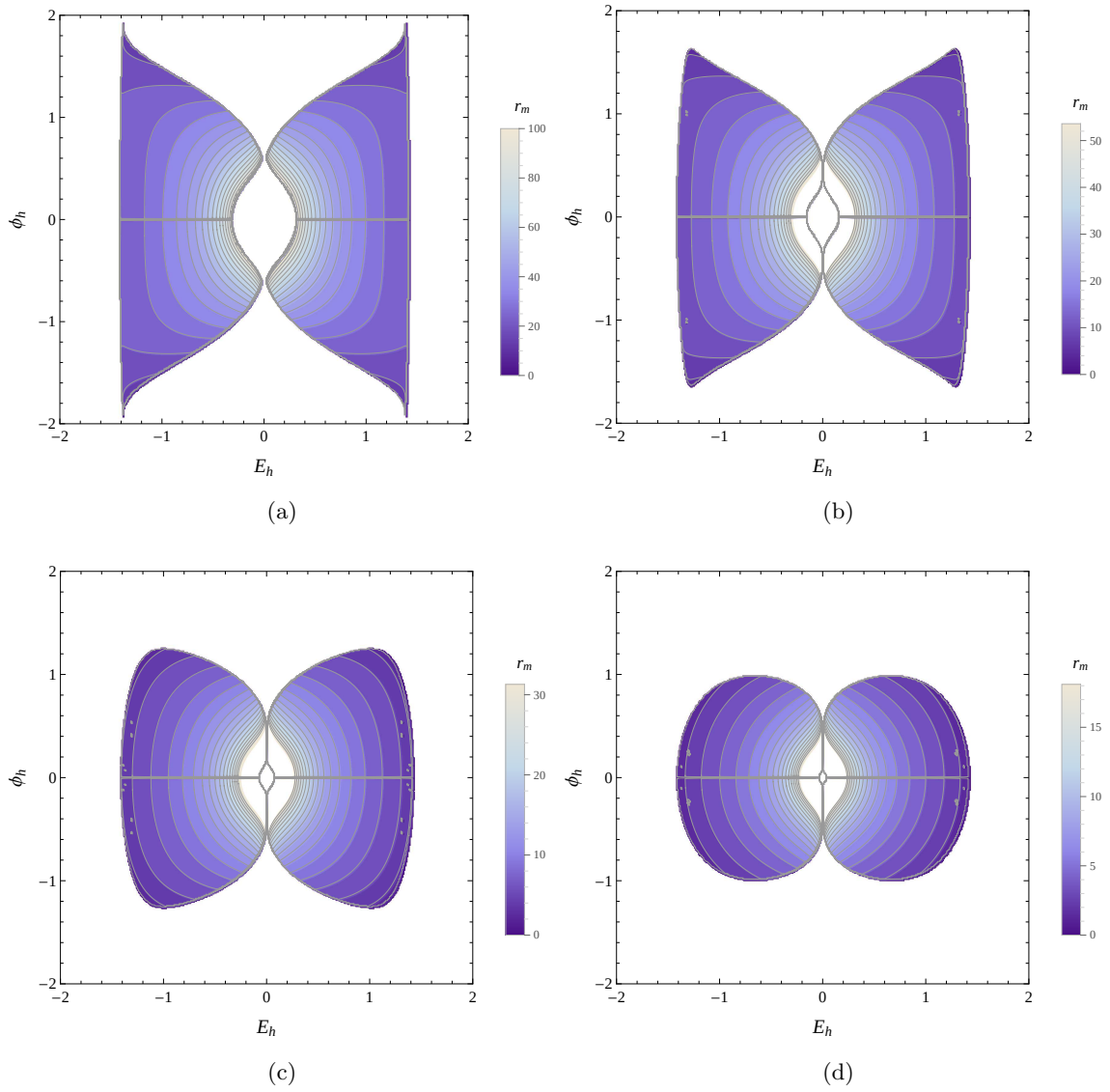

Figure 4.11: Phase space of black hole solutions with charged scalar hair in a cavity for four distinct values of scalar charge $q = 0.1, 0.2, 0.4$ and 0.8 (a)–(d), respectively. For fixed q, the black hole solutions are described by ϕ_h (vertical axis) and E_h (horizontal axis). The solutions possessing at least one node are indicated by the shaded area. The solutions defined on each contour line have the same mirror radius. The lighter the colour is, the larger the value of the mirror radius r_m. In the central region where E_h and ϕ_h approach zero, solutions also exist with $r_m > 100$. There is no solution on the $E_h = 0$ axis.

Finally we investigate how the free parameters, the value of the scalar field at the horizon ϕ_h, electric field at the horizon E_h and the scalar field charge q affect the mirror radius. In Fig 4.12(a), the mirror radius r_m is plotted as a function of ϕ_h for various values of fixed E_h. It is clear that as ϕ_h increases the radius of the mirror decreases. Nevertheless, the trend becomes less obvious as E_h gets larger. In fact, for $E_h = 1.4$, the mirror radius r_m slightly increases up to a certain value of ϕ_h before declining as ϕ_h approaches its upper limit. Mirror location as a function of electric field at the horizon E_h for five distinct values of ϕ_h is displayed in Fig 4.12(b). For lower values of ϕ_h, the mirror radius r_m decreases as E_h increases. As ϕ_h increases, this trend becomes less obvious. With $\phi_h = 1.4$, the mirror radius r_m monotonically increases as E_h increases. We also expect the same behaviour when $\phi_h > 1.4$. The plots for black hole solutions with $q = 0.1$ shown in Fig 4.12 are qualitatively very similar to those for solitons, shown in Fig 4.5.

In contrast to the soliton case, for the black hole scenario, the scalar field charge q is a free parameter. In Fig 4.13, we plot the mirror radius as a function of q for various equal fixed values of ϕ_h and E_h. As can be clearly seen, the location of the mirror decreases monotonically as the scalar field charge increases. Moreover, the overall value of r_m decreases as the fixed values of ϕ_h and E_h increase.

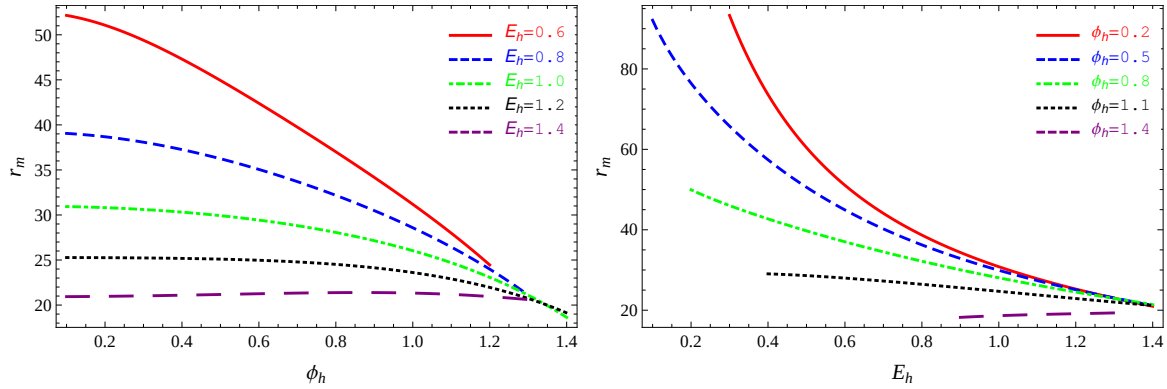

(a) (b)

Figure 4.12: The mirror radius r_m plotted as a function of (a) ϕ_h and (b) E_h for black hole solutions with fixed $q = 0.1$.

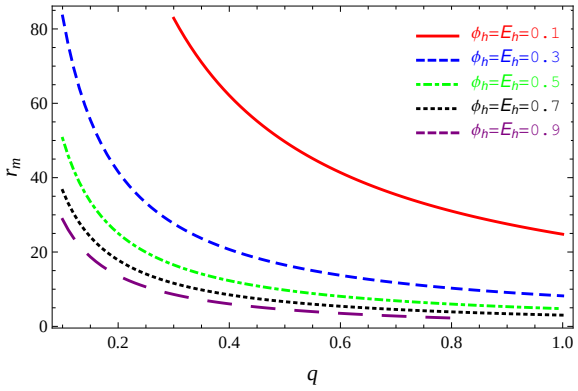

Figure 4.13: The mirror radius r_m plotted as a function of the scalar field charge q for fixed values of ϕ_h and E_h.

From these studies of r_m as a function of the other parameters, we observe that black holes only exist for r_m bigger than some minimum value, while in the soliton case, there is no minimum limit on the value of r_m. Moreover for the black holes, the behaviour of r_m is monotonic in ϕ_h, E_h or q (when other parameters are fixed). However for solitons, the behaviour of r_m as a function of ϕ_0 and a_0 is more complicated when a_0 is large.

§4.5 Stability analysis

In the previous section, we saw that a fully coupled system of gravity, an electromagnetic field and a charged massless scalar field admits numerical solitons and black holes with charged scalar hair. We found that the scalar field profiles oscillate around zero. By imposing a reflecting boundary condition (4.31) at the first node of the scalar field, we obtained soliton (black hole)-in-a-cavity solutions. If these black holes are shown to be stable, then they could be the final state of the superradiant instability of massless charged scalar perturbations on a Reissner-Nordström background, discussed in subsection 2.6.1. Thus in this section, we will consider spherically symmetric perturbations of both charged scalar solitons and black holes in a cavity.

4.5.1 Dynamical equations

To study the time evolution of the system, we now promote every field variable to a time-dependent quantity. Thus we consider the metric functions $f(t,r), h(t,r)$, the scalar field $\Phi = \phi(t,r)$ (which now becomes a complex field) and the gauge potential $A_a = [A_0(t,r), 0, 0, 0]$, where A_r, A_θ and A_φ are set to zero by the gauge transformation (4.11) and the spherical symmetry. It should be emphasized that, here we consider only spherically symmetric perturbations as the metric retains the form (4.12) and the field variables depend only on t and r.

The components of the time-dependent Einstein G_{ab} tensor are given by

$$\begin{aligned}
G_{00} &= -\frac{fh\left(rf' + f - 1\right)}{r^2}, \\
G_{01} &= -\frac{\dot{f}}{rf}, \\
G_{11} &= \frac{\left(rf' + f - 1\right)}{r^2 f} + \frac{h'}{rh}, \\
G_{22} &= \frac{r^2}{2h}\left(hf'' + fh'' + \frac{3f'h'}{2} - \frac{fh'^2}{2h} + \frac{2f'h}{r} + \frac{fh'}{r}\right. \\
&\quad \left. - \frac{2\dot{f}^2}{f^3} - \frac{\dot{f}\dot{h}}{2\gamma^2} + \frac{\ddot{f}}{f^2}\right),
\end{aligned} \tag{4.39}$$

and the energy-momentum tensor T_{ab} reads

$$\begin{aligned}
T_{00} &= \frac{1}{2}\left(\tau + fE^2\right), \\
T_{10} &= \mathrm{Re}\left(\dot{\phi}^*\phi'\right) + qA_0\mathrm{Im}\left(\phi'^*\phi\right), \\
T_{11} &= \frac{1}{2\gamma^2}\left(\tau - fE^2\right), \\
T_{22} &= \frac{r^2E^2}{2h} - \frac{r^2}{2}\left[f|\phi'|^2 - \frac{1}{fh}\left(|\dot{\phi}|^2 + q^2A_0^2|\phi|^2 + 2qA_0\mathrm{Im}(\dot{\phi}^*\phi)\right)\right],
\end{aligned} \tag{4.40}$$

where we introduce a new metric function γ and new variable τ by

$$\gamma = fh^{1/2}, \tag{4.41}$$

$$\tau \equiv |\dot{\phi}|^2 + |\gamma\phi'|^2 + q^2A_0^2|\phi|^2 + 2qA_0\mathrm{Im}(\phi\dot{\phi}^*). \tag{4.42}$$

Here $\{\ \dot{}\ ,\ '\ ,\ ^*\ \}$ denote partial derivative with respect to t, r and complex conjugate, respectively. We remark that the $\theta\theta-$component of the Einstein equations is a consequence of the other components, therefore we do not need to take it into consideration. Unlike the static case, we have an extra $tr-$component in the Einstein field equations (4.4).

We derive the four following dynamical equations. The first three come from specific components of the Einstein field equations (4.4); namely G_{00} and the linear combinations $G_{00} + \gamma^2 G_{11}$ and $G_{00} - \gamma^2 G_{11}$. The relevant equations are

$$\frac{f'}{f} = -\frac{r}{2\gamma^2}\left(\tau + fE^2\right) + \frac{1}{fr}(1-f), \tag{4.43}$$

$$\frac{h'}{h} = \frac{r\tau}{\gamma^2}, \tag{4.44}$$

$$\frac{\gamma'}{\gamma} = -\frac{r}{2\gamma^2}fE^2 + \frac{1}{fr}\left(1-f\right). \tag{4.45}$$

We note that, since γ does not depend on τ, therefore it does not explicitly depend on the scalar field ϕ. The $tr-$component of the Einstein field equations (4.4) is given by

$$-\frac{\dot{f}}{f} = r\mathrm{Re}\left(\dot{\phi}^*\phi'\right) + rqA_0\mathrm{Im}\left(\phi'^*\phi\right). \tag{4.46}$$

Unlike the static case, in the time-dependent scenario, the Maxwell equations (4.5) have two non-vanishing components. We obtain the following dynamical equations from the $t-$

and $r-$components. These are given by

$$\frac{\gamma}{r^2}\left(\frac{r^2 A_0'}{h^{1/2}}\right)' = J_t = q^2|\phi|^2 A_0 - q\mathrm{Im}\left(\dot{\phi}\phi^*\right), \tag{4.47}$$

$$\frac{1}{r}\partial_t\left(\frac{r A_0'}{h^{1/2}}\right) = \gamma J_r = -q\mathrm{Im}(\gamma\phi'\phi^*). \tag{4.48}$$

Finally the Klein-Gordon equation (4.6) is given by

$$0 = -\ddot{\phi} + \left(\frac{\dot{\gamma}}{\gamma} + 2iqA_0\right)\dot{\phi} + \gamma^2\phi'' + \left(\gamma\gamma' + \frac{2\gamma^2}{r}\right)\phi' + \left(iq\dot{A}_0 + q^2A_0^2 - iqA_0\frac{\dot{\gamma}}{\gamma}\right)\phi. \tag{4.49}$$

We now define a new variable ψ by

$$\phi = \frac{\psi}{r}. \tag{4.50}$$

Thus (4.49) becomes

$$0 = -\ddot{\psi} + \left(\frac{\dot{\gamma}}{\gamma} + 2iqA_0\right)\dot{\psi} + \gamma\left(\gamma\psi'\right)' + \left(-\frac{\gamma\gamma'}{r} + iq\dot{A}_0 - iq\frac{\dot{\gamma}}{\gamma}A_0 + q^2A_0^2\right)\psi. \tag{4.51}$$

The equations (4.43–4.48) and (4.51) describe how the metric, the electromagnetic field and the charged scalar field evolve dynamically with time.

4.5.2 Perturbation equations

To investigate the stability of the static solitons and black holes discussed in section 4.4, we now consider linear perturbations around these equilibrium solutions. As a set-up, we

introduce the following notation

$$\begin{aligned} f(t,r) &= \bar{f}(r) + \delta f(t,r), \\ h(t,r) &= \bar{h}(r) + \delta h(t,r), \\ \gamma(t,r) &= \bar{\gamma}(r) + \delta\gamma(t,r), \\ A_0(t,r) &= \bar{A}_0(r) + \delta A_0(t,r), \\ \psi(t,r) &= \bar{\psi}(r) + \delta\psi(t,r). \end{aligned} \tag{4.52}$$

In this formalism, $\bar{f}$ (and similarly for other quantities) denotes equilibrium solutions which depends on the coordinate r only while the perturbation part will be referred to as δf which is a function of t and r. We assume that all the perturbation fields are real, expect the scalar field $\delta\psi(t,r)$ which now is a complex quantity. From now on, we work up to first order in the perturbations.

Next we rewrite the dynamical equations (4.43–4.48) and (4.51) to first order in the perturbations. Firstly, (4.43) gives

$$\begin{aligned} \frac{\delta f'}{\bar{f}} + \left[\frac{1}{r\bar{f}^2} + \frac{r(\bar{A}_0')^2}{2\bar{\gamma}^2} - \frac{\bar{f}'}{\bar{f}^2}\right]\delta f = &-\frac{r\bar{f}\bar{A}_0'}{\bar{\gamma}^2}\delta A_0' - \frac{\bar{A}_0 q^2\bar{\psi}^2}{r\bar{\gamma}^2}\delta A_0 + \frac{1}{\bar{\gamma}^3}\left[\frac{q^2\bar{A}_0^2\bar{\psi}^2}{r} + r\bar{f}(\bar{A}_0')^2\right]\delta\gamma \\ &- \frac{iq\bar{A}_0\bar{\psi}}{2r\bar{\gamma}^2}\left(\delta\dot{\psi} - \delta\dot{\psi}^*\right) + \left[\frac{\bar{\psi}}{2r^2} - \frac{\bar{\psi}'}{2r}\right]\left(\delta\psi' + \delta\psi'^*\right) \\ &+ \left[\frac{\bar{\psi}'}{2r^2} - \frac{\bar{\psi}q^2\bar{A}_0^2}{2r\bar{\gamma}^2} - \frac{\bar{\psi}}{2r^3}\right]\left(\delta\psi + \delta\psi^*\right). \end{aligned} \tag{4.53}$$

From (4.44), we can construct an equation for δh in the same manner

$$\begin{aligned} \frac{\delta h'}{\bar{h}} - \frac{\bar{h}'}{\bar{h}^2}\delta h - \frac{2\bar{A}_0 q^2\bar{\psi}^2}{r\bar{\gamma}^2}\delta A_0 + \frac{2q^2\bar{A}_0^2\bar{\psi}^2}{r\bar{\gamma}^3}\delta\gamma = &\frac{iq\bar{A}_0\bar{\psi}}{r\bar{\gamma}^2}\left(\delta\dot{\psi} - \delta\dot{\psi}^*\right) + \left[\frac{\bar{\psi}'}{r} - \frac{\bar{\psi}}{r^2}\right]\left(\delta\psi' + \delta\psi'^*\right) \\ &+ \left[\frac{\bar{\psi}}{r^3} + \frac{\bar{\psi}q^2\bar{A}_0^2}{r\bar{\gamma}^2} - \frac{\bar{\psi}'}{r^2}\right]\left(\delta\psi + \delta\psi^*\right). \end{aligned} \tag{4.54}$$

Similarly, we can derive an equation for $\delta\gamma$ with the same structure, as this will be useful

for our later analysis. Hence from (4.45), we obtain

$$\frac{\delta\gamma'}{\bar{\gamma}} - \frac{1}{\bar{\gamma}^2}\left[\frac{r\bar{f}(\bar{A}_0')^2}{\bar{\gamma}} + \bar{\gamma}'\right]\delta\gamma + \frac{r\bar{f}\bar{A}_0'}{\bar{\gamma}^2}\delta A_0' + \left[\frac{1}{r\bar{f}^2} + \frac{r\bar{A}_0'^2}{2\bar{\gamma}^2}\right]\delta f = 0. \tag{4.55}$$

Note that (4.55) is not an independent equation because it can be derived directly from the definition of $\delta\gamma = \delta(fh^{1/2})$ and (4.53, 4.54). The final component of the Einstein field equations (4.46) takes the form

$$-\frac{\delta\dot{f}}{\bar{f}} = \left[\frac{\bar{\psi}'}{2r} - \frac{\bar{\psi}}{2r^2}\right]\left(\delta\dot{\psi} + \delta\dot{\psi}^*\right) + \frac{iq\bar{A}_0\bar{\psi}}{2r}\left(\delta\psi' - \delta\psi'^*\right) - \frac{iq\bar{A}_0\bar{\psi}'}{2r}\left(\delta\psi - \delta\psi^*\right). \tag{4.56}$$

The t and r components of the Maxwell equations (4.47) and (4.48) yield respectively,

$$\begin{aligned}\frac{\bar{\gamma}}{\sqrt{\bar{h}}}\delta A_0'' + \frac{\bar{\gamma}}{\sqrt{\bar{h}}}\left[\frac{2}{r} - \frac{\bar{h}'}{2\bar{h}}\right]\delta A_0' - \frac{q^2\bar{\psi}^2}{r^2}\delta A_0 = &-\frac{q^2\bar{A}_0\bar{\psi}^2}{r^2\bar{\gamma}}\delta\gamma + \frac{\bar{\gamma}\bar{A}_0'}{2\bar{h}\sqrt{\bar{h}}}\delta h' + \frac{1}{2\bar{h}}\left[\frac{\bar{A}_0q^2\bar{\psi}^2}{r^2}\right.\\ &\left. - \frac{\bar{\gamma}\bar{A}_0'\bar{h}'}{\bar{h}\sqrt{\bar{h}}}\right]\delta h + \frac{iq\bar{\psi}}{2r^2}\left(\delta\dot{\psi} - \delta\dot{\psi}^*\right)\\ &+ \frac{q^2\bar{A}_0\bar{\psi}}{r^2}\left(\delta\psi + \delta\psi^*\right),\end{aligned} \tag{4.57}$$

$$\frac{\delta\dot{A}_0'}{\sqrt{\bar{h}}} - \frac{\bar{A}_0'}{2\bar{h}\sqrt{\bar{h}}}\delta\dot{h} = \frac{iq\bar{\psi}\bar{\gamma}}{2r^2}\left(\delta\psi' - \delta\psi'^*\right) - \frac{iq\bar{\gamma}\bar{\psi}'}{2r^2}\left(\delta\psi - \delta\psi^*\right). \tag{4.58}$$

Lastly, the scalar field equation (4.51) reads

$$\begin{aligned}0 = &-\delta\ddot{\psi} + \bar{\gamma}^2\delta\psi'' + 2iq\bar{A}_0\delta\dot{\psi} + \bar{\gamma}\bar{\gamma}'\delta\psi' + \left[q^2\bar{A}_0^2 - \frac{\bar{\gamma}\bar{\gamma}'}{r}\right]\delta\psi - \frac{iq\bar{A}_0\bar{\psi}}{\bar{\gamma}}\delta\dot{\gamma} + \left[\bar{\gamma}\bar{\psi}' - \frac{\bar{\gamma}\bar{\psi}}{r}\right]\delta\gamma'\\ &+ \left[2\bar{\gamma}\bar{\psi}'' + \bar{\gamma}'\bar{\psi}' - \frac{\bar{\psi}\bar{\gamma}'}{r}\right]\delta\gamma + iq\bar{\psi}\delta\dot{A}_0 + 2q^2\bar{\psi}\bar{A}_0\delta A_0.\end{aligned} \tag{4.59}$$

It is clear either from (4.56) or (4.58) that $\mathrm{Im}(\delta\psi)$ is not in-phase with $\delta f, \delta h, \delta A_0$ and $\mathrm{Re}(\delta\psi)$. By this, we mean that these equations involve one more or one less time derivative of $\mathrm{Im}(\delta\psi)$ than other quantities. Thus we decompose the scalar perturbation into real and

imaginary parts as follows

$$\delta\psi(t,r) = \delta u(t,r) + i\delta\dot{w}(t,r), \tag{4.60}$$

where $u(t,r)$ and $w(t,r)$ are real quantities. With this decomposition, $\delta w(t,r)$ is only determined up to an arbitrary function of r. Apart from (4.55), which does not depend explicitly on the scalar field, equations (4.53–4.59) now can be re-written in terms of δu and δw. The $\delta f'$ (4.53) and $\delta h'$ (4.54) equations now become

$$\begin{aligned}\frac{\delta f'}{\bar{f}} + \left[\frac{1}{r\bar{f}^2} + \frac{r(\bar{A}_0')^2}{2\bar{\gamma}^2} - \frac{\bar{f}'}{\bar{f}^2}\right]\delta f + \frac{r\bar{f}\bar{A}_0'}{\bar{\gamma}^2}\delta A_0' = &-\frac{\bar{A}_0 q^2\bar{\psi}^2}{r\bar{\gamma}^2}\delta A_0 + \frac{1}{\bar{\gamma}^3}\left[\frac{q^2\bar{A}_0^2\bar{\psi}^2}{r} + r\bar{f}(\bar{A}_0')^2\right]\delta\gamma \\ &+ \frac{q\bar{A}_0\bar{\psi}}{r\bar{\gamma}^2}\delta\ddot{w} - \left(\frac{\bar{\psi}}{r}\right)'\delta u' \\ &+ \left[\frac{1}{r}\left(\frac{\bar{\psi}}{r}\right)' - \frac{q^2\bar{A}_0^2\bar{\psi}}{r\bar{\gamma}^2}\right]\delta u, \end{aligned} \tag{4.61}$$

$$\begin{aligned}\frac{\delta h'}{\bar{h}} - \frac{\bar{h}'}{\bar{h}^2}\delta h - \frac{2\bar{A}_0 q^2\bar{\psi}^2}{r\bar{\gamma}^2}\delta A_0 + \frac{2q^2\bar{A}_0^2\bar{\psi}^2}{r\bar{\gamma}^3}\delta\gamma = &-\frac{2q\bar{A}_0\bar{\psi}}{r\bar{\gamma}^2}\delta\ddot{w} + 2\left(\frac{\bar{\psi}}{r}\right)'\delta u' \\ &+ \left[\frac{2q^2\bar{A}_0^2\bar{\psi}}{r\bar{\gamma}^2} - \frac{2}{r}\left(\frac{\bar{\psi}}{r}\right)'\right]\delta u. \end{aligned} \tag{4.62}$$

The $\delta\dot{f}$ equation (4.56) is given by

$$-\frac{\delta\dot{f}}{\bar{f}} = \left(\frac{\bar{\psi}}{r}\right)'\delta\dot{u} - \frac{q\bar{A}_0\bar{\psi}}{r}\delta\dot{w}' + \frac{q\bar{A}_0\bar{\psi}'}{r}\delta\dot{w}. \tag{4.63}$$

The time and radial components of the Maxwell equations read (4.57, 4.58)

$$\begin{aligned}\frac{\bar{\gamma}}{\sqrt{\bar{h}}}\delta A_0'' + \frac{\bar{\gamma}}{\sqrt{\bar{h}}}\left[\frac{2}{r} - \frac{\bar{h}'}{2\bar{h}}\right]\delta A_0' - \frac{q^2\bar{\psi}^2}{r^2}\delta A_0 = &-\frac{q^2\bar{A}_0\bar{\psi}^2}{r^2\bar{\gamma}}\delta\gamma + \frac{\bar{\gamma}\bar{A}_0'}{2\bar{h}\sqrt{\bar{h}}}\delta h' + \frac{1}{2\bar{h}}\left[\frac{\bar{A}_0 q^2\bar{\psi}^2}{r^2}\right. \\ &\left. - \frac{\bar{\gamma}\bar{A}_0'\bar{h}'}{\bar{h}\sqrt{\bar{h}}}\right]\delta h - \frac{q\bar{\psi}}{r^2}\delta\ddot{w} + \frac{2q^2\bar{A}_0\bar{\psi}}{r^2}\delta u, \end{aligned} \tag{4.64}$$

$$\frac{\delta\dot{A}_0'}{\sqrt{\bar{h}}} - \frac{\bar{A}_0'}{2\bar{h}\sqrt{\bar{h}}}\delta\dot{h} = -\frac{q\bar{\psi}\bar{\gamma}}{r^2}\delta\dot{w}' + \frac{q\bar{\psi}'\bar{\gamma}}{r^2}\delta\dot{w}. \tag{4.65}$$

In addition, the scalar field equation (4.59) can now be split into two independent equa-

tions, corresponding to the real and imaginary parts. These are given by

$$0 = -\delta\ddot{u} + \bar{\gamma}^2\delta u'' + \bar{\gamma}\bar{\gamma}'\delta u' + \left[q^2\bar{A}_0^2 - \frac{\bar{\gamma}\bar{\gamma}'}{r}\right]\delta u - 2q\bar{A}_0\delta\ddot{w} + \bar{\gamma}\left[\bar{\psi}' - \frac{\bar{\psi}}{r}\right]\delta\gamma' + \left[2\bar{\gamma}\bar{\psi}'' + \bar{\psi}'\bar{\gamma}' - \frac{\bar{\psi}\bar{\gamma}'}{r}\right]\delta\gamma + 2q^2\bar{A}_0\bar{\psi}\delta A_0, \tag{4.66}$$

$$0 = -\delta\ddot{w} + \bar{\gamma}^2\delta\dot{w}'' + \bar{\gamma}\bar{\gamma}'\delta\dot{w}' + \left[q^2\bar{A}_0^2 - \frac{\bar{\gamma}\bar{\gamma}'}{r}\right]\delta\dot{w} + 2q\bar{A}_0\delta\dot{u} - \frac{q\bar{A}_0\bar{\psi}}{\bar{\gamma}}\delta\dot{\gamma} + q\bar{\psi}\delta\dot{A}_0. \tag{4.67}$$

We are now able to directly integrate (4.63) and (4.65) with respect to time t. We obtain

$$\frac{\delta f}{\bar{f}} = \frac{1}{r}\left[\frac{\bar{\psi}}{r} - \bar{\psi}'\right]\delta u - \frac{q\bar{A}_0\bar{\psi}'}{r}\delta w + \frac{q\bar{A}_0\bar{\psi}}{r}\delta w' + \delta\mathcal{F}(r), \tag{4.68}$$

$$\frac{\delta h}{\bar{h}\sqrt{\bar{h}}} = -\frac{2q\bar{\gamma}\bar{\psi}'}{r^2\bar{A}_0'}\delta w + \frac{2q\bar{\gamma}\bar{\psi}}{r^2\bar{A}_0'}\delta w' + \frac{2}{\sqrt{\bar{h}}\bar{A}_0'}\delta A_0' + \delta\mathcal{H}(r), \tag{4.69}$$

where $\delta\mathcal{F}(r)$ and $\delta\mathcal{H}(r)$ are arbitrary functions of the radial coordinate r. Therefore we can construct an equation for $\delta\gamma$ via $\delta\gamma = \delta(fh^{1/2})$,

$$\delta\gamma = \frac{\bar{\gamma}}{r}\left[\frac{\bar{\psi}}{r} - \bar{\psi}'\right]\delta u - \frac{q\bar{\gamma}\bar{\psi}'}{r^2\bar{A}_0'}\left[\bar{f}\bar{h} + r\bar{A}_0\bar{A}_0'\right]\delta w + \frac{q\bar{\gamma}\bar{\psi}}{r^2\bar{A}_0'}\left[\bar{f}\bar{h} + r\bar{A}_0\bar{A}_0'\right]\delta w' + \frac{\bar{\gamma}}{\bar{A}_0'}\delta A_0' + \bar{\gamma}\delta\mathcal{F} + \frac{\bar{f}\bar{h}}{2}\delta\mathcal{H}. \tag{4.70}$$

The results (4.68–4.70) are very helpful, since they allow us to replace any of the metric perturbations $\delta f, \delta h$ and $\delta\gamma$ in terms of the matter perturbations $\delta A_0, \delta u$ and δw. The functions $\delta\mathcal{F}(r)$ and $\delta\mathcal{H}(r)$ are arbitrary but they are subject to a linear first order constraint equation. To see this, we first eliminate the metric perturbations $\delta f, \delta f'$ and $\delta\gamma$ from (4.61) by using (4.68) and (4.70). This allows us to rewrite (4.61) with $\delta\ddot{w}$ in terms of scalar perturbations $\delta u, \delta w$, electromagnetic potential perturbation δA_0 and their derivatives. This can be used to eliminate $\delta\ddot{w}$ in (4.64), together with substituting for the metric

perturbations $\delta h, \delta h'$ and $\delta\gamma$ by using (4.69) and (4.70). Finally we arrive at

$$\delta\mathcal{F}' + \left[\frac{\bar{f}'}{\bar{f}} + \frac{\bar{h}'}{2\bar{h}} + \frac{1}{r}\right]\delta\mathcal{F} = \frac{r\bar{A}_0\bar{A}_0'}{2\bar{\gamma}}\delta\mathcal{H}' + \frac{r\bar{A}_0}{2\bar{\gamma}^2}\left[\frac{q^2\bar{A}_0\sqrt{\bar{h}}\bar{\psi}^2}{r^2} + \frac{\bar{\gamma}\bar{A}_0'^2}{\bar{A}_0} + \frac{\bar{f}\bar{A}_0'\bar{h}'}{2\sqrt{\bar{h}}}\right]\delta\mathcal{H}. \quad (4.71)$$

By using an integrating factor, this equation is solvable. Its solution is

$$\delta\mathcal{F} = \frac{r\bar{A}_0\bar{A}_0'}{2\bar{\gamma}}\delta\mathcal{H} + \frac{\mathcal{E}}{r\bar{\gamma}}, \quad (4.72)$$

where $\mathcal{E}$ is an arbitrary constant. Thus we can use this relation to eliminate $\delta\mathcal{H}$ from the perturbation equations.

We proceed further by considering (4.61), once the metric perturbations and $\delta\mathcal{H}$ have been substituted in terms of the matter perturbations and $\delta\mathcal{F}$, using (4.68), (4.70) and (4.72)

$$\begin{aligned} 0 = {} & \delta\ddot{w} - \bar{\gamma}^2\delta w'' + \left[\frac{q^2\bar{\psi}^2\bar{A}_0}{r^2\bar{A}_0'}\mathcal{A} - \bar{\gamma}\bar{\gamma}'\right]\delta w' + \left[\frac{\bar{f}\bar{h}}{r^2} - q^2\bar{A}_0^2 - \frac{\bar{\gamma}^2}{r^2} - \frac{\bar{f}\bar{A}_0'^2}{2} - \frac{q^2\bar{A}_0\bar{\psi}\bar{\psi}'}{r^2\bar{A}_0'}\mathcal{A}\right]\delta w \\ & + q\bar{A}_0\left[-2 + \frac{\bar{\psi}^2}{r^2} - \frac{\bar{\psi}\bar{\psi}'}{r}\right]\delta u + \frac{q\bar{A}_0\bar{\psi}}{\bar{A}_0'}\delta A_0' - q\bar{\psi}\delta A_0 - \frac{r\bar{\gamma}^2}{q\bar{A}_0\bar{\psi}}\delta\mathcal{F}' \\ & + \left[-\frac{\bar{f}\bar{h}}{q\bar{A}_0\bar{\psi}} - \frac{\bar{f}r^2\bar{A}_0'^2}{2q\bar{A}_0\bar{\psi}} + \frac{r\bar{f}\bar{A}_0'}{q\bar{\psi}\bar{A}_0^2}\mathcal{A} + \frac{q\bar{\psi}}{r\bar{A}_0'}\mathcal{A}\right]\delta\mathcal{F} - \sqrt{\bar{h}}\left[\frac{q\bar{\psi}}{r^2\bar{A}_0'} + \frac{\bar{f}\bar{A}_0'}{q\bar{A}_0^2\bar{\psi}}\right]\mathcal{E}, \end{aligned} \quad (4.73)$$

where

$$\mathcal{A} \equiv \bar{f}\bar{h} + r\bar{A}_0\bar{A}_0'. \quad (4.74)$$

In addition, we can integrate the imaginary part of the Klein-Gordon equation (4.67) with respect to time t to give

$$\begin{aligned} 0 = {} & \delta\ddot{w} - \bar{\gamma}^2\delta w'' + \left[-\bar{\gamma}\bar{\gamma}' + \frac{q^2\bar{\psi}^2\bar{A}_0}{r^2\bar{A}_0'}\mathcal{A}\right]\delta w' + \left[-q^2\bar{A}_0^2 - \frac{q^2\bar{A}_0\bar{\psi}\bar{\psi}'}{r^2\bar{A}_0'}\mathcal{A} + \frac{\bar{\gamma}\bar{\gamma}'}{r}\right]\delta w \\ & + q\bar{A}_0\left[-2 + \frac{\bar{\psi}^2}{r^2} - \frac{\bar{\psi}\bar{\psi}'}{r}\right]\delta u + \frac{q\bar{A}_0\bar{\psi}}{\bar{A}_0'}\delta A_0' - q\bar{\psi}\delta A_0 + \delta\mathcal{G}(r), \end{aligned} \quad (4.75)$$

where $\delta\mathcal{G}(r)$ is an arbitrary function of the radial coordinate r. By comparing (4.73) and

this equation, we obtain another linear first order equation, this time relating $\delta\mathcal{F}$ and $\delta\mathcal{G}$

$$0 = \delta\mathcal{F}' + \left[r\left(\frac{\bar{\psi}}{r}\right)'^2 - \frac{\bar{A}_0''}{\bar{A}_0'} - \frac{\bar{A}_0'}{\bar{A}_0} - \frac{1}{r} + \frac{\bar{f}'}{\bar{f}}\right]\delta\mathcal{F} + \frac{q\bar{A}_0\bar{\psi}}{r\bar{\gamma}^2}\delta\mathcal{G} + \frac{1}{r\bar{\gamma}}\left[\frac{\bar{A}_0'}{\bar{A}_0} + \frac{\bar{A}_0 q^2\bar{\psi}^2}{r^2\bar{f}\bar{A}_0'}\right]\mathcal{E}. \tag{4.76}$$

We will come back to this equation again when we consider the boundary conditions for the soliton and black hole cases. Next, we use (4.62) and (4.55) to eliminate $\delta\ddot{w}$ and $\delta A_0''$ from the real part of the dynamical scalar field equation (4.66).

Eventually, we obtain three perturbation equations for $\delta u, \delta w$ and δA_0. The first equation is derived from the real part of the Klein-Gordon equation (4.66) and takes the form

$$\begin{aligned}
0 = {} & \delta\ddot{u} - \bar{\gamma}^2\delta u'' - \bar{\gamma}\bar{\gamma}'\delta u' + \left[3q^2\bar{A}_0^2 + \frac{\bar{\gamma}\bar{\gamma}'}{r} - \bar{f}\bar{h}\left(\frac{\bar{\psi}}{r}\right)'^2 + \frac{\bar{f}\bar{A}_0'^2}{2}\left(\left(\frac{\bar{\psi}}{r}\right)^2 + \bar{\psi}'^2\right)\right. \\
& \left. - \frac{\bar{f}\bar{\psi}\bar{\psi}'\bar{A}_0'^2}{r}\right]\delta u + 2q\bar{A}_0\bar{\gamma}^2\delta w'' + q\bar{f}\bar{A}_0\left[2\sqrt{\bar{h}}\bar{\gamma}' + \left(-\frac{\bar{A}_0'}{\bar{A}_0}\mathcal{A} + \frac{\bar{h}}{r} + \frac{r\bar{A}_0'^2}{2}\right)\left(\frac{\bar{\psi}}{r}\right)'\bar{\psi}\right]\delta w' \\
& + q\bar{A}_0\left[2q^2\bar{A}_0^2 - \frac{2\bar{\gamma}\bar{\gamma}'}{r} + \bar{\gamma}\bar{\psi}'\left(\frac{\bar{\psi}}{r}\right)'\left(\frac{\bar{\gamma}\bar{A}_0'}{\bar{A}_0} - \bar{\gamma}' - \frac{\bar{\gamma}}{r}\right)\right]\delta w + \frac{2r\bar{\gamma}^2}{\bar{\psi}}\delta\mathcal{F}' \\
& + \bar{\gamma}\left(\left(\frac{\bar{\psi}}{r}\right)' + \frac{2}{\bar{\psi}}\right)\left[(r\bar{\gamma})' - \frac{r\bar{\gamma}\bar{A}_0'}{\bar{A}_0}\right]\delta\mathcal{F} + \frac{\bar{\gamma}}{\bar{A}_0}\left[\frac{2\bar{A}_0'}{\bar{\psi}} - \frac{\bar{\psi}\bar{A}_0'}{r^2} + \frac{\bar{A}_0'\bar{\psi}'}{r}\right]\mathcal{E}.
\end{aligned} \tag{4.77}$$

The second equation comes from (4.75) once $\delta\mathcal{G}$ is eliminated by using (4.76)

$$\begin{aligned}
0 = {} & \delta\ddot{w} - \bar{\gamma}^2\delta w'' + \left[-\bar{\gamma}\bar{\gamma}' + \frac{q^2\bar{A}_0\bar{\psi}^2}{r^2\bar{A}_0'}\mathcal{A}\right]\delta w' + \left[-q^2\bar{A}_0^2 - \frac{q^2\bar{A}_0\bar{\psi}\bar{\psi}'}{r^2\bar{A}_0'}\mathcal{A} + \frac{\bar{\gamma}\bar{\gamma}'}{r}\right]\delta w \\
& - q\bar{A}_0\left[2 + \bar{\psi}\left(\frac{\bar{\psi}}{r}\right)'\right]\delta u + \frac{q\bar{A}_0\bar{\psi}}{\bar{A}_0'}\delta A_0' - q\bar{\psi}\delta A_0 - \frac{r\bar{\gamma}^2}{q\bar{A}_0\bar{\psi}}\delta\mathcal{F}' \\
& + \frac{r\bar{\gamma}^2}{q\bar{A}_0\bar{\psi}}\left[\frac{1}{r} - \frac{\bar{f}'}{\bar{f}} + \frac{\bar{A}_0'}{\bar{A}_0} + \frac{\bar{A}_0''}{\bar{A}_0'} - r\left(\frac{\bar{\psi}}{r}\right)'^2\right]\delta\mathcal{F} - \left[\frac{q\bar{\psi}\sqrt{\bar{h}}}{r^2\bar{A}_0'} + \frac{\bar{\gamma}\bar{A}_0'}{q\bar{A}_0^2\bar{\psi}}\right]\mathcal{E}.
\end{aligned} \tag{4.78}$$

Lastly, the third equation is obtained from the Einstein field equation (4.55)

$$0 = \frac{q\bar{\psi}}{\bar{A}_0' r^2}\mathcal{A}\delta w'' + \frac{q\bar{\psi}\bar{A}_0}{r^2}\left[\frac{\bar{\gamma}'}{\bar{A}_0\bar{A}_0'\bar{\gamma}}\mathcal{A} - \frac{q^2\bar{\psi}^2\bar{h}}{r^2\bar{A}_0'^2}\right]\delta w' + \frac{q\bar{\psi}\bar{A}_0}{r^2}\left[\frac{\mathcal{A}}{r\bar{A}_0\bar{A}_0'\bar{\gamma}}\left(-\bar{\gamma}' + \frac{rq^2\bar{A}_0^2}{\bar{\gamma}}\right)\right.$$
$$\left. + \frac{q^2\bar{h}\bar{\psi}\bar{\psi}'}{r^2\bar{A}_0'^2}\right]\delta w - \left(\frac{\bar{\psi}}{r}\right)'\delta u' - \left[\left(\frac{\bar{\psi}}{r}\right)'' + \left(\frac{1}{r} + \frac{\bar{\gamma}'}{\bar{\gamma}}\right)\left(\frac{\bar{\psi}}{r}\right)'\right]\delta u + \left[\frac{\delta A_0'}{\bar{A}_0'}\right]' + \left[\frac{\mathcal{A}}{r\bar{A}_0\bar{A}_0'}\delta\mathcal{F}\right]'$$
$$- \left[-\frac{1}{r\bar{f}} + \frac{\bar{A}_0'}{\bar{A}_0} + \frac{r\bar{A}_0'^2}{2\bar{f}\bar{h}}\right]\delta\mathcal{F} + \frac{1}{r\bar{A}_0\bar{\gamma}}\left[\frac{\mathcal{A}}{r\bar{A}_0} + \frac{q^2\bar{\psi}^2\bar{A}_0\bar{h}_0}{r^3\bar{A}_0'^2}\right]\mathcal{E}. \tag{4.79}$$

These three perturbation equations (4.77–4.79) govern the evolution of the perturbations $\delta u, \delta w$ and δA_0. We obtain two dynamical equations (4.77) and (4.78) which involve time derivatives. The third equation (4.79) is a constraint equation since it contains only radial derivatives.

We also observe that these perturbation equations do not involve any time derivatives of the perturbation of the electromagnetic potential δA_0. This is because of the residual gauge freedom in the theory, which means that one can arbitrarily add a function of time multiplied by $\bar{A}_0$ to δA_0. To see this, consider an infinitesimal coordinate transformation generated by a vector field V^a [134]:

$$x^a \to \tilde{x}^a = x^a - V^a. \tag{4.80}$$

The gauge potential is then transformed to

$$\tilde{A}_a(\tilde{x}) = \frac{\partial x^b}{\partial \tilde{x}^a}A_b(x) = \frac{\partial\left(\tilde{x}^b + V^b\right)}{\partial\tilde{x}^a}\left[\bar{A}_b + \delta A_b\right] = \left(\delta_a^b + \frac{\partial V^b}{\partial\tilde{x}^a}\right)\left[\bar{A}_b + \delta A_b\right],$$
$$= \bar{A}_a + \delta A_a + \bar{A}_b\frac{\partial V^b}{\partial x^a} + O(V\cdot\delta A). \tag{4.81}$$

On the hand, we can consider a Taylor expansion of $\tilde{A}_a(\tilde{x})$ up to the first order in V^a:-

$$\tilde{A}_a(\tilde{x}) = \tilde{\bar{A}}_a(x^b - V^b) + \delta\tilde{A}_a = \tilde{\bar{A}}_a(x^b) - \left(\frac{\partial\bar{A}_a}{\partial x^b}\right)V^b + \delta\tilde{A}_a + O(V^2). \tag{4.82}$$

By comparing (4.81) and (4.82), we obtain the following (up to leading order)

$$\begin{aligned} \therefore \tilde{\bar{A}}_a + \delta\tilde{A}_a &= \bar{A}_a + \delta A_a + \bar{A}_b \left(\partial_a V^b\right) + \left(\partial_b \bar{A}_a\right) V^b, \\ &\equiv \bar{A}_a + \delta A_a + \mathcal{L}_V \bar{A}_a, \end{aligned} \tag{4.83}$$

where $\mathcal{L}_V$ is the Lie derivative along the $\vec{V}$ direction. Finally we conclude that under the infinitesimal coordinate transformation (4.80), the electric potential perturbation δA_a is transformed by

$$\delta A_a \to \delta A_a + \mathcal{L}_V \bar{A}_a. \tag{4.84}$$

We now consider coordinate transformations generated by the vector field V^a such that

$$V^a = (v(t), 0, 0, 0)\,, \tag{4.85}$$

where $v(t)$ is arbitrary function of time. Therefore (4.84) becomes

$$\delta A_0 \to \delta A_0 + \bar{A}_0 \partial_0 v, \tag{4.86}$$

with the other components of δA_a being unchanged. Note that the perturbation equations (4.78, 4.79) are invariant under coordinate transformations generated by (4.84).

4.5.3 Boundary conditions for solitons

In the previous section, we derived three perturbation equations which hold either for solitons or black holes. In this section, we derive the boundary conditions for the scalar perturbations and electromagnetic potential perturbation corresponding to soliton solutions. Later, we give numerical results which indicate either the stability or instability of these equilibrium solitons.

We assume that the metric perturbations $\delta f, \delta h$, the electromagnetic potential pertur-

bation δA_0 and the scalar perturbations $\delta u/r, \delta\dot{w}/r$ are all regular at the origin. These assumptions lead to the elimination of $\delta\mathcal{F}, \delta\mathcal{H}$ and $\delta\mathcal{G}$ in (4.68, 4.69) and (4.75), as follows. Firstly, we make use of the freedom to add an arbitrary function of r to δw in (4.69) to set $\delta\mathcal{H}(r) \equiv 0$. Then the first order equation (4.71) can be solved, to give

$$\delta\mathcal{F} = \frac{\mathcal{E}}{r\bar{\gamma}}, \tag{4.87}$$

where $\mathcal{E}$ is an arbitrary constant of integration. From (4.68), by applying the series expansions (4.28) and the assumption that δf is regular at the origin, then $\delta\mathcal{F}$ must be finite at the origin. For this to happen, (4.87) implies that $\mathcal{E} \equiv 0$ and therefore $\delta\mathcal{F} \equiv 0$. Thus (4.76) leads to $\delta\mathcal{G} \equiv 0$. Then the perturbation equations (4.77–4.79) can be simplified further by setting $\delta\mathcal{F}' = \delta\mathcal{F} = \mathcal{E} = 0$.

To numerically integrate these perturbation equations, all the perturbation variables are assumed to take the time-periodic form

$$\begin{aligned}
\delta u(t,r) &= \mathrm{Re}\left[e^{-i\sigma t}\tilde{u}(r)\right], \\
\delta w(t,r) &= \mathrm{Re}\left[e^{-i\sigma t}\tilde{w}(r)\right], \\
\delta A_0(t,r) &= \mathrm{Re}\left[e^{-i\sigma t}\tilde{A}_0(r)\right],
\end{aligned} \tag{4.88}$$

where $\tilde{u}, \tilde{w}$ and $\tilde{A}_0$ are complex functions. Near the origin $r = 0$, we require that the scalar and electromagnetic perturbations are regular. Thus we assume that the functions of r in (4.88) can be expressed as power series defined by

$$\begin{aligned}
\tilde{u} &= r\sum_{j=0}^{\infty} u_j r^j, \\
\tilde{w} &= r\sum_{j=0}^{\infty} w_j r^j, \\
\tilde{A}_0 &= \sum_{j=0}^{\infty} \alpha_j r^j,
\end{aligned} \tag{4.89}$$

where u_j, w_j and α_j are constants. By substituting the series (4.89) into the perturbation equations (4.77–4.79) and comparing powers of r, we obtain

$$u_1 = w_1 = \alpha_1 = u_3 = w_3 = \alpha_3 = 0, \tag{4.90}$$

where we have also demanded that the Ricci scalar curvature must be finite at the origin. In addition, we find that u_2 and α_2 can be written in terms of u_0, w_0, α_0, w_2 and σ^2. The explicit forms of u_2 and α_2 are:

$$u_2 = \frac{2q^3 a_0^3 w_0 + \left(3q^2 a_0^2 - \sigma^2\right) u_0}{6h_0} + 2qa_0 w_2, \tag{4.91}$$

$$\alpha_2 = \frac{q\phi_0}{6}\left(q\phi_0\alpha_0 + 2qa_0 u_0 + \sigma^2 w_0\right). \tag{4.92}$$

In these expressions, we retain h_0 merely for completeness. In our numerical analysis h_0 will always set to be unity using the time-scaling symmetry (4.25). The next order terms in (4.89) are also given in terms of the five constants, u_0, w_0, α_0, w_2 and σ^2.

At the mirror, the scalar perturbation $\delta\psi$ must vanish so that

$$\tilde{u}(r_m) = \tilde{w}(r_m) = 0. \tag{4.93}$$

However, the electromagnetic perturbation δA_0 is unconstrained at $r = r_m$. The boundary condition (4.93) provides two constraints on the perturbation fields. Thus we require only two shooting parameters in the series expansions (4.89). In contrast, we now have five free parameters u_0, w_0, α_0, w_2 and σ^2. Since the perturbation equations (4.77–4.79) are linear, we thus have freedom to choose the overall scale of the perturbations. Therefore we set $u_0 = 0.5$ for all of the cases that we have considered (unless otherwise stated), this leaves only four unconstrained parameters.

Now we consider an infinitesimal $U(1)$ gauge transformation (4.11) with $\chi = \mathrm{Re}[\chi_0 e^{-i\sigma t}]$,

where χ_0 is a complex constant. The scalar field transforms as

$$\begin{aligned}\phi \to e^{i\chi}\phi &\approx (1+i\chi)\,\phi,\\ &= \frac{\bar{\psi}}{r} + \left[\frac{\delta u}{r} + i\frac{\delta \dot{w}}{r}\right] + i\chi\left[\frac{\bar{\psi}}{r} + \frac{\delta u}{r} + i\frac{\delta \dot{w}}{r}\right],\\ &= \frac{\bar{\psi}}{r} + \mathrm{Re}\left[\frac{\tilde{u}e^{-i\sigma t}}{r}\right] + i\mathrm{Re}\left[\left(-i\sigma\tilde{w} + \chi_0\bar{\psi}\right)\frac{e^{-i\sigma t}}{r}\right] + ...,\end{aligned} \tag{4.94}$$

where higher order terms in $\chi, \delta u$ and δw are ignored. Since A_0 is real, therefore it transforms as

$$\begin{aligned}A_0 \to A_0 + q^{-1}\chi_{,_0} &= \bar{A}_0 + \mathrm{Re}\left[\tilde{A}_0 e^{-i\sigma t} - i\sigma q^{-1}\chi_0 e^{-i\sigma t}\right],\\ &= \bar{A}_0 + \mathrm{Re}\left\{\left[\tilde{A}_0 - \frac{i\sigma\chi_0}{q}\right]e^{-i\sigma t}\right\}.\end{aligned} \tag{4.95}$$

Therefore, this gauge transformation gives

$$\sigma\tilde{w} \to \sigma\tilde{w} + i\bar{\psi}\chi_0, \qquad \tilde{A}_0 \to \tilde{A}_0 - \frac{i\sigma\chi_0}{q}. \tag{4.96}$$

In principle, we can use the freedom in χ_0 to eliminate any one of w_0, w_2 or α_0. In this case, we choose

$$\chi_0 = \frac{i\sigma w_0}{\phi_0}, \tag{4.97}$$

where we have used the series expansions near the origin (4.28) and (4.89). This gauge choice is equivalent to setting $w_0 = 0$.

Beyond this residual $U(1)$ gauge freedom, we also have a residual diffeomorphism freedom. In this case, we will consider an infinitesimal coordinate transformation of the form (4.80) generated by the vector field V^a such that

$$V^a = \left(\mathrm{Re}[x_0 e^{-i\sigma t}], 0, 0, 0\right), \tag{4.98}$$

where x_0 is an arbitrary complex constant. We note that the metric perturbations δf and δh transform under (4.98) as [134]

$$\delta f \to \delta f, \qquad \delta h \to \delta h + \bar{h}\dot{V}^0. \tag{4.99}$$

Furthermore, under the transformation (4.84), we can show the following

$$\begin{aligned} \delta A_0 &\to \delta A_0 + \bar{A}_0 \partial_0 V^0, \\ &= \mathrm{Re}\left\{ \left[\tilde{A}_0 - i\sigma\chi_0 \bar{A}_0 \right] e^{-i\sigma t} \right\}. \end{aligned} \tag{4.100}$$

So, the transformation of the electromagnetic field δA_0 implies that

$$\tilde{A}_0 \to \tilde{A}_0 - i\sigma \bar{A}_0 x_0. \tag{4.101}$$

In a similar way to (4.97), we can use this freedom to eliminate α_0 by setting

$$x_0 = -\frac{i\alpha_0}{\sigma a_0}, \tag{4.102}$$

where again we use the series expansion near the origin (4.28). Thus without loss of generality, we can set $\alpha_0 = 0$. Therefore, we now have only two arbitrary free parameters σ^2 and w_2. As will be seen later, for the black hole case, the boundary condition at the horizon will not allow us to use the residual $U(1)$ gauge freedom and the diffeomorphism freedom.

We are now ready to numerically integrate the perturbation equations (4.77–4.79). The series expansions near the origin (4.89) will be used as initial conditions, we thus scan for values of the shooting parameters σ^2 and w_2 such that the boundary conditions at the mirror (4.93) are satisfied. Since the only time derivative terms in the perturbation equations are $\delta\ddot{u}$ and $\delta\ddot{w}$, the perturbation equations (4.77–4.79) and boundary conditions (4.89, 4.93) depend only on σ^2. These then form an eigenvalue problem with σ^2 as the

eigenvalue. Since our perturbation equations (4.77–4.79) are not self-adjoint, therefore we cannot be sure that the eigenvalue σ^2 will always be a real number. If σ^2 is real, we consider the sign of σ^2. In fact, as can be seen later, for all the solitons we investigate, we find that σ^2 is real. If $\sigma^2 > 0$, i.e. σ is real number, the time-periodic perturbations do not grow with time and the corresponding static solitons are linearly stable. Otherwise if $\sigma^2 < 0$ and hence σ is purely imaginary, there exist exponentially growing perturbation modes which indicate that the corresponding equilibrium solutions are unstable.

4.5.4 Results for solitons

Our numerical scheme is set-up as follow. Firstly, by fixing $q = 0.1$ (using the scaling symmetry (4.23)) and assigning some numerical values to a_0 and ϕ_0, the equilibrium field equations (4.18–4.21) are numerically solved. We thus obtain a static soliton solution for which the mirror location can be found. Secondly, we integrate the perturbation equations (4.77–4.79) by using (4.89) as initial values. Since both the real and imaginary parts of the scalar field perturbations need to vanish at the mirror, we require two shooting parameters (Appendix A). With other parameters fixed, σ^2 and w_2 will be used as the shooting parameters. We seek values of σ^2 and w_2 such that the perturbation fields $\tilde{u}$ and $\tilde{w}$ vanish at the mirror $r = r_m$. We cannot start the integration at the origin where $r = 0$ since our equations become singular there. Therefore we initiate our numerical integration of the perturbation equations (4.77–4.79) at some radius close to the origin i.e., $r_{origin} = 10^{-3}$. See also Appendix A for more details of the Mathematica implementation.

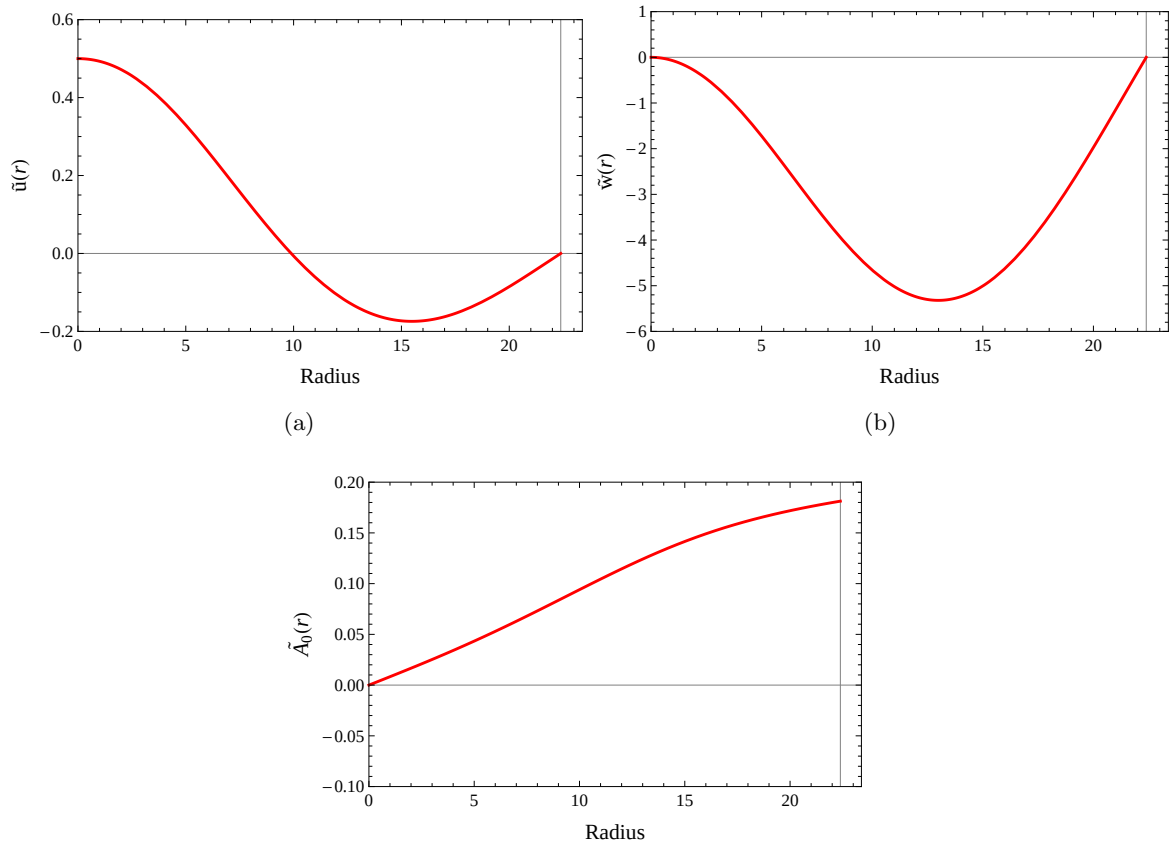

Figure 4.14: An example plot of the perturbation fields $\tilde{u}, \tilde{w}$ and $\tilde{A}_0$. We perturb a static soliton solution with scalar field charge $q = 0.1, a_0 = 1.5$ and $\phi_0 = 1.1$. The vertical line displays the location of the mirror which is $r_m \approx 22$. The corresponding eigenvalue is $\sigma^2 = 0.0083$ and $w_2 = -0.0250$. All three perturbations have been multiplied by an overall factor of 10^4, this is possible since the perturbation equations are linear.

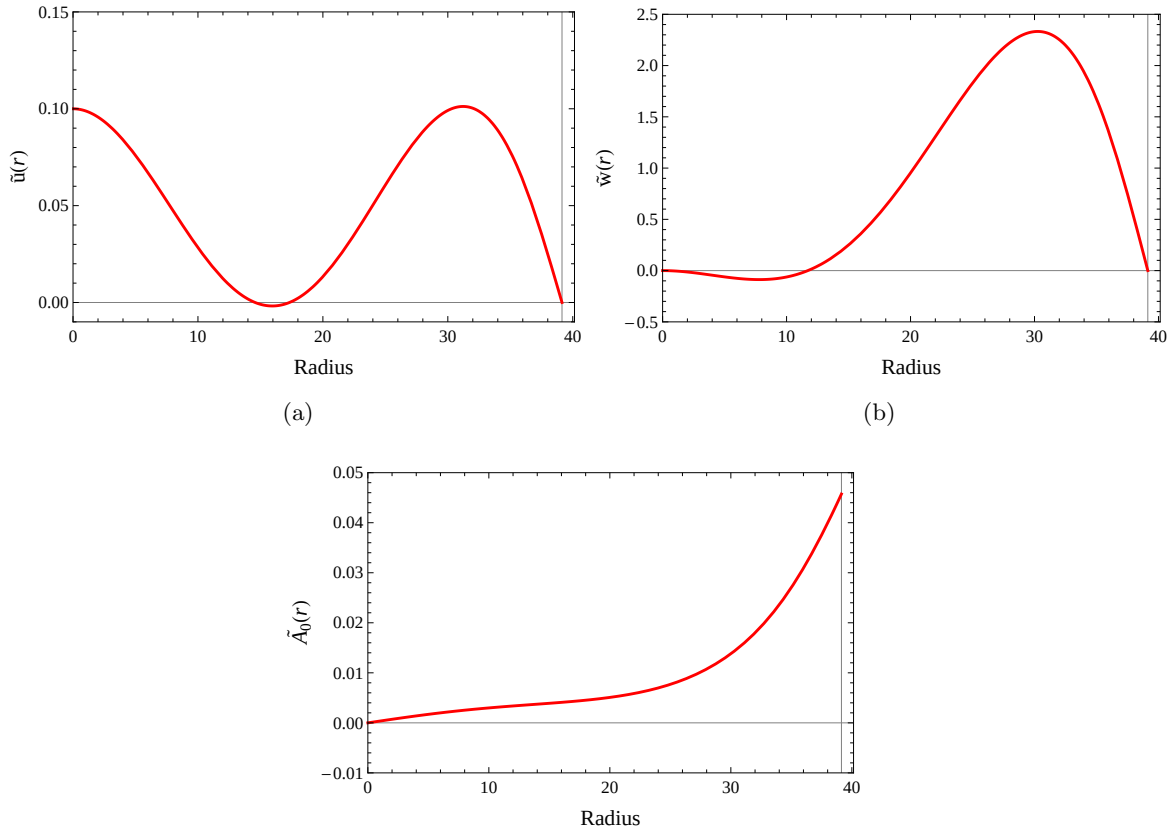

(a) (b)

(c)

Figure 4.15: An example plot of the perturbation fields $\tilde{u}, \tilde{w}$ and $\tilde{A}_0$. We perturb a static soliton solution with scalar field charge $q = 0.1, a_0 = 0.4$ and $\phi_0 = 0.9$. The vertical line displays the location of the mirror which is $r_m \approx 39$. The corresponding eigenvalue is $\sigma^2 = 0.0210$ and $w_2 = -0.0013$. All three perturbations have been multiplied by an overall factor of 10^4, this is possible since the perturbation equations are linear. Moreover in this case u_0 is fixed to be 0.1 rather than 0.5.

In Fig 4.14 and 4.15, the typical behaviour of the perturbations $\tilde{u}, \tilde{w}$ and $\tilde{A}_0$ is shown. As an example in Fig 4.14, an equilibrium soliton solution with scalar field charge $q = 0.1$, $a_0 = 1.5$ and $\phi_0 = 1.1$ is perturbed. The numerical values of the two free parameters are $\sigma^2 = 0.0083$ and $w_2 = -0.0250$. The mirror is located at $r_m \approx 22$. It is clear from the plots that $\tilde{u}$ and $\tilde{w}$ vanish at the mirror as demanded by the boundary conditions (4.93). Since the corresponding eigenvalue σ is real number, therefore this static soliton solution is

linearly stable. In Fig 4.15, the background parameters are given by $q = 0.1, a_0 = 0.4$ and $\phi_0 = 0.9$, with the first zero of the scalar field at $r_m \approx 39$. The corresponding eigenvalue σ^2 and free parameter w_2 are 0.0210 and -0.0013, respectively. Note that, we have set $u_0 = 0.1$ in this plot. This is just to illustrate that the value of u_0 does not affect the overall structure of the plot except the initial value of $\tilde{u}$. In these two figures, we have set $r_{origin} = 10^{-4}$. It appears in these plots that $\tilde{u}$ does not vanish at the origin. The reason behind this is that in our set-up both $\tilde{w}$ and $\tilde{A}_0$ vanish as $r \to 0$ much more quickly than $\tilde{u}$. In practice, we plot $\tilde{u}/r_{origin}, \tilde{w}/r_{origin}$ and $\tilde{A}_0/r_{origin}$ so that the scalar perturbations $\tilde{u}/r$ and $\tilde{w}/r$ are finite as $r \to 0$.

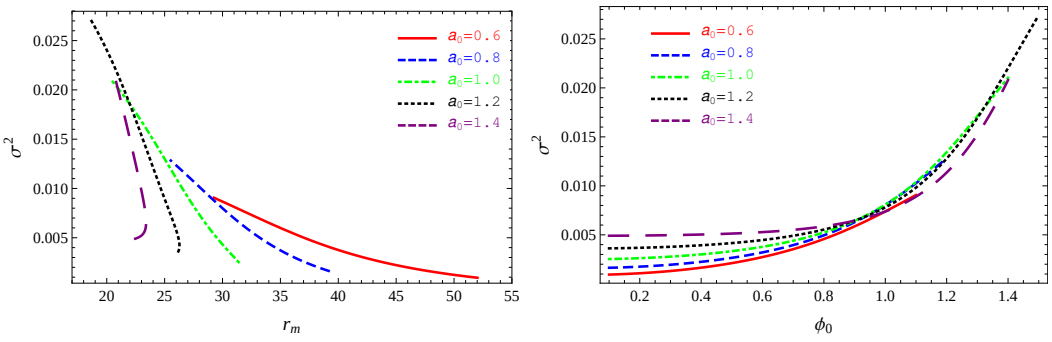

(a) (b)

Figure 4.16: The lowest eigenvalues σ^2 for equilibrium solitons with scalar field charge $q = 0.1$, various fixed values of a_0 and $\phi_0 \in [0.1, 1.6]$. (a) Plot of σ^2 as a function of mirror radius r_m, (b) Plot of σ^2 as a function of a_0.

With fixed scalar field charge $q = 0.1$, plots of σ^2 for various fixed values of a_0 and values of ϕ_0 lying in the interval $(0.1, 1.6)$ are shown in Fig 4.16. For the equilibrium solutions with $\phi_0 > 1.6$, our numerical method breaks down, the perturbation equations become stiff. In Fig 4.16, the same data for the eigenvalue σ^2 is plotted, firstly as a function of the mirror radius r_m in Fig 4.16(a) and secondly as a function of ϕ_0 in Fig 4.16(b). In general, for fixed a_0, the eigenvalue σ^2 decreases as r_m increases and ϕ_0 decreases. In Fig 4.16(a), there is a double-valued curve for $a_0 = 1.4$. This is because for this fixed value $a_0 = 1.4$, it is possible to have two static soliton solutions with different values of ϕ_0 but the same

value of mirror radius r_m as shown in Fig 4.4. Since we find that all the eigenvalues σ^2 in Fig 4.16 are positive, therefore the equilibrium solitons with these values of a_0 and ϕ_0 are all stable.

In Fig 4.17, we plot σ^2 for various fixed values of ϕ_0 and values of a_0 lying in the interval $(0.2, 3.0)$. The left-hand plots show the lowest eigenvalue σ^2 as a function of mirror radius r_m, while the right-hand plots show the same data for σ^2 but as a function of a_0. In Fig 4.18, the same data for σ^2 is repeated but with a few fixed values of ϕ_0 in each plot, in order to observe the behaviour of σ^2 more easily. In the left-hand plots of Fig 4.18, we find that when $\phi_0 = 0.8$, the eigenvalue σ^2 is always positive and also monotonically decreases as r_m increases. However for larger ϕ_0, namely $\phi_0 \geq 1.1$, the behaviour of the eigenvalue σ^2 becomes quite complicated. Firstly, as r_m decreases the eigenvalue σ^2 becomes smaller and is negative at some point, this is shown in Fig 4.18(a). Secondly in Fig 4.18(c), the plot of σ^2 as a function of r_m is double-valued because for certain values of ϕ_0, there are two values of a_0 that have the same r_m as illustrated in the phase space Fig 4.4. In contrast, in Fig 4.18(e), as r_m increases σ^2 decreases and becomes negative at a certain point. For the curves $\phi_0 = 1.9$ and 2.0, although we find no change of sign in σ^2, we would expect to see a transition from positive to negative σ^2 if we extended a_0 beyond 3.0. In addition, we observe that for all the cases explored here, the negative σ^2 occurs only when $r_m < 20$. With $\sigma^2 < 0$, these solutions are shown to be unstable.

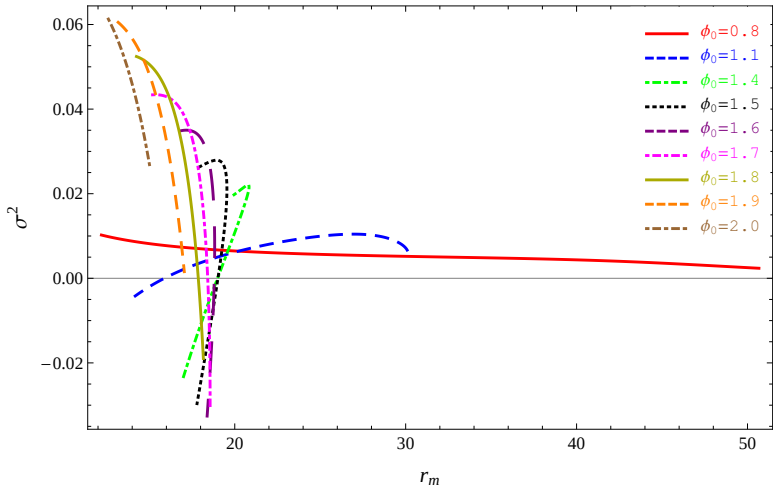

(a)

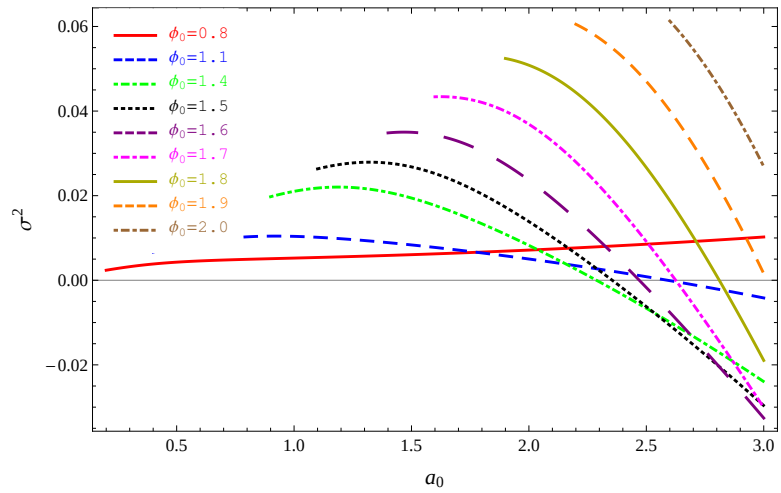

(b)

Figure 4.17: The lowest eigenvalues σ^2 for equilibrium solitons with scalar field charge $q = 0.1$, various values of fixed ϕ_0 and $a_0 \in [0.2, 3.0]$. (a) Plot of σ^2 as a function of mirror radius r_m, (b) Plot of σ^2 as a function of ϕ_0.

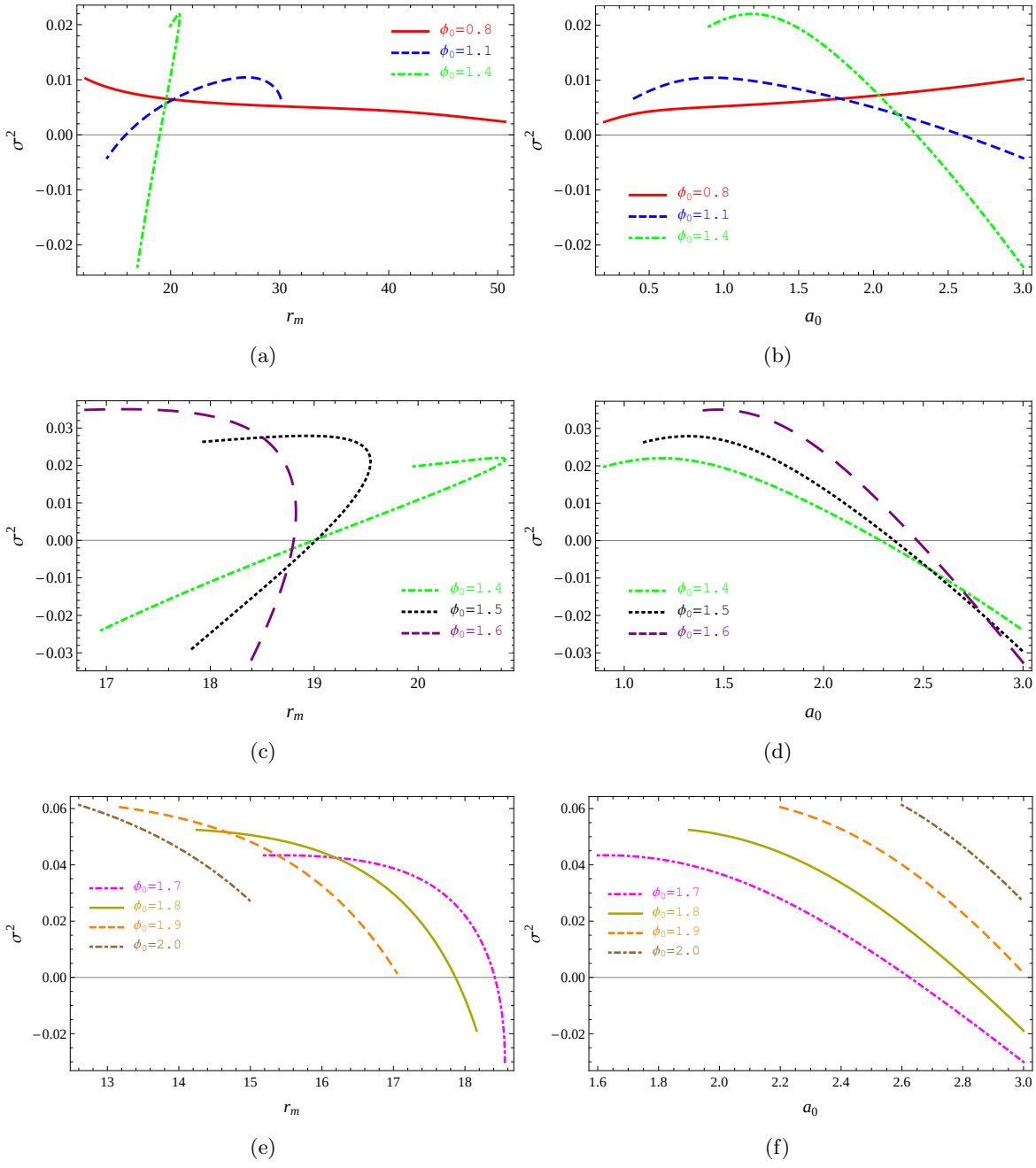

Figure 4.18: The same data for σ^2 is plotted here to make the behaviour in Fig 4.17 more visible.

We consider the behaviour of σ^2 as a function of a_0 in the plots in the right-hand column of Fig 4.18. At the lowest value of ϕ_0 considered here, namely $\phi_0 = 0.8$, the eigenvalue σ^2 is always positive and increasing as a_0 becomes larger. We expect similar behaviour for smaller values of ϕ_0. However as ϕ_0 gets larger, we start to see the transition from stability to instability. More specifically, as a_0 increases the eigenvalue σ^2 gradually decreases and becomes negative for sufficiently large a_0. The behaviour of the critical value of a_0 for which σ^2 changes the sign is not straightforward. For a lower value of ϕ_0, it decreases as ϕ_0 increases, this is illustrated by Fig 4.18(b). However for $\phi_0 \geq 1.4$, the "transition points" increase as ϕ_0 increases as can be seen from Fig 4.18(d) and 4.18(f). We see that the solitons with smaller values of a_0 are stable but become unstable with larger values of a_0. We deduce that the stability of the equilibrium soliton solutions depends on the value of the scalar field and electromagnetic potential at the origin, ϕ_0 and a_0 respectively. For sufficiently small ϕ_0 and a_0 (hence, large r_m), our numerical results suggest that the solitons are stable. In contrast, for sufficiently large ϕ_0 and a_0 (hence, small r_m), at least some of the solitons appear to be unstable.

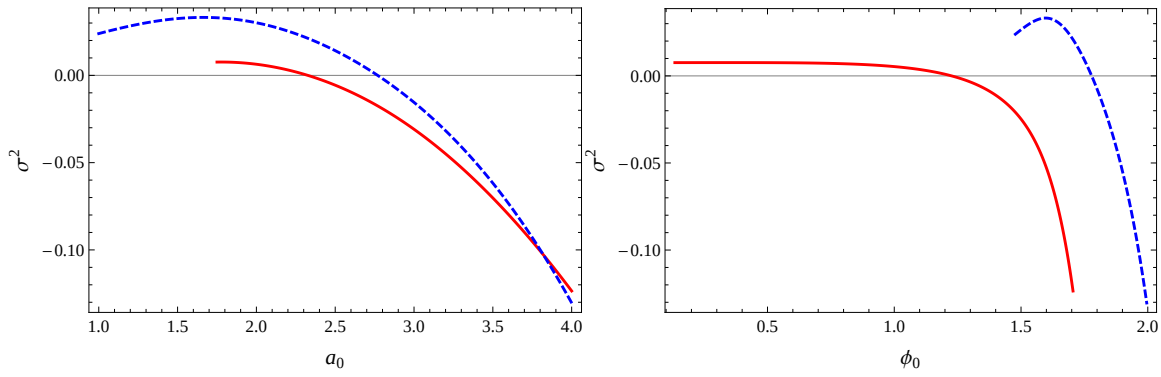

(a) (b)

Figure 4.19: Lowest eigenvalue σ^2 for static solitons with fixed scalar charge $q = 0.1$ and mirror radius $r_m = 18$. The solutions considered here belong to those lying on the portion of the contour displayed in Fig 4.7. (a) σ^2 as a function of a_0. (b) σ^2 as a function of ϕ_0.

For fixed mirror radius $r_m = 18$, we illustrate how the eigenvalue σ^2 depends on the parameters a_0 and ϕ_0 in Fig 4.19. The equilibrium solutions considered in this figure are lying on the part of $r_m = 18$ contour shown in Fig 4.7. That is, the red and blue curves in this figure correspond to the red and blue curves displayed in Fig 4.7. From Fig 4.19, the solitons are stable ($\sigma^2 > 0$) for small a_0 and ϕ_0. However for large a_0 and ϕ_0, the soliton solutions are found to be unstable ($\sigma^2 < 0$).

4.5.5 Interpretation of the stability of the solitons

As discussed in the previous subsection, the stability properties of charged scalar solitons are not straightforward. In fact, as will be seen later, the stability of the solitons is rather more complicated than the black hole case. More analysis is therefore needed to better understand the stability behaviour of the solitonic solutions. In this subsection, we will discuss how we may make sense of the stability of the solitons presented above.

Since AdS spacetime naturally provides a time-like boundary which is similar to the reflecting boundary, a close analogy to our charged scalar solitons in a cavity could be solitonic solutions in asymptotically AdS spacetime. Our length-scale r_m plays the same role as AdS radius of curvature l. Charged scalar solitons have been studied in four dimensional AdS spacetime [75] and in AdS_5 [59]. In addition, these works consider the $(M, Q)-$phase space of solitons, where M and Q are the mass and charge of the asymptotically AdS solitons. Therefore, to qualitatively compare our results with these solitons in AdS, it would be considered helpful to firstly construct the mass and charge of our charged scalar solitons.

We could define the mass M of the charged scalar solitons by using Komar mass formula

$$M = \frac{1}{4\pi} \int_{\partial\Sigma} d^2x \sqrt{\rho^{(2)}} n_a \varsigma_b \nabla^b \xi^a, \tag{4.103}$$

where $\partial\Sigma$ denotes the boundary of the space-like hypersurface Σ, $\rho^{(2)}$ is the determinant

of the two dimensional induced metric, n_a and ς_b are the unit normal vector to the hypersurface Σ and the outward-pointing normal vector associated to the boundary $\partial\Sigma$ and $\xi = \partial/\partial t$ is the time-like Killing vector. For a static spherically symmetric asymptotically flat spacetime, the time-like Killing vector ξ can be normalized by demanding that $\xi^a\xi_a \to -1$ as $r \to \infty$. The solitons considered here are static, hence each one possesses a time-like Killing vector ξ. However, we do not have an asymptotically flat spacetime. Thus, we cannot consistently normalize the time-like Killing vector across the solution space. Therefore, for the Komar integral above (4.103), it is not clear to us how to compare the masses of different solitonic solutions. For this reason, we decided not to define a total mass for our solitons. The absence of a robust definition of soliton mass makes it difficult to draw comparisons between our solitons in a cavity and those solutions in AdS space.

In contrast, for each static equilibrium solution, we can define its electric charge by

$$\begin{aligned} Q &= -\frac{1}{4\pi}\int_\Sigma d^3x\sqrt{\rho^{(3)}}n_a J^a, \\ &= -\frac{1}{4\pi}\int_\Sigma d^3x\sqrt{\rho^{(3)}}n_a \nabla_b F^{ba}, \end{aligned} \tag{4.104}$$

where we make use of the Maxwell equation (4.5) in the last step. This integral is taken over a t = constant hypersurface Σ where $\rho^{(3)}$ is the determinant of the induced three dimensional metric. Applying Stokes' theorem, we can rewrite this integral as

$$Q = -\frac{1}{4\pi}\int_{\partial\Sigma} d^2x\sqrt{\rho^{(2)}}n_a\varsigma_b F^{ba}. \tag{4.105}$$

The unit normal vectors n_a and ς_b to $\partial\Sigma$ are given by

$$n_a = (-(\bar{f}\bar{h})^{1/2}, 0, 0, 0), \qquad \varsigma_b = (0, \bar{f}^{-1/2}, 0, 0). \tag{4.106}$$

Integrating the charge integral (4.105) over the two sphere on the mirror yields

$$\begin{aligned} Q &= -\frac{1}{4\pi}\int d^2x\sqrt{\rho^{(2)}}\left(\frac{\bar{A}_0'(r_m)}{\sqrt{\bar{h}(r_m)}}\right), \\ &= -\frac{1}{4\pi}\int d\theta d\varphi\left(\frac{r_m^2\bar{A}_0'(r_m)\sin\theta}{\sqrt{\bar{h}(r_m)}}\right), \\ &= -\frac{r_m^2\bar{A}_0'(r_m)}{\sqrt{\bar{h}(r_m)}}. \end{aligned} \tag{4.107}$$

This formula reduces to the usual definition of the electric charge for the Reissner-Nordstörm solution when $r_m \to \infty$. According to (4.107), we shall now explore how the charge Q of the equilibrium solitons depends on r_m, a_0 and ϕ_0.

In Fig 4.20, we plot the charge Q as a function of mirror radius r_m for solitons with $q = 0.1$ for fixed values of a_0 and ϕ_0. The same data is repeated in the right-hand plots of this figure but as a function of a_0 and ϕ_0 as applicable. With fixed ϕ_0, the behaviour of the charge Q is displayed in the top row of Fig 4.20. We observe that at lower values of fixed ϕ_0, the charge Q increases as r_m increases. Also from Fig 4.6, we see that r_m decreases as a_0 increases for small ϕ_0. Therefore, the charge Q decreases monotonically as a_0 increases for all ϕ_0 shown. At larger fixed values of ϕ_0, such as, $\phi_0 = 1.5$, it is possible to have two different values of electric charge Q at the same mirror radius r_m. This is because there are two equilibrium solutions with the same r_m and ϕ_0 but different a_0. We expect the same behaviour for $\phi_0 = 2.0$ if we extend the curve by including larger values of a_0. For fixed a_0, the behaviour of the charge Q as a function of r_m and ϕ_0 is shown in the bottom row of Fig 4.20. For the values of a_0 shown, there are two values of charge Q, one larger than the other, for the same mirror radius r_m. In addition, the charge Q increases monotonically as ϕ_0 increases.

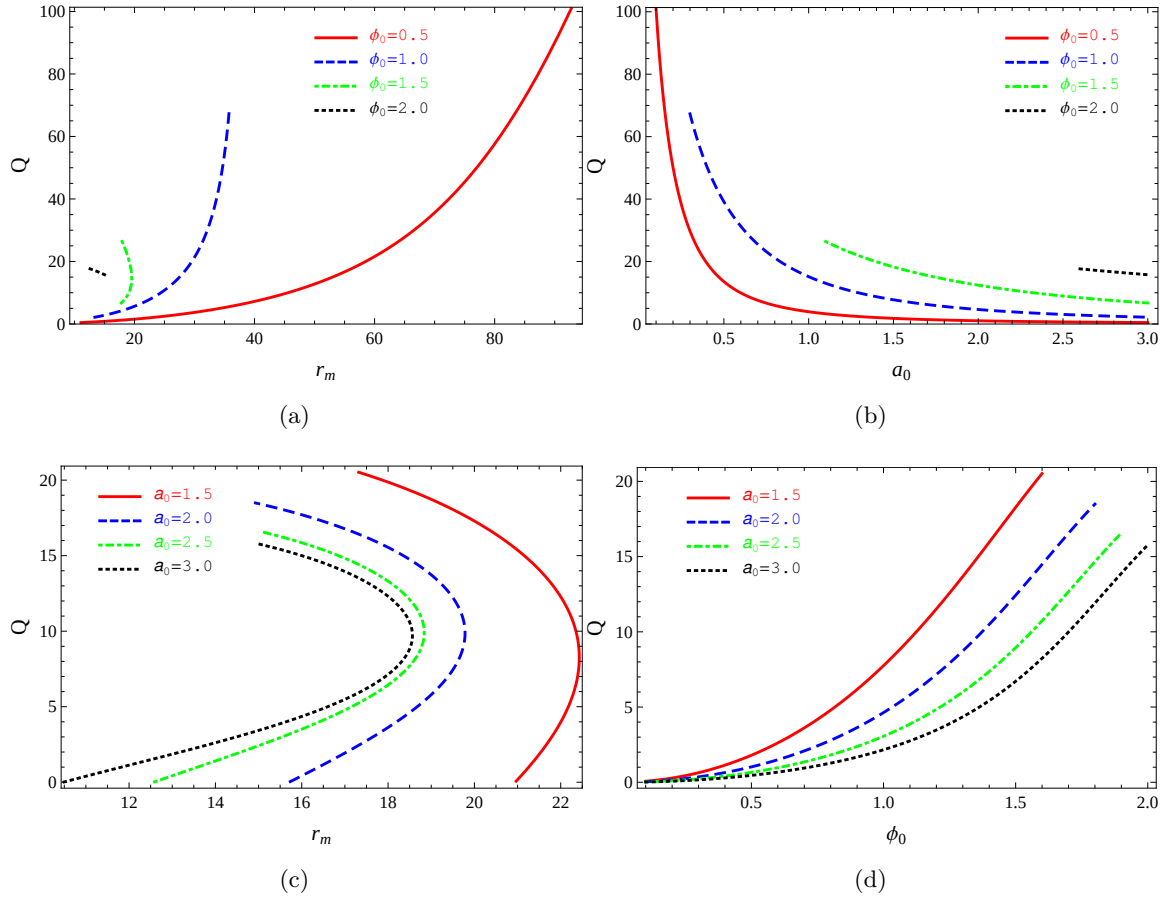

Figure 4.20: The electric charge Q of equilibrium solitons as a function of the parameters r_m, a_0 and ϕ_0 for fixed scalar charge $q = 0.1$. (a)–(b) various fixed values of ϕ_0 and $a_0 \in [0.1, 3.0]$. (c)–(d) various fixed values of a_0 and $\phi_0 \in [0.1, 2.0]$. We remark that the data from the left-hand plots is repeated in the right-hand plots, but with the electric charge Q as a function of a_0 or ϕ_0 rather than mirror radius r_m.

With fixed $r_m = 18$, Fig 4.21 illustrates the charge Q as a function of the parameters ϕ_0 and a_0 for a static scalar field with $q = 0.1$. The electric charge in this figure corresponds to those soliton solutions shown in Fig 4.7. In Fig 4.21, there are two distinct branches of solutions corresponding to the two parts of the contour curves shown in Fig 4.7. The two plots show the same data but with different parameters ϕ_0 and a_0. At fixed a_0, the solutions with larger ϕ_0 have also larger Q. From now on, we will refer to the branch of

solutions with larger charge Q as the "high-charge" branch and the branch with smaller Q as the "low-charge branch".

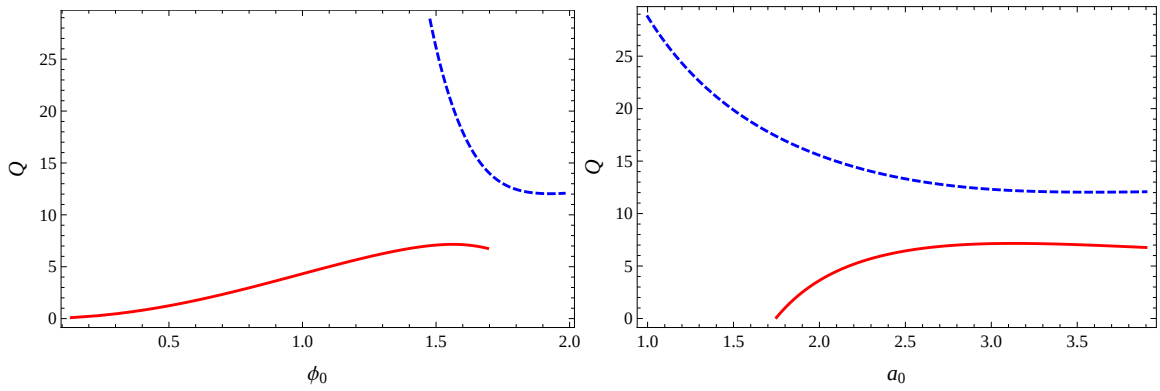

(a) (b)

Figure 4.21: The electric charge Q of equilibrium solitons with scalar field charge $q = 0.1$ as a function of the parameters ϕ_0 and a_0. The mirror is at the first node of the equilibrium scalar field and is fixed at $r_m = 18$. The red and blue curves correspond to the portions of the contour displayed in Fig 4.7. The two plots display the same data, but plotted as a function of different parameters ϕ_0 and a_0.

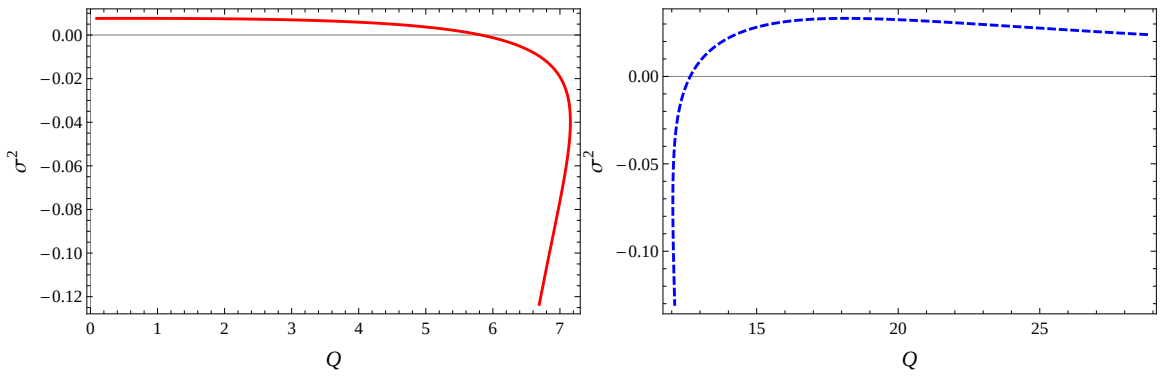

(a) (b)

Figure 4.22: Lowest eigenvalue σ^2 for static solitons with fixed scalar charge $q = 0.1$ and mirror radius $r_m = 18$ as a function of the electric charge Q. The solutions considered here belong to those lying on the portion of the contour displayed in Fig 4.7. (a) σ^2 as a function of Q for the low-charge branch. (b) σ^2 as a function of Q for the high-charge branch.

The lowest eigenvalue σ^2 is plotted against the electric charge Q for static solitons with fixed scalar field charge $q = 0.1$ and mirror radius $r_m = 18$ in Fig 4.22. Note that the red and blue curves in this figure correspond to the red and blue curves in Fig 4.7, Fig 4.19 and also Fig 4.21. The stability of the low-charge branch (the branch of solutions with smaller ϕ_0 for fixed a_0) is illustrated in Fig 4.19(a) and the high-charge branch (the branch of solutions with larger ϕ_0 for fixed a_0) is displayed in Fig 4.19(b). We find both stable and unstable solitons on both of these branches. On the low-charge branch, the solitons with smaller charge Q are stable and those with larger charge Q are unstable. In contrast, on the high-charge branch, solitons with larger values of Q are stable while those with lower values of Q are unstable.

Now let us briefly summarize the stability of solitons. We have seen that if the mirror radius r_m is sufficiently large, the lowest eigenvalue σ^2 is positive for all the soliton solutions we have examined. Therefore the frequency σ is real and the solitons are linearly stable. On the other hand, for sufficiently small values of the mirror radius r_m, some of the solitons we have considered possess negative σ^2, so that the frequency σ is imaginary. Hence some equilibrium solitons are found to be unstable when they live in a small cavity. The phase space (a_0, ϕ_0) for a constant small r_m has a complicated structure. For fixed a_0, there are two soliton solutions with two distinct ϕ_0. The branch of solutions with larger ϕ_0 typically has higher soliton charge Q than the branch of solutions with lower ϕ_0. There are both stable and unstable solutions on both the high-charge and low-charge branches. In addition, the solitons on both branches are unstable when a_0 and ϕ_0 become sufficiently large.

Instead of the solitons in AdS spacetime, we consider a system that more closely analogous to our solitons in a cavity which is boson stars. A boson star is a soliton solution in models containing a time-dependent complex scalar field with a self-interacting term. For a recent review on boson stars see [118]. In asymptotically flat spacetime, stable boson stars are found if the central density is smaller than a certain critical value and boson stars become

unstable if the central density is larger than the critical value [78, 116]. In our case, the value of the scalar field at the origin ϕ_0 plays the same role as the central density in boson stars. For charged boson stars in asymptotically flat spacetime [103] and boson stars in asymptotically AdS spacetime [64], the same behaviour is observed. A non-linear study [65] has shown that an unstable boson star in asymptotically flat spacetime will either collapse to form a black hole or the scalar field radiates away to infinity leaving a stable boson star. Another possibility is that the unstable boson stars radiate the excess energy and migrate to the stable branch.

So what could be the end-point of the instability of the solitons we have found? In our case, there is no mechanism that allows the scalar field to escape to infinity. Therefore we conjecture that unstable charged solitons could collapse and form black holes. These black holes could either be Reissner-Nordström or a black hole with charged scalar hair [61] (see subsection 4.4.2). To determine the actual end-point of this instability, a full non-linear evolution of this system would be needed.

4.5.6 Boundary conditions for black holes

In this subsection, we derive the boundary conditions on the perturbations of the scalar field $\delta\psi$ and electromagnetic potential δA_0 at the horizon $r = r_h$. In subsection 4.5.7 we will show that by putting the mirror at the first node of the scalar field, all the black hole solutions we have considered are stable. On the other hand, if the mirror is located at the second node of the scalar field, our results show that these configurations are unstable.

At the horizon, we impose ingoing boundary conditions defined by

$$\begin{aligned}
\delta u(t,r) &= \mathrm{Re}\left[e^{-i\sigma(t+r_*)}\tilde{u}(r)\right], \\
\delta w(t,r) &= \mathrm{Re}\left[e^{-i\sigma(t+r_*)}\tilde{w}(r)\right], \\
\delta A_0(t,r) &= \mathrm{Re}\left[e^{-i\sigma(t+r_*)}\tilde{A}_0(r)\right],
\end{aligned} \tag{4.108}$$

where $\tilde{u}, \tilde{w}$ and $\tilde{A}_0$ are complex functions of the radial coordinate r only. The tortoise coordinate r_* is given by

$$\frac{dr_*}{dr} = \frac{1}{\bar{\gamma}}. \tag{4.109}$$

We assume that near the horizon the complex functions $\tilde{u}, \tilde{w}$ and $\tilde{A}_0$ have regular Taylor series expansions of the form

$$\begin{aligned}
\tilde{u} &= \tilde{u}_0 + \tilde{u}_1(r - r_h) + O(r - r_h)^2, \\
\tilde{w} &= \tilde{w}_0 + \tilde{w}_1(r - r_h) + O(r - r_h)^2, \\
\tilde{A}_0 &= \tilde{A}_1(r - r_h) + \tilde{A}_2(r - r_h)^2 + O(r - r_h)^3.
\end{aligned} \tag{4.110}$$

Unlike the soliton case, with the ingoing boundary conditions (4.108), we loose the residual $U(1)$ gauge freedom and diffeomorphism freedom. By choosing the boundary conditions (4.108), we have effectively fixed our choice of time-coordinate. There is also no gauge transformation (4.11) which preserves the form of the electromagnetic potential near the horizon. By substituting these series expansions (4.108, 4.110) into the perturbation equations (4.77–4.79), we find that $\tilde{u}_1, \tilde{w}_1, \tilde{A}_1, \tilde{A}_2$ and all higher-order coefficients can be written

in terms of $\tilde{u}_0, \tilde{w}_0$ and σ. They are given by

$$\tilde{u}_1 = \frac{-8q\mathcal{E}_h r_h^2 \sigma^2 \tilde{w}_0 + \mathcal{B}^2 \tilde{u}_0}{r_h \mathcal{B}\left(4ir_h\sigma + \mathcal{B}\right)}, \tag{4.111}$$

$$\tilde{w}_1 = \frac{-8q\mathcal{E}_h r_h^2 \left(\mathcal{B} + 2ir_h\sigma\right)\tilde{u}_0 + \left[\mathcal{B}^2\left(\mathcal{B} + 2ir_h\sigma\right) + 4ir_h\sigma\left(\mathcal{B}+4\right)\mathcal{Q}_h^2\right]\tilde{w}_0}{r_h\mathcal{B}\left(\mathcal{B}+2ir_h\sigma\right)\left(\mathcal{B}+4ir_h\sigma\right)}, \tag{4.112}$$

$$\tilde{A}_1 = -\frac{i\left(\mathcal{B}+4\right)q\phi_h\sigma\tilde{w}_0}{r_h\left(\mathcal{B}+2ir_h\sigma\right)}, \tag{4.113}$$

$$\begin{aligned}\tilde{A}_2 = {} & \frac{\left(4q\mathcal{Q}_h\mathcal{E}_h\mathcal{B}^3 - 2iqr_h\mathcal{Q}_h\mathcal{E}_h\left(\mathcal{B}-6\right)\mathcal{B}^2\sigma - 16qr_h^2\mathcal{Q}_h\mathcal{E}_h\mathcal{B}\sigma^2\right)}{r_h^2\mathcal{B}^2\left(\mathcal{B}+ir_h\sigma\right)\left(\mathcal{B}+2ir_h\sigma\right)\left(\mathcal{B}+4ir_h\sigma\right)}\tilde{u}_0 \\ & + \frac{\mathcal{Q}_h\sigma\tilde{w}_0}{r_h^3\mathcal{B}^2\left(\mathcal{B}+ir_h\sigma\right)\left(\mathcal{B}+2ir_h\sigma\right)\left(\mathcal{B}+4ir_h\sigma\right)}\left[i\mathcal{B}^2\left\{\left(\mathcal{B}+4\right)\mathcal{B}^2 - 2\left(5\mathcal{B}+12\right)\mathcal{Q}_h^2\right\}\right. \\ & + \mathcal{B}r_h\left\{\left(88+34\mathcal{B}-3\mathcal{B}^2\right)\mathcal{Q}_h^2 - 2\mathcal{B}^2\left(3\mathcal{B}+11\right)\right\}\sigma \\ & \left. - 4ir_h^2\left\{\mathcal{B}^2\left(3\mathcal{B}+10\right) + \left(\mathcal{B}-12\right)\mathcal{E}_h^2\mathcal{Q}_h^2\right\}\sigma^2\right],\end{aligned} \tag{4.114}$$

where we introduce $\mathcal{B} \equiv \left(\mathcal{E}_h^2 - 2\right), \mathcal{E}_h \equiv r_h E_h$ and $\mathcal{Q}_h \equiv q r_h \phi_h$. When the background parameters q, ϕ_h and E_h are given, the boundary conditions only depend on the three complex parameters $\tilde{u}_0, \tilde{w}_0$ and σ.

As in the soliton case, at the mirror $r = r_m$, we demand that only the scalar perturbations $\delta\psi$ (hence δu and δw) vanish (4.93). In particular, we require that both the real and imaginary part of $\tilde{u}$ and $\tilde{w}$ vanish at the mirror. This is to make sure that the real and imaginary part of the scalar field perturbations $\delta\psi$ vanish for all time t when the real part is taken (4.108). Moreover, there are no constraints on other perturbation fields, i.e., $\delta A_0, \delta f, \delta h$ and $\delta\gamma$ at the mirror.

Similarly to the soliton case, we can make use the freedom to add any function of r to δw in (4.69), to set $\delta\mathcal{H}(r) \equiv 0$. We then can write $\delta\mathcal{F}$ purely in terms of $\mathcal{E}$ as shown in (4.87). At the horizon, it must be the case that $\delta f = 0$ so that the black hole event horizon does not change. This implies that $\delta f / \bar{f}$ is finite at the horizon. Then, from (4.68), $\delta\mathcal{F}$ must be finite at the horizon as well. This can only happen if $\mathcal{E} \equiv 0$ from (4.87), so that $\delta\mathcal{F} = 0$. Thus (4.76) yields $\delta\mathcal{G} \equiv 0$. Hence once again, we can eliminate the $\delta\mathcal{F}', \delta\mathcal{F}$ and $\mathcal{E}$ terms

from the perturbation equations (4.77–4.79).

Since all the perturbation equations and boundary conditions are linear, we can fix the overall scale of the perturbations such that $\tilde{w}_0 = 1$. This leaves only σ and $\tilde{u}_0$ as free parameters when the background quantities q, ϕ_h and E_h are given. Therefore, with a fixed value of $\tilde{w}_0$, the perturbation equations (4.77–4.79) together with the boundary conditions (4.93, 4.108) define an eigenvalue problem with σ as the eigenvalue. In this case, we seek the eigenvalue σ such that $\mathrm{Im}(\sigma) \leq 0$ for stable equilibrium solutions, whereas $\mathrm{Im}(\sigma) > 0$ will imply that the black hole solutions are unstable. This is because $\mathrm{Im}(\sigma) = 0$, $\mathrm{Im}(\sigma) < 0$ and $\mathrm{Im}(\sigma) > 0$ correspond to stationary, exponential decay and growth of the perturbation fields, respectively.

4.5.7 Results for black holes

The numerical method for the black hole case is very similar to that used in the soliton case. In this case we make use of the length scaling symmetry (4.23) to set the black hole radius r_h to be unity. Therefore, the black hole solution space is described by the three background parameters q, ϕ_h and E_h as shown in Fig 4.11. Once these quantities are given, we can numerically solve the static field equations (4.18–4.21) and obtain a hairy black hole solution. After that, we can find the mirror location r_m. We then integrate the perturbation equations (4.77–4.79) by using the boundary conditions (4.110) as initial data. We seek the eigenvalue σ and parameter $\tilde{u}_0$ such that the scalar field perturbations satisfy the boundary conditions at the mirror (4.93). Hence in this case, σ and $\tilde{u}$ will become our shooting variables for the numerical shooting scheme (see Appendix A). Unlike the soliton case, here σ is in general complex, therefore $\tilde{u}, \tilde{w}$ and $\tilde{A}_0$ in (4.108) will also be complex functions. For most of the cases we will examine below, the mirror will be placed at the first zero of the equilibrium scalar field unless otherwise stated.

Fig 4.23 displays an example plot of $\tilde{u}, \tilde{w}$ and $\tilde{A}_0$ for a static black hole solution with fixed values of scalar field charge $q = 0.1, E_h = 0.8$ and $\phi_h = 1.2$. The corresponding eigenvalue

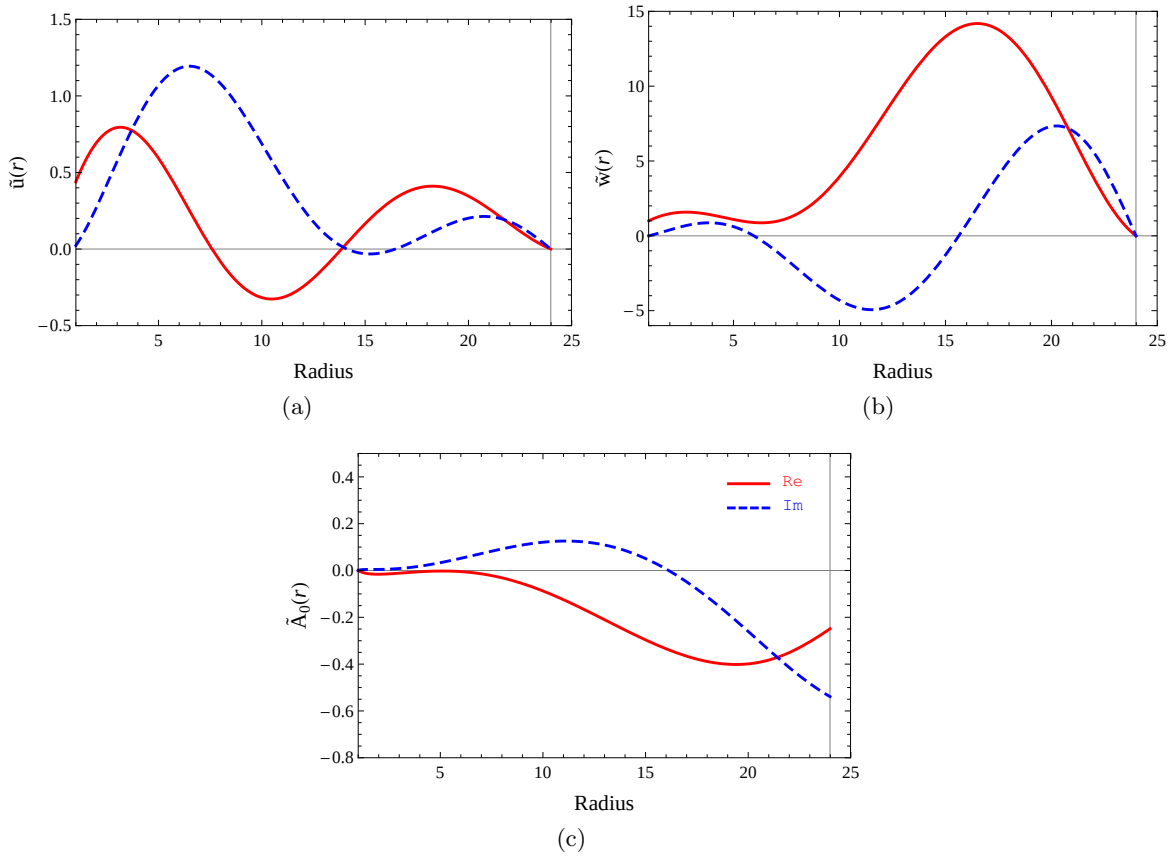

Figure 4.23: An example plot of the perturbation fields $\tilde{u}, \tilde{w}$ and $\tilde{A}_0$. We perturb a static black hole solution with scalar field charge $q = 0.1, E_h = 0.8$ and $\phi_h = 1.2$. The vertical line displays the location of the mirror which is $r_m \approx 24$. The corresponding eigenvalue is $\sigma = 0.1731 - 0.0038i$ and $\tilde{u}_0 = 0.4397 + 0.0231i$.

σ is $0.1731 - 0.0038i$ and the shooting parameter $\tilde{u}_0 = 0.4397 + 0.0231i$. In these plots, we can clearly see that both the real and the imaginary parts of $\tilde{u}$ and $\tilde{w}$ vanish at the mirror location $r_m \approx 24$. On the other hand, the perturbation of the electric potential $\tilde{A}_0$ is not required to be zero at the mirror. This example demonstrates that this particular black hole is stable since the perturbation mode decays exponentially with time, i.e., $\mathrm{Im}(\sigma) < 0$.

As shown in the black hole solution space Fig 4.11, the static black hole solutions are defined by three parameters, charge of the scalar field q, electric field at the horizon E_h and the equilibrium scalar field at the horizon ϕ_h. Therefore we will now present a selection

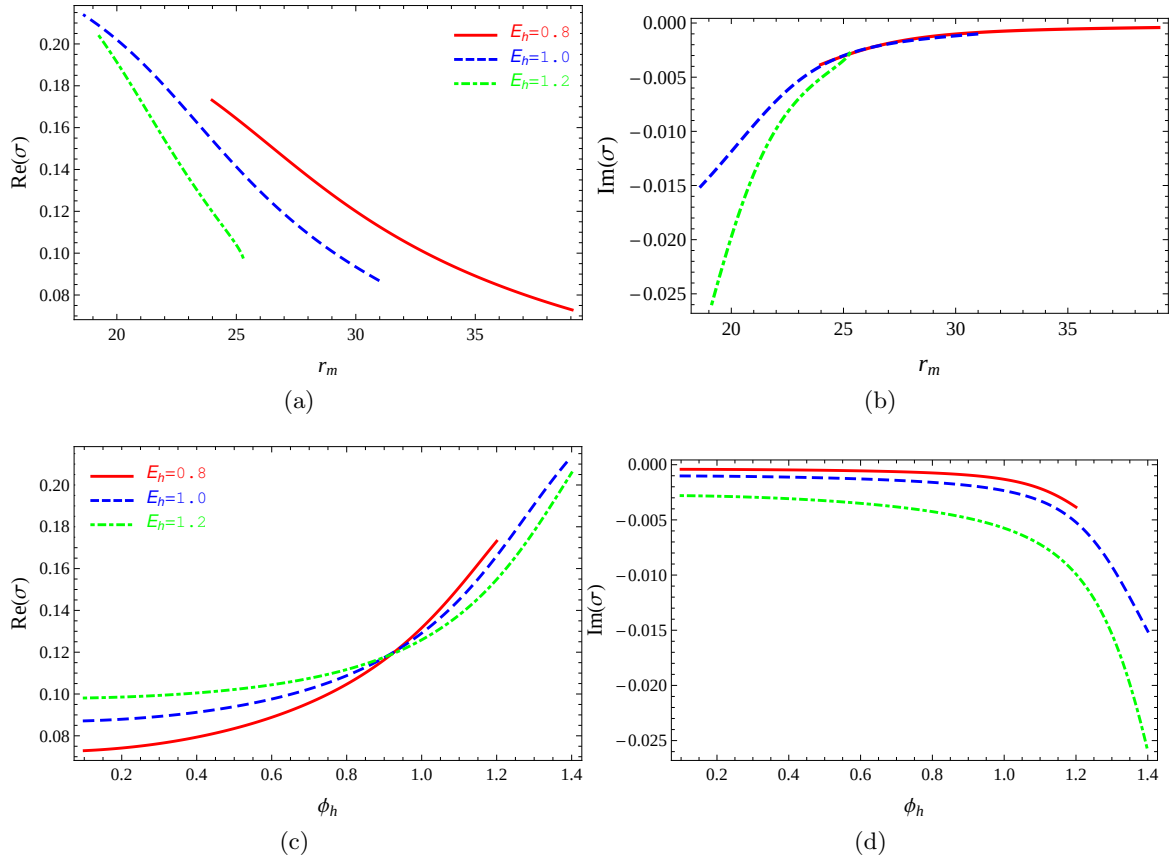

Figure 4.24: The real (left) and imaginary (right) part of the eigenvalue σ plotted as a function of mirror radius r_m (top) and the equilibrium scalar field at the horizon ϕ_h (bottom), for black holes with $q = 0.1$, $\phi_h \in [0.1, 1.4]$ and various values of E_h. The mirror is located at the first node of the equilibrium scalar field. We note that the black holes considered here are all stable since $\mathrm{Im}(\sigma) < 0$.

of numerical results for which two of the parameters q, E_h and ϕ_h are fixed and we vary the third. Fig 4.24 illustrates the real (left) and imaginary (right) part of the eigenvalue σ against the mirror location r_m (top) and the value of the static scalar field at the horizon ϕ_h (bottom). The background parameters are given to be $q = 0.1, \phi_h \in [0.1, 1.4]$ for three distinct values of electric field at the horizon E_h. There is no non-trivial black hole solution with scalar hair when $\phi_h > 1.4$, since in this case the metric function $f(r)$ develops a second horizon before $\phi(r)$ has a node (see Fig 4.11). When $E_h = 0.8$, we find no hairy black hole solutions for $\phi_h > 1.2$. We see that the imaginary part of σ

decreases (so that the perturbation modes decay more quickly) as r_m decreases and as ϕ_h increases. In addition, for fixed ϕ_h, $\mathrm{Im}(\sigma)$ decreases as E_h increases. The real part of the frequency mode σ increases as the mirror moves towards the black hole horizon and as ϕ_h increases. More importantly, we find that all the equilibrium hairy black holes we have considered are linearly stable under spherically symmetric perturbations. This is because the perturbation modes decay exponentially with time as $\mathrm{Im}(\sigma) < 0$.

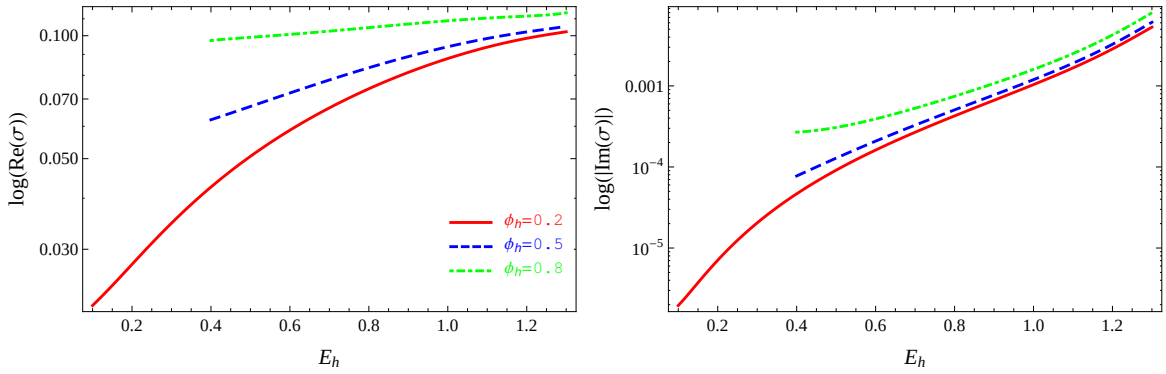

Figure 4.25: The real (left) and imaginary (right) part of the eigenfrequency σ plotted as a function of electric field at the horizon E_h, for $q = 0.1, E_h \in [0.1, 1.3]$ and various values of ϕ_h. In the right-hand plot, we have plotted the logarithm of the modulus of $\mathrm{Im}(\sigma)$. The mirror is located at the first zero of the equilibrium scalar field. We note that the black holes considered here are all stable since $\mathrm{Im}(\sigma) < 0$.

The real (left) and imaginary (right) part of the mode frequency σ are plotted against electric field at the horizon E_h in Fig 4.25 for $q = 0.1$ and $E_h \in [0.1, 1.3]$ where each curve corresponds to a different value of ϕ_h. We find that for fixed ϕ_h, the real part of σ increases as E_h increases. We emphasize that as the imaginary part of frequency can take a very small value, therefore we display the logarithm of the modulus of $\mathrm{Im}(\sigma)$. Moreover, the imaginary part of σ decreases (so that the perturbation modes decay more quickly) as the electric field at the horizon becomes stronger. In addition, as ϕ_h increases, we see that $\mathrm{Re}(\sigma)$ increases and $\mathrm{Im}(\sigma)$ decreases. Since $\mathrm{Im}(\sigma) < 0$, therefore the static black hole solutions considered here are all linearly stable.

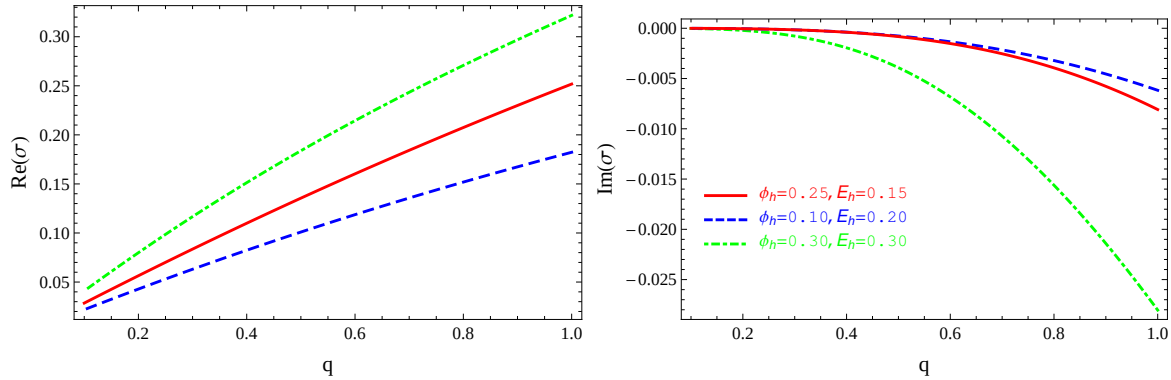

(a) (b)

Figure 4.26: The real (left) and imaginary (right) part of the frequency σ plotted as a function of scalar field charge q for black holes with various fixed values of ϕ_h and E_h. The mirror is located at the first zero of the equilibrium scalar field. We note that all black holes considered here are stable since $\mathrm{Im}(\sigma) < 0$.

We now investigate the effect of scalar field charge q on the eigenvalue σ. Fig 4.26 illustrates the real (left) and imaginary (right) part of eigenvalue σ as a function of scalar field charge q for fixed values of ϕ_h and E_h. As the scalar charge q increases, $\mathrm{Re}(\sigma)$ increases and $\mathrm{Im}(\sigma)$ decreases. We find once again that $\mathrm{Im}(\sigma) < 0$, therefore these equilibrium hairy black holes are also stable. $\mathrm{Re}(\sigma)$ and $\mathrm{Im}(\sigma)$ plotted against electric field at the horizon E_h for fixed equilibrium scalar field at the horizon $\phi_h = 0.2$ and various values of scalar field charge q are displayed in Fig 4.27. As the numerical value of σ is small, we present the results on a logarithmic scale for the real part and the magnitude of the imaginary part. For fixed q, as E_h increases, $\mathrm{Re}(\sigma)$ increases and $\mathrm{Im}(\sigma)$ decreases (the mode decays more rapidly). Additionally, as q increases, the numerical value of $\mathrm{Re}(\sigma)$ increases and $\mathrm{Im}(\sigma)$ decreases. We see that as q becomes bigger, the maximum value of E_h decreases. Beyond these values, the system of equations (4.18–4.21) become stiff and no non-trivial solutions are found. This is accordance with the behaviour of the solution space shown in Fig 4.11 where we find that as q increases, the area of the solution space of hairy black holes decreases. Since we find negative imaginary part of σ for all black holes considered here, therefore these hairy black holes are stable.

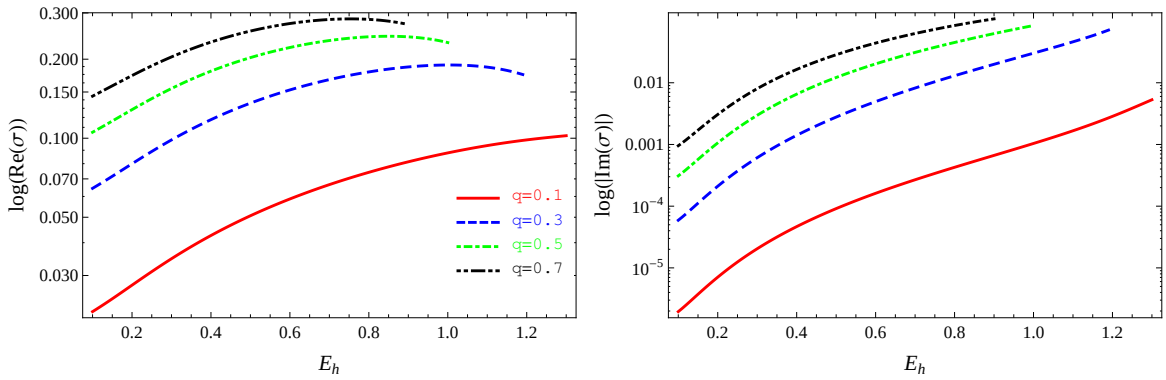

Figure 4.27: The real (left) and imaginary (right) part of the mode frequency σ plotted as a function of electric field at the horizon E_h, for black holes with fixed $\phi_h = 0.2, E_h \in [0.1, 1.3]$ and various values of q. In the right-hand plot, we have plotted the logarithm of the modulus of $\mathrm{Im}(\sigma)$. The mirror is located at the first zero of the equilibrium scalar field. We note that all black holes considered here are stable since $\mathrm{Im}(\sigma) < 0$.

Fig 4.28 shows the real (left) and imaginary (right) part of the eigenvalue σ against the mirror location r_m (top) and the value of the static scalar field at the horizon ϕ_h (bottom). The background parameters are given to be $q = 0.2, \phi_h \in [0.1, 1.3]$ for various values of the electric field at the horizon E_h. The results are displayed on a logarithmic scale for the real part and the modulus of the imaginary part. For fixed values of E_h, $\mathrm{Re}(\sigma)$ decreases as r_m increases and $\mathrm{Im}(\sigma)$ increases as r_m increases. Moreover, increasing ϕ_h, we find that $\mathrm{Re}(\sigma)$ increases and $\mathrm{Im}(\sigma)$ decreases. We can compare the results in Fig 4.28 with the results shown in Fig 4.24. Generally speaking, we see that for $q = 0.2$, the numerical results behave in a similar way to those results for $q = 0.1$ in Fig 4.24. We also see from Fig 4.28 that the results cover a smaller range of values of ϕ_h. In addition, as E_h increases the range of values of ϕ_h also increases. These patterns can be seen from the black hole solution space Fig 4.11 ($q = 0.2$ case). Since $\mathrm{Im}(\sigma) < 0$ for all the perturbation modes examined here, these modes are exponentially decaying with time. All the black holes considered here are all stable.

So far in Fig 4.23–4.28, we have considered the stability of hairy black hole solutions with

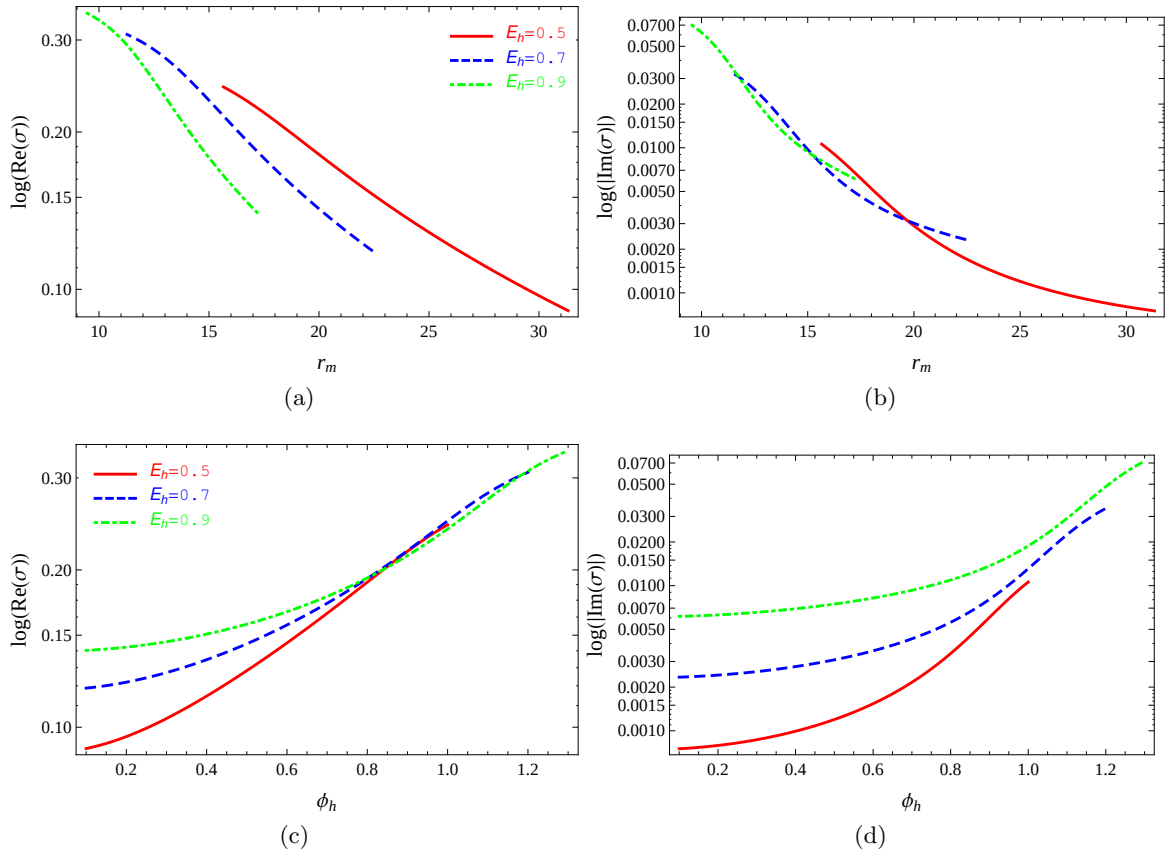

Figure 4.28: The real (left) and imaginary (right) part of the eigenfrequency σ plotted as a function of mirror radius r_m (top) and the equilibrium scalar field at the horizon ϕ_h (bottom), for black holes with fixed $q = 0.2, \phi_h \in [0.1, 1.3]$ and various values of E_h. In the right-hand plot, we show the logarithm of the modulus of $\mathrm{Im}(\sigma)$. The mirror is located at the first node of the equilibrium scalar field. We note that the black holes considered here are all stable since $\mathrm{Im}(\sigma) < 0$.

the mirror located at the first node of the equilibrium solutions. We find only perturbation modes which decay exponentially with time. Therefore, we conclude that the static hairy black holes with the mirror located at the first zero of the equilibrium scalar field are stable. To complete this section, we shall now consider the results when the mirror is located at the *second* zero of the equilibrium scalar field. As an example, in Fig 4.29, we plot the real (left) and imaginary (right) part of the mode frequency σ as a function of the mirror location r_m (top) and the value of the static scalar field at the horizon ϕ_h

(bottom). The background parameters are $q = 0.1, \phi_h \in [0.1, 1.4]$ for three distinct values of the electric field at the horizon E_h. Unlike the plots for the first-zero case, on the right-hand plot, we present our numerical results by using a logarithmic scale for $\mathrm{Im}(\sigma)$ rather than the modulus of $\mathrm{Im}(\sigma)$. We see that, with fixed E_h, as r_m increases, both the real and imaginary part of σ decrease (so that the perturbation modes grow more slowly). On the other hand, increasing ϕ_h, $\mathrm{Re}(\sigma)$ and $\mathrm{Im}(\sigma)$ also increase. In contrast with the first-node case, when the mirror is placed at the second zero of the static scalar field, we find perturbations with $\mathrm{Im}(\sigma) > 0$. Hence the perturbation modes are growing exponentially with time. Therefore we conclude that static hairy black holes with the mirror at the *second* node of the scalar field are unstable. We expect that the static black holes would remain unstable, if the mirror is located at any zero after the second zero of the equilibrium solutions.

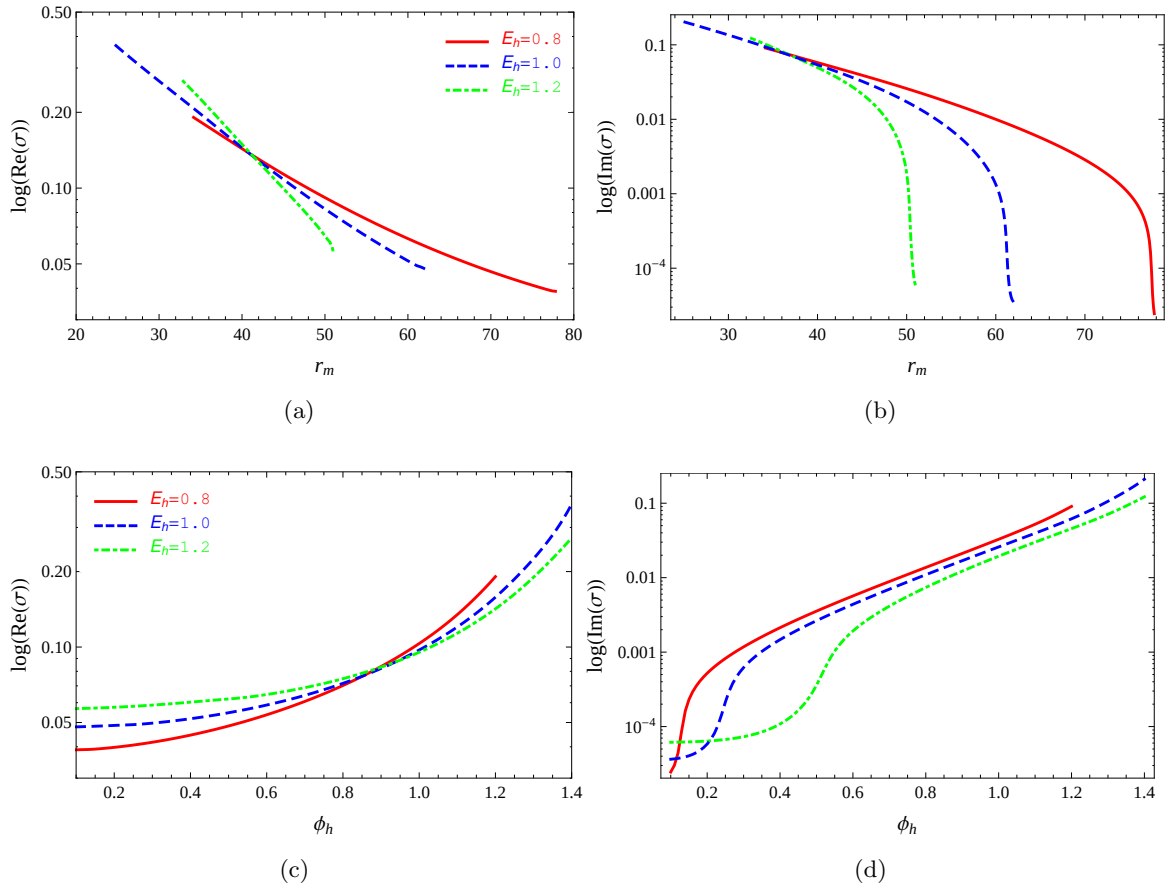

Figure 4.29: The real (left) and imaginary (right) part of the eigenvalue σ plotted as a function of mirror radius r_m (top) and the equilibrium scalar field at the horizon ϕ_h (bottom), for black holes with $q = 0.1, \phi_h \in [0.1, 1.4]$ and various values of E_h. The mirror is now located at the *second* node of the equilibrium scalar field. Note that in this plot, the imaginary part of the frequency is positive, implying that the perturbation modes grow exponentially in time.

§4.6 Summary

Finding one possible end-point of the charged superradiant instability for a charged black hole surrounded by a reflecting mirror was our main goal in this chapter. Thus we investigated the Einstein-charged-scalar field system in a cavity. We showed numerically that solitons and black holes in a cavity with charged scalar hair are admitted in this theory. An analytic argument was made to confirm that there are no asymptotically flat solutions

except the trivial ones, i.e., Minkowski, Schwarzschild or Reissner-Nordström solutions. We imposed reflecting boundary conditions at the mirror, such that the scalar field must vanish at $r = r_m$. We used this requirement to fix the mirror at the first zero of the scalar field for most of the cases we have considered. By fixing the scalar field charge to be $q = 0.1$, two parameters are needed to define the soliton solutions, namely, the scalar field and electric potential at the origin ϕ_0 and a_0. For hairy black holes, we fix the black hole radius r_h to be unity and this leaves only three quantities to describe the black hole solutions, which are the scalar field charge q, the scalar field and electric field at the horizon ϕ_h and E_h.

The phase spaces of soliton and black hole solutions share many common characters. For instance, in the central area of the phase space for both solitons and black holes where a_0, ϕ_0 or E_h, ϕ_h approach zero, there exist solitons/black holes with $r_m > 100$. Also as one moves away from the centre, the mirror radius decreases. Furthermore, at a fixed value of a_0/E_h, we found that there is an upper limit on the value of ϕ_0/ϕ_h such that beyond these points we find no well-defined solutions.

However there are also some significant differences between the solution spaces of solitons and black holes. Since we fix the scalar field charge q in the soliton case, the soliton solution space is therefore much simpler than the black hole solution space. In addition we find no upper bound on a_0 since there is no horizon. In fact, we can find a well-defined solution when a_0 is extremely large. In contrast, in the black hole case, the maximum value of E_h is limited by the condition $|E_h| < \sqrt{2}$ when $r_h = 1$. Moreover, as q increases, the size of the black hole phase space decreases.

The stability of solitons and black holes was also discussed. Spherically symmetric linear perturbations of the metric functions, scalar field and electric potential were considered. Three perturbation equations which govern the evolution of linear perturbations were derived. By applying suitable boundary conditions for these perturbation fields, the system

of perturbation equations was solved numerically by a two-parameter shooing method. Our numerical analysis revealed the following:

- If the mirror radius is sufficiently large, we find stable soliton solutions; unstable modes for some solitons are found when the mirror radius is small. For all the solitons we have considered here, the mirror location is always at the first zero of the equilibrium scalar field.
- For black holes, stable solutions are found when the mirror is located at the first zero of the equilibrium scalar field; when the mirror is fixed at the second node, unstable black hole solutions are found.
- We also anticipate that if the mirror is located at further zeroes of the scalar field, the black hole solutions would be unstable.

From these results, we can make the following arguments. In the first scenario where we have stable solitons with complex scalar field, the stable hairy black hole can be interpreted as a bound state of a Reissner-Nordström black hole and a charged scalar soliton. In the second scenario, since there is no known mechanism that allows the scalar field to escape to infinity, therefore we conjecture that unstable solitons would collapse to either a Reissner-Nordström black hole or a black hole with charged scalar hair. We therefore conclude that a stable black hole-in-a-cavity could be interpreted as a possible end-point of the charged superradiant instability in a cavity. This result is in accordance with the conjecture made in [86], that with the exclusion of a single real scalar field, *a (hairless) black hole which is afflicted by the superradiant instability of a given field must allow hairy generalizations with that field.*

In a recent study by Sanchis-Gual et.al., [157] a time-domain analysis was applied to investigate the development of the superradiant instability of a charged massive scalar field into the non-linear regime. By using the techniques of numerical relativity, they

discovered that there are two possible end-points for the charged black hole bomb. For small electric scalar field charge (up to $qM \sim 10$), where M is the ADM mass of the original Reissner-Nordström black hole, the unstable charged configuration evolves smoothly into the end-state of a hairy black hole. On the other hand, they demonstrate numerically that for larger qM, the energy extraction overcomes the final equilibrium configuration and an explosive event, namely a bosenova, occurs and the system settles down to a hairy black hole after that. They also found that these hairy black holes exist at the threshold of the superradiant instability. This work clearly supports our finding that hairy black holes are possible end-points of the charged superradiant instability [61]. The connection between our hairy black hole-in-a-cavity solutions and those found in [157] can be understood by the following argument. By making a gauge transformation such that the electric potential at the horizon $A_0(r_h)$ becomes Q/r_h rather than zero, the scalar field obtains a harmonic time dependence and the scalar field oscillates at the precise superradiance threshold frequency. Furthermore, the final state of the superradiant instability of a charged massless scalar field in asymptotically AdS spacetime was recently investigated in [31]. Their non-linear study also revealed that the ultimate fate of the charged superradiant instability in AdS spacetime is a stable hairy black hole.

Chapter 5

Conclusions

Two self-gravitating systems have been studied in this thesis; $SU(2)$ Einstein-non-Abelian-Proca (ENAP) theory in asymptotically AdS spacetime and Einstein-charged-scalar theory in a cavity. Combining analytic and numerical work, we found spherically symmetric solitons and hairy black holes in each model. The linear stability of these solutions was also investigated.

In chapter 2, we reviewed basic ideas of black hole solutions, the no-hair theorem and black hole superradiance. Schwarzschild, Reissner-Nordström, Kerr and Kerr-Newman black holes were discussed. The casual structures of these black hole solutions were also studied by investigating their Penrose diagrams. Inspired by the uniqueness theorems of asymptotically flat black hole solutions, we discussed the no-hair theorem and its consequences. We saw that if the electrovac condition is relaxed, then the no-hair theorem no longer holds. In fact, we discussed a generalized no-hair conjecture [25, 52]. This conjecture leads to a new type of black hole solution called hairy black hole. We then discussed some important works on black holes with various types of hair. Since one of the main interests in this thesis is ENAP theory, therefore, we focussed mainly on black hole solutions with non-Abelian gauge hair. Later, we considered superradiance in black hole physics.

We demonstrated how the amplitude of a matter wave on a black hole spacetime can be amplified. We derived a necessary condition for superradiant scattering in the charged and rotating cases. By providing a confining mechanism, we saw that a superradiance process can lead to an instability of spacetime. At the end of chapter 2, we presented how a massless charged scalar field on a Reissner-Nordström black hole enclosed by a mirror becomes superradiantly unstable.

The particle-like solutions [7] and coloured black holes [24] were the first solitons and hairy black holes found in $SU(2)$ Einstein-Yang-Mills (EYM) theory in asymptotically flat spacetime. Since then, many studies have been devoted to finding the existence of solitons/black holes with non-Abelian hair and their stability. In chapter 3, we studied spherically symmetric solutions of $SU(2)$ ENAP theory in asymptotically AdS spacetime. By using the numerical shooting method, we discovered purely magnetic soliton and black hole solutions with non-Abelian Proca hair. Our solutions share common features with those solutions found earlier in ENAP-flat [79] and EYM-Higgs-AdS [183] theories. Firstly, our solitons and hairy black holes have two branches: ordinary and quasi branches. Secondly, for fixed Proca mass μ, there exists a maximum value of the magnitude of the cosmological constant $|\Lambda|$ for which we still obtain solutions. Likewise, for fixed $|\Lambda|$, there is maximum value of μ for which we still obtain solutions. We proved that these solutions cannot be nodeless. Then we showed that dyon solutions and dyonic black holes are not allowed in ENAP theory in both asymptotically flat and asymptotically AdS spacetimes. The equilibrium hairy black holes found in this chapter violate the generalized no-hair conjecture [25, 52], since at infinity, they are indistinguishable from the Schwarzschild-AdS solution.

Spherically symmetric linear perturbations about these solutions were also studied. It turned out that the perturbation equations can be divided into two classes; the gravitational and sphaleronic sectors. Our numerical studies revealed that equilibrium solitons and hairy black holes are linearly unstable in both sectors. We also investigated the stabil-

ity of the equilibrium solutions of ENAP-flat and found unstable modes for both solitons and hairy black holes. Our work concludes that solitons and black holes with non-Abelian Proca hair are unstable against a small perturbation.

A charged scalar field on a Reissner-Nordström background in a cavity experiences superradiant phenomena [55, 85]. A mirror-like boundary also provides a trapping mechanism that keeps a superradiant mode of the scalar field in the vicinity of the charged black hole. This process eventually leads to an instability. In this thesis, we attempted to provide a plausible end-point of this charged superradiant instability. To address this problem, we considered Einstein-charged-scalar field theory with a reflecting boundary condition in chapter 4. By solving the field equations, we obtained numerical spherically symmetric solitons and black holes with charged scalar hair. A mirror-like boundary condition is imposed by requiring that the scalar field must vanish at the location of a mirror. Therefore we can put the mirror at any zero of the equilibrium scalar field. We focused mostly on those solutions for which the mirror is located at the first zero of the scalar field. It is not possible to have either solitons or hairy black holes in asymptotically flat spacetime. We gave an analytic proof that supported this statement. We found that the only non-trivial asymptotically flat black hole (soliton) solutions of the Einstein-Maxwell-Klein-Gordon equations are either Reissner-Nordström or Schwarzschild (Minkowski) spacetimes.

The stability of these solitons and hairy black holes against perturbations of the metric, electromagnetic field and scalar field was investigated. By fixing the mirror's location at the first zero of the equilibrium scalar field, we found no numerical evidence of unstable perturbations for equilibrium black hole solutions, which are all linearly stable. On the other hand, we found unstable modes for black hole solutions when the mirror is at the second zero of the scalar field. We conjecture that the same result would hold if the mirror was located at the third or subsequent zeros of the equilibrium scalar field. Thus these stable black hole solutions could represent the end-point of the charged superradiant instability. The non-linear evolution of the charged superradiant instability was recently

studied in [156, 157] by applying numerical relativity techniques. Their study revealed that the system settles down to a hairy black hole which clearly agrees with our findings.

It turned out that the stability of solitons is not as straightforward as in the black hole case. It required a careful analysis to understand the stability behaviour of solitons. We note that for all the soliton solutions considered in this thesis, the mirror's location is at the first zero of the equilibrium scalar field. We found that if the mirror radius r_m is sufficiently large, all the equilibrium solitons examined were shown to be stable. On the other hand, some soliton solutions were found to be unstable when r_m is sufficiently small (corresponding to sufficiently large values of ϕ_0 and a_0). We made sense of this result by comparing our solitons with asymptotically flat boson stars. Non-linear studies of the dynamics of boson stars revealed that unstable boson stars can either collapse to form a black hole or the scalar field radiates to infinity and the system settles down to a stable boson star [65]. However, in our scenario, the charged scalar field cannot simply escape to infinity due to the reflective mirror. Therefore we expect that the unstable solitons discovered here would collapse to form either stable black holes with charged scalar hair or a Reissner-Nordström black hole. We remark that to test this conjecture, a fully non-linear evolution is required.

How can the hairy black holes discussed in chapter 3 and 4 be described under the no-hair conjecture framework? We saw that black holes with non-Abelian Proca hair in asymptotically AdS spacetime are indistinguishable from Schwarzschild-AdS at infinity, but they are also unstable. Therefore they do not violate Bizon's no-hair conjecture [25]. For the models with a non-Abelian gauge field in asymptotically AdS spacetime, pure EYM theory seems to be a very special case. This is because EYM-AdS theory appears to be the only system that contains stable hairy black holes. In addition, these black holes can also be characterized by global charges which can be measured at infinity. On the other hand, it is difficult to see how stable black holes with charged scalar hair could fit into the picture of the no-hair conjecture. This is because there is no infinity due to the

presence of the mirror.

In both scenarios, the asymptotic structure of the spacetimes is a timelike boundary (AdS and mirror respectively). Therefore one might argue that both models are not physically interesting. However we hope that studying these toy models may shed some light on the stability of rotating hairy black holes which is considered to be more astrophysically relevant (but of course relatively more complicated and challenging).

We complete this chapter by commenting on what could be extended from the works presented in this thesis. It was found in [156, 157] that a hairy black hole is the final state of the superradiant instability induced by a massive charged scalar field on a Reissner-Nordström black hole in a cavity. Therefore one natural extension is to consider a coupled system of gravity, electromagnetic field and a *massive* charged scalar field with a reflective mirror. This coupled system can be obtained by simply adding a scalar field mass term to our work presented in chapter 4. It would be straightforward to obtain soliton and hairy black hole solutions as well as providing a stability analysis for these solutions. However we expect that the results in the massive case would not be much different from our results for a massless scalar field. We note that the authors in [156] recently discuss the difference between the massless and massive case under charged superradiant instability framework.

As mentioned above, the end-point of the unstable charged scalar solitons is still unclear. The final state of this instability could be either a Reissner-Nordström black hole or a hairy black hole. To answer this question properly, a time evolution study of the soliton solutions is required. This means we have to follow the development of the metric, electromagnetic and scalar perturbations into the non-linear regime. To tackle this problem systematically, one would be required to implement numerical relativity techniques. It could be a technically challenging problem but also interesting to have a complete picture of the instability of the charged scalar solitons.

Ultimately, one would like to explore possible end-points of the superradiant instability

in the rotating case. To fully track down the evolution of the superradiant instability, a non-linear evolution of the perturbations must be investigated. The rotating case is, however, considerably more difficult than the spherically symmetric charged case. This is because the former has less symmetry and also its instability time scale is longer than the latter. Despite this being very hard problem, it is also very interesting since it could have direct astrophysical applications. We leave this as an open question for future work.

Appendix A

Numerical method

Throughout our work, one of the main problems that we have encountered is we end up having many ordinary differential equations (ODEs) which cannot be solved analytically. Therefore some numerical scheme is required to solve these ODEs. There are various numerical methods on the market and each one has an advantage over the others in some type of particular problem. In our work, however, we solely deal with the situation where we know the initial values of the variables and then try to find the solution that matches certain conditions at the boundary. The numerical technique that suits our needs the best is the shooting method. By adopting the spirit of the shooting technique, we construct numerical code in Mathematica to attack our problems both in the ENAP and the Einstein-charged-scalar projects. In this appendix, we will outline the basic principles behind this numerical method and also describe briefly how we can implement this in Mathematica.

§A.1 Initial and boundary value problems

Before discussing the shooting method, it is useful to mention initial value problems (IVPs) and boundary value problems (BVPs). IVPs and BVPs are ordinary differential equations with "initial conditions" and "boundary conditions" respectively. From a mathemati-

cal point of view, initial conditions consist of specified values of the functions and their derivatives at some initial point of the independent variable. Boundary conditions are given by values of the functions at the endpoints of the interval of the independent variable under consideration. From a physical point of view, IVPs and BVPs are found in many physical systems. In addition, IVPs are mostly found in problems involving how the system will evolve if initial conditions are specified. However BVPs most often occur in time-independent physical situations.

These two problems are different in terms of the uniqueness of their respective solutions. One can almost guarantee to obtain a unique solution when solving IVPs. However under some circumstances, BVPs could have either no solution or many solutions. To illustrate this, consider the following equation,

$$y''(x) = -y(x), \tag{A.1.1}$$

with general solution

$$y(x) = c_1 \cos x + c_2 \sin x, \tag{A.1.2}$$

where c_1 and c_2 are arbitrary constants and $'$ denotes the derivative with respect to x. Then consider the initial value problem by adding the following initial conditions to (A.1.1),

$$y(0) = A, \qquad y'(0) = B, \tag{A.1.3}$$

which implies that

$$c_1 = A, \qquad c_2 = B. \tag{A.1.4}$$

The solution becomes

$$y(x) = A \cos x + B \sin x. \tag{A.1.5}$$

Thus this initial value problem has the unique solution (A.1.5) for each possible pair of values of A and B.

Now consider the following examples of BVPs. We use the same equation (A.1.1), however, with the new boundary conditions,

$$y(0) = 0, \qquad y(\pi) = 0. \tag{A.1.6}$$

These boundary values yield

$$y(0) = 0 = c_1, \qquad y(\pi) = 0 = c_1, \tag{A.1.7}$$

which tells us nothing about the value of c_2. Hence c_2 can take any arbitrary value. Thus the solution of this system is given as

$$y(x) = c_2 \sin x, \tag{A.1.8}$$

which is not a unique solution. Finally, another example of a BVP takes the form

$$y(0) = 0, \qquad y(\pi) = 1. \tag{A.1.9}$$

Hence

$$y(0) = 0 = c_1, \qquad y(\pi) = 1 = -c_1, \tag{A.1.10}$$

which gives a contradiction. Thus there is no solution in this case. So one can see that with ill-defined boundary conditions, BVPs could yield a non-unique solution and sometimes no solution at all. For more details on IVPs and BVPs see, for example, [5, 178].

§A.2 Shooting method

The shooting method is a numerical technique for solving one particular type of ordinary differential equation, i.e. boundary value problems. The basic principle of the shooting method is to reduce BVPs to IVPs by replacing one boundary condition with an arbitrary initial condition. Thus boundary value problems become initial value problems which can be solved by numerical integration methods, e.g. Runge-Kutta [178]. For example, we

consider the following boundary value problem

$$y''(x) = f\left(y'(x), y(x), x\right), \tag{A.2.1}$$

with boundary conditions

$$y(x_i) = \alpha, \qquad y(x_f) = \beta, \tag{A.2.2}$$

where α and β are some particular values that needed to be specified. The starting and the boundary point are denoted by x_i and x_f, respectively. We apply the shooting method by changing one of the boundary conditions to an initial condition. That is, we set

$$y(x_i) = \alpha, \qquad y'(x_i) = \gamma, \tag{A.2.3}$$

where γ is an arbitrary constant. Then we solve the above IVP by applying a conventional method, e.g. Runge-Kutta. The name "shooting" comes from the fact that we have to make an educated guess of the initial value γ. With this initial condition, we see how close the solution is to satisfying the other boundary condition ($y(x_f) = \beta$). Then we appropriately adjust the initial value of γ and shoot again until we can match the boundary condition at x_f.

Fig A.1 displays a graphical scheme of the shooting method. In this case, we first make a guess by choosing $\gamma = \gamma_1$. This choice yields the initial slope too low to satisfy the other boundary condition. Thus we shoot again with $\gamma = \gamma_2$ which is too high. Then we follow an aim-shoot-adjust process so that the other boundary condition is satisfied. Then the BVP is solved.

If the boundary value problem has a solution, it is possible to find the root of the following function

$$Y(\gamma) = y(x_f; \gamma) - \beta. \tag{A.2.4}$$

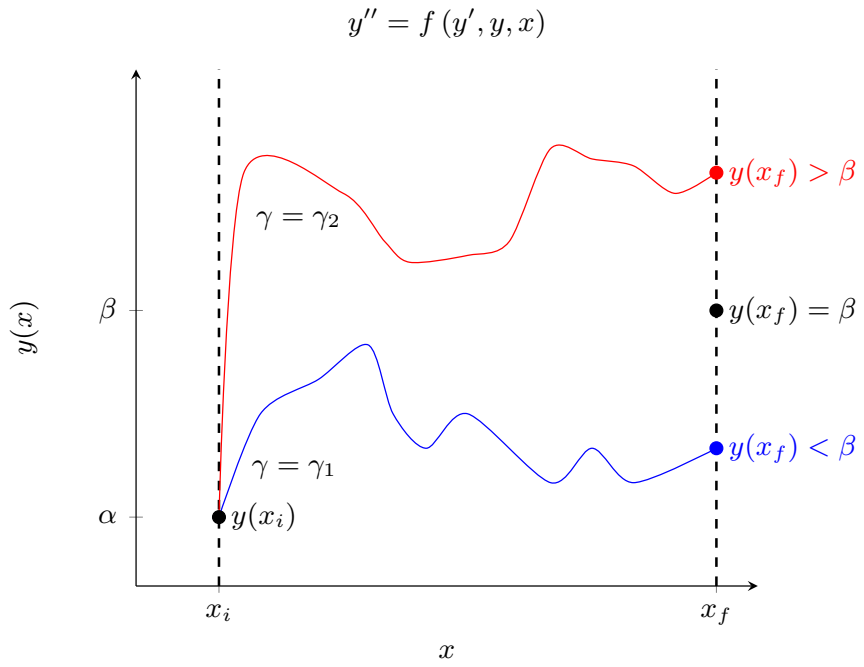

Figure A.1: Diagram of the shooting method scheme.

With a given value of γ, the solution at x_f is defined by $y(x_f; \gamma)$. For more details on the subject, we refer the reader to [142, 166].

§A.3 Coding

In our work, all the numerical calculations are performed in Mathematica, including the part where we solve ODEs with the shooting method. Therefore in this section, we will describe how the numerical shooting scheme can be constructed via Mathematica code. Since both the ENAP and Einstein-charged-scalar project heavily involve this technique, we will outline the computational steps for each case separately.

A.3.1 ENAP

For the ENAP case, the shooting method is used to find both the equilibrium solitons/black holes (section 3.5) and also to demonstrate the instability of these solutions (section 3.7). Firstly the static field equations (3.22–3.24) together with the boundary conditions (3.26,

3.29, 3.31) define the BVP. By the virtue of shooting scheme, we will replace (3.31) with some initial conditions. As a result, the BVP now becomes an IVP. If e, μ, Λ and r_h are given, the initial data (3.26) and (3.29) depend only on ω_2 (which later will be renamed as b) and ω_h. The quantities b and ω_h are the shooting parameters for the soliton and black hole cases respectively. The computational steps are given as follows:

1. We specify numerical values to $e, \mu,\ \Lambda$ and r_h (for black hole solutions).

2. The initial conditions (3.26, 3.29) and their derivatives are used as initial data to integrate the ODEs (3.22–3.24) numerically. Note that at this stage, these initial values now only depend on b and ω_h for the soliton and black hole cases respectively.

3. We solve the ODEs with the help of the NDSolve function in Mathematica. The function is constructed in the following way: NDSolve[field equations, initial conditions ,$\{r, r_{origin/horizon}, 10^i\}$], where i is an integer. In practice, we cannot start the integration from the origin $r = 0$ (for solitons) or from the horizon $r = r_h$ (for black holes), since these points are singular point of the ODEs. Instead, we define $r_{origin} = \epsilon$ and $r_{horizon} = r_h + \epsilon_1$, where ϵ and ϵ_1 measure how close to the origin/horizon we can start our integration. The typical values of ϵ and ϵ_1 are 10^{-3} and 10^{-13} respectively.

4. We try to find the values of shooting parameter b/ω_h such that the following equation is satisfied $\omega(10^i) + 1 = 0$, where the output of NDSolve[.....] is substituted into $\omega(10^i)$. This equation needs to be satisfied since the boundary condition (3.31) says that $\omega = -1$ (at the leading order) as $r \to \infty$. This is the equivalent of the "target" that we need to aim for.

5. We then need to construct an algorithm to "aim-shoot-compare (the result with the target)-adjust-shoot again". To do that, we begin by defining a new function $T\left[10^i, b\right] := \omega(10^i) + 1$. Hence we aim for $T\left[10^i, b\right] = 0$ with particular values of i.

The function T is equivalent to (A.2.4).

6. We then construct such an algorithm by using the Findroot Mathematica function i.e., Findroot $[T[10^i, b],\ \{b, b_{initial}, b_{final}\}]$, where $b_{initial}$ and b_{final} need to be given numerical values. This restricts the interval that Findroot needs to search for an appropriate value of b. Then we define the "new" $b_{initial}$, b_{final} in a suitable way such that the "new" interval is narrower than the previous interval.

7. Next we construct a "For" loop for the Findroot function to run the value of i which corresponds to the value of the upper limit of integration. At each particular value of i, Findroot will return a value of b. Then the loop will continue such that at $i + 1$, the Findroot will search for an appropriate b within a narrower interval than the previous step. In our case, the typical starting value of i is 3 and the loop is normally terminated when $i > 8$. This step is equal to the "shoot-compare-adjust-shoot again" procedure in the standard shooting method.

8. We check the correctness of the result by testing that the function T defined above has to be zero. We tend to choose the value of b with the largest possible i, since this ensures that our solution would behave smoothly to a very large distance.

9. Then we substitute final value of b into NDSolve function to solve for the solutions and then plot the solutions.

In these steps, we can replace b with ω_h for the black hole solutions. Although there are many numerical techniques for solving ODEs and for root finding, we allow Mathematica to select the most suitable method for us via NDSolve and FindRoot functions.

For the stability analysis, the computational scheme is almost the same as the one discussed above, therefore here we will only point out the differences between the two scenarios. In the case of stability, the computational steps are given by:

1. Firstly, we solve the static equations and obtain the relevant equilibrium soliton/black hole solutions by using the numerical scheme discussed above. These solutions are then substituted into the perturbation equations (3.85) for the gravitational sector and (3.100, 3.101) for the sphaleronic sector.

2. To integrate the perturbation equations, once again we use the following command: NDSolve[perturbation equations, initial conditions, $\left\{r, r_{origin/horizon}, 10^i\right\}$]. However, the initial data for both solitons and black holes depend solely on σ^2, see equations (3.87, 3.88) and (3.102–3.104). Thus the shooting parameter is σ^2.

3. We demand that the perturbation fields, i.e., ω_1 for the gravitational sector and χ_1 and $\tilde{\Theta}_1$ for the sphaleronic sector, vanish at infinity. Therefore in this case the "testing" function is now defined as: $T\left[10^i, \sigma^2\right] := \omega_1(10^i)$ for the gravitational sector and $T\left[10^i, \sigma^2\right] := \chi_1(10^i)$ or $T\left[10^i, \sigma^2\right] := \tilde{\Theta}_1(10^i)$ for the sphaleronic sector.

4. We remark that in the sphaleronic sector both variables χ_1 and $\tilde{\Theta}_1$ need to vanish as $r \to \infty$. However, there is only one shooting parameter σ^2, therefore we can only use one "testing" function. In practice, we choose χ_1 as "testing" function and it turned out that the other one also vanished when the correct σ^2 was found.

5. Then the root of the "testing function" is obtained by the FindRoot command. Together with the algorithm mentioned above, we can find the final value of σ^2. Then the perturbation equations can be solved via NDSolve.

A.3.2 Einstein-charged-scalar

In general, the numerical techniques used in this project are similar to those employed in the ENAP project. We still use the shooting method to solve the main ODEs defined in this system. However since the nature of the problem is different, thus we have to modify the shooting algorithm such that it suits our particular problem. Unlike the ENAP project, it is not necessary to implement the shooting method when solving the equilibrium field

equations (4.18–4.21). This is because we can always fix the mirror location at any node of the equilibrium scalar field. By giving appropriate numerical values to q, a_0, ϕ_0, r_h, E_h and ϕ_h, NDSolve itself is sufficient to solve the field equations for soliton and black hole solutions (see section 4.4).

Nevertheless, numerical analysis of the stability of these static solutions requires the shooting technique. More precisely, with the perturbation equations (4.77–4.79) and the initial data (4.89) and (4.110) for solitons and black holes, we now have a two-parameter shooting problem, i.e., σ^2 and w_2 or σ and $\tilde{u}_0$ become shooting parameters in the soliton and black hole cases, respectively. Another difference comes from the very nature of the problem itself. In the ENAP case, the field variable ω and the perturbation field need to be -1 and 0, respectively as $r \to \infty$. However in the Einstein-charged-scalar case, the scalar perturbations are required to vanish at the exact location of the mirror $r = r_m$, and beyond the mirror we assume that the spacetime ceases to exist. Therefore the perturbation equations (4.77–4.79) need to be integrated from (near) the origin/horizon up to the location of the mirror. Hence the "For" loop of i is irrelevant in this case.

The basic computational steps are given as follows:

1. For fixed q, a_0 and ϕ_0, we can integrate the static field equations numerically (using basic NDSolve) and obtain soliton solutions as a result. For black holes, the background parameters that need to be defined are q, r_h, E_h and ϕ_h. Once we obtain solitons and black holes, the location of the mirror can be determined by finding the first root of the equilibrium scalar field solution.

2. Based on the profile of the equilibrium soliton or black hole, we can now solve the perturbation equations which correspond to each particular case. We construct the following command: NDSolve[perturbation equations, initial conditions, $\{r, r_{origin/horizon}, r_m\}$]. The "target" for the shooting is the requirement that the perturbation of the scalar field must be zero at the mirror. Therefore both the real

and imaginary parts of the scalar perturbation need to vanish at r_m.

3. We thus need to construct two "testing" functions, one for the real part and another for the imaginary part of the scalar perturbation. We can define $U\left[r_m, \sigma^2, w_2\right] := \tilde{u}(r_m)$ and $W\left[r_m, \sigma^2, w_2\right] := \tilde{w}(r_m)$ for solitons, and similarly for black holes. The FindRoot command in Mathematica can find the simultaneous root of the functions U and W. As a result, we obtain σ^2 and w_2 or σ and $\tilde{u}_0$ for solitons or black holes, respectively.

References

[1] B. P. Abbott et al. Observation of gravitational waves from a binary black hole merger. *Phys. Rev. Lett.*, 116:061102, 2016.

[2] B. P. Abbott et al. Tests of general relativity with GW150914. *Phys. Rev. Lett.*, 116:221101, 2016.

[3] M. Abramowitz and A. Stegun. *Handbook of mathematical functions*. Dover Publications, 1970.

[4] P. C. Aichelburg and P. Bizon. Magnetically charged black holes and their stability. *Phys. Rev. D*, 48:607–615, 1993.

[5] G. B. Arfken, H. J. Weber, and F. E. Harris. *Mathematical methods for physicists: A comprehensive guide*. Academic Press; seventh edition, 2012.

[6] J. M. Bardeen, B. Carter, and S. W. Hawking. The four laws of black hole mechanics. *Commun. Math. Phys.*, 31:161–170, 1973.

[7] R. Bartnik and J. McKinnon. Particle-like solutions of the Einstein-Yang-Mills equations. *Phys. Rev. Lett.*, 61:141–144, 1988.

[8] P. Basu, A. Mukherjee, and H. Shieh. Supercurrent: Vector hair for an AdS black hole. *Phys. Rev. D*, 79:045010, 2009.

[9] J. E. Baxter. Existence of topological hairy dyons and dyonic black holes in anti-de Sitter $SU(N)$ Einstein-Yang-Mills theory. *J. Math. Phys.*, 57:022505, 2016.

[10] J. E. Baxter, M. Helbling, and E. Winstanley. Soliton and black hole solutions of $SU(N)$ Einstein-Yang-Mills theory in anti-de Sitter space. *Phys. Rev. D*, 76:104017, 2007.

[11] J. E. Baxter, M. Helbling, and E. Winstanley. Abundant stable gauge field hair for black holes in anti-de Sitter space. *Phys. Rev. Lett.*, 100:011301, 2008.

[12] J. E. Baxter and E. Winstanley. On the stability of soliton and hairy black hole solutions of $SU(N)$ Einstein-Yang-Mills theory with a negative cosmological constant. *J. Math. Phys.*, 57:022506, 2016.

[13] J. E. Baxter and E. Winstanley. Topological black holes in $SU(N)$ Einstein-Yang-Mills theory with a negative cosmological constant. *Phys. Lett. B*, 753:268–273, 2016.

[14] J. D. Bekenstein. Nonexistence of baryon number for static black holes. *Phys. Rev. D*, 5:1239–1246, 1972.

[15] J. D. Bekenstein. Nonexistence of baryon number for black holes II. *Phys. Rev. D*, 5:2403–2412, 1972.

[16] J. D. Bekenstein. Transcendence of the law of baryon-number conservation in black hole physics. *Phys. Rev. Lett.*, 28:452–455, 1972.

[17] J. D. Bekenstein. Extraction of energy and charge from a black hole. *Phys. Rev. D*, 7:949–953, 1973.

[18] J. D. Bekenstein. Exact solutions of Einstein conformal scalar equations. *Annals Phys.*, 82:535–547, 1974.

[19] J. D. Bekenstein. Black holes with scalar charge. *Annals Phys.*, 91:75–82, 1975.

[20] J. D. Bekenstein. Novel "no scalar hair" theorem for black holes. *Phys. Rev. D*, 51:6608–6611, 1995.

[21] J. D. Bekenstein. Black hole hair: twenty five years later. *arXiv:9605059 [gr-qc]*, 1996.

[22] S. Bhattacharya and A. Lahiri. Black-hole no-hair theorems for a positive cosmological constant. *Phys. Rev. Lett.*, 99:201101, 2007.

[23] G. D. Birkhoff. *Relativity and modern physics*. Harvard University Press, 1923.

[24] P. Bizon. Colored black holes. *Phys. Rev. Lett.*, 64:2844–2847, 1990.

[25] P. Bizon. Gravitating solitons and hairy black holes. *Acta. Phys. Polon.*, B25:877–898, 1994.

[26] P. Bizon and T. Chmaj. Gravitating skyrmions. *Phys. Lett. B*, 297:55–62, 1992.

[27] P. Bizon and R. M. Wald. The n=1 colored black hole is unstable. *Phys. Lett. B*, 267:173–174, 1991.

[28] J. Bjoraker and Y. Hosotani. Monopoles, dyons, and black holes in the four-dimensional Einstein-Yang-Mills theory. *Phys. Rev. D*, 62:043513, 2000.

[29] J. Bjoraker and Y. Hosotani. Stable monopole and dyon solutions in the Einstein-Yang-Mills theory in asymptotically Anti-de Sitter space. *Phys. Rev. Lett.*, 84:1853–1856, 2000.

[30] N. M. Bocharova, K. A. Bronnikov, and V. N. Melnikov. An exact solution of the system of Einstein equations and mass-free scalar field. *Vestnik Moskov. Univ. Fizika*, 25:706–709, 1970.

[31] P. Bosch, S. R. Green, and L. Lehner. Nonlinear evolution and final fate of charged anti-de Sitter black hole superradiant instability. *Phys. Rev. Lett.*, 116:141102, 2016.

[32] P. Boschung, O. Brodbeck, F. Moser, N. Straumann, and M. S. Volkov. Instability of gravitating sphalerons. *Phys. Rev. D*, 50:3842–3846, 1994.

[33] P. Breitenlohner, P. Forgacs, and D. Maison. On static spherically symmetric solutions of the Einstein-Yang-Mills equations. *Commun. Math. Phys.*, 163:141–172, 1994.

[34] P. Breitenlohner, P. Forgács, and D. Maison. Classification of static, spherically symmetric solutions of the Einstein-Yang-Mills theory with positive cosmological constant. *Commun. Math. Phys.*, 261:569–611, 2006.

[35] P. Breitenlohner, D. Maison, and G. Lavrelashvili. Non-Abelian gravitating solitons with negative cosmological constant. *Class. Quant. Grav.*, 21:1667–1684, 2004.

[36] Y. Brihaye and T. Delsate. Skyrmion and Skyrme-black holes in de Sitter spacetime. *Mod. Phys. Lett. A*, 21:2043–2054, 2006.

[37] R. Brito, V. Cardoso, C. A. R. Herdeiro, and E. Radu. Proca stars: Gravitating Bose-Einstein condensates of massive spin 1 particles. *Phys. Lett. B*, 752:291–295, 2016.

[38] R. Brito, V. Cardoso, and P. Pani. Superradiance. *Lect. Notes Phys.*, 906:1–237, 2015.

[39] O. Brodbeck, M. Heusler, G. Lavrelashvili, N. Straumann, and M. S. Volkov. Stability analysis of new solutions of the EYM system with a cosmological constant. *Phys. Rev. D*, 54:7338–7352, 1996.

[40] O. Brodbeck and N. Straumann. Instability of Einstein-Yang-Mills solitons for arbitrary gauge groups. *Phys. Lett. B*, 324:309–314, 1994.

[41] O. Brodbeck and N. Straumann. Instability proof for Einstein-Yang-Mills solitons and black holes with arbitrary gauge groups. *J. Math. Phys.*, 37:1414–1433, 1996.

[42] A. E. Broderick, T. Johannsen, A. Loeb, and D. Psaltis. Testing the no-hair theorem with Event Horizon Telescope observations of Sagittarius A*. *Astrophys. J.*, 784:7–20, 2014.

[43] K. A. Bronnikov and Yu. N. Kireev. Instability of black holes with scalar charge. *Phys. Lett. A*, 67:95–96, 1978.

[44] G. L. Bunting. Proof of the uniqueness conjecture for black holes. *PhD Thesis*, Univ. of New England, Armidale, N.S.W., 1983.

[45] G. L. Bunting and A. K. M. Masood-ul Alam. Nonexistence of multiple black holes in asymptotically Euclidean static vacuum space-time. *Gen. Rel. Grav.*, 19:147–154, 1987.

[46] V. Cardoso and O. J. C. Dias. Small Kerr-anti-de Sitter black holes are unstable. *Phys. Rev. D*, 70:084011, 2004.

[47] V. Cardoso, Ó. J. C. Dias, J. P. S. Lemos, and S. Yoshida. Black-hole bomb and superradiant instabilities. *Phys. Rev. D*, 70:044039, 2004.

[48] S. M. Carroll. *Spacetime and geometry: an introduction to general relativity*. Addison Wesley, 2003.

[49] B. Carter. Axisymmetric black hole has only two degrees of freedom. *Phys. Rev. Lett.*, 26:331–333, 1971.

[50] S. Chandrasekhar. *The mathematical theory of black holes*. Oxford classic texts in the physical sciences. Clarendon Press, 1998.

[51] J. E. Chase. Event horizons in static scalar-vacuum space-times. *Comm. Math. Phys.*, 19:276–288, 1970.

[52] P. T. Chrusciel, J. L. Costa, and M. Heusler. Stationary black holes: uniqueness and beyond. *Living Rev. Rel.*, 15, 2012.

[53] T. Damour, N. Deruelle, and R. Ruffini. On quantum resonances in stationary geometries. *Lett. Nuovo Cim.*, 15:257–262, 1976.

[54] J. C. Degollado and C. A. R. Herdeiro. Stationary scalar configurations around extremal charged black holes. *Gen. Rel. Grav.*, 45:2483–2492, 2013.

[55] J. C. Degollado and C. A. R. Herdeiro. Time evolution of superradiant instabilities for charged black holes in a cavity. *Phys. Rev. D*, 89:063005, 2014.

[56] S. Deser. Absence of static solutions in source-free Yang-Mills theory. *Phys. Lett. B*, 64:463–464, 1976.

[57] S. Deser. Absence of static Einstein-Yang-Mills excitations in three-dimensions. *Class. Quant. Grav.*, 1:L1, 1984.

[58] S. Detweiler. Klein-Gordon equation and rotating black holes. *Phys. Rev. D*, 22:2323–2326, 1980.

[59] O. J. C. Dias, P. Figueras, S. Minwalla, P. Mitra, R. Monteiro, and J. E. Santos. Hairy black holes and solitons in global AdS5. *JHEP*, 08:117, 2012.

[60] S. R. Dolan. Superradiant instabilities of rotating black holes in the time domain. *Phys. Rev. D*, 87:124026, 2013.

[61] S. R. Dolan, S. Ponglertsakul, and E. Winstanley. Stability of black holes in Einstein-charged scalar field theory in a cavity. *Phys. Rev. D*, 92:124047, 2015.

[62] E. E. Donets and D. V. Galtsov. Stringy sphalerons and non-Abelian black holes. *Phys. Lett. B*, 302:411–418, 1993.

[63] S. Droz, M. Heusler, and N. Straumann. New black hole solutions with hair. *Phys. Lett. B*, 268:371–376, 1991.

[64] A. Dumitru and E. Radu. Boson stars with negative cosmological constant. *Nucl. Phys. B*, 665:594–622, 2003.

[65] S. Edward and W. M. Suen. Dynamical evolution of boson stars: Perturbing the ground state. *Phys. Rev. D*, 42:384–403, 1990.

[66] R. Emparan and H. S. Reall. Black holes in higher dimensions. *Living Rev. Rel.*, 11, 2008.

[67] A. A. Ershov and D. V. Galtsov. Nonexistence of regular monopoles and dyons in the $SU(2)$ Einstein-Yang-Mills theory. *Phys. Lett. A*, 150:159–162, 1990.

[68] P. Forgacs and S. Reuillon. On the number of instabilities of cosmological solutions in an Einstein-Yang-Mills system. *Phys. Lett. B*, 568:291–297, 2003.

[69] P. Forgacs and S. Reuillon. Spatially compact solutions and stabilization in Einstein-Yang-Mills-Higgs theories. *Phys. Rev. Lett.*, 95:061101, 2005.

[70] V. Frolov and I. D. Novikov. *Black hole physics: basic concepts and new developments*. Fundamental Theories of Physics. Springer Netherlands, 1998.

[71] D. V. Galtsov and A. A. Ershov. Non-Abelian baldness of colored black holes. *Phys. Lett. A*, 138:160–164, 1989.

[72] D. V. Galtsov and M. S. Volkov. Sphalerons in Einstein-Yang-Mills theory. *Phys. Lett. B*, 273:255–259, 1991.

[73] D. V. Gal'tsov and M. S. Volkov. Charged non-Abelian $SU(3)$ Einstein-Yang-Mills black holes. *Phys. Lett. B*, 274:173–178, 1992.

[74] D. Garfinkle, G. T. Horowitz, and A. Strominger. Charged black holes in string theory. *Phys. Rev. D*, 43:3140–3143, 1991.

[75] S. A. Gentle, M. Rangamani, and B. Withers. A soliton menagerie in AdS. *JHEP*, 05:106, 2012.

[76] G. W. Gibbons. Antigravitating black hole solitons with scalar hair in $N = 4$ supergravity. *Nucl. Phys. B*, 207:337–349, 1982.

[77] G. W. Gibbons and K. Maeda. Black holes and membranes in higher dimensional theories with dilaton fields. *Nucl. Phys. B*, 298:741–775, 1988.

[78] M. Gleiser and R. Watkins. Gravitational stability of scalar matter. *Nucl. Phys. B*, 319:733–746, 1989.

[79] B. R. Greene, S. D. Mathur, and C. M. O'Neill. Eluding the no hair conjecture: black holes in spontaneously broken gauge theories. *Phys. Rev. D*, 47:2242–2259, 1993.

[80] D. Griffiths. *Introduction to elementary particles*. Wiley VCH; 2nd revised edition, 2008.

[81] H. P. Kunzle and A. K. M. Masood-ul-Alam. Spherically symmetric static $SU(2)$ Einstein-Yang-Mills fields. *J. Math. Phys.*, 31:928–935, 1990.

[82] J. B. Hartle. Long-range neutrino forces exerted by Kerr black holes. *Phys. Rev. D*, 3:2938–2940, 1971.

[83] S. W. Hawking. Gravitational radiation from colliding black holes. *Phys. Rev. Lett.*, 26:1344–1346, 1971.

[84] C. Herdeiro, E. Radu, and H. Rúnarsson. Kerr black holes with Proca hair. *Class. Quant. Grav.*, 33:154001, 2016.

[85] C. A. R. Herdeiro, J. C. Degollado, and H. F. Rúnarsson. Rapid growth of superradiant instabilities for charged black holes in a cavity. *Phys. Rev. D*, 88:063003, 2013.

[86] C. A. R. Herdeiro and E. Radu. A new spin on black hole hair. *Int. J. Mod. Phys. D*, 23:1442014, 2014.

[87] C. A. R. Herdeiro and E. Radu. Kerr black holes with scalar hair. *Phys. Rev. Lett.*, 112:221101, 2014.

[88] C. A. R. Herdeiro and E. Radu. Asymptotically flat black holes with scalar hair: a review. *Int. J. Mod. Phys. D*, 24:1542014, 2015.

[89] M. Heusler. On the uniqueness of the Reissner–Nordström solution with electric and magnetic charge. *Class. Quant. Grav.*, 11:L49–L53, 1994.

[90] M. Heusler. *Black hole uniqueness theorems*. Cambridge University Press, 1996.

[91] M. Heusler. No hair theorems and black holes with hair. *Helv. Phys. Acta*, 69:501–528, 1996.

[92] M. Heusler, S. Droz, and N. Straumann. Stability analysis of self-gravitating skyrmions. *Phys. Lett. B*, 271:61–67, 1991.

[93] M. Heusler, S. Droz, and N. Straumann. Linear stability of Einstein Skyrme black holes. *Phys. Lett. B*, 285:21–26, 1992.

[94] S. Hod. Analytic treatment of the charged black-hole-mirror bomb in the highly explosive regime. *Phys. Rev. D*, 88:064055, 2013.

[95] S. Hod. No-bomb theorem for charged Reissner-Nordström black holes. *Phys. Lett. B*, 718:1489–1492, 2013.

[96] S. Hod. Stability of highly-charged Reissner-Nordström black holes to charged scalar perturbations. *Phys. Rev. D*, 91:044047, 2015.

[97] Y. Hosotani and J. Bjoraker. Monopole and dyon solutions in the Einstein-Yang-Mills theory in asymptotically anti-de Sitter space. *AIP Conf. Proc.*, 493:285–290, 1999.

[98] R. Ibadov, B. Kleihaus, J. Kunz, and Y. Shnir. New regular solutions with axial symmetry in Einstein-Yang-Mills theory. *Phys. Lett. B*, 609:150–156, 2005.

[99] R. Ibadov, B. Kleihaus, J. Kunz, and M. Wirschins. New black hole solutions with axial symmetry in Einstein-Yang-Mills theory. *Phys. Lett. B*, 627:180–187, 2005.

[100] W. Israel. Event horizons in static vacuum space-times. *Phys. Rev.*, 164:1776–1779, 1967.

[101] W. Israel. Event horizons in static electrovac space-times. *Commun. Math. Phys.*, 8:245–260, 1968.

[102] B. R. Iyer and A. Kumar. Note on the absence of massive fermion superradiance from a Kerr black hole. *Phys. Rev. D*, 18:4799–4801, 1978.

[103] P. Jetzer. Stability of charged boson stars. *Phys. Lett. B*, 231:433–438, 1989.

[104] T. Johannsen. Testing the no-hair theorem with Sgr A*. *Adv. Astron.*, 2012:486750, 2012.

[105] T. Johannsen. Sgr A* and general relativity. *Class. Quant. Grav.*, 33:113001, 2016.

[106] I. Kamaretsos, M. Hannam, S. Husa, and B. S. Sathyaprakash. Black-hole hair loss: Learning about binary progenitors from ringdown signals. *Phys. Rev. D*, 85:024018, 2012.

[107] R. P. Kerr. Gravitational field of a spinning mass as an example of algebraically special metrics. *Phys. Rev. Lett.*, 11:237–238, 1963.

[108] B. Kleihaus and J. Kunz. Static axially symmetric solutions of Einstein-Yang-Mills-dilaton theory. *Phys. Rev. Lett.*, 78:2527–2530, 1997.

[109] B. Kleihaus and J. Kunz. Static black hole solutions with axial symmetry. *Phys. Rev. Lett.*, 79:1595–1598, 1997.

[110] B. Kleihaus, J. Kunz, and A. Sood. Charged $SU(N)$ Einstein-Yang-Mills black holes. *Phys. Lett. B*, 418:284–293, 1998.

[111] F. R. Klinkhamer and N. S. Manton. A saddle-point solution in the Weinberg-Salam theory. *Phys. Rev. D*, 30:2212–2220, 1984.

[112] K. D. Kokkotas and B. G. Schmidt. Quasi-normal modes of stars and black holes. *Living Rev. Rel.*, 2, 1999.

[113] R. A. Konoplya and A. Zhidenko. Massive charged scalar field in the Kerr-Newman background I: quasinormal modes, late-time tails and stability. *Phys. Rev. D*, 88:024054, 2013.

[114] B. Kuchowics. On the massive vector field of a black hole and of a naked singularity. *Phys. Lett. A*, 51:47–48, 1975.

[115] G. V. Lavrelashvili and D. Maison. A remark on the instability of the Bartnik-McKinnon solutions. *Phys. Lett. B*, 343:214–217, 1995.

[116] T. D. Lee and Y. Pang. Stability of mini-boson stars. *Nucl. Phys. B*, 315:477–516, 1989.

[117] R. Li, J. Zhao, and Y. Zhang. Superradiant instability of D-dimensional Reissner-Nordström black hole mirror system. *Commun. Theor. Phys.*, 63:569–574, 2015.

[118] S. L. Liebling and C. Palenzuela. Dynamical boson stars. *Living Rev. Rel.*, 15, 2012.

[119] H. S. Liu, H. Lu, and C. N. Pope. Thermodynamics of Einstein-Proca AdS black holes. *JHEP*, 1406:109, 2014.

[120] J. M. Maldacena. The Large N limit of superconformal field theories and supergravity. *Int. J. Theor. Phys.*, 38:1113–1133, 1999.

[121] M. Martellini and A. Treves. Absence of superradiance of a Dirac field in a Kerr background. *Phys. Rev. D*, 15:3060–3061, 1977.

[122] A. K. M. Masood-ul Alam. Uniqueness proof of static charged black holes revisited. *Class. Quant. Grav.*, 9:L53–L55, 1992.

[123] N. E. Mavromatos and E. Winstanley. Aspects of hairy black holes in spontaneously broken Einstein-Yang-Mills systems: Stability analysis and entropy considerations. *Phys. Rev. D*, 53:3190–3214, 1996.

[124] A. E. Mayo and J. D. Bekenstein. No hair for spherical black holes: charged and nonminimally coupled scalar field with selfinteraction. *Phys. Rev. D*, 54:5059–5069, 1996.

[125] P. O. Mazur. Proof of uniqueness of the Kerr-Newman black hole solution. *J. Phys. A*, 15:3173–3180, 1982.

[126] P. O. Mazur. Black uniqueness theorems. *arXiv:0101012 [hep-th]*, 2000.

[127] P. L. McFadden and N. G. Turok. Effective theory approach to brane world black holes. *Phys. Rev. D*, 71:086004, 2005.

[128] C. W. Misner and D. H. Sharp. Relativistic equations for adiabatic, spherically symmetric gravitational collapse. *Phys. Rev.*, 136:B571–B576, 1964.

[129] H. Müller zum Hagen, D. C. Robinson, and H. J. Seifert. Black holes in static vacuum space-times. *Gen. Rel. Grav.*, 4:53–78, 1973.

[130] H. Müller zum Hagen, D. C. Robinson, and H. J. Seifert. Black holes in static electrovac space-times. *Gen. Rel. Grav.*, 5:61–72, 1974.

[131] E. T. Newman, R. Couch, K. Chinnapared, A. Exton, A. Prakash, and R. Torrence. Metric of a rotating, charged mass. *J. Math. Phys.*, 6:918–919, 1965.

[132] E. T. Newman and A. I. Janis. Note on the Kerr spinning particle metric. *J. Math. Phys.*, 6:915–917, 1965.

[133] B. C. Nolan and E. Winstanley. On the existence of dyons and dyonic black holes in Einstein-Yang-Mills theory. *Class. Quant. Grav.*, 29:235024, 2012.

[134] B. C. Nolan and E. Winstanley. On the stability of dyons and dyonic black holes in Einstein-Yang-Mills theory. *Class. Quant. Grav.*, 33:045003, 2016.

[135] G. Nordström. On the energy of the gravitational field in Einstein's theory. *Verhandl. Koninkl. Ned. Akad. Wetenschap., Afdel. Natuurk., Amsterdam*, 26:1201–1208, 1918.

[136] Y. N. Obukhov and E. J. Vlachynsky. Einstein-Proca model: Spherically symmetric solutions. *Annals Phys.*, 8:497–510, 1999.

[137] P. Pani, V. Cardoso, L. Gualtieri, E. Berti, and A. Ishibashi. Black hole bombs and photon mass bounds. *Phys. Rev. Lett.*, 109:131102, 2012.

[138] P. Pani, V. Cardoso, L. Gualtieri, E. Berti, and A. Ishibashi. Perturbations of slowly rotating black holes: massive vector fields in the Kerr metric. *Phys. Rev. D*, 86:104017, 2012.

[139] S. Ponglertsakul and E. Winstanley. Solitons and hairy black holes in Einstein-non-Abelian-Proca theory in anti-de Sitter space-time. *arXiv:1606.04644 [gr-qc]*, 2016.

[140] S. Ponglertsakul, E. Winstanley, and S. R. Dolan. Stability of gravitating charged-scalar solitons in a cavity. *Phys. Rev. D*, 94:024031, 2016.

[141] W. H. Press and S. A. Teukolsky. Floating orbits, superradiant scattering and the black-hole bomb. *Nature*, 238:211–212, 1972.

[142] W. H. Press, S. A. Teukolsky, W. T. Vetterling, and B. P. Flannery. *Numerical recipes: the art of scientific computing*. New York: Cambridge University Press, 2007.

[143] D. Psaltis, N. Wex, and M. Kramer. A quantitative test of the no-hair theorem with Sgr A* using stars, pulsars, and the event horizon telescope. *Astrophys. J.*, 818:121–139, 2016.

[144] E. Radu and E. Winstanley. Conformally coupled scalar solitons and black holes with negative cosmological constant. *Phys. Rev. D*, 72:024017, 2005.

[145] T. Regge and J. Wheeler. Stability of a Schwarzschild singularity. *Phys. Rev.*, 108:1063–1069, 1957.

[146] H. Reissner. About the self-gravity of the electric field according to Einstein's theory. *Annalen der Physik*, 50:106–120, 1916.

[147] D. C. Robinson. Four decades of black hole uniqueness theorems. `http://www.mth.kcl.ac.uk/staff/dc_robinson/blackholes.pdf`. [Online; accessed 15-Feb-2016].

[148] D. C. Robinson. Uniqueness of the Kerr black hole. *Phys. Rev. Lett.*, 34:905–906, 1975.

[149] D. C. Robinson. A simple proof of the generalization of Israel's theorem. *Gen. Rel. Grav.*, 8:695–698, 1977.

[150] W. H. Ruan. Existence of infinitely-many black holes in $SU(3)$ Einstein-Yang-Mills theory. *Nonlinear Analysis: Theory, Methods and Applications*, 47:6109–6119, 2001.

[151] W. H. Ruan. Hairy black hole solutions to $SU(3)$ Einstein-Yang-Mills equations. *Commun. Math. Phys.*, 224:373–397, 2001.

[152] P. Ruback. A new uniqueness theorem for charged black holes. *Class. Quant. Grav.*, 5:L155–L159, 1988.

[153] H. Ruegg and M. Ruiz-Altaba. The Stueckelberg field. *Int. J. Mod. Phys. A*, 19:3265–3348, 2004.

[154] R. Ruffini and J. A. Wheeler. Introducing the black hole. *Physics Today*, 24:905–906, 1971.

[155] M. O. P. Sampaio, C. Herdeiro, and M. Wang. Marginal scalar and Proca clouds around Reissner-Nordström black holes. *Phys. Rev. D*, 90:064004, 2014.

[156] N. Sanchis-Gual, J. C. Degollado, C. Herdeiro, J. A. Font, and P. J. Montero. Dynamical formation of a Reissner-Nordström black hole with scalar hair in a cavity. *arXiv:1607.06304 [gr-qc]*, 2016.

[157] N. Sanchis-Gual, J. C. Degollado, P. J. Montero, J. A. Font, and C. Herdeiro. Explosion and final state of an unstable Reissner-Nordström black hole. *Phys. Rev. Lett.*, 116:141101, 2016.

[158] K. Schwarzschild. About the gravitational field of a particle according to the Einstein theory. *Proceedings of the Royal Prussian Academy of Sciences*, 1:189–196, 1916.

[159] B. L. Shepherd and E. Winstanley. Characterizing asymptotically anti-de Sitter black holes with abundant stable gauge field hair. *Class. Quant. Grav.*, 29:155004, 2012.

[160] B. L. Shepherd and E. Winstanley. Dyons and dyonic black holes in $SU(N)$ Einstein-Yang-Mills theory in anti-de Sitter spacetime. *Phys. Rev. D*, 93:064064, 2016.

[161] N. Shiiki and N. Sawado. Regular and black hole solutions in the Einstein-Skyrme theory with negative cosmological constant. *Class. Quant. Grav.*, 22:3561–3574, 2005.

[162] W. Simon. A simple proof of the generalized electrostatic Israel theorem. *Gen. Rel. Grav.*, 17:761–768, 1985.

[163] T. P. Sotiriou. Black holes and scalar fields. *Class. Quant. Grav.*, 32:214002, 2015.

[164] A. A. Starobinskii. Amplification of waves during reflection from a rotating black hole. *JETP*, 37:28–32, 1973.

[165] A. A. Starobinskii and S. M. Churilov. Amplification of electromagnetic and gravitational waves scattered by a rotating black hole. *JETP*, 38:1–5, 1974.

[166] J. Stoer and R. Bulirsch. *Introduction to numerical analysis*. New York: Springer-Verlag, 1980.

[167] N. Straumann and Z. Zhou. Instability of the Bartnik-Mckinnon solution of the Einstein-Yang-Mills equations. *Phys. Lett. B*, 237:353–356, 1990.

[168] N. Straumann and Z. H. Zhou. Instability of a colored black hole solution. *Phys. Lett. B*, 243:33–35, 1990.

[169] D. Sudarsky and T. Zannias. Spherical black holes cannot support scalar hair. *Phys. Rev. D*, 58:087502, 1998.

[170] C. Teitelboim. Nonmeasurability of the baryon number of a black-hole. *Lett. Nuovo Cim.*, 3S2:326–328, 1972.

[171] C. Teitelboim. Nonmeasurability of the lepton number of a black hole. *Lett. Nuovo Cim.*, 3S2:397–400, 1972.

[172] C. Teitelboim. Nonmeasurability of the quantum numbers of a black hole. *Phys. Rev. D*, 5:2941–2954, 1972.

[173] T. Torii, K. Maeda, and M. Narita. Toward the no-scalar-hair conjecture in asymptotically de Sitter spacetime. *Phys. Rev. D*, 59:064027, 1999.

[174] T. Torii, K. Maeda, and M. Narita. Scalar hair on the black hole in asymptotically anti-de Sitter spacetime. *Phys. Rev. D*, 64:044007, 2001.

[175] T. Torii, K. Maeda, and T. Tachizawa. Cosmic colored black holes. *Phys. Rev. D*, 52:R4272–R4276, 1995.

[176] W. Toubal. On the mass of black holes with scalar field hair in anti-de Sitter spacetime. *PhD Thesis*, Univ. of Sheffield, Sheffield, U.K., 2015.

[177] M. Toussaint. A numeric solution for Einstein's gravitational theory with Proca matter and metric-affine gravity. *Gen. Rel. Grav.*, 32:1689–1709, 2000.

[178] W. F. Trench. *Elementary differential equations*. Faculty Authored Books. Book 8., 2013.

[179] R. W. Tucker and C. Wang. An Einstein-Proca-fluid model for dark matter gravitational interactions. *Nucl. Phys. Proc. Suppl.*, 57:259–262, 1997.

[180] N. Uchikata and S. Yoshida. Quasinormal modes of a massless charged scalar field on a small Reissner-Nordström-anti-de Sitter black hole. *Phys. Rev. D*, 83:064020, 2011.

[181] N. Uchikata, S. Yoshida, and T. Futamase. Scalar perturbations of Kerr-AdS black holes. *Phys. Rev. D*, 80:084020, 2009.

[182] W. Unruh. Separability of the neutrino equations in a Kerr background. *Phys. Rev. Lett.*, 31:1265–1267, 1973.

[183] J. J. van der Bij and E. Radu. Gravitating sphalerons and sphaleron black holes in asymptotically anti-de Sitter space-time. *Phys. Rev. D*, 64:064020, 2001.

[184] J. J. Van der Bij and E Radu. On rotating regular non-Abelian solutions. *Int. J. Mod. Phys. A*, 17:1477–1490, 2002.

[185] K. S. Virbhadra and J. C. Parikh. A conformal scalar dyon black hole solution. *Phys. Lett. B*, 331:302–304, 1994. [Erratum: *Phys. Lett. B*,340:265,1994].

[186] M. S. Volkov. Hairy black holes in the XX-th and XXI-st centuries. *arXiv:1601.08230 [gr-qc]*, 2016.

[187] M. S. Volkov, O. Brodbeck, G. V. Lavrelashvili, and N. Straumann. The number of sphaleron instabilities of the Bartnik-McKinnon solitons and non-Abelian black holes. *Phys. Lett. B*, 349:438–442, 1995.

[188] M. S. Volkov and D. V. Galtsov. Non-Abelian Einstein-Yang-Mills black holes. *JETP Lett.*, 50:346–350, 1989.

[189] M. S. Volkov and D. V. Galtsov. Gravitating non-Abelian solitons and black holes with Yang-Mills fields. *Physics Reports*, 319:1–83, 1990.

[190] M. S. Volkov and D. V. Galtsov. Odd parity negative modes of Einstein-Yang-Mills black holes and sphalerons. *Phys. Lett. B*, 341:279–285, 1995.

[191] M. S. Volkov and N. Straumann. Slowly rotating non-Abelian black holes. *Phys. Rev. Lett.*, 79:1428–1431, 1997.

[192] M. S. Volkov, N. Straumann, G. V. Lavrelashvili, M. Heusler, and O. Brodbeck. Cosmological analogs of the Bartnik-McKinnon solutions. *Phys. Rev. D*, 54:7243–7251, 1996.

[193] C. Vuille, J. Ipser, and J. Gallagher. Einstein-Proca model, micro black holes, and naked singularities. *Gen. Rel. Grav.*, 34:689–696, 2002.

[194] E. Winstanley. Existence of stable hairy black holes in $SU(2)$ Einstein-Yang-Mills theory with a negative cosmological constant. *Class. Quant. Grav.*, 16:1963–1978, 1999.

[195] E. Winstanley. On the existence of conformally coupled scalar field hair for black holes in (anti-)de Sitter space. *Found. Phys.*, 33:111–143, 2003.

[196] E. Winstanley. Dressing a black hole with non-minimally coupled scalar field hair. *Class. Quant. Grav.*, 22:2233–2248, 2005.

[197] E. Winstanley. Classical Yang-Mills black hole hair in anti-de Sitter space. *Lecture Notes in Physics*, 769:49–87, 2009.

[198] E. Winstanley. Instability of sphaleron black holes in asymptotically anti-de Sitter space-time. *Phys. Lett. B*, 758:239–243, 2016.

[199] E. Winstanley and N. E. Mavromatos. Instability of hairy black holes in spontaneously broken Einstein-Yang-Mills-Higgs systems. *Phys. Lett. B*, 352:242–246, 1995.

[200] E. Witten. Some exact multipseudoparticle solutions of classical Yang-Mills theory. *Phys. Rev. Lett.*, 38:121–124, 1977.

[201] S. Yang, K. Lin, and J. Li. Hawking radiation of black hole in Einstein-Proca theory. *Int. J. Theor. Phys.*, 53:1710–1716, 2014.

[202] H. Yoshino and H. Kodama. Bosenova collapse of axion cloud around a rotating black hole. *Prog. Theor. Phys.*, 128:153–190, 2012.

[203] D. Youm. Black holes and solitons in string theory. *Phys. Rept.*, 316:1–232, 1999.

[204] Y. B. Zel'dovich. Generation of waves by a rotating body. *Sov. Phys. JETP Lett.*, 14:180–181, 1971.

[205] Y. B. Zel'dovich. Amplification of cylindrical electromagnetic waves reflected from a rotating body. *JETP*, 35:1085–1087, 1972.

[206] Z. H. Zhou. Instability of $SU(2)$ Einstein-Yang-Mills solitons and non-Abelian black holes. *Helv. Phys. Acta*, 65:767–819, 1992.

[207] Z. H. Zhou and N. Straumann. Nonlinear perturbations of Einstein-Yang-Mills solitons and non-Abelian black holes. *Nucl. Phys. B*, 360:180–196, 1991.

[208] T. J. M. Zouros and D. M. Eardley. Instabilities of massive scalar perturbations of a rotating black hole. *Annals of Physics*, 118:139–155, 1979.